Growth and Applications of Photorefractive Potassium Lithium Tantalate Niobate (KLTN)

Thesis by

Rudolf Hofmeister

In Partial Fulfillment of the Requirements

for the Degree of

Doctor of Philosophy

California Institute of Technology

Pasadena, CA
1993
May 12, 1993

Acknowledgements

First, I would like to thank Dr. Amnon Yariv for the support and instruction he has given me over the last four years as a graduate student, and earlier as an undergraduate. I am also especially grateful to Dr. Aharon (Ronnie) Agranat for introducing me to the field of crystal growth, and for the enthusiasm he shared with me. Also, I am indebted to Drs. Mordechai (Moti) Segev and Yaakov Shevy for numerous enlightening discussions on physics and experimental techniques.

Other members, past and present, of the Quantum Electronics Group and greater Caltech community deserve recognition as well for their assistance and support: Dr. Victor Leyva for introducing me to the study of photorefractive KTN; Drs. George Rakuljic and Koichi Sayano for many helpful suggestions on experiments; Jana Mercado for her clerical support; Ali Ghaffari, who assisted in organization in the lab and repair of equipment; Charles Neugebauer for instructing me at length in the art of electronics and computers; and Dr. John Armstrong, Suzanne Lin, and Paul Carpenter for assistance with chemical and structural analyses. I had the pleasure of collaborating with Tony Kewitsch, Doruk Engin, Jim Werner, Korhan Gurkan, and especially Shogo Yagi.

Dr. Peter Fay was my first contact with Caltech; he reinforced my decision to pursue undergraduate studies at Caltech. During my undergraduate years, I was slowly lured away from astronomy by physics, and for a brief period of time, pure mathematics held some attraction for me. Thankfully, noth-

ing came of that. My bent towards the study of optics must have been incited by the instruction of Drs. Demetri Psaltis and William Bridges. In particular, Dr. Psaltis's in-class demonstrations of lasers and acousto-optics and Dr. Bridges's enthusiasm in optics lab classes were instrumental in sparking my interest in the field.

Finally, I would like to thank my parents and Lori Taylor for their unfaltering support during my years of study at Caltech.

Abstract

This thesis describes the growth of photorefractive potassium lithium tantalate niobate (KLTN) single crystal material and characterization of its physical and photorefractive properties. The band transport model is used to discuss the conventional photorefractive effect. The coupled mode formalism is introduced to determine the interaction of interfering light beams in a photorefractive material. Solutions for intensity coupling and phase coupling between two beams, as well as diffraction off a dynamic index grating, are presented for both the copropagating and counterpropagating experimental geometries. These solutions are obtained for arbitrary photorefractive phase, ϕ. The linear- and quadratic electro-optic effects are discussed. The influence of electric field application on the electro-optic tensor is described.

The top seeded solution growth method is reviewed. The design and construction of a crystal growth system is described. The growth procedures of KLTN are enumerated for several compositions and dopant types. Phase diagrams of the KLTN system are determined. Structural properties of the grown crystals are presented. Certain material characteristics of KLTN are discussed. These include the phase transition temperatures, dielectric properties, and the optical absorption properties.

Electric field control of the photorefractive effect, beam coupling and diffraction, is demonstrated for paraelectric KLTN. A theory is developed to describe the diffraction of beams off photorefractive index gratings in para-

electric KLTN. The solutions of the coupled mode equations are used to develop methods of determining the photorefractive phase ϕ in a photorefractive material. These methods are experimentally demonstrated for several types of photorefractive material. In addition, they are used to corroborate a theory describing the magnitude and phase of the net holographic grating in paraelectric KLTN under applied electric field.

A new effect, the Zero External Field Photorefractive (ZEFPR) effect is studied, as well as the application of its unique zero phase ($\phi = 0$) photorefractive gratings. The ZEFPR effect is forbidden by the conventional photorefractive theory; its origin is shown to be due to the creation of strain gratings under spatially periodic illumination. A theory of coordination of microscopic strains by a macroscopic (growth induced) strain is presented. The ZEFPR gratings are shown to possess identically zero phase when no external electric field is applied. This property is employed in the implementation of various new linear phase-to-intensity transduction devices. In particular, an all-optical phase modulation/vibration sensor (microphone) is described. This device is expected to have numerous applications in environments where electric fields cannot be permitted. The possible implementation of ZEFPR gratings in high speed self aligning interferometric data links is discussed, as well as implementation of a novel self aligning holographic image subtraction device.

The final chapter is devoted to the solution of beam coupling and diffraction off of a "fixed" photorefractively written holographic plane grating. The solutions and mathematical tools developed in this chapter are used extensively throughout the thesis: in chapters two and five to describe diffrac-

tion off a photorefractive grating, in chapters seven and eight to solve for the beam coupling off a grating when one beam is phase modulated, and in chapter nine to study the spectral response of fixed holographic interference filters. The techniques are presented with sufficient generality to allow application to numerous other problems, not limited to the ones described here.

Table of Contents

Chapter One

Introduction to the Photorefractive Effect, Materials, and Applications

1.1 Introduction

The photorefractive effect refers to a light induced change in the index of refraction of a material. The effect usually allows large refractive index changes ($\Delta n \sim 10^{-4}$) with relatively low intensities of incident light. The photorefractive effect arises through the photoexcitation, transport, and subsequent retrapping of charge carriers. When a photorefractive medium is illuminated with a spatially nonuniform beam, for example a pattern of dark and bright fringes caused by the interference of two intersecting laser beams, charges are photoexcited in the bright areas, and tend to be retrapped in the dark areas. If a photoexcited charge is retrapped in a bright area of the grating, it is likely that it will be repeatedly photoexcited until it becomes trapped in a dark region where photoexcitation ceases. This process eventually leads to a spatial pattern of trapped charges, and thus an electric space charge field, both of which mimic the spatial intensity pattern. In the conventional photorefractive effect it is this space charge field which leads to a change in the index of refraction via the electro-optic effect.

The effect was first noticed in frequency doubling experiments in lithium niobate ($LiNbO_3$) by Ashkin[1] and independently by Chen[2]. Since the effect was deleterious to the nonlinear optical experiment, the effect was termed "optical damage." Not until Chen[3] realized how the "damage" could be harnessed to provide optical data storage did the effect receive its present name and attention as anything but a nuisance. Numerous applications were realized for the new effect. One of the first was holographic data storage, where it was predicted that the ultimate storage capacity would be ~ 10^{12} bits cm^{-3}.[4,5] The holographic storage of multiple pages of data was another early application, culminating in the simultaneous storage of 500 fixed holograms in one crystal by Staebler[6]. Since the photorefractive effect leads to an index grating which, in general, is not in-phase with the intensity pattern, the coupling of two beams leads to power transfer between them[7]. Beam coupling was used to demonstrate amplification of weak signal beams by factors of several thousand[8].

In 1978 Yariv[9] illustrated that the wave formalism used to describe photorefractive four-wave mixing was identical to the formalism employed to discuss nonlinear optical degenerate four-wave mixing. Optical phase conjugation of a signal beam is the generation of a light beam with an identical phase front to the signal, but propagating in the opposite direction[10,11]. The advantage of using the photorefractive effect would be the possibility of performing optical phase conjugation with low-light intensities. Soon afterwards, this prediction was verified by Huignard[12]. This new application led

to a resurgence of interest in the photorefractive field. Pattern recognition and various types of image processing were demonstrated[13-16], as well as optical distortion correction[17,18].

However, various factors inhibited the commercial implementation of photorefractive based technologies. To the author's knowledge it was not until recently[19] that a single photorefractive device had ever left the laboratory and successfully entered the market. Severe material limitations are responsible for most devices remaining on the lab bench.

One of the most serious problems for most photorefractives is the tendency for transmitted beams to "fanout." Fanout[20-24] is the process of diffuse scattering of light from an incident beam into a continuum of directions towards the optic axis of the crystal. The scattering tends to build up over a long period of time (many times longer than the characteristic grating write time). The name derives from the broad fan of light which forms pointing toward the optic axis (**c**-axis). This process is not fully understood but is believed to result from amplification of scattered light beams partially generated by optical inhomogeneities on the surface or in the bulk of a material. Potassium tantalate niobate (KTN) and potassium lithium tantalate niobate (KLTN) do not display fanout except with application of large electric fields. Fanout diverts optical power from the signal beams, reducing the amount of light transmitted and usually the efficiency of the process being performed. Nevertheless, several applications for the phenomenon have been demonstrated. These include passive phase conjugation[25,26] and optical limiters[27].

For most applications, however, the effect is considered deleterious to photorefractive performance.

The second major problem in implementing photorefractive materials is the erasure of holograms which occurs on readout. The process of writing and erasure are symmetric. Thus when a stored hologram is read out with plane wave illumination, the plane wave redistributes the trapped charge, erasing the grating. Several mechanisms for fixing holograms are known.[28-34] The most well known method is the thermal fixing method wherein a hologram is stored and the crystal is heated to 80-150°C. At these temperatures ionic defects become mobile and drift under the influence of the space charge field. This charge drift compensates the ionic charge pattern. The crystal is then cooled and uniformly illuminated to redistribute the electronic charge, revealing the now fixed ionic charge pattern. This procedure has been demonstrated in $LiNbO_3$ and $KNbO_3$. Other fixing processes including electric field controlled domain reversal in SBN (strontium barium niobate) have been documented[35-37], and recent results at Caltech indicate that other fixing mechanisms are possible in SBN without an applied field[38] . Fixing in KTN was observed by writing a grating in the paraelectric phase, cooling the crystal through its three phase transitions, and then revealing the grating with uniform illumination at low temperature[39]. Recently, a proprietary technique has been reported for efficient hologram fixation in $LiNbO_3$[40]. With the possible exception of the recently reported proprietary technique, these methods have proved problematic and have not seen widespread implementation.

Beyond these fundamental problems are the pure material deficiencies. Most materials lack either large photorefractive coupling constants or fast time response. Many materials lose photorefractive sensitivity at wavelengths longer than approximately 600nm (this cutoff depends somewhat on the photorefractive dopant used). Some crystals are excessively fragile, especially when operated near their phase transition temperature. Finally, most materials, excepting $LiNbO_3$, are still considered difficult to grow. As a consequence, they are expensive and difficult to obtain. The lead time for a high quality $BaTiO_3$ sample, as an example, can be over a year.

1.2 Photorefractive Materials

A material must meet several requirements to become photorefractive. First, it must possess a mid-gap, partially filled, photoionizable impurity level. Second, it must be linearly electro-optic to exhibit the conventional photorefractive effect, or quadratically electro-optic to display the electric field controlled photorefractive effect. A few photorefractive effects exist which do not rely on the electro-optic effect. These include the photorefractive scattering by absorption gratings[41-47] and the zero external field photorefractive (ZEFPR) effect[48]. The nonlinear response of materials to electric fields at temperatures near a structural phase transition has also been shown to produce a photorefractive effect. The dielectric photorefractive effect[49-51] is one example.

The materials[52] which exhibit photorefractive effects include the oxygen-octahedra photorefractives, the sillenites, and certain semiconductors.

Some characteristics which are used to distinguish the various materials from each other are the magnitude of the induced index change, the photorefractive phase (phase between the index grating and the intensity grating), the response time, the dark current and possibility of fixing the grating, and the sensitivity of the material. This last quantity is usually defined as the change in index per unit of absorbed incident intensity.

1.2.1 Ferroelectric Oxygen-Octahedra Photorefractive Materials

The ferroelectric oxygen-octahedra photorefractives are the most widely known and studied photorefractive materials. They include the ilmenite structures, lithium niobate ($LiNbO_3$) and lithium tantalate ($LiTaO_3$), the perovskites potassium niobate ($KNbO_3$), potassium tantalate niobate ($KTa_{1-x}Nb_xO_3$ or KTN), potassium lithium tantalate niobate ($K_{1-y}Li_yTa_{1-x}Nb_xO_3$ or KLTN), and barium titanate ($BaTiO_3$), and finally the tungsten bronzes strontium barium niobate ($Sr_{1-x}Ba_xNbO_3$ or SBN), $Ba_{2-x}Sr_xK_{1-y}Na_yNb_5O_{15}$ (BSKNN), and barium sodium niobate ($Ba_2NaNb_5O_{15}$).

The perovskites, KTN, KLTN, and $BaTiO_3$ are characterized by a high temperature centrosymmetric (cubic) phase and undergo successive transitions to tetragonal, orthorhombic, and finally rhombohedral phases as the temperature is lowered. Lithium niobate and lithium tantalate have a point group symmetry of 3m at room temperature and only assume a high symmetry phase at temperatures above 1200°C (lithium niobate decomposes before reaching this temperature). SBN is the archetype of the tungsten bronze structure,and becomes tetragonal in its high temperature paraelectric phase at tem-

peratures from ~0°C - 120°C depending on composition.

All the ferroelectric oxides are readily amenable to doping by photorefractively active species (usually first row transition metals or lanthanides). They tend to have slow response times and relatively low sensitivities because of their low carrier mobilities. These materials are the only ones in which hologram fixing has been observed.

1.2.2 Sillenites

The photorefractive sillenites include the materials $Bi_{12}SiO_{20}$ (BSO), $Bi_{12}GeO_{20}$ (BGO)[53], and $Bi_{12}TiO_{20}$ (BTO), and recently, Bi_2TeO_5[54]. They are noncentrosymmetric cubic materials. They tend to have much smaller dielectric constants and higher photoconductivities than the ferroelectric oxides, thus the photorefractive sensitivities are higher. The mobilities are about the same as for the ferroelectric oxides, but the electro-optic coefficients tend to be smaller.

1.2.3 Semiconductor- and Other Photorefractives

The photorefractive effect has been demonstrated in several semiconductor materials[55]. These include GaAs, InP[56], and CdFe. The mobilities are much higher in these materials than in the previous two classes, with similar electro-optic coefficients, and the sensitivities are the highest for any type of photorefractive. Semiconductor photorefractives usually respond best in the near infrared, while the other classes of material discussed respond well in the visible.

1.3 Outline of the Thesis

The field of photorefractive materials shows great promise for numerous applications in optical processing and data storage. Unfortunately a lack of high quality photorefractive materials has restricted the development of salable products and devices. It has been the aim of this thesis to develop and characterize a new type of photorefractive material, potassium lithium tantalate niobate (KLTN), to help overcome the material limitations. In addition, the unique properties of KLTN, such as its composition controlled phase transition temperature and electric field controlled photorefractive response, were studied in order to unveil new applications for which such photorefractives are well suited.

In chapter two a band transport model of the photorefractive effect is described. Solutions for both a single charge carrier and two charge carriers are presented. Photorefractive two beam coupling and diffraction are discussed for holograms written with beams propagating in the same direction (copropagating or transmission geometry) and in opposite directions (counterpropagating or reflection geometry). The electro-optic effect is described in chapter three. The linear electro-optic effect and its contribution to the photorefractive effect is discussed first. The distinction between the clamped and unclamped electro-optic coefficients is derived. Effects of an applied electric field on the index ellipsoid are discussed. A study of the quadratic electro-optic effect follows, including the effective linear electro-optic coefficients induced by an electric field in a quadratic medium. Symmetry properties of the linear and quadratic electro-optic tensors are discussed. Lastly, the rotation of the **c**-axis

under application of an electric field in a Kerr material is derived.

Chapter four illustrates the design and construction of a crystal growth system and the growth of paraelectric KLTN with the top seeded solution growth (TSSG) method. Sample growths are described and a range of feasible compositions elaborated. Determination of the compositions of the grown KLTNs along with the seeding temperatures and the flux compositions allows the construction of phase diagrams for the KLTN system. These phase diagrams are presented. Structural characteristics and material properties of the TSSG grown KLTNs are enumerated. The influence of composition on the type and number of phase transitions is discussed, as well as the influence of composition on the phase transition temperature; dielectric properties of several compositions of KLTN are presented. The optical absorption properties are also examined as functions of crystal composition.

Chapter five describes results of experiments demonstrating the electric field control of the photorefractive response in the paraelectric phase. Crystals in the paraelectric phase exhibit no linear electro-optic effect so the conventional photorefractive effect can be modulated by an external field. In diffraction experiments, voltage controlled diffraction efficiencies of 75% are reported. This is the highest reported value for a photorefractive known to the author. A theory is developed to describe the diffraction off a dynamically written grating when the coupling constant g changes between the writing and the reading phase. The theory is shown to agree well qualitatively with experimental data.

Chapters six and seven describe the zero external field photorefractive

(ZEFPR) effect and its device applications. The ZEFPR effect was discovered in paraelectric KTN and KLTN[57,58] but was not identified as a new photorefractive mechanism until recently[48]. It is expected to exist in many photorefractives but was observed in KTN/KLTN first because the conventional photorefractive effect which would otherwise dominate the ZEFPR effect, is forbidden in these materials. Experiments described in chapter six allow the conclusion that the ZEFPR effect is due to a valence state dependent Jahn-Teller relaxation of the oxygen octahedra surrounding the photorefractive centers. This relaxation yields strain gratings in-phase with the intensity pattern. Finally, the strain gratings result in a refractive index change via the photoelastic effect. The ZEFPR effect is unique in the respect that the index grating is identically in-phase with the intensity pattern. This property is shown, in chapter seven, to be the basis of numerous novel devices. The development of a ZEFPR based vibration sensor/ microphone is described. This sensor is all-optical and self aligning, no electric signals are required for operation. It has potential applications for sound/vibration sensing in environments where electrical signals cannot be tolerated or are impractical. These include corrosive or explosive environments. Two other devices are theoretically described in chapter seven: a high speed self aligning interferometric data link, and a self aligning image subtraction device. Both devices would operate by implementation of the ZEFPR effect.

Chapter eight discusses several methods of determining the photorefractive phase and coupling constant of a material. The photorefractive phase ϕ is the material parameter which determines the nature of the coupling be-

tween two interfering beams in a photorefractive crystal, i.e., the relative proportions of phase coupling and intensity coupling. The coupling constant determines the overall magnitude of the coupling. The methods are used to determine the photorefractive phase of crystals of $LiNbO_3$, $BaTiO_3$, and KLTN. A theory is derived to describe the interaction of a ZEFPR grating with a conventional electro-optic grating as a function of applied field. The predicted coupling constants and photorefractive phases are shown to agree with experimentally determined values.

Chapter nine essentially develops a new and exact mathematical formalism for solving certain first-order coupled equations. In this chapter, results are derived that have been implemented in chapters two, five, seven, and eight. The results in all of these prior chapters hinge on the development of the mathematical tools in chapter nine. In addition, the mathematical method is applied in chapter nine to the solution of frequency response of the reflectivity from fixed photorefractive gratings written in the counterpropagating (reflection) geometry.

In chapter nine, the treatment describes the beam coupling and diffraction of beams off a fixed dynamically written holographic grating. The grating can be written in either the copropagating or the counterpropagating geometry (transmission or reflection mode). The analysis for counterpropagating geometry is applied to solving the spectral response of fixed holographic grating interference filters. A numerical study is also reported. The copropagating analysis is applied to the vibration response of beam coupling to a dynamically written grating. The diffraction off a grating is also derived. These last two

results are the ones referred to in chapters two, seven, and eight. The copropagating analysis is also the basis of the theoretical treatment of chapter five describing the diffraction off a fixed photorefractive grating with a non-constant coupling value g.

References for chapter one

[1] A. Ashkin, G. D. Boyd, J. M. Dziedzic, R. G. Smith, A. A. Ballman, H. J. Levinstein, K. Nassau, "Optically-induced refractive index inhomogeneities in $LiNbO_3$ and $LiTaO_3$," Appl. Phys. Lett. **9**, 72 (1966).

[2] F. S. Chen, "A laser-induced inhomogeneity of refractive indices in KTN," J. Appl. Phys. **38**, 3418 (1967).

[3] F. S. Chen, J. T. LaMacchia, D. B. Fraser, "Holographic storage in lithium niobate," Appl. Phys. Lett. **13**, 223 (1968).

[4] P. J. van Heerden, "Theory of optical information storage in solids," Appl. Opt. **2**, 393 (1963).

[5] T. Jannson, "Structural information in volume holography," Opt. Appl. **IX**, 169 (1979).

[6] D. L. Staebler, W. J. Burke, W. Phillips, J. J. Amodei, "Multiple storage and erasure of fixed holograms in Fe-doped $LiNbO_3$," Appl. Phys. Lett. **26**, 182 (1975).

[7] N. V. Kukhtarev, V. B. Markov, S. G. Odulov, M. S. Soskin, and V. L. Vinetskii, "Holographic storage in electro-optic crystals. I. steady state," Ferroelec. **22**, 949-960 (1979).

[8] F. Laeri, T. Tschudi, J. Albers, "Coherent cw image amplifier and oscillator using two wave interaction in a $BaTiO_3$ crystal," Opt. Comm. **47**, 387 (1983).

[9] A. Yariv, "Phase conjugate optics and real-time holography," IEEE J. Quant. Elect. **QE 14**, 650 (1978).

[10] B. Ya. Zel'dovich, N. F. Pilipetsky, and V. V. Shkunov, *Principles of Phase Conjugation*, Springer-Verlag (1985).

[11] R. A. Fisher Ed. , *Optical Phase Conjugation*, Academic Press, Orlando (1983).

[12] J. P. Huignard, J. P. Herriau, P. Aubourg, and E. Spitz, "Phase conjugate wavefront generation via real time holography in $Bi_{12}SiO_{20}$ crystals," Opt. Lett. **4**, 21 (1979).

[13] S. K. Kwong, Y. Tomita, and A. Yariv, "Optical tracking filter using transient energy coupling effect," J. Opt. Soc. Am. B **5**, 1788-1791 (1988).

[14] J. O. White and A. Yariv, "Real-time image processing via four-wave mixing in a photorefractive medium," Appl. Phys. Lett. **37**, 5-7 (1980).

[15] S. K. Kwong, G. A. Rakuljic, and A. Yariv, "Real-time image subtraction and 'exclusive or' operation using a self-pumped phase conjugate mirror," Appl. Phys. Lett. **48**, 201-203 (1986).

[16] S. K. Kwong, G. A. Rakuljic, V. Leyva, and A. Yariv, "Real-time image processing using a self-pumped phase conjugate mirror," Proc. SPIE **613**, 36-42 (1986).

[17] M. Cronin-Golomb, B. Fischer, J. Nilsen, J. O. White, and A. Yariv, "Laser with dynamic holographic intracavity distortion correction capability," Appl. Phys. Lett. **41**, 219-220 (1982).

[18] V. Wang and C. R. Giuliano, "Correction of phase aberrations via stimulated Brillouin scattering," Opt. Lett. **2**, 4-6 (1978).

[19] Accuwave corporation has recently introduced a holographic photorefractive interference filter tuned to the H_α line for solar observation. Its spectral bandpass of 1/8 Å is apparently superior to that of conventional Lyot filters.

[20] M. Segev, Y. Ophir, and B. Fischer, "Nonlinear multi 2-wave mixing, the fanning process and its bleaching in photorefractive media," Opt. Comm. **77**, 265- 274 (1990).

[21] M. Segev, Y. Ophir, and B. Fischer, "Photorefractive self-defocusing," Appl. Phys. Lett. **56**, 1086-1088 (1990).

[22] C. L. Adler, W. S. Rabinovich, A. E. Clement, G. C. Gilbreath, and B. J. Feldman, "Comparison of photorefractive beam fanning using monochromatic and achromatic 2-wave mixing in SBN," Opt. Comm. **94**, 609 -618 (1992).

[23] R. S. Hathcock, D. A. Temple, C. Warde, "Beam fanning in $BaTiO_3$-Cr," J. Opt. Soc. Am. A **2**, 63 -73 (1985).

[24] M. S. Tobin and M. R. Stead, "Measurements of beam fanning in barium-titanate," J. Opt. Soc. Am. A **2**, 37 -47 (1985).

[25] V. A. Dyakov, S. A. Korolkov, A. V. Mamaev, V. V. Shkunov, and A. A. Zozulya, "Reflection-grating photorefractive self-pumped ring mirror," Opt. Lett. **16**, 1614 -1616 (1991).

[26] M. Cronin-Golomb, K. Y. Lau, A. Yariv, "Infrared photorefractive passive phase conjugation with $BaTiO_3$ - demonstrations with GaAlAs and 1.09μm

Ar & lasers" Appl. Phys. Lett. **47**, 567 -569 (1985).

[27] S. E. Bialkowski, "Application of the $BaTiO_3$ beam-fanning optical limiter as an adaptive spatial filter for signal enhancement in pulsed infrared laser-excited photothermal spectroscopy," Opt. Lett. **14**, 1020 - 1022 (1989).

[28] L. Arizmendi, P. D. Townsend, M. Carrascosa, J. Baquedano, and J. M. Cabrera, "Photorefractive fixing and related thermal effects in $LiNbO_3$," J. Phys: Condens. Matter **3**, 5399 -5406 (1991).

[29] G. Montemezzani and P. Gunter, "Thermal hologram fixing in pure and doped $KNbO_3$," J. Opt. Soc. Am. B **7**, 2323 - 2328 (1990).

[30] S. W. McCahon, D. Rytz, G. C. Valley, M. B. Klein, and B. A. Wechsler, "Hologram fixing in $Bi_{12}TiO_{20}$ using heating and an AC electric field," Appl. Opt. **28**, 1967 - 1969 (1989).

[31] P. Hertel, K. H. Ringhofer, R. Sommerfeldt, "Theory of thermal hologram fixing and application to $LiNbO_3$-Cu," Phys. St. S. A **104**, 855 -862 (1987).

[32] J. P. Herriau and J. P. Huignard, "Hologram fixing process at room-temperature in photorefractive $Bi_{12}SiO_{20}$ crystals," Appl. Phys. Lett. **49**, 1140 -1142 (1986).

[33] F. Elguibaly, "Information storage in ferroelectrics - thermal fixing," Can. J. Phys. **66**, 655 -658 (1988).

[34] R. Sommerfeldt, R.A. Rupp, H. Vormann, E. Kratzig, "Thermal fixing of volume phase holograms in $LiNbO_3$-Cu," Phys. St. S. A **99**, 15 -18 (1987).

[35] F. Micheron and G. Bismuth, "Electrical control of fixation and erasure of

holographic patterns in ferroelectric materials," Appl. Phys. Lett. , **20**, 79-81, (1972).

[36] F. Micheron and J. C. Trotier, "Photoinduced phase transitions in (Sr,Ba)Nb_2O_6 crystals and applications," Ferroelectrics, **8**, 441-442, (1974).

[37] F. Micheron and G. Bismuth, "Field and time thresholds for the electrical fixation of holograms recorded in $(Sr_{0.75}Ba_{0.25})Nb_2O_6$ crystals," Appl. Phys. Lett. , **23**, 71-72, (1973).

[38] A. Kewitsch, M. Segev, and A. Yariv, unpublished.

[39] V. Leyva, A. Agranat, and A. Yariv, "Fixing of a photorefractive grating in $KTa_{1-x}Nb_xO_3$ by cooling through the ferroelectric phase transition," Opt. Lett. **16**, 554-556 (1991).

[40] G. Rakuljic, A. Yariv, and V. Leyva, "High resolution volume holography using orthogonal data storage," Photorefractive Materials, Effects, and Devices Conference of OSA, July 29-31, 1991, Beverley, MA, paper MD-3; G. Rakuljic, private communication.

[41] A. A. Kamshilin, "Simultaneous recording of absorption and photorefractive gratings in photorefractive crystals," Opt. Comm. **93**, 350 -358 (1992).

[42] M. H. Garrett, P. Tayebati, J. Y. Chang, H. P. Jenssen, and C. Warde, "Shallow-trap-induced positive absorptive 2-beam coupling gain and light-induced transparency in nominally undoped barium-titanate," J. Appl. Phys. **72**, 1965 -1969 (1992).

[43] R. S. Cudney, R. M. Pierce, G. D. Bacher, and J. Feinberg, "Absorption

gratings in photorefractive crystals with multiple levels," J. Opt. Soc. B **8**, 1326 -1332 (1991).

[44] T. Jaaskelainen and S. Toyooka, "Analysis of absorption reflection gratings," Opt. Comm. **71**, 133 - 137 (1989).

[45] S. A. Boothroyd, J. Chrostowski and M. S. OSullivan, "2-wave mixing by phase and absorption gratings in saturable absorbers," J. Opt. Soc. Am. B **6**, 766 - 771 (1989).

[46] K. Walsh, T. J. Hall, and R. E. Burge, "Influence of polarization state and absorption gratings on photorefractive 2-wave mixing in GaAs," Opt. Lett. **12**, 1026 -1028 (1987).

[47] M. Gehrtz, J. Pinsl, C. Brauchle, "Sensitive detection of phase and absorption gratings - phase modulated homodyne detected holography," Appl. Phys. B **43**, 61 -77 (1987).

[48] R. Hofmeister, A. Yariv, S. Yagi, and A. Agranat, "A new photorefractive mechanism in paraelectric crystals : A strain coordinated Jahn-Teller relaxation," Phys. Rev. Lett. , **69**, 1459-1462, (1992).

[49] A. Agranat and Y. Yacoby, "Dielectric photorefractive crystals as the storage medium in holographic memory systems," J. Opt. Soc. Am. B **5**, 1792 - 1799 (1988).

[50] A. Agranat, Y. Yacoby, "The dielectric photorefractive effect - a new photorefractive mechanism," IEEE Ultras. **33**, 797 -799 (1986).

[51] A. Agranat and Y. Yacoby, "Temperature dependence of the dielectric in-

duced photorefractive effect," Ferroelec. Lett. **4**, 19 -25 (1985).

[52] G. C. Valley, M. B. Klein, R. A. Mullen, D. Rytz, and B. Wechsler, "Photorefractive materials," Ann. Rev. Mater. Sci. , **18**, 165-188, (1988).

[53] V. N. Astratov and A. V. Ilinskii, "The evolution of the photoinduced space-charge and electric-field distribution in photorefractive sillenite ($Bi_{12}GeO_{20}$, $BI_{12}SiO_{20}$) crystals," Ferroelec. **75**, 251 -269 (1987).

[54] I. Foldvari, H. M. Liu, R. C. Powell, and A. Peter, "Investigation of the photorefractive effect in Bi_2TeO_5," J. Appl. Phys. **71**, 5465 -5473 (1992).

[55] D. F. Eaton, "Nonlinear optical materials - the great and near great," ACS Symp. S. **455**, 128 -156 (1991).

[56] D. D. Nolte, D. H. Olsen, E. M. Monberg, P. M. Bridenbaugh, and A. M. Glass, "Optical and photorefractive properties of InP-Ti - a new photorefractive semiconductor," Opt. Lett. **14**, 1278 - 1280 (1989).

[57] A. Agranat, R. Hofmeister, and A. Yariv, "Characterization of a new photorefractive material: $K_{1-y}L_yT_{1-x}N_x$," Opt. Lett. , **17**, 713-715 (1992).

[58] Changxi Yang, Dadi Wang, Peixian Ye, Qincai Guan, and Jiyang Wang, "Photorefractive diffraction dynamic during writing in paraelectric KTN crystals," Opt. Letters **17**, 106-108 (1992).

Chapter Two

The Photorefractive Effect

2.1 Introduction

The photorefractive effect can be defined as a change in the refractive index of a material caused by illumination with light. The incident light photo-excites free carriers preferentially in regions of high intensity where they undergo transport, are repeatedly trapped and re-excited, and are finally trapped in a region of low-light intensity (see Fig. 2-1). The result is a space charge field spatially correlated with the intensity pattern creating an index of refraction pattern (grating) via the electro-optic effect. Two beams propagating in a photorefractive medium can interact with each other by coherent scattering from the grating formed by their interference. The phases and the intensities of the two beams can be coupled. This chapter describes the band transport mechanism of the photorefractive effect, and the formation of the space charge field. The coupled mode equations are used to calculate the influence of index gratings on propagation of beams through the material. Since the index gratings are written dynamically, the solution for the interaction is performed self-consistently.

The photorefractive effect[1,2,3] was first noticed in frequency doubling

experiments in $LiNbO_3$ by Ashkin[4]. Soon thereafter Chen[5-7] reported the effect in KTN and proposed that a space charge field could be formed by photoexcitation of electrons, subsequent drift in an electric field, and retrapping in regions of low-light intensity. This work is the basis of modern theories on the effect. Since then, the role of defects and transition metal dopants[8-10] has been recognized as the source of the photoionizable charge carriers. Three transport processes have been identified: thermal diffusion[11], drift[12,13] (when an external field is applied), and the photovoltaic effect[14,15].

A hopping model for charge transport in $BaTiO_3$ has been suggested by Feinberg[16]. In this model, the charges hop from filled to vacant sites when exposed to optical radiation. Although the model is statistical, for short hopping lengths the results are similar to those obtained with the band transport model. For large hopping distances the results depend strongly on the statistics of the hopping. This model has not seen a great deal of attention since it is difficult to ascertain a plausible physical justification for the statistical behavior required to obtain good correlation with experiments.

2.2 Band Transport Model

The band transport model requires the photogeneration of charge carriers. The atomic species which generates the charge carriers (the donor species) must be stable in the crystal in at least two valence configurations. We write $N_D = N_D^+ + N_D^0$ where N_D is the total donor ion concentration. The more negative of these two states, designated as N_D^0 can act as an electron donor al-

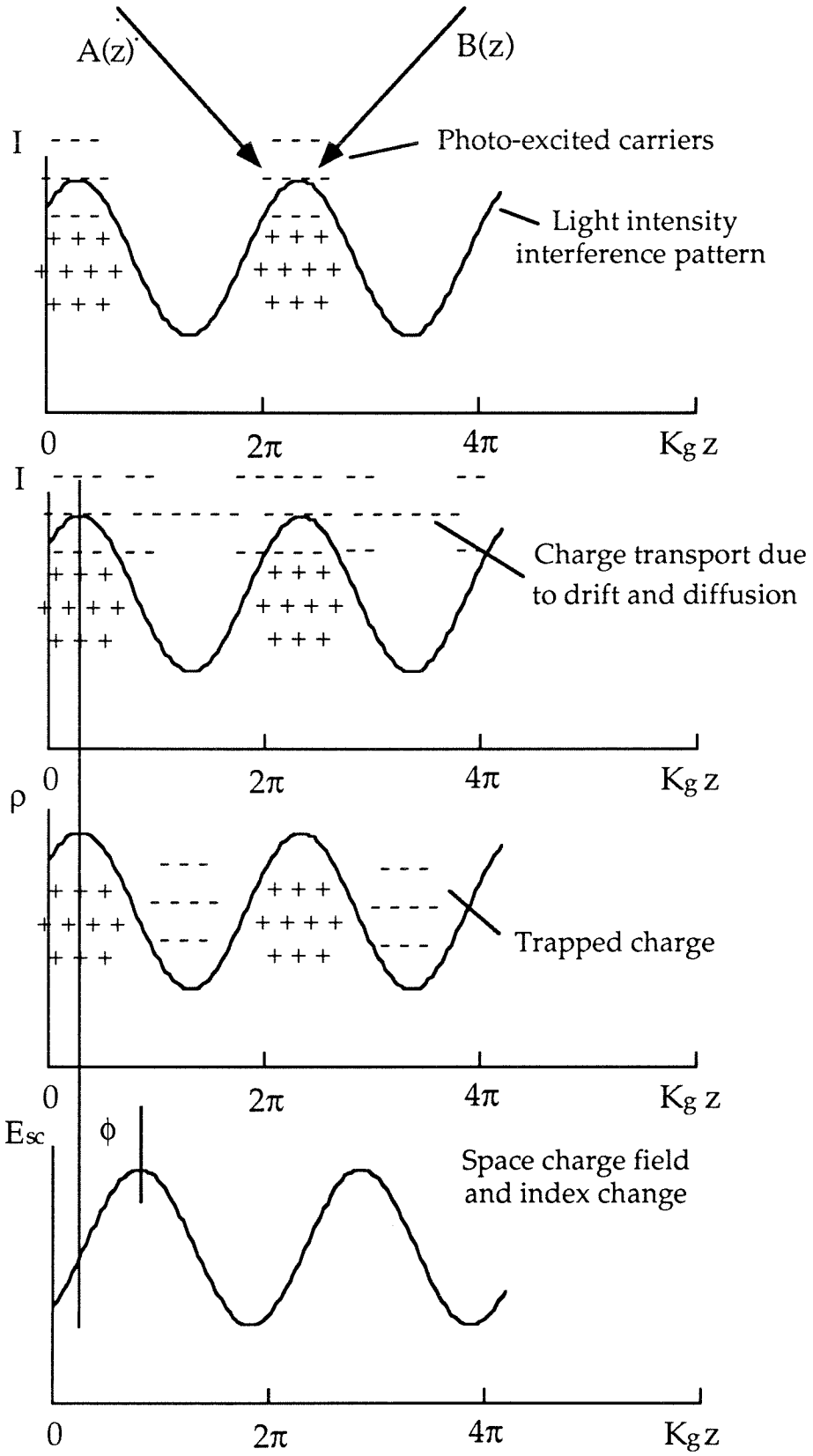
A(z)
B(z)
I
Photo-excited carriers
Light intensity
interference pattern
0
2π
4π
Kg z
I
Charge transport due
to drift and diffusion
0
2π
4π
Kg z
ρ
Trapped charge
0
2π
4π
Kg z
Esc
ϕ
Space charge field
and index change
0
2π
4π
Kg z

Figure 2-1 Diffusion Limited Photorefractive Mechanism (previous page)

The photorefractive effect is a change in the refractive index of a material caused by illumination with light. Two incident laser beams A(z) and B(z) interfere in a photorefractive material. Free carriers are preferentially photoexcited in regions of high intensity where they undergo transport, are repeatedly trapped and re-excited, and are finally trapped in a region of low-light intensity. The steady-state charge distribution ρ creates a space charge field. In the diffusion limited case the charge modulation is in phase with the intensity pattern. The field is shifted exactly one-quarter grating wavelength because $\mathrm{div}E = 4\pi\rho/\varepsilon$. Thus the phase between the intensity pattern and the space charge field is $\phi = \pi/2$.

Figure 2-2 Drift Limited Photorefractive Mechanism (next page)

The light intensity pattern forms a space charge field as in Fig. 2-1, but the large applied field (drift limited case) prevents the charge from accumulating exactly in phase with the intensity minima; instead it is shifted by a phase $\pi/2$, so that the space charge field is shifted by $\phi = \pi$ from the intensity pattern. This can be shown by considering the conductivity which must be in phase with the intensity. Since the current $J = \sigma E$ must be uniform in the steady state, we conclude that E_{SC} is exactly out of phase with the conductivity σ.

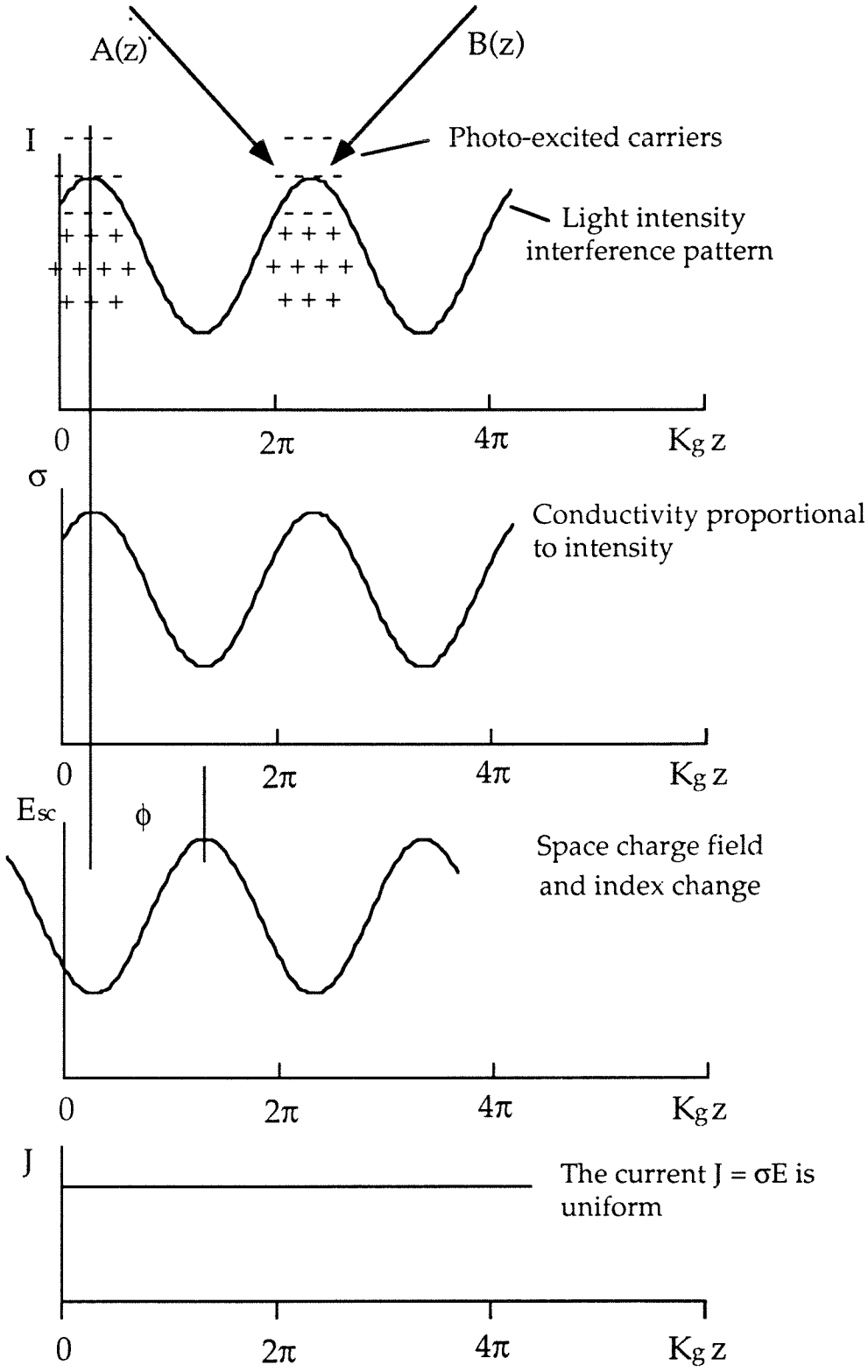
A(z)
B(z)
I
Photo-excited carriers
Light intensity
interference pattern
0
2π
4π
Kg z
σ
Conductivity proportional
to intensity
0
2π
4π
Kg z
Esc
ϕ
Space charge field
and index change
0
2π
4π
Kg z
J
The current J = σE is
uniform
0
2π
4π
Kg z

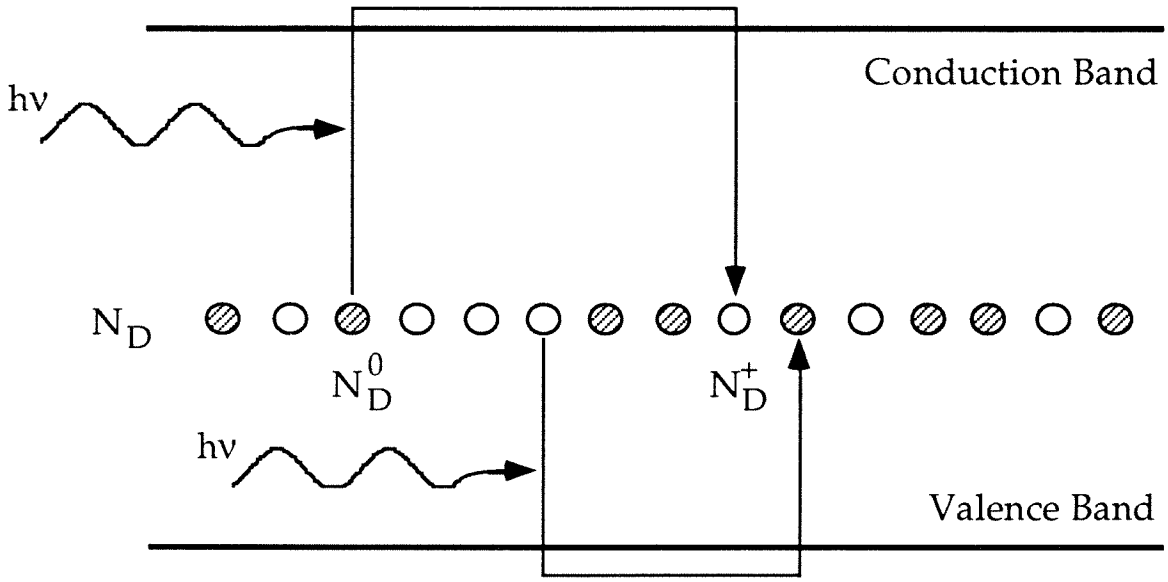

Figure 2-3 The Band Transport Model

The energy diagram for the single photorefractive species, two charge carrier band transport model. A mid-band dopant level is occupied with $N_D = N^+_D + N^0_D$ dopant ions. An electron (hole) is photoexcited from an N^0_D (N^+_D) ion by incident radiation to the conduction (valence) band where it diffuses and/or drifts under an applied field before being retrapped at an N^+_D (N^0_D) site.

lowing photoexcitation or thermal excitation of charge to the conduction band leaving an ionized N_D^+ site behind. The mobile charge is retrapped at one of the more positive sites, called N_D^+, turning it into an unionized N_D^0 in the process. At the same time, hole mobility can occur when a hole is photoexcited from an N_D^+ site to the valence band and is retrapped at an N_D^0 site. These processes are illustrated in Fig. 2-3. Charge neutrality is preserved by postulating a number of non photoactive acceptor sites $N_A = N_D^+$ whose only purpose is to provide the two species of ions N_D. If no N_D^+ sites existed, the excited charge would always be forced to recombine with the N_D^+ site from which it was photoexcited. This would eliminate any transport.

The designations N_D^+ and N_D^0 are meant to convey the relative ionization state. In practice, the N_D^0 site is always positively ionized. In the materials discussed in this thesis, the two stable states of ions are given by Cu^{1+} and Cu^{2+} or Fe^{2+} and Fe^{3+}. In both cases, the less positively charged of the two ionic species acts as the donor while the more positive acts as the trap.

The earliest recognized form of transport was thermal diffusion. Amodei realized[11] that in the diffusion dominated case a space charge is set up with magnitude $E_{SC} = kTK/e$ which is shifted by one quarter of a wavelength relative to the intensity grating. K is the grating wavevector, T is the temperature, and k is Boltzman's constant. Fig. 2-1 illustrates the diffusion dominated formation of space charge. The crystal is illuminated with a periodic (sinusoidal) intensity pattern. Charges tend to accumulate in the dark re-

gions. By Poisson's equation $E_{sc} \sim \int \rho \, dz$, the space charge field is exactly $\pi/2$ out of phase with the intensity pattern.

The transport caused by the drift in an electric field leads to a different result. In Fig. 2-2 the case for the drift dominated case is illustrated. The intensity pattern is again taken to be sinusoidal, and it is known that in the steady state the current must be constant to prevent the build up of charge within the crystal (continuity equation). Since the local conductivity is taken to be proportional to the excitation rate, i.e., to the intensity, the space charge field must be inversely proportional to the intensity. Only in this way can the product of the conductivity and the field (the current) remain constant.

Glass et al. were responsible for equations describing the photovoltaic current[14]. All non centrosymmetric crystals can display a photovoltaic effect in which a photocurrent is generated without the application of an external field. When charges are photoexcited they are generated with a preferred direction of motion. The retrapping of electrons can also proceed anisotropically, thus contributing to the current. The effect was explained as an asymmetric charge transfer process. A directional photocurrent can result if the orbitals of the defect ions overlap asymmetrically with the host lattice ion orbitals along the polar axis. This condition is only forbidden in centrosymmetric materials. Since the photovoltaic effect yields a current in the same way as does application of an electric field, it also holds that, in the steady state, the current must become uniform by the continuity conditions. Thus the space charge field must be exactly out of phase with the intensity pattern by the same argument as in the drift dominated case above.

In photorefractive materials it can happen that any one of these transport processes is dominant, in which case the space charge field behaves as indicated in the preceding paragraphs. In general, however, two or three of the mechanisms play a significant role and the solution of the space charge field is determined by a set of rate equations. The development and solution of the photorefractive rate equations follows.

2.2.1 The Rate Equations

In the following section the rate equations for the space charge field are solved neglecting the photovoltaic contribution. It is noted that electrons are excited into the conduction band at a rate $[\beta_e + s_e I/(h\nu)]\,(N_D - N_D^+)$, and they combine at a rate $\gamma_e n N_D^+$. Similarly, the excitation rate for holes is given by $[\beta_h + s_h I/(h\nu)]\,N_D^+$ and the recombination rate by $\gamma_h p\,(N_D - N_D^+)$. The variables are defined on the next page. The rate equations for electrons and holes are written as

$$\frac{\partial n}{\partial t} - \nabla\cdot\frac{j_e}{e} = \left(s_e\frac{I}{h\nu} + \beta_e\right)(N_D - N_D^+) - \gamma_e\, n\, N_D^+ \qquad (2.1a)$$

$$\frac{\partial p}{\partial t} - \nabla\cdot\frac{j_h}{e} = \left(s_h\frac{I}{h\nu} + \beta_h\right)N_D^+ - \gamma_h\, p\,(N_D - N_D^+). \qquad (2.1b)$$

The continuity equation is given by

$$\nabla\cdot J = \nabla\cdot j_e + \nabla\cdot j_h = e\,\frac{\partial}{\partial t}(n - N_D^+ - p). \qquad (2.2)$$

The current equations for electrons and holes are

$$j_e = n\,e\,\mu_e\,E + e\,D_e\,\nabla n + \kappa_e\,s_e\,(N_D - N_D^+)\,I \qquad (2.3a)$$

$$j_h = p\, e\, \mu_h E + e\, D_h \nabla p + \kappa_h s_h N_D^+ I. \qquad (2.3b)$$

Equations (2.3a,b) are often expressed using the Einstein relation $eD = kT\mu$, where T is the temperature. Finally, the Poisson equation gives

$$\nabla \cdot E = \frac{\rho}{\varepsilon\varepsilon_0} = -\frac{e}{\varepsilon\varepsilon_0}(n + N_A - N_D^+ - p). \qquad (2.4)$$

The variables used are defined (in order of appearance)

I = incident light intensity

$h\nu$ = optical energy of incident photon

β_e (β_h) = thermal generation rate for electrons (holes)

s_e (s_h) = photoexcitation cross section for electrons (holes)

N_D = density of defect ions = $N_D^0 + N_D^+$

N_D^+ = density of ionized defect ions

N_D^0 = density of unionized defect ions

γ_e (γ_h) = recombination rate of electrons (holes)

n = free electron density

p = free hole density

j_e (j_h) = total electron (hole) current density

e = electronic charge

E = electric field

μ_e (μ_h) = electron (hole) mobility

D_e (D_h) = diffusion coefficient for electrons (holes)

κ_e (κ_h) = photovoltaic coefficient for electrons (holes)

ε = relative dielectric constant

ε_0 = permittivity of free space

ρ = total charge density.

The equations given above are used to solve for the space charge field when the material is illuminated with the intensity pattern given by

$$I(x) = I\,(1 + m\,e^{i\,K\,x} + c.\,c.\,) \tag{2.5}$$

where m is the modulation index. If the intensity pattern is caused by coherent interfering beams then m is given by $m = (I_1\,I_2)^{1/2}/\,I$ where I_1 and I_2 are the intensities of the individual interfering beams and $I = I_1 + I_2$. K is the grating wavevector $K = 2\pi/\lambda_g$ which is also directed along x. When $m<<1$ the spatial dependence of n, p, N_D^+, and E can be approximated by linearized Fourier expansions. In the following analysis only terms at the fundamental spatial frequency are included. In the case of large modulation depth, higher order harmonics of these quantities should be considered[17,18]. It should be noted that if one of the interfering beams is an image containing numerous spatial frequencies, the modulation depth of the image as a whole might be

quite high while the modulation depth of any individual spatial frequency remains small. In this case, the model for m<<1 would still apply.

2.2.2 Single-Charge Carrier Solution

The simplest case of the band transport model is the case of only a single type and species of charge carrier, usually considered to be the electron. Most materials can be approximated by this case. All parameters describing holes in equations (2.1) through (2.4) are set to zero: $p = \gamma_h = s_h = \beta_h = 0$. The photovoltaic contribution is neglected. The following identities hold in this case:

$$\frac{\partial N_D^+}{\partial t} = \frac{\partial n}{\partial t} - \nabla.\frac{j_e}{e}. \tag{2.6}$$

The set of equations (2.1), (2.3), and (2.4) given above reduce to

$$\frac{\partial}{\partial t}(n - N_D^+) = \mu_e\left(E \cdot \nabla n + n\,\nabla\cdot E + \frac{kT}{e}\nabla^2 n\right) \tag{2.7}$$

$$\frac{\partial N_D^+}{\partial t} = \left(s_e\frac{I}{h\nu} + \beta_e\right)(N_D - N_D^+) - \gamma_e\, n\, N_D^+ \tag{2.8}$$

$$\nabla\cdot E = -\frac{e}{\varepsilon\varepsilon_0}(n + N_A - N_D^+). \tag{2.9}$$

Linearized Fourier expansions.are postulated as the solutions for N_D^+, n, and E. They are of the form

$$N_D^+ = N_{D,0}^+ + \frac{1}{2}N_{D,1}^+ e^{iKx} + \text{c. c.} \tag{2.10a}$$

$$n = n_0 + \frac{1}{2}n_1 e^{iKx} + \text{c. c.} \tag{2.10b}$$

$$E = E_0 + \frac{1}{2} E_1 e^{i K x} + c.c. \tag{2.10c}$$

Since the crystals are charge balanced $N^+_{D,0} - n_0 - N_A = 0$. In addition the approximations $N_D >> N_A >> n_0$ and $N^+_{D,1} \approx N_A >> n_1$ are used. After some work a solution for the space charge field is obtained[19,20]

$$E_{sc} = -i\, m \frac{E_N(E_0 + i\, E_d)}{E_0 + i\,(E_N + E_d)} (1 - e^{-t/\tau}) \tag{2.11}$$

$$E_N = \frac{e\, N_A}{\varepsilon\, K}\left(1 - \frac{N_A}{N_D}\right) \qquad E_d = \frac{k_b T K}{e} \tag{2.12a,b}$$

where E_N is the charge limited space charge field, E_d is the thermal field, and E_0 is the spatially uniform applied field. The time constant[21] τ is given by

$$\tau = t_0 \frac{E_0 + i\,(E_{\mu_e} + E_d)}{E_0 + i\,(E_N + E_d)} \tag{2.13}$$

$$t_0 = \frac{h\nu\, N_A}{s_e\, I_0\,(1 + \beta_e\, h\nu/(s_e I_0))\, N_D} \tag{2.14}$$

where

$$E_{\mu_e} = \frac{\gamma\, N_A}{\mu_e\, K}. \tag{2.15}$$

The time constant for approaching the steady-state value of the space charge field is inversely proportional to the incident intensity. When an electric field is applied the response time τ becomes imaginary so that the space charge field oscillates before reaching the steady state.

2.2.3 Two-Charge Carrier Solution

Here the case of a single photorefractive species with two charge carriers - both the electron and the hole- is considered. Equations (2.1) - (2.5) apply in this case. The solution for the space charge field has been obtained in the steady state with no applied field[22,23,24]. It is

$$E_{sc} = i\,m\,E_N \frac{E_d\,(\sigma_h - \sigma_e)}{(E_d + E_N)\,(\sigma_h + \sigma_e)} \tag{2.16}$$

where E_N and E_d are the same as above. The electron and hole conductivities are given by[25]

$$\sigma_e = n\,e\,\mu_e = \frac{e\,\mu_e\,s_e\,I_0}{h\nu\,\gamma_e}\left(\frac{N_D}{N_D^+} - 1\right) \tag{2.17}$$

$$\sigma_h = p\,e\,\mu_h = \frac{e\,\mu_h\,s_h\,I_0}{h\nu\,\gamma_h}\left(\frac{N_D}{N_D^+} - 1\right)^{-1}. \tag{2.18}$$

When the electron and hole conductivities are equal, no space charge field can be written in the steady state. Whenever the hole mobility is nonzero, the space charge field given by (2.17) will be smaller than that predicted by the single-charge carrier solution (2.11).

2.2.4 Photorefractive Index Change

The space charge field modifies the index of refraction of the material via the electro-optic effect. As described in further detail in chapter three, the index ellipsoid is modified by an amount

$$\Delta\beta_{ij} = \Delta\left(\frac{1}{n_{ij}^2}\right) = r_{ijk}\,E_k + g_{ijkl}\,\varepsilon_0^2\,(\varepsilon_k - 1)\,(\varepsilon_l - 1)\,E_k E_l \tag{2.19}$$

where $\Delta\beta_{ij}$ are the electric field induced changes in the "axis lengths" of the

index ellipsoid, and n_{ij} are the components of the index of refraction tensor. r_{ijk} and g_{ijkl} are, respectively, components of the linear and quadratic electro-optic tensors, while ε_i and E_i are the dielectric constant and electric field along the axis i. The approximation $\varepsilon_i - 1 \approx \varepsilon_i$ is usually made.

In noncentrosymmetric materials, r_{ijk} is nonzero, in general. The quadratic coefficients are often neglected in these materials. If the space charge field is directed along the c-axis, as it is in the symmetric geometry (Fig. 2-4), equation (2.19) reduces to

$$\Delta\left(\frac{1}{n_{ij}^2}\right) = r_{ij3}\, E_{sc} \tag{2.20a}$$

$$\Delta n_{ij} = -\frac{n_0^3}{2}\, r_{ij3}\, E_{sc} \tag{2.20b}$$

where n_0 is the nominal index of refraction with no applied field, and we have used the relation $\Delta(1/n^2) = -(2/n^3)\,\Delta n$. Also, the convention of designating the c axis the "3" axis has been followed.

For centrosymmetric materials, i.e., ones with a center of inversion, the linear electro-optic coefficient is required to be zero (see chapter three). Thus the quadratic electro-optic effect is the lowest order effect allowed. If the space charge field is directed along axis 3 and an external field E_0 is applied along the same axis, then $E_3 = E_{sc} + E_0$. The change in the refractive index due to E_{sc} alone is given by

$$\Delta n_{ij}(E_0+E_{sc}) - \Delta n_{ij}(E_0) = \frac{n_0^3}{2}\, g_{ij33}\, (\varepsilon_3\varepsilon_0)^2 \left((E_{sc} + E_0)^2 - E_0^2 \right). \tag{2.21a}$$

Since we are interested in an index grating with the same spatial dependence as the intensity pattern, that is, e^{iKz}, the E_{sc}^2 term is ignored. The useful, Bragg matched part of the index grating reduces to

$$\Delta n_{ij} = n_0^3 \, g_{ij33} \, (\varepsilon_3 \varepsilon_0)^2 \, E_{sc} \, E_0. \qquad (2.21b)$$

Thus the Bragg matched contribution to the index grating is present only with, and is proportional to, an applied electric field.

In paraelectric materials the relative dielectric constant obeys the Curie-Weiss law and near the Curie temperature can reach values as high as 10^5 [26]. This can lead to large index gratings when a field is applied. When the external applied field is time varying the photorefractive response is modulated. This has been demonstrated in KTN[26] and KLTN at frequencies up to 20kHz.

2.3 Photorefractive Beam Coupling

When two beams interfere in a photorefractive medium they create an index grating as described above. This index grating is shifted in phase with respect to the intensity grating by an amount ϕ[27]. In chapter one it was mentioned that this nonzero photorefractive phase leads to energy transfer between the two beams. The intensity coupling allows several interesting applications. These include the amplification of a weak signal beam by a pump beam as well as optical signal processing. But most importantly, the possibility of gain affords the possibility of oscillation, just as with a laser. Photorefractive resonators and phase conjugate reflectors are two of a host of devices[28] which utilize this characteristic.

The magnitude of the intensity coupling, known as the two beam coupling coefficient, is often the basis of characterization for photorefractive materials. Yet the two-beam intensity coupling is only half of the story, and this fact must be stressed: The dynamic coupling of the beams affects the phases of the beams also. The true variables which describe the interaction are the photorefractive phase ϕ and the coupling constant g (see below); using these fundamental variables, the two-beam intensity coupling coefficient is given by $\Gamma = 2\,g\sin\phi$ (the amplitude coupling coefficient is given by $g\sin\phi$). Meanwhile the phase coupling is described by a coefficient $g\cos\phi$. Unfortunately, most experimental results conspire to yield only the value $g\sin\phi$ as a parameter, so it is difficult to experimentally separate g and ϕ. This may explain the tendency to conceptually lump the two variables into one. Also, many characteristics of beam coupling and diffraction are calculated ignoring the change of amplitude of the index grating throughout the material. Instead, the diffraction, for example, is usually taken to be given by the Kogelnik solution for a fixed amplitude grating[29]. These problems are addressed below and again more fully in chapter nine.

In this section the coupled mode equations are developed from the wave equation. Then the equations are used to describe coupling from a thick constant amplitude index grating. This analysis was first performed by Kogelnik. Subsequently, we consider scattering off the dynamic gratings written with the photorefractive effect. Both copropagating and counterpropagating (transmission and reflection) geometries are examined.

2.3.1 Coupled Mode Equations, Fixed Grating

We consider two coherent optical beams[30]

$$\mathbf{E}(\mathbf{r}) = \frac{1}{2} A(\mathbf{r})\, e^{-i\mathbf{k}_1\cdot\mathbf{r}}\, \hat{\mathbf{e}}_1 + \frac{1}{2} B(\mathbf{r})\, e^{-i\mathbf{k}_2\cdot\mathbf{r}}\, \hat{\mathbf{e}}_2 + \text{c. c.} \tag{2.22}$$

where $\mathbf{e}_1$, $\mathbf{e}_2$ and $\mathbf{k}_1$, $\mathbf{k}_2$ are the polarization and propagation directions of the two beams. For simplicity, the polarizations are taken to be parallel; in the general case, the coupling between the beams would be multiplied by the factor $\mathbf{e}_1\cdot\mathbf{e}_2$.

The beams propagate in a medium with a spatially modulated index grating

$$n(\mathbf{r}) = n_0 + \frac{n_1}{2} \cos[\mathbf{K}\cdot\mathbf{r} + \phi] \tag{2.23}$$

where ϕ is the net shift in phase between the index grating and the intensity grating, i.e., ϕ includes the individual phases of beams A and B. The beams obey the scalar wave equation

$$\nabla^2\mathbf{E} + \omega^2 \mu\, \varepsilon(\mathbf{r}) = 0 \tag{2.24}$$

where the high frequency dielectric constant is given by

$$\varepsilon(\mathbf{r}) = \varepsilon_0\, n^2(r) \approx \varepsilon_0 \left[n_0^2 + \frac{1}{2}(n_0\, n_1 e^{-i(\mathbf{K}\cdot\mathbf{r} + \phi)} + \text{c. c.}) \right]. \tag{2.25}$$

Equations (2.22) and (2.23) are used in (2.24) using

$$\frac{d^2A}{dr^2} << k\, \frac{dA}{dr} \tag{2.26}$$

to obtain

$$\frac{1}{2}\left(-2ik_1 \frac{dA}{dr_1} - k_1^2 A\right) e^{-i\,\mathbf{k}_1\cdot\mathbf{r}} + \text{c. c.} \quad +$$

$$\frac{1}{2}\left(-2ik_2 \frac{dB}{dr_2} - k_2^2 B\right) e^{-i\,\mathbf{k}_2\cdot\mathbf{r}} + \text{c. c.} \quad +$$

$$\omega^2 \mu \varepsilon_0 \left[n_0^2 + \frac{1}{2}(n_0 n_1 e^{-i(\mathbf{K}\cdot\mathbf{r} + \phi)} + \text{c. c.}) \right] \quad \times$$

$$\left[\frac{A}{2} e^{-i\,\mathbf{k}_1\cdot\mathbf{r}} + \frac{B}{2} e^{-i\,\mathbf{k}_2\cdot\mathbf{r}} + \text{c. c.}\right] = 0. \tag{2.27}$$

It is clear by inspection that cumulative power exchange takes place only when

$$\mathbf{k}_1 - \mathbf{k}_2 - \mathbf{K} \approx 0. \tag{2.28}$$

Note that the power exchange reverses sign with a phase matching length $\Delta L = \pi/(|\mathbf{k}_1 - \mathbf{k}_2 - \mathbf{K}|)$. Thus only synchronous terms need to be considered in (2.27). Using $k_i = \omega \mu \varepsilon_0 n_0$ (2.27) simplifies to

$$A'(z)\cos\beta = \frac{i\pi n_1}{2\lambda} e^{i\phi} B(z) - \frac{\alpha}{2} A(z) \tag{2.29a}$$

$$B'(z)\cos\beta = \frac{i\pi n_1}{2\lambda} e^{-i\phi} A(z) - \frac{\alpha}{2} B(z). \tag{2.29b}$$

The loss terms are added phenomenologically to account for optical absorption, λ is the wavelength in the medium, β is the half angle of beam incidence inside the material (see Fig. 2-4), and z is the distance along the bisector of the beam angles, $z = r_{1,2}\cos\beta$. For convenience, z is redefined to be the scalar distance along the beam propagation direction, $z \rightarrow z\cos\beta$. This en-

ables one to avoid carrying the factor $\cos\beta$ through all the formulas. As a consequence one must take the effective thickness of the crystal as $L = d/\cos\beta$, where d is the true thickness of the crystal.

To solve (2.29) the optical absorption term is eliminated by the change of independent variable $A(z) = A(z)\exp[\alpha z/2]$ and $B(z) = B(z)\exp[\alpha z/2]$. The resultant equations are differentiated and are substituted into the result of the differentiation to obtain simple second-order equations. The boundary conditions are $A(z=0) = A(0)$ and $B(z=0) = B(0)$. A(0) and B(0) are real because the phases of the two beams have already been incorporated into the index grating; this simply means that the only relevant quantity is the relative phase between the intensity interference pattern and the index grating. The solution for A and B is easily shown to be[31]

$$A(z)\, e^{\alpha z/2} = A(0)\cos(g\, z/2) + i\, e^{i\phi} B(0)\sin(g\, z/2) \qquad (2.30a)$$

$$B(z)\, e^{\alpha z/2} = B(0)\cos(g\, z/2) + i\, e^{-i\phi} A(0)\sin(g\, z/2) \qquad (2.30b)$$

from which the intensities are given by

$$|A(z)|^2 e^{\alpha z} = A^2(0)\cos^2(g\, z/2) + B^2(0)\sin^2(g\, z/2) - A(0)\, B(0)\sin(g\, z)\sin\phi \qquad (2.31a)$$

$$|B(z)|^2 e^{\alpha z} = B^2(0)\cos^2(g\, z/2) + A^2(0)\sin^2(g\, z/2) + A(0)\, B(0)\sin(g\, z)\sin\phi. \qquad (2.31b)$$

We note that the beam coupling is nonzero for all values of ϕ, except for the special case $\phi = 0$ and $A(0) = B(0)$. This is at first surprising, because it will be

shown that in the case of dynamic holography the intensity coupling must be zero when $\phi = 0$ for all values of A and B.

When only one beam is incident on the grating, i.e., B(0) = 0, equations (2.31) give the diffraction from the grating. The transmitted and diffracted intensities are

$$|A(z)|^2 e^{\alpha z} = A^2(0) \cos^2(g z/2) \tag{2.32a}$$

$$|B(z)|^2 e^{\alpha z} = A^2(0) \sin^2(g z/2). \tag{2.32b}$$

Comparison with (2.31) yields the interesting observation that when $\phi = 0$ the output intensities of (2.31) are precisely the sum of the diffracted beams which result from incident beams A(0) and B(0) separately. In other words, when the index grating and the intensity grating are in phase, the two incident beams do not affect each others' intensity diffraction; each beam diffracts as it would if the other beam were not present. Nevertheless, intensity coupling does occur ($A(0) \neq A(L)$) unless A(0) = B(0) because each beam diffracts an intensity proportional to its own incident intensity. This point will be referred to in the next section.

In the preceding paragraphs we have described the coherent scattering of two beams incident on a constant amplitude index grating at the Bragg angle. The scattering associated with photorefractive gratings is more complex because the index grating is created by the interfering beams themselves. Thus when the grating causes power or phase transfer between the beams, the index grating is affected. In the succeeding paragraphs, this problem of scattering from a dynamically written grating is treated self consistently.

2.3.2 Copropagating Geometry, Dynamic Grating

When two beams as in (2.18) interfere within a photorefractive material (Fig. 2-4), an index grating is written

$$n(z) = n_0 + \frac{1}{2}\left(\Delta n(z) e^{i\phi} e^{i K z} + c.c.\right) \tag{2.33}$$

where K is the nominal grating wavevector created by the incident beams, with $\mathbf{K} = \mathbf{k}_1 - \mathbf{k}_2$, so that $K = 2\,k\,\sin\beta$. The magnitude of the index modulation is independent of the total incident intensity; it only depends on the beam intensity ratios of A(z) and B(z) and is given by[32]

$$\Delta n(z) = n_1\, A(z)\, B^*(z)/\, I(z) \tag{2.34}$$

where n_1 is a material parameter equal to the peak to peak index modulation when $|A(z)| = |B(z)|$ (see Fig. 2-5). I(z) is the total intensity $I(z) = |A(z)|^2 + |B(z)|^2$. When $\Delta n(z)$ is defined in this way, ϕ becomes the phase between the index grating and the intensity grating.

After a similar analysis to that leading to (2.29), the coupled equations are obtained:

$$A'(z)\cos\beta = \frac{i\pi\Delta n}{\lambda} e^{i\phi} B(z) - \frac{\alpha}{2} A(z) \tag{2.35a}$$

$$B'(z)\cos\beta = \frac{i\pi\Delta n^*}{\lambda} e^{-i\phi} A(z) - \frac{\alpha}{2} B(z). \tag{2.35b}$$

Using the value for the dynamic grating in (2.34), (2.35) is rewritten as

$$A'(z)\cos\beta = i\,g\,e^{i\phi}\frac{|B(z)|^2}{I(z)}A(z) - \frac{\alpha}{2}A(z) \tag{2.36a}$$

$$B'(z)\cos\beta = i\,g\,e^{-i\phi}\frac{|A(z)|^2}{I(z)}B(z) - \frac{\alpha}{2}B(z) \tag{2.36b}$$

where the coupling constant is defined as $g = \pi n_1/\lambda$. Note that since g is defined in terms of n_1 rather than Δn, it becomes a pure material parameter, the dependence on the relative beam intensities being factored out. Also (2.36) is different from (2.29) in that the dynamic grating has canceled the phase dependence of B(z) in (2.36a) and of A(z) in (2.36b). This property leads to a different method of solution.

The method of solution of equation (2.36a) and (2.36b) is straightforward. The $\cos\beta$ term is eliminated as before by defining z to be the distance along the propagation directions. The optical absorption term is eliminated by the change of independent variable $A(z) = A(z)\exp[\,\alpha z/2\,]$ and $B(z) = B(z)\exp[\,\alpha z/2\,]$. Then solutions of the form

$$A(z) = a(z)e^{i\zeta_1} \qquad B(z) = b(z)e^{i\zeta_2} \tag{2.37}$$

are postulated where a(z) and b(z) are real. Equations (2.36a, b) can be separated into two equations each describing the evolution of the amplitude and phase of the two beams:

$$a'(z) = -\sin\phi\; g\; b(z)^2 / I(z)\;\; a(z) \tag{2.38a}$$

$$b'(z) = +\sin\phi\; g\; a(z)^2 / I(z)\;\; b(z) \tag{2.38b}$$

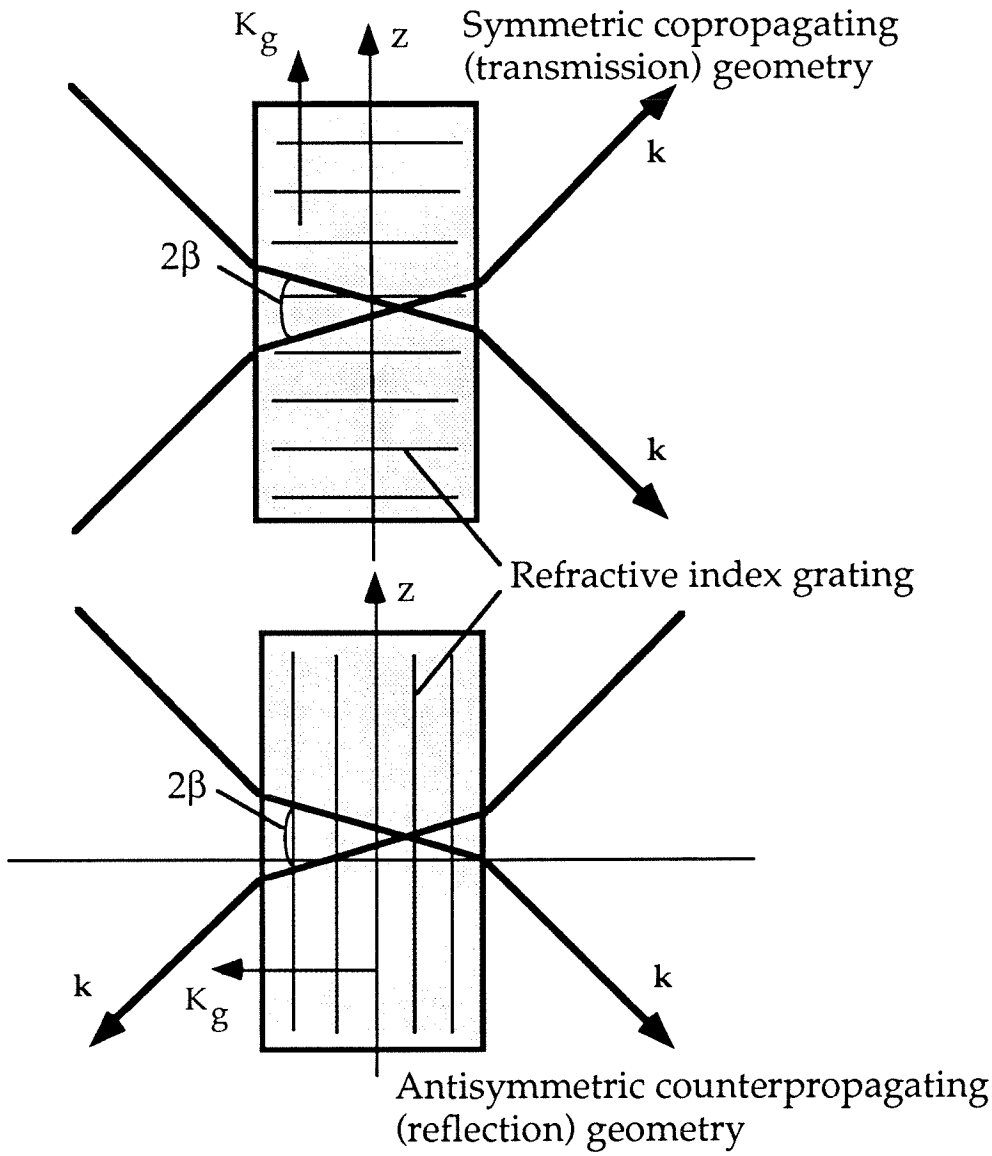

Figure 2-4. Beam Coupling Geometries

The beam incidence angles for copropagating and counterpropagating geometries. The grating wavevector is $K_g = 2k \sin\beta$ in the copropagating case, and $K_g = 2k \cos\beta$ in the counterpropagating case.

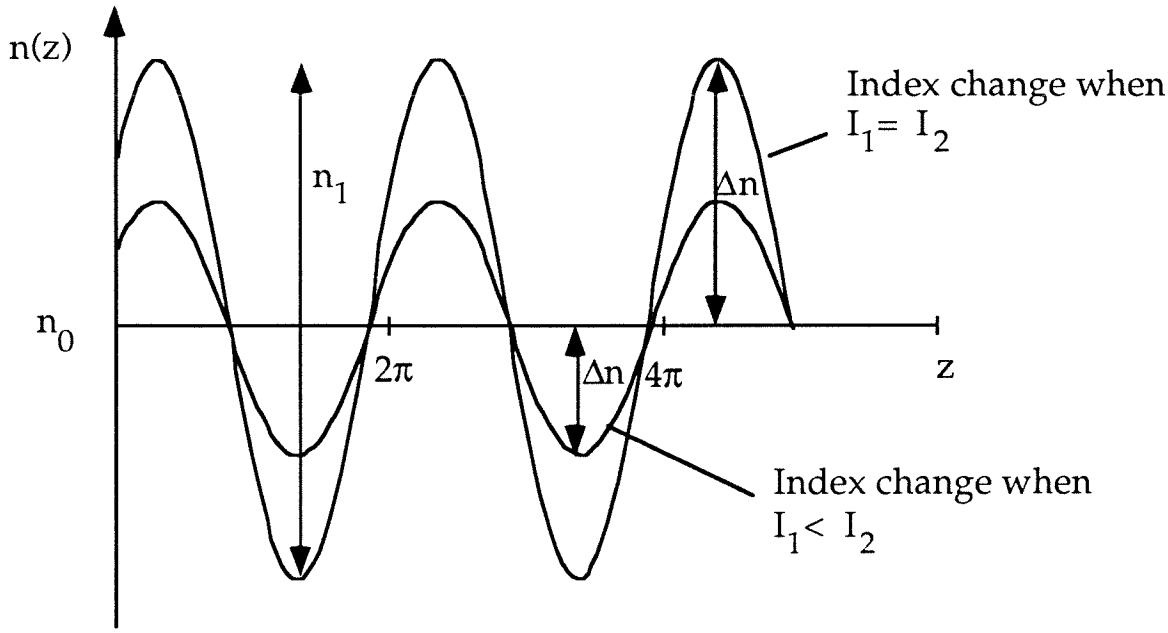

Figure 2-5 Parameters of the Index Grating

The parameters used to describe the index grating in the coupled mode equations. Δn is half the peak to peak modulation of the grating and is a function of the relative beam intensities with $\Delta n = n_1 (I_1 I_2)^{1/2} / I$. n_1 is a material parameter independent of the incident beams. The coupling constant $g = n_1 \pi / \lambda$.

$$\zeta_1'(z) = \cos\phi \; g \; b(z)^2 / I(z) \tag{2.39a}$$

$$\zeta_2'(z) = \cos\phi \; g \; a(z)^2 / I(z). \tag{2.39b}$$

Equations (2.38a,b) are solved by converting them to equations for intensities using $I_1' = (a^2)' = 2\,a\,a'$, and similarly for I_2. Note that these "intensities" are not the true optical intensities, but are related to them by the multiplication of exp[αz]. Use of the identity $b(z)^2 = I(z) - a(z)^2$ in (2.38a) and $b(z)^2 = I(z) - a(z)^2$ in (2.38b) yields simple Bernoulli equations[33] which are readily solved to yield true intensities

$$I_1(z) = e^{-\alpha L} \frac{I_1 (I_1 + I_2)}{I_1 + I_2 e^{+\Gamma z}} \tag{2.40a}$$

$$I_2(z) = e^{-\alpha L} \frac{I_2 (I_1 + I_2)}{I_1 e^{-\Gamma z} + I_2} \tag{2.40b}$$

where $A(z) = [I_1(z)]^{1/2}\exp[i\zeta_1]$ and $B(z) = [I_2(z)]^{1/2}\exp[i\zeta_2]$, and $\Gamma = 2g \sin\phi$ is the power coupling coefficient. As above, L is the effective thickness of the crystal: $L = d/\cos\beta$. We have defined $I_1 = I_1(0)$ and $I_2 = I_2(0)$. Inspection of (2.40) reveals that when $\phi = 0$, there is no intensity coupling and, in the absence of absorption, $I_i(z) = I_i(0)$. Since the intensities are constant the dynamic index grating will have a constant amplitude so one might naively expect (2.40) (with $\phi = 0$) to correlate with the constant amplitude grating case (2.31). The analysis above shows that the two equations disagree except when $I_1 = I_2$. Since the grating leading to (2.31) was Bragg matched to the incident beams, one must conclude that the grating of (2.40) is <u>not Bragg matched</u> except in the

case $I_1 = I_2$. The amount of Bragg mismatch in (2.40) is such that $I_i(z) = I_i(0)$. It follows also that the diffraction off a dynamically written grating will be maximum for beams not of the same frequency as the writing beams. Maximum diffraction for $\phi = 0$ occurs for a frequency mismatch of $\Delta\beta = -g\,(I_2 - I_1)/(2I)$ (see below and chapter 9). This fundamental result seems to be ignored in the literature.

The phases of the two beams are readily determined from equations (2.40a,b) and (2.39a,b) to be

$$\zeta_1(z) = \frac{1}{2}\cot\phi\,\ln[I_1 + I_2\,e^{+\Gamma z}] \tag{2.41a}$$

$$\zeta_2(z) = -g\cos\phi\,z - \frac{1}{2}\cot\phi\,\ln[I_1 + I_2\,e^{+\Gamma z}]. \tag{2.41b}$$

Equations (2.40) and (2.41) are used in (2.34) to determine the index grating written in the material. It is given by

$$\Delta n(z) = n_1\sqrt{I_1\,I_2}\,\left(I_1\,e^{-\Gamma z/2} + I_2\,e^{+\Gamma z/2}\right)^{i\cot\phi\,-\,1}. \tag{2.42a}$$

When $\phi = 0$, special care must be taken when using (2.42a). It is easier in this case to backtrack to equations (2.41) to determine Δn. The index grating in this case reduces to

$$\Delta n(z) = n_1\frac{\sqrt{I_1\,I_2}}{I}\,\exp[\,i\,g\,z\,(I_2 - I_1)/I]. \tag{2.42b}$$

The influence of the phase coupling has modified the index grating by a phasor $\exp[\,i\,g\,z\,(I_2 - I_1)/I]$ in the zero phase case. Thus as predicted above, the index grating is no longer Bragg matched to the (uncoupled) beams which

wrote the grating. This Bragg mismatch, in the $\phi = 0$ case, is just enough to ensure that the transmitted intensities are equal to the incident intensities, unlike (2.31) where the more intense beam diffracted more strongly and amplified the weaker beam.

The diffraction off the gratings (2.42) is derived in chapter 9; it is obtained by solving the differential equations (2.35) with (2.42) inserted. The results for the transmitted and diffracted intensities are given by

$$I_1(z) = e^{-\alpha z} \frac{I_1}{I_1 + I_2} \frac{\left[I_2^2 e^{\Gamma z} + I_1^2 + 2 I_1 I_2 e^{\Gamma z/2} \cos[\, g \cos\phi\, z]\right]}{I_1 + I_2 e^{\Gamma z}} \tag{2.43a}$$

$$I_2(z) = e^{-\alpha z} \frac{I_1^2 I_2}{I_1 + I_2} \frac{\left[e^{\Gamma z} + 1 - 2 e^{\Gamma z/2} \cos[\, g \cos\phi\, z]\right]}{I_1 + I_2 e^{\Gamma z}}. \tag{2.43b}$$

Two special cases deserve attention. When $I_1 = I_2 = I$, (2.43) reduces to

$$I_1(z)/I = \frac{e^{-\alpha z}}{2} \left(1 + \cos[g \cos\phi\, z]/\cosh[g \sin\phi\, z]\right) \tag{2.44a}$$

$$I_2(z)/I = \frac{e^{-\alpha z}}{2} \left(1 - \cos[g \cos\phi\, z]/\cosh[g \sin\phi\, z]\right). \tag{2.44b}$$

When $\phi = 0$ and the index grating amplitude is constant (2.43) reduces to

$$I_1(z)/I_1 = e^{-\alpha z} \left(1 - \frac{4 I_1 I_2}{(I_1 + I_2)^2} \sin^2[g z/2]]\right) \tag{2.45a}$$

$$I_2(z)/I_1 = e^{-\alpha z} \frac{4 I_1 I_2}{(I_1 + I_2)^2} \sin^2[g z/2]]. \tag{2.45b}$$

Comparison with (2.32) shows exactly how the Bragg mismatch reduces diffraction. When $I_1 = I_2$, (2.45) reduces to (2.32).

2.3.3 Counterpropagating Geometry, Dynamic Grating

We perform a similar analysis to that done in the previous section for beams coupled by an index grating written in the counterpropagating geometry (Fig. 2-4). Here the beams write an index grating with wavevector $\mathbf{K} = \mathbf{k}_1 - \mathbf{k}_2$. and $K = 2\,k\cos\beta$. In exactly counterpropagating geometry $K = 2k$. In analogy to work leading up to (2.29) we obtain for this case

$$A'(z)\cos\beta = \frac{i\pi\Delta n}{\lambda} e^{i\phi} B(z) - \frac{\alpha}{2} A(z) \tag{2.46a}$$

$$B'(z)\cos\beta = \frac{-i\pi\Delta n^*}{\lambda} e^{-i\phi} A(z) + \frac{\alpha}{2} B(z). \tag{2.46b}$$

Using the dynamic grating as before we write

$$A'(z)\cos\beta = i\,g\,e^{i\phi}\frac{|B(z)|^2}{I(z)} A(z) - \frac{\alpha}{2} A(z) \tag{2.47a}$$

$$B'(z)\cos\beta = -i\,g\,e^{-i\phi}\frac{|A(z)|^2}{I(z)} B(z) + \frac{\alpha}{2} B(z). \tag{2.47b}$$

It is difficult to obtain solutions of (2.47) when optical absorption is considered except for certain values of ϕ (see chapter 9); in this section the equations are solved for the case $\alpha = 0$. The solution proceeds similarly as before with expressions for the intensities and phases of the two beams given by

$$I_1(z) = \frac{1}{2}\left(\sqrt{c^2+v^2e^{-\Gamma z}} + c\right) \tag{2.48a}$$

$$I_2(z) = \frac{1}{2}\left(\sqrt{c^2+v^2e^{-\Gamma z}} - c\right) \tag{2.48b}$$

$$\psi_1(z) = \frac{1}{2}\left(g\cos\phi\, z - \cot\phi\, \coth^{-1}[\sqrt{1+(v/c)^2 e^{-\Gamma z}}]\right) \qquad (2.49a)$$

$$\psi_2(z) = -\frac{1}{2}\left(g\cos\phi\, z + \cot\phi\, \coth^{-1}[\sqrt{1+(v/c)^2 e^{-\Gamma z}}]\right) \qquad (2.49b)$$

where the definitions $c = I_1(z) - I_2(z)$ and $v^2 = 4\, I_1(0)\, I_2(0) = 4\, I_1(z)\, I_2(z)\, e^{\Gamma z}$ are used. Also $I_1(z) = |A(z)|^2$ and $I_2(z) = |B(z)|^2$. From (2.48) and (2.49) we readily calculate the index grating in the material

$$\Delta n(z) = n_1 \frac{v}{2} \frac{e^{-\Gamma z/2} + i\, g\cos\phi\, z}{\sqrt{c^2+v^2 e^{-\Gamma z}}} \qquad (2.50)$$

where all parameters are as in the previous section.

From (2.50) it is seen that the Bragg mismatch caused by the phase coupling is given by the phasor exp[i g cosϕ z] regardless of the relative intensities of the two beams. Thus the reflection (diffraction) maximum off the grating occurs at a frequency shift $\Delta\beta = (g/2)\cos\phi = 2\pi n\, \Delta\lambda/\lambda^2$ for any combination of beam intensities. This property would be of importance in the manufacture of holographic interference filters (chapter 9). As a numerical example, if a grating is written in the counterpropagating geometry with 656nm laser beams in a material with g cosϕ = 10/cm and an index of refraction n= 2.0, the diffraction maximum will be shifted approximately 0.15Å. Since the full width at half maximum (FWHM) response of such a grating scales inversely with the length, a crystal with a length $L \geq 5$mm may show little or no reflectivity at the frequency with which the grating was written. These results assume that the temperature of the crystal is kept constant.

The diffraction observed from the grating (2.46) is relatively easy to de-

termine when the Bragg mismatch term is absent or the grating is constant amplitude. This occurs under three conditions: **1)** when $\phi = \pi/2$, **2)** when the frequency of the reading beam is shifted to compensate the g cosϕ term, or **3)** when the grating is constant amplitude (either $\phi = 0$, or $c = 0$). In other cases the solution is quite difficult. The general solution for the diffraction is given in (9.39,40,41) with the modifications $\eta = -\cot[\phi]/2$ and $\beta = 1/4$. It is too long to reproduce here.

When $\phi = \pi/2$, the solution, as stated above, simplifies considerably. One obtains

$$A(z) = C_1 \sqrt{1 + \left(\frac{\nu}{c}\right)^2 e^{-\Gamma z}} + C_2 \left(\frac{\nu}{c}\right) e^{-\Gamma z/2} \tag{2.51a}$$

$$B(z) = C_3 \sqrt{1 + \left(\frac{\nu}{c}\right)^2 e^{-\Gamma z}} + C_4 \left(\frac{\nu}{c}\right) e^{-\Gamma z/2} \tag{2.51b}$$

where the coefficients are given by

$$C_1 = A(0) \frac{\sqrt{1 + \left(\frac{\nu}{c}\right)^2 e^{-\Gamma z}}}{\sqrt{1 + \left(\frac{\nu}{c}\right)^2} \sqrt{1 + \left(\frac{\nu}{c}\right)^2 e^{-\Gamma z}} - \left(\frac{\nu}{c}\right)^2 e^{-\Gamma z/2}} \tag{2.52a}$$

$$C_2 = -A(0) \frac{\left(\frac{\nu}{c}\right) e^{-\Gamma z/2}}{\sqrt{1 + \left(\frac{\nu}{c}\right)^2} \sqrt{1 + \left(\frac{\nu}{c}\right)^2 e^{-\Gamma z}} - \left(\frac{\nu}{c}\right)^2 e^{-\Gamma z/2}} \tag{2.52b}$$

$$C_3 = 2\, C_2 \qquad C_4 = 2\, C_1 \tag{2.52c,d}$$

The cases when the index grating is constant amplitude are also interesting in that they simplify to conventional looking results[34] and are of pedagogic value. This condition occurs either when $c = 0$, i.e., $I_1(z) = I_2(z)$, or

when $\phi = 0$ with arbitrary intensity. These cases are illustrated and described in detail in chapter 9.

2.4 Summary

The band transport model of the photorefractive effect was discussed. Photorefractive rate equations were introduced and solved to yield the photorefractive space charge field magnitude and phase. Limiting cases dominated by the effects of diffusion, drift, and the photovoltaic effect were mentioned. The coupled mode equations were derived and solved in both the copropagating and counterpropagating geometries. The solutions for the two beam coupling as well as the phase coupling allowed the determination of the index gratings. Formulas for the diffraction off the index gratings were presented. They are thrashed out in detail in chapter nine. Several important differences between coupling off a fixed grating and dynamic coupling were discussed.

References for chapter two

[1] A. M. Glass, "The photorefractive effect," Opt. Eng. **17**, 470-479 (1978).

[2] T. J. Hall, R. Jaura, L. M. Connors, and P. D. Foote, "The photorefractive effect - a review," Prog. Quantum Electr. **10**, 77-146 (1985).

[3] G. C. Valley and J. F. Lam, in *Photorefractive Materials and their Applications I.* , P. Guenther and J. P. Huignard eds. , chapter 3, Springer-Verlag, Berlin (1987).

[4] A. Ashkin, G. D. Boyd, J. M. Dziedzic, R. G. Smith, A. A. Ballman, H. J. Levinstein, K. Nassau, "Optically-induced refractive index inhomogeneities in $LiNbO_3$ and $LiTaO_3$, " Appl. Phys. Lett. **9**, 72-74 (1966).

[5] F. S. Chen, "A laser-induced inhomogeneity of refractive indices in KTN," J. Appl. Phys. **38**, 3418 (1967).

[6] F. S. Chen, J. Appl. Phys. **40**, 3389 (1969).

[7] F. S. Chen, J. T. LaMacchia, D. B. Fraser, "Holographic storage in lithium niobate," Appl. Phys. Lett. **13**, 223-225 (1968).

[8] H. Kurz, E. Kratzig, W. Keune, H. Engelmann, U. Gonser, B. Dischler, and A. Rauber, "Photorefractive centers in $LiNbO_3$ studied by optical-, Mossbauer-, and epr-methods," Appl. Phys. **12**, 355 (1977).

[9] W. Phillips, J. J. Amodei, and D. L. Staebler, "Optical and holographic properties of transition metal doped lithium niobate," RCA Rev. **33**, 94 (1972).

[10] M. G. Clark, F. J. DiSalvo, A. M. Glass and G. E. Peterson, "Electronic

structure and optical index damage of iron-doped lithium niobate," J. Chem. Phys. **59**, 6209 (1973).

[11] J. J. Amodei, "Electronic diffusion effects during hologram recording in crystals," Appl. Phys. Lett. **18**, 22-24 (1971).

[12] J. B. Thaxter, "Electrical control of holographic storage in strontium-barium- niobate," Appl. Phys. Lett. **15**, 210 (1969).

[13] J. J. Amodei, "Analysis of transport processes during holographic recording in insulators," RCA Rev. **32**, 185 (1971).

[14] A. M. Glass, D. von der Linde, and T. J. Negran, "High voltage bulk photovoltaic effect and photorefractive process in $LiNbO_3$," Appl. Phys. Lett. **25**, 233-235 (1974).

[15] A. M. Glass, D. von der Linde, D. H. Auston, and T. J. Negran, "Excited state polarization, bulk photovoltaic effect, and the photorefractive effect in electrically polarized media," J. Elect. Matls. **4**, 915 (1975).

[16] J. Feinberg, D. Heiman, A. R. Tanguay, and R. W. Hellwarth, "Photorefractive effects and light induced charge migration in barium titanate," J. Appl. Phys. **51**, 1297 (1980).

[17] E. Ochoa, F. Vachss, and L. Hesselink, "Higher-order analysis of the photorefractive effect for large modulation depths," J. Opt. Soc. Am. B, **3**, 181-187 (1986).

[18] A. Bledowski, J. Otten, and K. H. Ringhofer, "Photorefractive hologram writing with modulation 1," Opt. Lett. **16**, 672-674 (1991).

[19] N. V. Kukhtarev, V. B. Markov, S. G. Odulov, M. S. Soskin, and V. L. Vinetskii, "Holographic storage in electrooptic crystals. I. steady state," Ferroelectrics **22**, 949-960 (1979).

[20] K. Sayano, Ph. D. Dissertation, California Institute of Technology, Pasadena, California, unpublished, (1990).

[21] A. Yariv, *Optical Electronics* , chapter 18, Saunders College Publishing, Philadelphia, (1991).

[22] G. C. Valley, "Simultaneous electron hole transport in photorefractive materials," J. Appl. Phys. **59**, 3363 (1986).

[23] M. B. Klein and G. C. Valley, J. Appl. Phys. **57**, 4901 (1985).

[24] M. C. Bashaw, T. -P. Ma, R. C. Barker, S. Mroczkowski, and R. R. Dube, "Theory of complementary holograms arising from electron-hole transport in photorefractive media," J. Opt. Soc. Am. B **7**, 2329-2338 (1990).

[25] G. Rakuljic, Ph. D. Dissertation, California Institute of Technology, Pasadena, California, unpublished, (1987).

[26] A. Agranat, V. Leyva, and A. Yariv, "Voltage-controlled photorefractive effect in paraelectric $KTa_{1-x}Nb_xO_3$:Cu,V," Opt. Lett. **14**, 1017-1019 (1989).

[27] V. Kondilenko, V. Markov, S. Odulov, and M. Soskin, "Diffraction of coupled waves and determination of phase mismatch between holographic grating and fringe pattern," Optica Acta **26**, 239-251 (1979).

[28] V. A. Dyakov, S. A. Korolkov, A. V. Mamaev, V. V. Shkunov, and A. A. Zozulya, "Reflection-grating photorefractive self-pumped ring mirror," Opt.

Lett. **16**, 1614-1616 (1991).

[29] H. Kogelnik, "Coupled wave theory for thick hologram gratings," Bell Syst. Tech. J. **48**, 2909-2947 (1969).

[30] A. Yariv, "Coupled Mode Theory for Guided-Wave Optics," IEEE J. Q. Elec. **9**, 919-933 (1973).

[31] A. Yariv, private communication (1992).

[32] J. P. Huignard, J. P. Herriau, P. Aubourg, E. Spitz, "Phase conjugate wavefront generation via real time holography in $Bi_{12}SiO_{20}$ crystals," Opt. Lett. **4**, 21-23 (1979).

[33] J. Mathews and R. L. Walker, *Mathematical Methods of Physics* , chapter 1, Addison-Wesley, Redwood City, California, (1970).

[34] A. Yariv, *Optical Electronics* , p. 498, Saunders College Publishing, Philadelphia, (1991).

Chapter Three

The Electro-optic Effect

3.1 Introduction

The electro-optic effect generally refers to a change in the index of refraction of a material under the influence of an applied electric field. This effect, in conjunction with the photorefractive space charge field, leads to the index grating formation in the conventional photorefractive effect. Thus the character of the photorefractive response of a material varies with direction of light propagation or with direction of an applied field in a way dictated by the transformation properties of the electro-optic tensor. Furthermore, the response of all photorefractive materials hinges on the form of the electro-optic tensor which, in turn, is governed by the crystallographic space group of the material. For these reasons, a separate chapter is devoted to an introduction of the electro-optic effect.

In 1815 Sir David Brewster discovered that transparent jellies developed artificial birefringence when subjected to mechanical stress.[1] Further investigations soon revealed that all materials displayed this photoelastic effect. About 60 years later Kerr discovered the quadratic electro-optic effect (Kerr effect)[2] in which the index change of the material is proportional to the square

of the applied electric field. The Kerr effect also occurs in all materials. In 1883 Röntgen[3,4] and Kundt[5] independently discovered the linear electro-optic effect (also known as the Pockels effect) in crystals of quartz and tourmaline. Pockels soon extended their investigations to numerous other materials[6,7] and developed the first phenomenological theory of the effect.

The Pockels effect has generally replaced the Kerr effect in device applications because the linear electro-optic coefficients are usually larger than the quadratic ones. Also the linear electro-optic response can be increased substantially by applying an alternating electric field at a frequency near a mechanical resonance of the crystal. This latter effect is caused by the indirect (or converse piezoelectric) contribution to the Pockels effect, which is discussed later. Under certain conditions, however, the quadratic effect remains the preferred means of index modulation. In particular, it will be shown that the quadratic effect with an applied electric field can lead to an effective linear electro-optic coefficient which is useful for voltage control of the photorefractive response. The strength of the quadratic effect increases when the material is operated at temperatures near a structural phase transition.

The development of ferroelectric materials beginning with ADP and KDP[8,9] in the mid 1940s which exhibit large electro-optic coefficients led to the first applications of the electro-optic effect for light modulation and optical shutters. Since then, the effect has seen renewed interest as an integral part of the photorefractive effect. The electro-optic effect is treated theoretically in the following sections with an emphasis on its role in the photorefractive effect. The treatment begins with a description of the index ellipsoid.

3.2 The Index Ellipsoid

Electric fields are known to influence several optical properties of materials. These include the optical absorption and the spectral lines which can exhibit splitting in the Stark effect. The electro-optic effect, however, usually refers to the influence of an electric field on the index of refraction of a material, i.e., the modification of the index ellipsoid, also known as the optical indicatrix. We present a brief review of beam propagation in anisotropic materials which leads to the concept of the index ellipsoid.

The energy density of the stored electric field in a material is given by

$$U = \frac{1}{2}\,\mathbf{E}\cdot\mathbf{D} = \frac{1}{2}\,E_i\varepsilon_{ij}E_j \tag{3.1}$$

where the displacement field is defined as $D_i = \varepsilon_{ij}E_j$ and summation over indices is implied. ε_{ij} is the second rank symmetric dielectric tensor. The medium is considered to be nonabsorbing so that the dielectric tensor is real. Equation (3.1) can be reexpressed as

$$\frac{D_x^2}{\varepsilon_x} + \frac{D_y^2}{\varepsilon_y} + \frac{D_z^2}{\varepsilon_z} = 2\,U \tag{3.2}$$

where "x," "y," and "z" are defined as the principal axes of the material, that is, they describe the coordinate system in which the dielectric tensor has only on-axis components given by ε_x, ε_y and ε_z. If we define the principal indices of refraction $n_i^2 = \varepsilon_i/\varepsilon_0$ (i = x, y, z), and let a vector **r** be given by $\mathbf{D}/(2U)^{1/2}$ we obtain

$$\frac{x^2}{n_x^2} + \frac{y^2}{n_y^2} + \frac{z^2}{n_z^2} = 1 \qquad (3.3)$$

which is the equation of an ellipsoid with major axes parallel to x, y, and z with lengths $2n_x$, $2n_y$ and $2n_z$. This construction is known as the index ellipsoid (Fig. 1). It is used to determine the two indices of refraction and directions of polarization for light propagating in an arbitrary direction in an anisotropic medium[10,11]. The recipe for determining these parameters is illustrated in figure 3-1 for a positive uniaxial crystal. Here the direction of propagation is designated **s**. It is clear that $\mathbf{D} \cdot \mathbf{s} = 0$ (by Maxwell's equation $\nabla \cdot \mathbf{D} = 0$), so that the indices of refraction are given by the major and minor axes of the ellipse intersecting the optical indicatrix normal to **s**. For a rigorous derivation justifying this procedure see Refs. 10 and 11.

A crystal may have zero, one, or two optic axes, in which case it is designated anaxial, uniaxial, and biaxial. We only consider the anaxial and uniaxial cases here. For a uniaxial material the index ellipsoid is simply an ellipsoid of revolution as in figure 3-1. Here two axes have the same index of refraction n_o ("o" for ordinary) and the remaining (optic) axis has $n = n_e$ (extraordinary). Thus the index ellipsoid is given by

$$\frac{x^2}{n_o^2} + \frac{y^2}{n_o^2} + \frac{z^2}{n_e^2} = 1 \qquad (3.4)$$

If $n_e > n_o$ the crystal is positive uniaxial, and if $n_e < n_o$ it is negative uniaxial. From the graphical derivation of $n(\theta)$[12] in figure 3-1, where θ is the propagation angle in the material measured from the optic axis, trigonometry yields

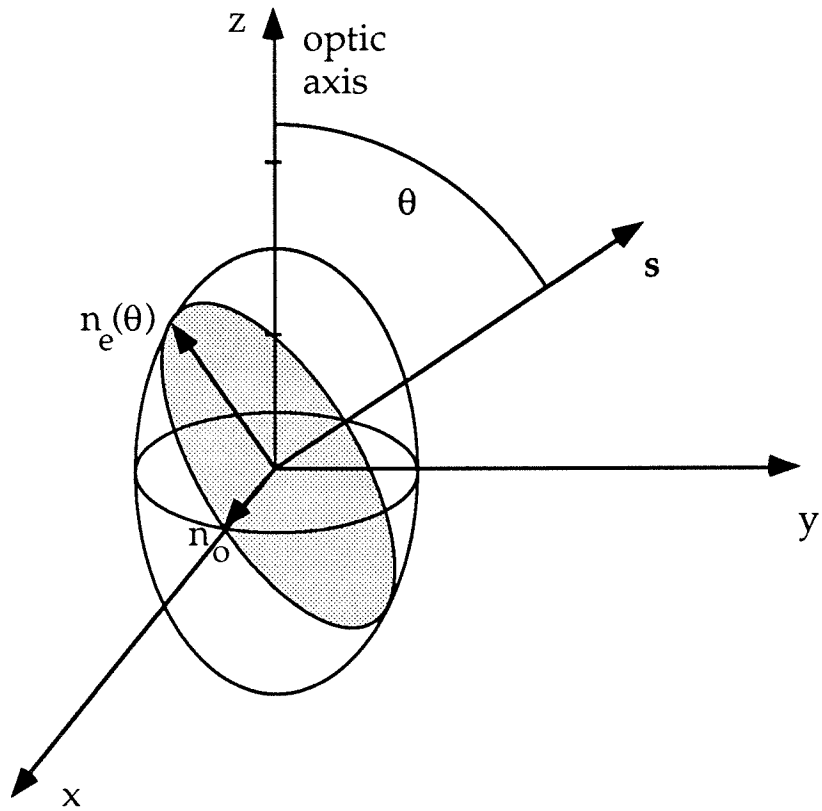

Figure 3-1. The index ellipsoid method

The index ellipsoid and the coordinate axes defined by equation (3.4) are illustrated. For a given direction of propagation **s**, the indices of refraction and the eigenaxes of polarization can be read off from the semimajor and semiminor axes of the ellipse formed by the intersection of the index ellipsoid with the plane normal to **s**.

$$\frac{1}{n_e^2(\theta)} = \frac{\cos^2\theta}{n_o^2} + \frac{\sin^2\theta}{n_e^2} \tag{3.5a}$$

$$n_o(\theta) = n_o. \tag{3.5b}$$

The designations "ordinary" and "extraordinary" follow from this result. Quartz, rutile, and water ice are examples of positive uniaxial materials, while tourmaline, emerald, and barium titanate are negative uniaxial.

Often the index ellipsoid is defined in terms of the optical impermeability tensor which has components $\beta_{ij} = 1/n_{ij}^2$. In analogy to (3.3) it is then given by

$$\beta_{11}^0 x^2 + \beta_{22}^0 y^2 + \beta_{33}^0 z^2 + 2\beta_{12}^0 xy + 2\beta_{23}^0 yz + 2\beta_{13}^0 xz = 1 \tag{3.6a}$$

$$\beta_{ij}^0 x_i x_j = 1 \tag{3.6b}$$

where $\beta_{ij} = \beta_{ji}$ is used. Equation (3.6b) is simply (3.6a) using implied summation notation. In the principal coordinate system (3.6a) reduces to a form similar to (3.3):

$$\beta_{11}^0 x^2 + \beta_{22}^0 y^2 + \beta_{33}^0 z^2 = 1. \tag{3.6c}$$

As a final note on beam propagation in anisotropic materials the phase and group velocities are discussed. The phase and group velocities are given by[13]

$$v_p = \frac{\omega}{k}\mathbf{s} \tag{3.7a}$$

$$v_g = \nabla_{\mathbf{k}}\omega(\mathbf{k}). \tag{3.7b}$$

They are often graphically calculated with the normal surface, a construction related to the index ellipsoid. This is the surface defined by constant $\omega(\mathbf{k})$, where $\mathbf{k} = k\mathbf{s}$[10]. Here instead, the coordinate diagram of figure 3-2 is used. From equation (3.7a) the phase velocity is in the direction of propagation, i.e., normal to both **H** and **D**. The group velocity is perpendicular to the tangent to the normal surface by definition, but it also points in the direction of power flow[14]. Power flow is in the direction of the Poynting vector $\mathbf{S} = \mathbf{E} \times \mathbf{H}$, which is normal to both **E** and **H**. Since **D** and **E** are in general not parallel in anisotropic media, one concludes that the direction of propagation (perpendicular to lines of equal phase) and the direction of power flow are not parallel. Thus two beams of different polarization, propagating in the same direction, may nevertheless diverge from each other. This phenomenon is known as "walkoff" and is often a limiting factor of the interaction length of certain nonlinear optical processes. In nonlinear optics experiments, angles of propagation and geometries are often chosen to minimize walkoff.

As an example, consider two beams propagating at an angle θ from the z axis in the z-y plane in a medium with a principal dielectric tensor given by

$$\varepsilon = \begin{pmatrix} 1 & 0 & 0 \\ 0 & 1 & 0 \\ 0 & 0 & 2 \end{pmatrix} \tag{3.8}$$

Note that this is the dielectric tensor which describes the optical indicatrix of figure 3-1. One beam is taken to be ordinary polarized so that $\mathbf{E} = E_x = D_x$. In this case the phase velocity and the group velocity are parallel. The other

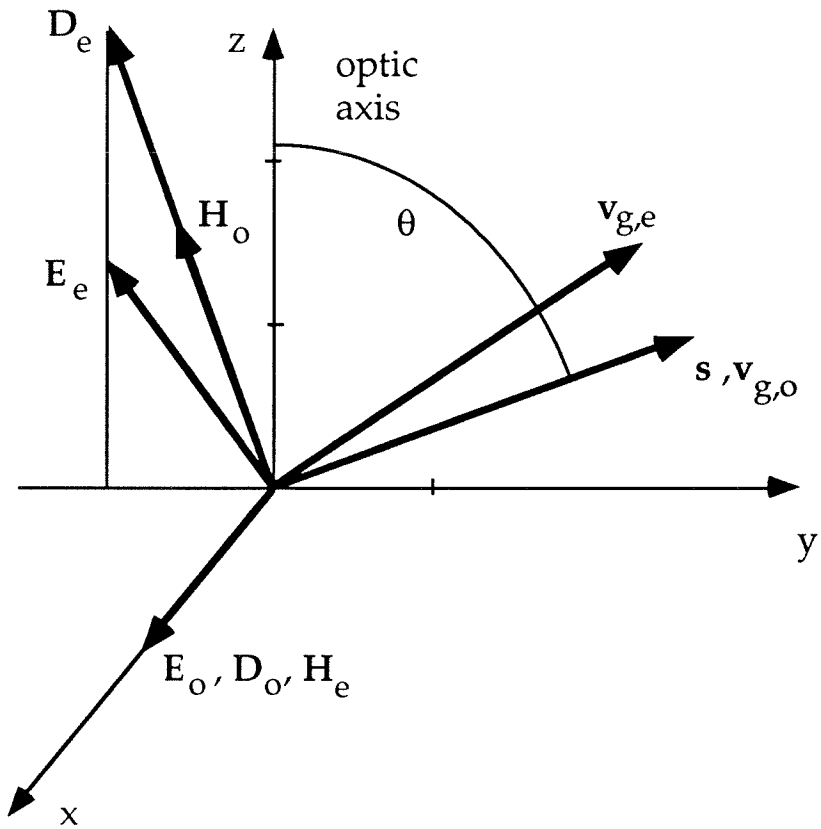

Figure 3-2. Phase velocity and group velocity

In an anisotropic medium, **E** and **D** are not generally parallel; in the illustration above they are related by (3.8). The phase velocity is in the direction of propagation **s**, normal to both **H** and **D**. The group velocity (direction of power flow) is in the direction of the Poynting vector **S** = **E** x **H**, which is normal to both **E** and **H**. For ordinary polarized beams, **D** and **E** are parallel, so that **s** is parallel to $\mathbf{v}_{g,o}$. For extraordinary beams, $E_y = D_y$, but $2E_z = D_z$, so that **s** is at angle to $\mathbf{v}_{g,e}$. Thus two beams of different polarization, propagating in the same direction, may nevertheless diverge from each other. This phenomenon is known as "walkoff."

beam is extraordinarily polarized so that $E_y = D_y$ and $E_z = 2D_z$. The directions of phase and group velocity are illustrated graphically in figure 3-2. The two beams will walkoff from each other as they propagate through the crystal.

3.3 The Linear Electro-optic Effect (Pockels Effect)

3.3.1 Symmetry Properties; Third Rank Tensors

According to Pockels' theory[15] the optical indicatrix is modified by application of an electric field so that

$$\beta_{ij} - \beta_{ij}^0 = \Delta\beta_{ij} = \Delta\left(\frac{1}{n_{ij}^2}\right) = \sum_k r_{ijk} E_k \tag{3.9}$$

where E_k is the *k* th Cartesian component of an applied field E. r_{ijk} are components of the linear electro-optic tensor. The tensor is of the third rank and satisfies $r_{ijk} = r_{jik}$ because it relates a vector E with a second rank symmetric tensor, i.e., the optical indicatrix or optical polarizability tensor. The symmetry properties of the Pockels tensor are identical to that of the piezoelectric tensor **d**, which relates a vector E to a strain field. Thus all piezoelectric crystals can display a linear electro-optic effect and the form of the two tensors is identical for all crystal classes. The maximum number of independent Pockels (or piezoelectric) coefficients is 18, reduced from a maximum of 27 for an arbitrary third rank tensor. This reduction is a result of the symmetry of the relevant second rank tensor ($r_{ijk} = r_{jik}$ and $d_{ijk} = d_{jik}$), i.e., the optic indicatrix for the Pockels effect and the strain field in the piezoelectric effect. The linear electro-optic effect was first discovered in tourmaline which had already been noted for its piezoelectric and pyroelectric properties. Its pyro-

electric effect is particularly strong and as a result tourmaline is known to the jeweler as the gemstone which attracts dust more rapidly than any other.

Only crystals which lack a center of inversion can display the Pockels effect. This can readily be shown by the transformation properties of tensors. One writes[16]

$$r'_{ijk} = \alpha_{il}\,\alpha_{jm}\,\alpha_{kn}\,r_{lmn} \tag{3.10}$$

where α_{ij} are 3x3 rotation matrices. The transformation matrix for inversion is given by $\alpha_{ij} = -\delta_{ij}$, i.e., the negative of the identity matrix. Application of the inversion transformation on (3.10) yields $r'_{ijk} = (-1)(-1)(-1)\,r_{ijk} = -r_{ijk}$. But for a crystal which has a center of inversion, the inversion transformation is a symmetry operation and must leave all tensor properties unchanged. Thus $r'_{ijk} = r_{ijk}$. These two requirements can only be met when $r_{ijk} = 0$. However not all acentric crystals can possess the linear electro-optic effect. The octahedral class (O) with symmetry designation 432 is noncentrosymmetric but is forbidden by symmetry from displaying a linear electro-optic effect:

Crystals of space group 432 have three four fold axes (C_4), four triad axes (C_3), and six diad axes (C_2). It is the combination of the tetrahedral symmetry C_4 and the characteristic cubic symmetry C_3 which conspire to disallow the linear electro-optic effect. Figure 3-3 shows a hypothetical unit cell of a crystal with 432 symmetry with the symmetry axes illustrated. It is clear by inspection that the structure is noncentrosymmetric; the operation I (inversion) carries the structure into its mirror image. In fact crystals of 432 symmetry, as well as many other noncentrosymmetric materials, exist as right- and left

handed enantiomers.

It can be shown[15,17] that crystals of class 4, i.e., crystals obeying the tetrahedral symmetry C_4, have their Pockels tensor components restricted to the following nonzero values

$$\mathbf{r} = \begin{pmatrix} 0 & 0 & r_{13} \\ 0 & 0 & r_{13} \\ 0 & 0 & r_{33} \\ r_{41} & r_{51} & 0 \\ r_{51} & -r_{41} & 0 \\ 0 & 0 & 0 \end{pmatrix}. \tag{3.11}$$

Thus only the above nonzero coefficients need be further considered. If the above coefficients are subjected to the C_3 symmetry operation it can be shown that $r_{321} = r_{132} = r_{123}$, that is $r_{41} = r_{52} = r_{63}$ (see following pages for the contracted index notation definition). Thus comparison with (3.11) yields $r_{41} = 0$. Also it is directly required that $r_{51} = 0$ and that $r_{11} = r_{22} = r_{33} = 0$ and $r_{13} = r_{12} = 0$. The nonzero coefficients for a material with three diad axes and a C_3 axis are as illustrated in (3.12)

$$\mathbf{r} = \begin{pmatrix} 0 & 0 & 0 \\ 0 & 0 & 0 \\ 0 & 0 & 0 \\ r_{41} & 0 & 0 \\ 0 & r_{41} & 0 \\ 0 & 0 & r_{41} \end{pmatrix}. \tag{3.12}$$

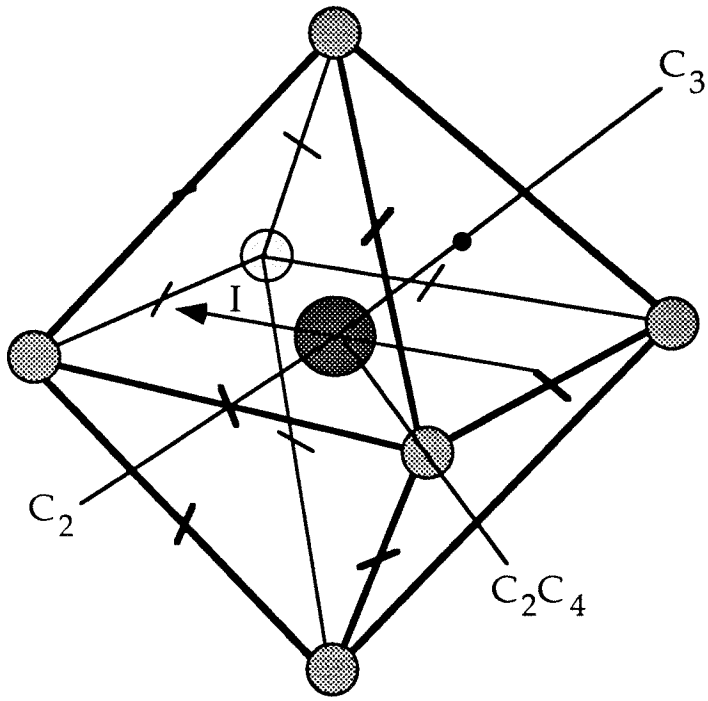
C3
I
C2
C2C4

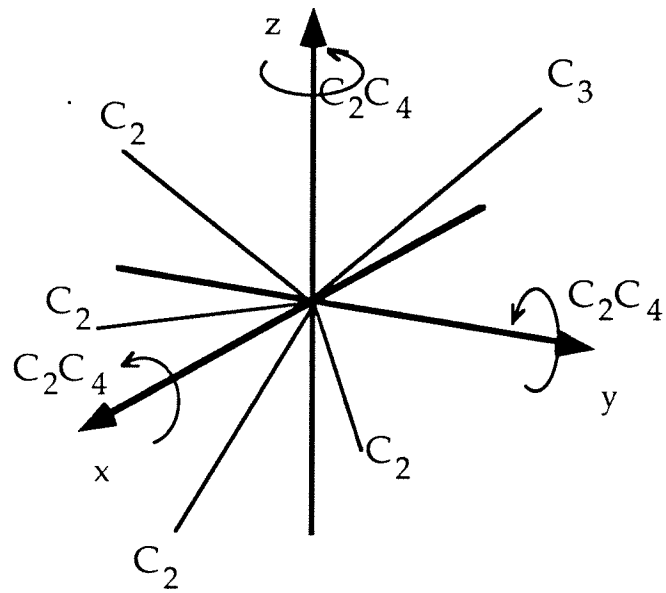
z
C2C4
C3
C2
C2
C2C4
C2C4
y
x
C2
C2

Figure 3-3. 432 symmetry unit cell (previous page)

An example of a unit cell displaying 432 symmetry is illustrated. The chiral "bars" in the (110) positions of the octahedron make the crystal noncentrosymmetric. The inversion operation **I**, when applied to the unit cell, gives the mirror image of the unit cell. Nevertheless, the cell has C_4 symmetry axes along the (100) directions, C_2 axes along (110) (and (100)), and C_3 axes along (111). The symmetry axes are shown separately from the unit cell for clarity. The combination of C_4 and C_3 symmetries conspire to eliminate the possibility of a linear electro-optic effect.

Equations (3.11) and (3.12) can only be simultaneously met when all $r_{ijk} = 0$. The octahedral 432 class is the only noncentrosymmetric system which is not piezoelectric and not linearly electro-optic.

The application of an electric field on a centrosymmetric material along a crystal axis or along a cube diagonal will make the material uniaxial. All other directions of applied field result in a biaxial material. Likewise, a uniaxial material with a field applied along the optic axis remains uniaxial, whereas a field applied along any other crystallographic axis or along an arbitrary direction yields a biaxial material. In general, a biaxial material remains biaxial when subjected to a field. Thus the application of an electric (or any other) field usually lowers the symmetry of a material. Therefore one might expect that the material, under the influence of that field, might display nonzero electro-optic coefficients which were previously forbidden. This does occur, and the magnitude of these previously forbidden coefficients is proportional to the applied field, so that the field acting on these coefficients yields a quadratic response. This process is known as a morphic lowering of the symmetry and was first observed by Mueller[18]. In the case of the electro-optic effect the change in the refractive index is expected to scale roughly with the applied electric field relative to the mean interatomic fields. For this reason, quadratic effects such as morphic symmetry changes and the Kerr effect are usually ignored when the linear effect is present. These two quadratic effects are distinct, however, and should not be confused. The Kerr effect is only a particular subset of the effects which lower crystal symmetry.

Since the maximum number of independent coefficients is 18, it is pos-

sible to compress the index notation of the r_{ijk}. In contracted notation the coefficients r_{ijk} are compressed to r_{mn} where (ij) -> m and k = n under the following scheme:

(ij)		**m**	(3.13)
(11)	->	1	
(22)	->	2	
(33)	->	3	
(32),(23)	->	4	
(13),(31)	->	5	
(12),(21)	->	6.	

This notation often simplifies equations considerably and will be used where ever convenient. However, it must be used with care because tensors contracted using this notation no longer obey tensor transformation and multiplication properties. Additionally, for many tensors encountered, the contracted coefficient does not have the same numerical value as the original, i.e., for a tensor T, T_{ijkl} may not be equal to T_{mn}. For example in the compliance tensor, $s_{1111} = s_{11}$, but $s_{1112} = s_{16}/2$ and $s_{1212} = s_{66}/4$. However, the elastic tensor, which is the inverse of the compliance tensor, has $c_{ijkl} = c_{mn}$ for all i, j, k, l, and m, n[19].

3.3.2 True and Indirect Linear Electro-optic Effect

In equation (3.9) we have not specified the mechanical state of the crystal, i.e., whether stress free or strain free (clamped). These two cases will lead to different electro-optic responses because the applied field causes a strain in

the unclamped case, and thus to a contribution to the index change from the photoelastic effect. Considering both electro-optic and photoelastic effects the changes in the index ellipsoid under application of fields can be written

$$\Delta\beta_{ij} = \sum_{k=1}^{3} r_{ijk} E_k + \sum_{m,n=1}^{3} q_{ijmn} \sigma_{mn} \tag{3.14a}$$

$$\Delta\beta_{ij} = \sum_{k=1}^{3} r'_{ijk} E_k + \sum_{m,n=1}^{3} p_{ijmn} \varepsilon_{mn} \tag{3.14b}$$

where σ_{ij} and ε_{ij} are components of the stress and strain tensors respectively. q_{ijkl} and p_{ijkl} are the components of the stress-optical and strain-optical tensors, and r_{ijk} and r'_{ijk} are components of the free and clamped electro-optic tensors. The strain tensor components in (3.14b) are resolved as

$$\varepsilon_{mn} = \sum_{o,p=1}^{3} s_{mnop} \sigma_{op} + \sum_{k=1}^{3} d_{mnk} E_k \tag{3.15}$$

where **s** is the compliance tensor and **d** the converse piezoelectric tensor. Insertion of (3.15) into (3.14a) yields

$$\Delta\beta_{ij} = \sum_{k=1}^{3} \left(r'_{ijk} + \sum_{m,n=1}^{3} p_{ijmn} d_{mnk} \right) E_k + \sum_{m,n=1}^{3} \sum_{o,p=1}^{3} p_{ijmn} s_{mnop} \sigma_{op}. \tag{3.16}$$

Comparison with (3.14a) reveals that

$$q_{ijkl} = \sum_{m,n=1}^{3} p_{ijmn} s_{mnkl} \tag{3.17}$$

$$r_{ijk} = r'_{ijk} + \sum_{m,n=1}^{3} p_{ijmn} d_{mnk}. \tag{3.18}$$

Therefore the electro-optic coefficient r'_{ijk} measured with zero strain (clamped) differs from the free coefficient r_{ijk} by the product of the converse piezoelectric tensor with the strain-optical tensor. The clamped value r'_{ijk} is usually referred to as the true electro-optic effect while the free value r_{ijk} is the sum of the true and the indirect electro-optic effects. The indirect contribution can be either negative or positive. Substantial increases in the electro-optic response can be achieved by operating an electro-optic material with a time varying field applied at frequencies near a mechanical resonance. As a historical note, both Röntgen and Kundt believed that the linear electro-optic effect was due entirely to the indirect effect. It remained for Pockels to prove the existence of the true linear electro-optic effect[6].

3.3.3 Application to the Photorefractive Effect

3.3.3.1 Electric field applied along z

As described in chapter two, when a photorefractive material is illuminated with a spatially periodic intensity pattern a spatially periodic electric space charge field is formed. If the geometry used is as illustrated in figure 2-4, then the space charge field will be nominally directed along the z axis: $E_{sc} = E_{sc}\cos(K_g z)\mathbf{z}$. Referring to equation (3.9) the index ellipsoid is modified according to

$$\Delta\beta_{ij} = \Delta\left(\frac{1}{n_{ij}^2}\right) = r_{ij3}\,E_{sc}. \tag{3.19}$$

In a crystal of barium titanate with crystal symmetry 4mm the relevant non zero coefficients are $r_{113} = r_{223}$ and r_{333} (see equation (3.23) and Refs. 10, 11 for

a list of material electro-optic coefficients). Thus the index ellipsoid in the presence of the field is given by

$$(\beta_{11}^0 + r_{13}E_{sc})x^2 + (\beta_{22}^0 + r_{13}E_{sc})y^2 + (\beta_{33}^0 + r_{33}E_{sc})z^2 = 1 \qquad (3.20)$$

where as stated above, $\beta_{11} = \beta_{22} = 1/n_0^2$ and $\beta_{33} = 1/n_e^2$. Since there are no cross terms in expression (3.20) it is of the form (3.4) and we may read the new indices of refraction directly. Using $\Delta(1/n^2) = -2\, n^{-3}\Delta n$ we can write

$$n_x = n_y = n_0 - \frac{n_0^3}{2} r_{13}\, E_{sc} \qquad (3.21a)$$

$$n_z = n_e - \frac{n_e^3}{2} r_{33}\, E_{sc} \qquad (3.21b)$$

where it is still to be understood that E_{sc} is a function of z. From the above we can conclude that a plane wave propagating in the x direction and polarized in the y direction, i.e., ordinary polarization, will see an index grating given by (3.21a)

$$\Delta n_y(z) = -\frac{n_0^3}{2} r_{13}\, E_{sc}\cos[K_g z] \qquad (3.22a)$$

while the same beam extraordinarily polarized (along z) sees a grating

$$\Delta n_z(z) = -\frac{n_e^3}{2} r_{33}\, E_{sc}\cos[K_g z]. \qquad (3.22b)$$

If the space charge field had been applied along another direction cross terms would have appeared in an equation analogous to (3.20) signaling a rotation of the index ellipsoid. This effect is covered in the literature[10] and will be illustrated later in the chapter.

3.3.3.2 Effective electro-optic coefficient for arbitrary electric field

The effect of a space charge field directed along the z axis on the index ellipsoid was calculated in (3.22a,b). When two beams interfere in a photorefractive material at an arbitrary angle the effective electro-optic coefficient must be calculated as a function of the beam geometry. In this section we calculate the effective electro-optic coefficient for propagation in crystals such as barium titanate with 4mm symmetry[20,21]. The nonzero electro-optic coefficients of the 4mm class are given by

$$\mathbf{r} = \begin{pmatrix} 0 & 0 & r_{13} \\ 0 & 0 & r_{13} \\ 0 & 0 & r_{33} \\ 0 & r_{42} & 0 \\ r_{42} & 0 & 0 \\ 0 & 0 & 0 \end{pmatrix}. \tag{3.23}$$

The index change is then defined in the literature as $\Delta n = r_{eff} E_{sc}/2n$ [22], so that the effective electro-optic coefficient is related to the conventional ones by a factor of n^4. In figure 3-4 two beams are shown propagating at angles α and β with respect to the optic axis (z axis). Propagation vectors of the two beams are given by $\mathbf{k}_1 = k(0, \sin\alpha, \cos\alpha)$ and $\mathbf{k}_2 = k(0, \sin\beta, \cos\beta)$ so that the index grating wavevector is given by

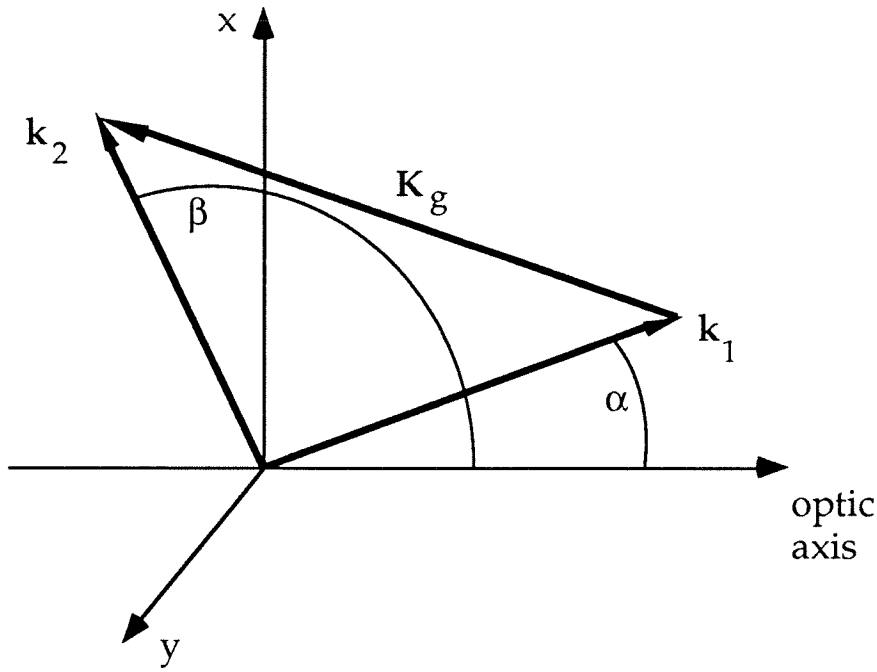

Figure 3-4. Geometry for arbitrary angle two-beam propagation

Two beams propagate at angles α and β from the optic axis, and in the zx plane, of a uniaxial photorefractive material. The space charge field has grating wavevector $\mathbf{K}_g = \mathbf{k}_2 - \mathbf{k}_1$.

$$\mathbf{k}_g = \mathbf{k}_2 - \mathbf{k}_1 = k(0,\ \cos\beta-\cos\alpha,\ \sin\beta-\sin\alpha) =$$

$$2\,k\,\sin\left(\frac{\alpha-\beta}{2}\right)\left(0,\ -\cos\left(\frac{\alpha+\beta}{2}\right),\ \sin\left(\frac{\alpha+\beta}{2}\right)\right) \qquad (3.24)$$

$$= 2\,k\,\sin\left(\frac{\alpha-\beta}{2}\right)(0,\ k_2,\ k_3\ ).$$

Therefore the unit vector specifying the direction of the grating wavevector and the space charge field is $\mathbf{e}_{sc} = (0, k_2, k_3)$. If a quantity **A** is defined with **A** $= \varepsilon \cdot \mathbf{r} \cdot \mathbf{e}_{sc} \cdot \varepsilon$ where **r** is the electro-optic tensor and ε is the dielectric tensor with nonzero components $\varepsilon_{11} = \varepsilon_{22} = n_0^2$ and $\varepsilon_{33} = n_e^2$, then the index change is given by[23,24] $\Delta n(x) = 1/(2n)\ e^*_\beta \cdot \mathbf{A} \cdot \mathbf{e}_\alpha$ where e is the polarization vector of wave α or β. For 4mm materials $\mathbf{r} \cdot \mathbf{e}_{sc} = r_{ijk}\, e_{sc,k}$ is given by

$$\mathbf{r} \cdot \mathbf{e}_{sc} = \begin{pmatrix} r_{13}\,k_3 & 0 & 0 \\ 0 & r_{13}\,k_3 & r_{42}\,k_2 \\ 0 & r_{42}\,k_2 & r_{33}\,k_3 \end{pmatrix} \qquad (3.25)$$

where, as an example, the first term in the matrix of (3.25) is given by $\Sigma\, r_{11j}\, k_j$ $= r_{13}k_3$. For ordinary polarized beams we have $e^* = (1,0,0)$, and application of the above relations yields

$$r_{eff} = n_0^4\, r_{13}\, k_3 = n_0^4\, r_{13} \sin\left(\frac{\alpha+\beta}{2}\right). \qquad (3.26)$$

For extraordinary polarized beams we have $e^*_\alpha = (0, \cos\alpha, -\sin\alpha)$ and $e^*_\beta = (0,$ $\cos\beta, -\sin\beta)$ by inspection of figure 3-4. In analogy to (3.26) we obtain[23]

$$r_{eff} = \sin\left(\frac{\alpha+\beta}{2}\right)\left[\begin{array}{c} n_o^4\, r_{13}\cos\alpha\cos\beta + 2\, n_e^2\, n_o^2\, r_{42}\cos^2\left(\frac{\alpha+\beta}{2}\right) \\ + n_e^4\, r_{33}\sin\alpha\sin\beta \end{array}\right]. \qquad (3.27)$$

In $BaTiO_3$, for example, $r_{42} >> r_{13}, r_{33}$ so the best photorefractive response occurs not in the symmetric geometry of Fig. 2-4 because in that case $\cos[(\alpha+\beta)/2] = 0$.

The index change as defined after equation (3.23) is proportional to the space charge field which is also a function of the propagation angles α and β. When no external field is applied, the magnitude of E_{sc} for extraordinary polarized beams is given by (see chapter two)

$$|E_{sc}| = \frac{k\,T}{e}\,\frac{k_g}{1+(k_g/k_0)^2}\cos[\alpha - \beta] \qquad (3.28)$$

where kT is the thermal energy, e the electronic charge, k_g the grating wavevector, and $k_0 = [N_A e^2/(\varepsilon\varepsilon_0 kT)]^{1/2}$. When α and β are approximately equal, E_{sc} will be proportional to k_g and thus by (3.23) to $\sin[(\alpha - \beta)/2]$.

In the following section we describe the electro-optic effect in materials which are forbidden by symmetry from displaying the Pockels effect. The tensor transformation properties become slightly more involved because the relevant tensor is of higher rank, but many problems are simplified by the isotropy of the index ellipsoid in centrosymmetric materials, i.e., $n_x = n_y = n_z$.

3.4 The Quadratic Electro-optic Effect (Kerr Effect)

The quadratic electro-optic effect (Kerr effect) was discovered by Kerr

several years before the Pockels effect was known. It is a higher order effect and follows from Pockels theory[25] when higher order susceptibilities of the optical indicatrix are considered. If we consider higher order terms in equation (3.9) we obtain

$$\Delta\beta_{ij} = \Delta\left(\frac{1}{n_{ij}^2}\right) = \sum_{k} r_{ijk} E_k + \sum_{k,l} K_{ijkl} E_k E_l$$

$$= r_{ijk} E_k + K_{ijkl} E_k E_l \qquad (3.29)$$

where K_{ijkl} are the quadratic electro-optic coefficients. The quadratic electro-optic effect is more commonly expressed in terms of polarizations so that

$$K_{ijmn} E_k E_l = g_{ijmn} P_k P_l \qquad (3.30)$$

$$g_{ijkl} = \frac{K_{ijkl}}{\varepsilon_0^2 (\varepsilon_k - 1)(\varepsilon_l - 1)}. \qquad (3.31)$$

The quadratic coefficients are usually ignored when the linear effect is present.

The Kerr effect can be resolved into a true and an indirect quadratic effect in an analysis similar to that leading up to equation (3.18). The result is

$$g_{ijkl}^{u} - g_{ijkl}^{c} = \sum_{m,n=1}^{3} p_{ijmn} Q_{mnkl} \qquad (3.32)$$

where the subscripts "u" and "c" refer to unclamped and clamped conditions. Here **p** is the strain-optic tensor and **Q** is the electrostrictive tensor.

Contracted notation is often used to reduce the number of indices of fourth rank tensors. A tensor with components T_{ijkl} is contracted to T_{mn}

where (ij) -> m and (kl) -> n in the same way as performed above for the linear electro-optic coefficients. The Kerr effect is most often studied for centrosymmetric materials for which only three independent g_{ijkl} exist. They are $g_{11} = g_{22} = g_{33}$, $g_{12} = g_{13} = g_{23}$, and $g_{44} = g_{55} = g_{66}$, which in the original notation are

$$g_{11} = g_{1111}, g_{2222}, g_{3333}$$

$$g_{12} = g_{1122}, g_{1133}, g_{2233}, g_{3322}, g_{2211}, g_{3311}$$

$$g_{44} = g_{1212}, g_{1313}, g_{2323}, g_{3232}, g_{2121}, g_{3131}$$

$$= g_{1221}, g_{1331}, g_{2332}, g_{3223}, g_{2112}, g_{3113}.$$

Unless the electric fields are applied only along one axis, numerous terms must be considered in the calculation of the index ellipsoid.

Of the perovskites used as photorefractive materials, most have comparable values of the quadratic electro-optic coefficients. For potassium tantalate niobate ($KT_{.65}N_{.35}$) the values are $g_{11} = 0.136\ m^4/C^2$, $g_{12} = -0.038\ m^4/C^2$, and $g_{44} = 0.147\ m^4/C^2$ [26,27]. For KLTN the values are comparable. In chapter six the Kerr coefficients of a KLTN are determined by measuring the birefringence as a quadratic function of the applied electric field.

3.4.1 Symmetry Considerations, Fourth Rank Tensors

As proved in the previous section the Pockels effect must vanish in centrosymmetric materials. Another way to see this is to consider the effect of an applied electric field E on a material. Let the material be centrosymmetric. If the crystal is reversed with respect to the field it is equivalent to reversing

the direction of the electric field. By the symmetry of the material, a reversal of the crystal orientation must not affect the physical situation and the refractive index change, but the sign of E_k and E_l is reversed. Thus the index ellipsoid is modified by $\Delta\beta_{ij} = r_{ijk}(-E_k) + K_{ijkl}(-E_k)(-E_l)$. Comparison with (3.29) shows that $r_{ijk} = 0$ but K_{ijkl} is not restricted. If the material did not possess a center of symmetry there would be no reason why the two orientations of the crystal would lead to the same physical situation, and therefore neither K_{ijkl} nor r_{ijk} would be required to equal zero. Thus we can conclude that the Kerr electro-optic effect can exist in any material.

The Kerr electro-optic tensor relates the square of a vector (the electric field) with a second rank symmetric tensor (optical indicatrix). Since the order in which the electric fields are applied is immaterial and as discussed above, the optical indicatrix is symmetric, we can write $K_{ijkl} = K_{ijlk} = K_{jikl}$. Therefore the number of independent coefficients is reduced from 81 (for an arbitrary fourth rank tensor) to 6x6 = 36. The quadratic electro-optic tensor has the same symmetry properties as the electrostrictive tensor **Q** and each of these tensors is of identical form for a given crystal class. In fact, the electrostrictive tensor and the Kerr tensor have the same relationship to each other as the piezoelectric and the Pockels tensors.

The symmetry of **Q** and **K** must be distinguished from that of both **p**, the photoelastic (strain-optic) tensor, and **c**, the elastic tensor. All are fourth rank, but each has distinct symmetry properties. The photoelastic tensor relates two second rank symmetric tensors (the strain field and optical indicatrix) and has 6x6 = 36 independent coefficients. Reversal of an applied stress

field will reverse the photoelastic response, whereas reversal of an applied electric field leaves the Kerr response invariant, i.e., the Kerr effect is quadratic while the photoelastic effect is linear. Thus the forms of these two tensors must be distinct. Meanwhile the elastic tensor **c** relates the stress field with the strain field, also both second rank symmetric tensors[28]. But **c** has the additional constraint that $c_{ijkl} = c_{klij}$, so that only at most 21 independent coefficients remain. This last requirement follows by conservation of energy: The elastic energy is $U = c_{ijkl} e_{ij} e_{kl}$, and must be conserved under interchange of strain components e_{ij}. No analogous conserved quantity exists for the other tensors considered.

3.4.2 Application to Photorefractive Effect

When a centrosymmetric photorefractive material is illuminated with two interfering monochromatic plane waves, a spatially modulated intensity pattern and a space charge field are formed, both having a grating vector $k_g = 2k \sin\theta$. Here k is the wavevector of the interfering beams and θ is the angle between the beams. The space charge field can be written

$$\mathbf{E}_{sc}(\mathbf{r}) = \frac{E_{sc}}{2}\left(e^{i\,\mathbf{k}_g\cdot\,\mathbf{r}} + c.\,c.\right). \tag{3.33}$$

The optical indicatrix is modified by

$$\Delta\beta_{ij}(\mathbf{r}) = g_{ijkl}\,\varepsilon_0^2\,(\varepsilon_k - 1)(\varepsilon_l - 1)\,E_{sc,k}(\mathbf{r})\,E_{sc,l}(\mathbf{r}). \tag{3.34}$$

The quadratic form in E will clearly yield a term with spatial dependence $2\,k_g$ as well as a constant term. The index grating thus formed cannot meet the Bragg condition; this grating cannot cause coupling between the beams and is

useless from the standpoint of photorefractive coupling.

If a uniform externally applied field E_0 is maintained across the crystal then the net electric field inside the material becomes $\mathbf{E}(\mathbf{r}) = E_0 + E_{sc}(\mathbf{r})$ so that the change in optical permittivity in (3.34) will have cross terms of the form $E_{0,k}E_{sc,l} \exp[\, i\, k_g\, r]$. These terms will be Bragg matched to the beams which wrote the index grating and will be able to cause coupling between them. Only these contributions to the index change are considered useful in the following sections.

3.4.2.1 Electric field applied along z

In a centrosymmetric material consider the experimental geometry as shown in figure 2-4. The laser beams are symmetrically incident so that E_{sc} is directed along z. The applied electric field E_0 is also directed along z. The optical indicatrix is modified by

$$\Delta\beta_{ij} = 2\, g_{ij33}\, \varepsilon_0^2\, \varepsilon^2\, E_0\, E_{sc} \tag{3.35a}$$

$$\Delta\beta_{11} = \Delta\beta_{22} = 2\, g_{12}\, \varepsilon_0^2\, \varepsilon^2\, E_0\, E_{sc} \tag{3.35b}$$

$$\Delta\beta_{33} = 2\, g_{11}\, \varepsilon_0^2\, \varepsilon^2\, E_0\, E_{sc} \tag{3.35c}$$

So that the index ellipsoid becomes

$$\left(\frac{1}{n_0^2} + 2\, g_{12}\, \varepsilon_0^2\, \varepsilon^2\, E_0\, E_{sc}\right) x^2 + \left(\frac{1}{n_0^2} + 2\, g_{12}\, \varepsilon_0^2\, \varepsilon^2\, E_0\, E_{sc}\right) y^2 + \left(\frac{1}{n_0^2} + 2\, g_{33}\, \varepsilon_0^2\, \varepsilon^2\, E_0\, E_{sc}\right) z^2 = 1. \tag{3.36}$$

Thus an ordinary polarized beam propagating along x (polarized along y) will see an index grating given by

$$\Delta n_y(z) = - n_0^3 g_{12} \varepsilon_0^2 \varepsilon^2 E_0 E_{sc} \tag{3.37a}$$

while the same beam polarized along z will see

$$\Delta n_z(z) = - n_0^3 g_{11} \varepsilon_0^2 \varepsilon^2 E_0 E_{sc}. \tag{3.37b}$$

Inspection of (3.35) reveals that the applied field has made the initially centrosymmetric material uniaxial with the optic axis directed along the direction of applied field. We also note that the applied electric field has induced in the material "effective" linear electro-optic coefficients given by

$$"r_{13}" = 2 g_{12} \varepsilon_0^2 \varepsilon^2 E_0 \tag{3.38a}$$

$$"r_{33}" = 2 g_{11} \varepsilon_0^2 \varepsilon^2 E_0. \tag{3.38b}$$

If a space charge field is introduced in the x or y directions it is readily shown that effective $r_{42} = r_{51}$ coefficients have also been generated by the application of E_0 along z with magnitude

$$"r_{42}" = "r_{51}" = 2 g_{44} \varepsilon_0^2 \varepsilon^2 E_0. \tag{3.38c}$$

Thus application of an external field along z makes a centrosymmetric material with space group m3m (O_h) exhibit effective linear electro-optic coefficients with the symmetry of a 4mm tetragonal crystal (see (3.23)). This result stands to reason because many perovskites, including KLTN and $BaTiO_3$, have high temperature paraelectric phases with O_h symmetry and undergo a ferroelectric transition to a tetragonal 4mm state. The main difference between these two phases is the development of a uniform spontaneous polarization in the material along the direction of the optic axis. The applied field in the centrosymmetric phase serves to emulate the internal spontaneous field so that the crystal behaves as if in the ferroelectric phase.

3.4.2.2 Electric field applied in an arbitrary direction

It has been shown above that a centrosymmetric material becomes uniaxial when a field is applied along a crystallographic axis. When the field is applied off axis, the situation is complicated by the multiple Cartesian components of electric field. The symmetric geometry is considered again (Fig. 2-4). The index ellipsoid in the presence of the field $\mathbf{E} = E(\cos\alpha, \sin\alpha, 0)$ is given by

$$\left(\frac{1}{n_0^2} + K_{11} E_x^2 + K_{12} E_y^2\right) x^2 + \left(\frac{1}{n_0^2} + K_{12} E_x^2 + K_{11} E_y^2\right) y^2$$
$$+ \left(\frac{1}{n_0^2} + K_{12} \left(E_x^2 + E_y^2\right)\right) z^2 + 4 K_{44} E_x E_y \, x \, y = 1. \qquad (3.39)$$

We can immediately solve for n_z by inspection

$$n_z = n_0 - \frac{n_0^3}{2} K_{12} E^2. \qquad (3.40)$$

However the x and y terms of the ellipsoid have cross terms so we must find a rotated set of coordinates x′ and y′ to diagonalize the expression. It is readily shown that the axes are rotated by an amount θ where[10]

$$\tan[2\theta] = \frac{4 K_{44}}{K_{11} - K_{12}} \frac{E_x E_y}{E_x^2 - E_y^2} = \frac{2 g_{44}}{g_{11} - g_{12}} \tan[2\alpha]. \qquad (3.41)$$

The semimajor and semiminor axes lengths in the xy plane (i.e., the ordinary and extraordinary indices of refraction for beams propagating along z) can then be calculated using a similar expression to that following (3.24):

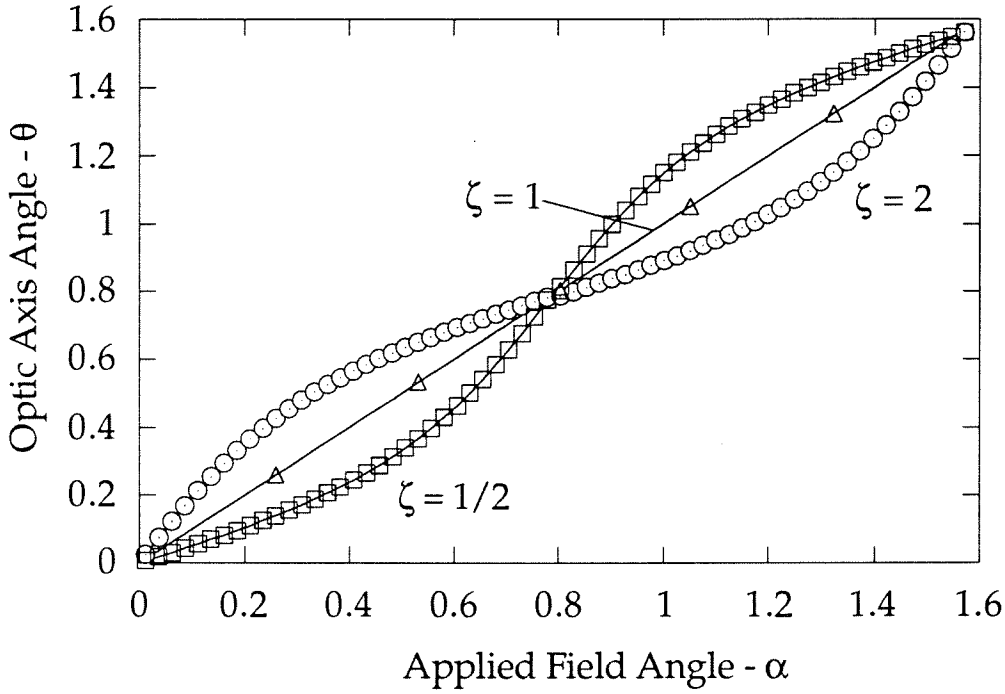

Figure 3-5. Applied field effective c axis

In paraelectric materials the c axis is defined by the application of an electric field. However, unless $\zeta = 2g_{44}/(g_{11}-g_{12}) = 1$ (isotropic case) the optic axis is not parallel to the applied field. The relationship between the angle of the optic axis and the angle of applied field is illustrated above for the cases $\zeta = 1/2$, 1, and 2.

$$\frac{1}{n_{x'}^2} = \sigma_{x'}^* \cdot \beta \cdot \sigma_{x'} \tag{3.42a}$$

$$\frac{1}{n_{y'}^2} = \sigma_{y'}^* \cdot \beta \cdot \sigma_{y'} \tag{3.42b}$$

where β is the optical indicatrix matrix and σ is a unit vector in the direction of the semimajor or semiminor axis, that is $\sigma_{x'} = (\cos\theta, \sin\theta, 0)$ and $\sigma_{y'} = (-\sin\theta, \cos\theta, 0)$. We need not explicitly state the resultant indices of refraction to conclude that the crystal is now biaxial with one optic axis along z and the other at an angle θ to x in the xy plane. Thus the angle of the optic axis is not generally equal to the angle of the applied field α. Figure 3-5 plots θ versus α from(3.41) for several values of $\zeta = 2g_{44}/(g_{11}-g_{12})$. When $\zeta = 1$ the optic axis is always parallel to the applied field. The condition $\zeta = 1$ is well known as the isotropy condition for cubic materials (Ref. 10 p. 323); for example, the number of independent elastic constants of a material drops from three for a cubic system to two for an isotropic system when the condition $c_{44} = (c_{11}-c_{12})/2$ is fulfilled. When g_{44} is larger than in the isotropic case, $\theta \geq \alpha$, so that the optic axis is at a greater angle to the crystallographic axis than the applied field. This occurs because g_{44} is the term responsible for rotating the index ellipsoid. When g_{44} is smaller than in the isotropic case, the optic axis resists deviation away from the crystallographic axis, i.e., $\theta \leq \alpha$.

3.5 Summary

The basic elements of the electro-optic theory were presented, and their

application to the photorefractive effect discussed. The linear electro-optic (Pockels) effect was shown to be forbidden in materials with a center of inversion, and also in noncentrosymmetric cubic materials of symmetry 432. The Pockels effect can be resolved into the true- and the indirect Pockels effects, where the indirect term arises from a photoelastic/piezoelectric contribution. The quadratic electro-optic (Kerr) effect is allowed in all materials but does not lead to a photorefractive (Bragg matched) grating without a uniform applied field. The applied field serves to induce an effective linear electro-optic coefficient.

References for chapter three

[1] D. Brewster, "On the effects of simple pressure in producing that species of crystallization which forms two oppositely polarized images and exhibits the complementary colours by polarized light," Philos. Trans. A **105**, 60-64 (1815).

[2] J. Kerr, "A new relation between electricity and light: dielectrified media birefringent," Philos. Mag. **50**, 337-348 (1875).

[3] W. C. Röntgen, "Ueber die durch elektrische Kräfte erzeugte Aenderung der Doppelbrechung des Quartzes," Ann. Phys. Chem. **18**, 213-228 (1883).

[4] W. C. Röntgen, "Bemerkung zu der Abhandlung des Hrn. A. Kundt: Ueber des optisches Verhalten des Quartzes im elektrischen Felds," Ann. Phys. Chem. **19**, 319-323 (1883).

[5] A. Kundt: Ueber des optisches Verhalten des Quartzes im elektrischen Felds," Ann. Phys. Chem. **18**, 228-233 (1883).

[6] F. Pockels, "Ueber den Einfluss des elektrostatischen Feldes auf das optische Verhalten piezoelektrische Kristalle," Abh. Gött. **39**, 1-204 (1894).

[7] F. Pockels, *Lehrbuch der Kristalloptik* , B. G. Teubner, Leipzig, Germany (1906).

[8] B. Zwicker and P. Scherrer, "Electro-optical behavior of KH_2PO_4 and KD_2PO_4 crystals," Helv. Phys. Acta **16**, 214-216 (1943).

[9] B. Zwicker and P. Scherrer, "Electro-optical properties of the signette-elec-

tric crystals KH_2PO_4 and KD_2PO_4," Helv. Phys. Acta **17**, 346-373 (1944).

[10] A. Yariv and P. Yeh, *Optical Waves in Crystals* , chapter 4, John Wiley & Sons, New York (1984).

[11] M. Born and E. Wolf, *Principles of Optics* , Pergamon Press, New York (1965).

[12] A. Yariv, *Optical Electronics* , p. 15, Saunders College Publishing, Philadelphia, (1991).

[13] J. D. Jackson, *Classical Electrodynamics* , p. 302, J. Wiley & Sons, New York (1975).

[14] ibid. p. 237.

[15] T., S. Narasimhamurty, *Photoelastic and electro-optic properties of Crystals* , chapter 8, Plenum Press, New York (1981).

[16] ibid. chapter 2.

[17] S. Bhagavantam, *Crystal Symmetry and Physical Properties* , Academic Press, New York (1966).

[18] H. Mueller, "Properties of rochelle salt, IV ," Phys. Rev. **58**, 805-811 (1940).

[19] see Ref. 15, p. 152.

[20] M. Segev, California Institute of Technology, Pasadena CA, private communication (1992).

[21] D. F. Nelson, *Electrical, Optic, and Acoustic Interactions in Dielectrics* , J. Wiley & Sons (1979).

[22] J. Feinberg, D. Heiman, A. R. Tanguay, Jr. , and R. W. Hellwarth, "Photorefractive effects and light-induced charge migration in barium titanate," J. Appl. Phys. **51**, 1297-1305 (1980).

[23] J. Feinberg, "Asymmetric self-defocusing of an optical beam from the photorefractive effect," J. Opt. Soc. Am. , **72**, 46-51 (1982).

[24] K. R. MacDonald and J. Feinberg, "Theory of a self-pumped phase conjugator with two coupled interaction regions," J. Opt. Soc. Am. , **73**, 548-553 (1983).

[25] F. L. Wang and A. Y. Wu, "Analytical model for the quadratic electro-optic effect of perovskites," Phys. Rev. B **46**, 3709 -3712 (1992).

[26] J. E. Geusic, S. K. Kurtz, L. G. Van Uitert, and S. H. Wemple, "Electro-optic properties of some ABO_3 perovskites in the paraelectric phase," Appl. Phys. Lett. **4**, 141-143 (1964).

[27] F. S. Chen, J. E. Geusic, S. K. Kurtz, J. G. Skinner, and S. H. Wemple, "Light modulation and beam deflection with potassium tantalate-niobate crystals," J. Appl. Phys. **37**, 388-398 (1966).

[28] R. P. Feynman, *The Feynman Lectures on Physics* , volume II, chapter 38, Addison-Wesley, New York (1964).

Chapter Four

Crystal Growth and Material Properties of Potassium Lithium Tantalate Niobate (KLTN)

4.1 Introduction

As discussed in the introductory chapter of this thesis the potential of volume holography for the construction of memory systems and computer interconnects is well established. It is expected that the data storage density of holographic media will reach 10^{12} bit cm^{-3} (in the diffraction limit), with data retrieval rates up to 10Gbit/sec. Moreover, the special nature of holographic memories makes them especially attractive for implementing unconventional computing architectures such as associative memories and neural networks. However, this potential has never been realized primarily due to the absence of suitable storage media. The motivation behind the crystal growth effort at Caltech in the last few years has been the development of a new type of storage medium, the paraelectric photorefractives. These materials were known to have three chief advantages: a) very high diffraction efficiency[1,2], b) control of the photorefractive diffraction by an external electric field[1-4], and c) special fixing mechanisms[1,5].

Potassium niobate was the archetype of the crystal classes grown at

Caltech. It has been established as one of the most promising photorefractive materials, but it cannot be operated at room temperature in the paraelectric phase since its primary phase transition occurs at 716 K; below that temperature it is ferroelectric. In order to overcome this problem, tantalum was added to partially replace niobium in the crystal. In a preliminary set of experiments at Caltech, potassium tantalate niobate ($K_{1-x}Ta_xNbO_3$ or KTN) crystals were grown[6]. The object was to add enough tantalum to the material to achieve a phase transition at or near room temperature. This condition is desired because the paraelectric photorefractives operate most efficiently about 10K above the phase transition (see chapter 3). Unfortunately, it was found that in KTN the operating point could not be raised above 220K because the phase transition becomes first order[7] and the optical quality deteriorates substantially. It was therefore necessary to find a composition in which the phase transition can be raised without loss of optical quality. This composition was found to be potassium lithium tantalate niobate ($K_{1-y}Li_yTa_{1-x}Nb_xO_3$ or KLTN). (Since the inception of the project to develop KLTN, the growth techniques for KTN have been improved and it is now possible to operate KTNs at approximately 280K, but the KLTNs grown are found to have superior optical properties). This chapter describes the growth of KLTN crystals and their material properties.

$K_{1-y}Li_yTa_{1-x}Nb_xO_3$ forms a solid solution for all values of x between 0 and 1[8], and for $y \leq 0.13$. Crystals with these compositions are transparent ferroelectrics which show very large electro-optic effects just above their Curie temperature. They have the cubic perovskite structure and are readily doped

with transition metals. The Curie temperature increases with increasing niobium or lithium concentration[9]. For very small values of the lithium concentration the material undergoes successive phase transitions on cooling, from cubic to tetragonal, then orthorhombic, and finally rhombohedral.

KLTN crystals are grown in a non-stoichiometric flux containing an excess of potassium carbonate, since both potassium tantalate and potassium niobate melt incongruently. The growing crystal nucleates on a cooled seed which touches the flux.

In section 4.2 we describe the top seeded solution growth method (TSSG), and in 4.3, the crystal growth system. In section four, the specifics of particular growths and the compositions grown to date are enumerated. Phase diagrams for the KLTN system and structural characteristics of crystals grown with the TSSG method are discussed in section five. Optical absorption spectra are also presented in this section. In section six, the influence of lithium in KLTN on the ferroelectric transition temperature and character is described; the contrast with KTN is illustrated. The effects of niobium concentration on the phase transition is discussed as well.

4.2 Top Seeded Solution Growth Method

The KLTN crystals are grown using the top seeded solution growth method[10-15]. First, the powder ingredients including an excess of an appropriate solvent, in this case potassium carbonate, are thoroughly mixed and packed into a 100ml high form pure platinum crucible. The crucible is placed in the center of the growth furnace and its contents heated and melted togeth-

er. The molten flux is soaked at a high temperature to ensure thorough mixing. Then it is cooled to approximately thirty degrees above the anticipated growth temperature. Meanwhile a seed crystal is attached to a ceramic pulling tube with pure platinum wire, and is lowered into the furnace through an opening at the top. After the seed and pulling tube are allowed to reach the temperature of the furnace (~ 1 hour), the seed is touched to the surface of the flux for about one minute. The seed is then raised to see if melting has occurred. If so, the temperature is dropped ten degrees. If no melting has occurred, the temperature is dropped two degrees. This process is repeated until the rounded edges of the slightly melted seed are seen to sharpen up into a square outline. This indicates that growth has started. The seed is then redipped and is left undisturbed for at least twenty hours while the temperature is ramped down at 0.5-1.0°C/hr. Then if the crystal appears to have grown properly, the pulling is started. Throughout the entire process, the seed is rotated at about 20rpm to maintain a homogeneous mix in the flux.

The pulling is usually done at 0.5mm/hr until the crystal is free of the flux (24-36 hours). Often the cooling rate is increased to 1-1.5°C/hr during the pulling stage. After pulling the crystal is slowly annealed to room temperature at a rate between about 10°C to about 30°C per hour.

4.3 Crystal Growth System

The crystal growth system is composed of a high temperature furnace, a seed support and pulling assembly, and driving and control electronics. A cross section of the furnace used for crystal growth is shown in figure 4-1. The

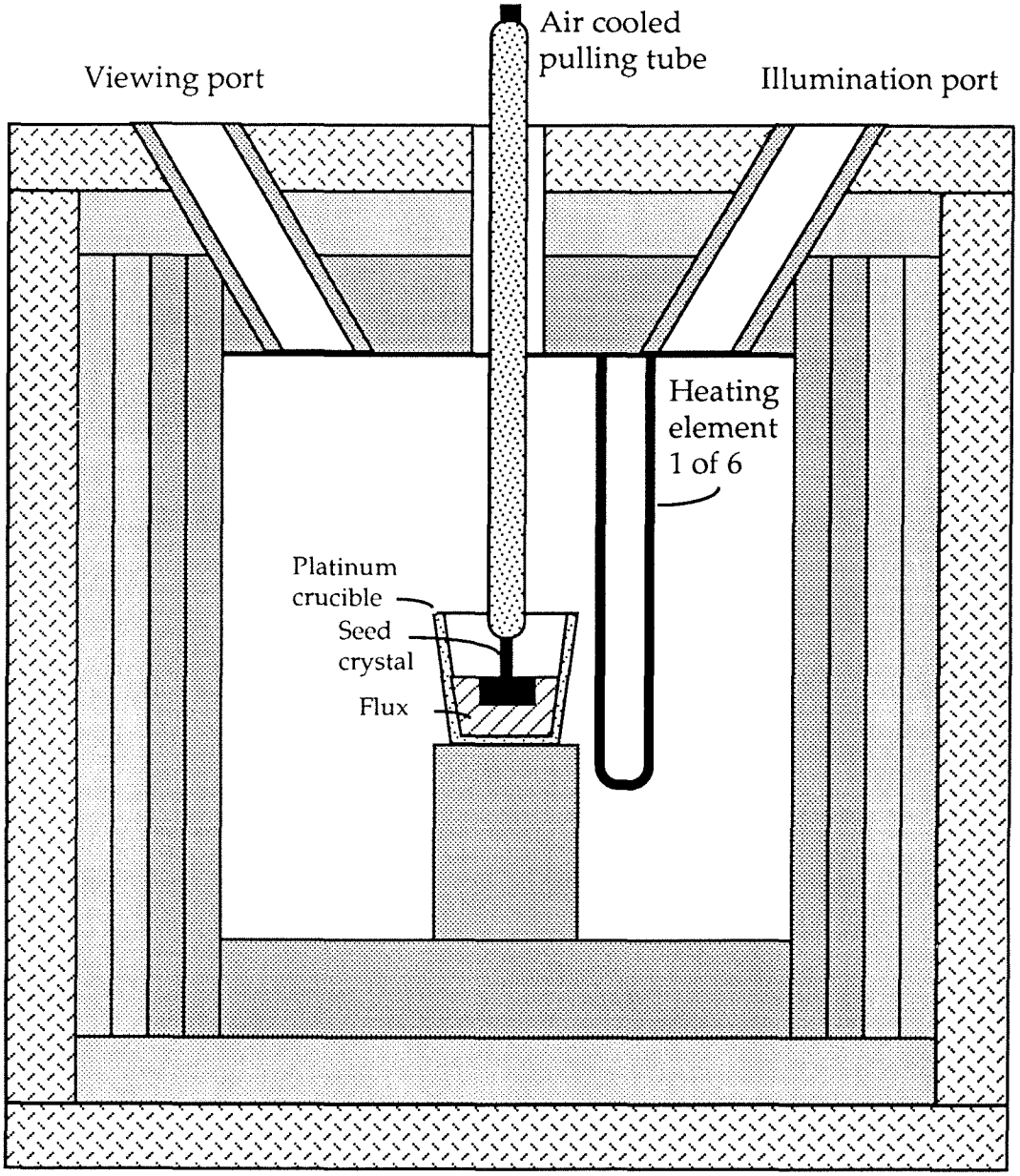

Figure 4-1. The growth furnace

A cross section of the growth furnace is shown. Insulation consists of concentric alumina ceramic cylinders. Viewing and illumination ports allow observation of the platinum crucible and seed during growth. Six heating elements and the pulling tube are admitted through ports in the top plate.

furnace of figure 4-1 was used for the KLTN growths reported in this chapter. (A second furnace has been constructed which incorporates several design improvements to allow higher temperature operation and more uniform mixing of the flux. It is not further reported on here.) The furnace consists of a series of concentric rings of aluminum oxide ceramic material. The inner rings are dense and insulate against high temperature radiation. The outer rings are of a less dense "ash" material which insulate against heat conduction. The top and bottom of the furnaces consist of disks of the same materials and cap the ends of the cylinders. Two diagonal holes are machined into the top plates to allow illumination and viewing of the crystal growth process. A central hole in the top plates allows the insertion of the pulling tube with its attached seed. Six molybdenum disilicide heating elements are mounted in the top plates in symmetrically placed slots around the center. The entire top plate assembly is removable to afford access to the interior of the furnace. Four 1/2" holes are machined in the bottom plates through which thermocouples are inserted. The inner dimensions of the furnace is 9" high by 9" in diameter.

Several type S thermocouples (Pt/ Pt + 13%Rh) are used to monitor the temperature inside the furnace. Their outputs are fed to a Eurotherm 818P temperature controller which senses temperature to an accuracy of 0.1°C. The temperature controller connects to a silicon control relay (SCR) which adjusts the current to the heating elements. The SCR is driven by line voltage stepped down to 30 volts by a variable transformer. The furnace operates at up to 1600°C with a temperature stability of 0.1°C. The operating power is

900W at 1300°C.

The pulling assembly is mounted above the furnace. Its function is to support the seed crystal in the flux during growth and provide a supply of cooling air. It consists of a stand on which a motor driven translation stage is mounted, and a rotatable stainless steel tube. An aluminum oxide ceramic tube is attached to the steel tube and is inserted into the furnace. A stabilized supply of cooling air flows through the stainless steel tube and through an inner steel tube to the end of the ceramic tube. The cooling air flows back out the ceramic tube and is vented in a fixture connecting the ceramic and steel tubes.

4.4 Growth of KLTN

4.4.1 Sample Growths

The composition for a sample growth of KLTN ($H2271)with a low niobium concentration is listed in table 1. The powder amounts listed in the "Final Weight" column were packed into a 100ml platinum crucible. The powder was then heated to 1300°C at 45°C/hr. After 15 hours of soaking at 1300°C, the furnace was ramped down at 45°C/hr to 1260°C. During the ramp, the pulling tube with the attached seed crystal was slowly lowered into the furnace, and allowed to come to thermal equilibrium. It was rotated at 25rpm with the rotation direction reversed every 195sec; approximately 5liters/minute of air flowed through the tube for cooling. The seed crystal was a 3x3x9mm^3 sample cut from a previously grown crystal with similar composition.

Material	Formula Weight	Mole %	Final Weight (gm)
K_2CO_3	138.21	50.0	44.0000
Li_2CO_3	73.82	7.0	3.2900
Ta_2O_5	441.90	24.7	69.5000
Nb_2O_5	265.82	13.3	22.5100
2CuO	159.09	2.5	2.5300
V_2O_5	181.88	2.5	2.9000

Table 4-1. The flux composition of a KLTN:Cu,V ($H2271). The seeding temperature was 1250°C. The resultant crystal had a composition of $K_{0.95}Li_{0.051}Ta_{0.867}Nb_{0.129}O_{3.0}$:$Cu_{0.004}$ and a phase transition temperature of T_c = 180K.

Material	Formula Weight	Mole %	Final Weight (gm)
K_2CO_3	138.21	53.0	38.00
Li_2CO_3	73.82	5.0	1.9148
Ta_2O_5	441.90	11.10	25.4457
Nb_2O_5	265.82	25.90	35.7141
2CuO	159.09	2.5	2.0633
V_2O_5	181.88	2.5	2.3588

Table 4-2. The flux composition of a KLTN:Cu,V ($H2294). The seeding temperature was 1142°C. The resultant crystal had a composition of $K_{1.013}Li_{.0044}Ta_{.635}Nb_{.359}O_3$. and a phase transition temperature of T_c = 310K.

When the system came to thermal equilibrium the seed was dipped into the flux. It was observed to melt slightly after two minutes of dipping. Then the temperature was lowered and the process repeated. Finally, growth began at 1250°C. After five minutes of growth the seed was again raised out of the flux to verify that the crystal was developing a sharp square profile. Then it was left in the flux to grow while the furnace was cooled at -0.5°C/hour.

After 24 hours of growth a rectangular outline of the submerged crystal was clearly visible in the flux, and pulling was started. The pulling was done at 0.55mm/hr, and lasted for 36 hours. When the crystal was out of the flux it was annealed at 15°C/hr to room temperature. The entire growth process took 9 days.

The resultant crystal was an oblong rectangle 7.60 x 15.60 x 20.75mm^3 with subadamantine polish on all facets. It is shown in figures 4.2a,b (see also figure 4-3 for an optical quality KLTN photograph). Small facets of [110] growth surrounded the seed; otherwise all facets were [100]. The crystal was of high optical quality under magnification, though slight striations were visible with crossed polarizers. It weighed 16.33gm including the seed. Electron microprobe and atomic absorption analysis were performed on an identically manufactured crystal, and the composition was determined to be $K_{0.95}Li_{0.0511}Ta_{0.867}Nb_{0.129}O_{3.0}$:$Cu_{0.004}$. Powder X-ray diffraction indicated a perovskite structure, with lattice spacing of a=3.99Å. The highest temperature phase transition, i.e., the transition from the cubic to the tetragonal state, occurred at 180°K.

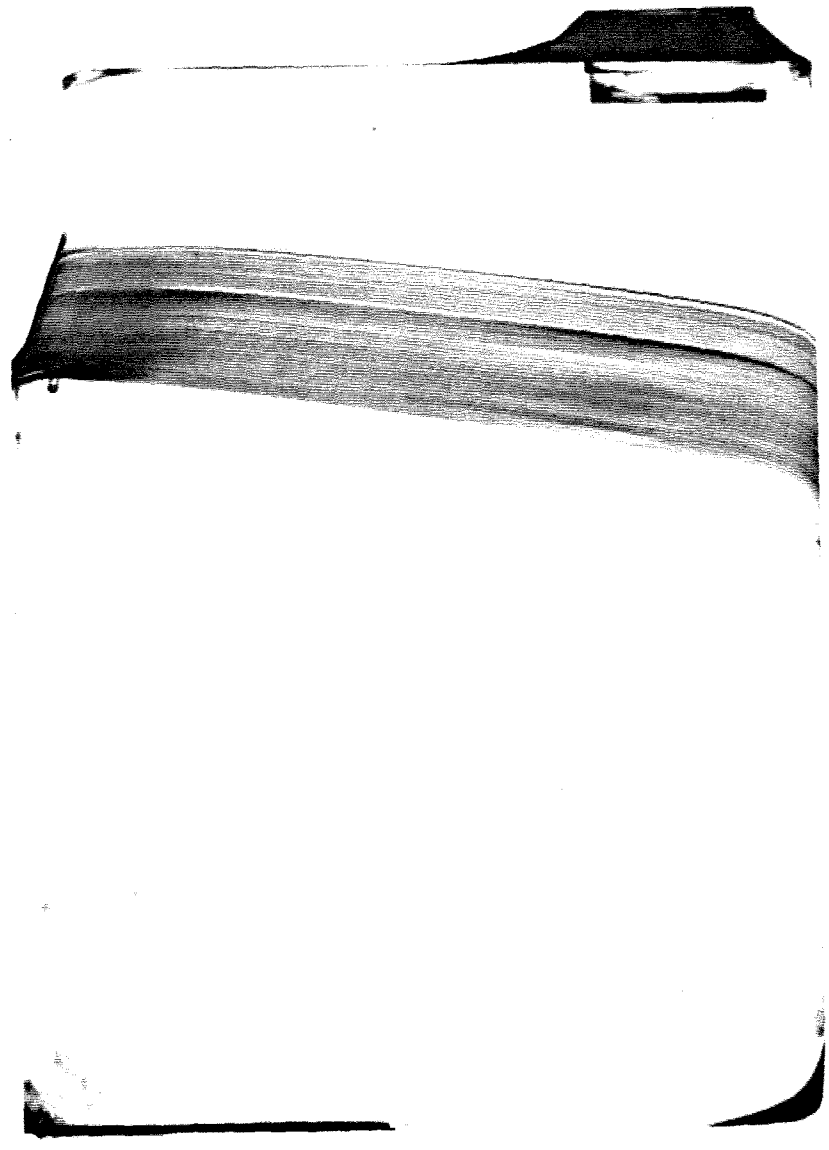

Figure 4-2a. Photograph of transparent crystal #71 as grown (no cutting or polishing). It is viewed with transmitted illumination and is seen to be flawless except for minor inclusions directly beneath the seed stump. The seed crystal has been cut off.

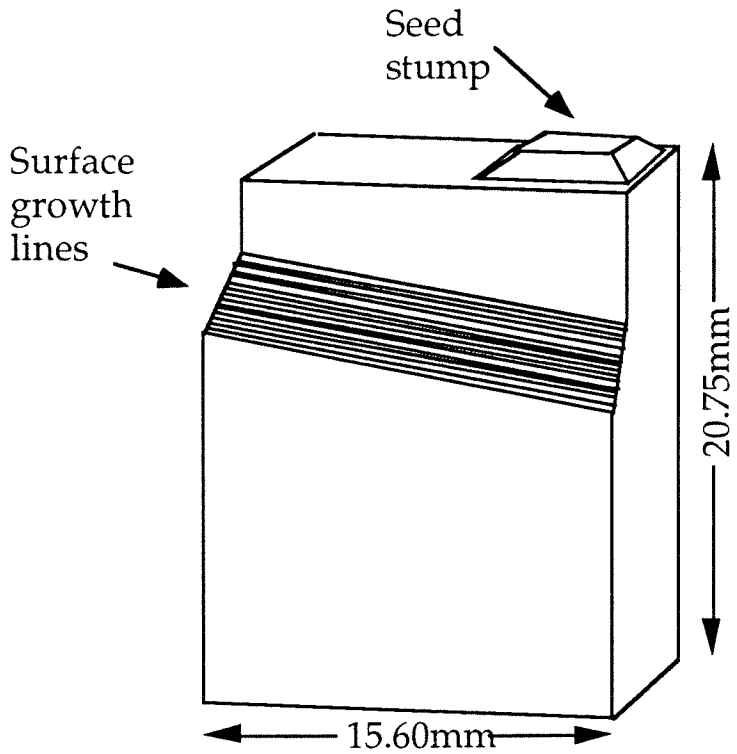

Figure 4-2b. Perspective drawing of crystal #71 with composition $K_{.95}Li_{.05}Ta_{.857}Nb_{.138}O_3$:Cu. Surface growth lines are external features showing the expansion of the crystal during growth.

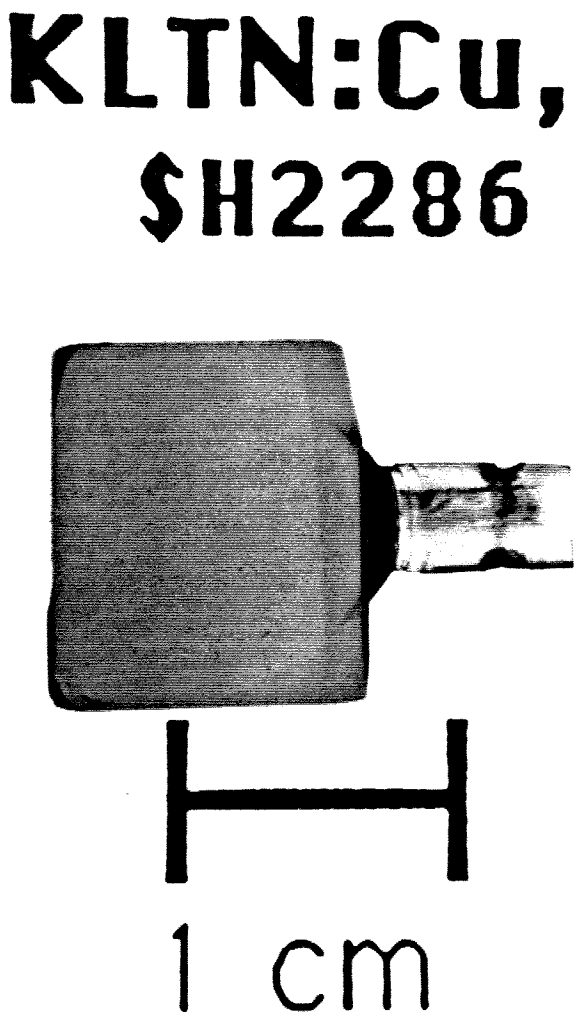

Figure 4-3. Photograph of transparent crystal #86 as grown (no cutting or polishing). It is viewed with transmitted illumination and, again, is seen to be flawless except for minor inclusions directly beneath the seed.

A growth of a KLTN ($H2294) with high niobium concentration following the same crystal growth procedure as set forth in the preceding example was performed using the powdered ingredients listed in Table 4-2. For the flux composition of Table 4-2, crystal growth on the seed began at 1142^{o}C. The crystal pulling and annealing was carried out under the same conditions as set forth in the previous example. The resulting crystal was cube shaped and of high optical quality. Its color was greenish yellow in the core and became slightly yellowish green at the extremities. Its composition was determined to be $K_{1.013}Li_{.0044}Ta_{.635}Nb_{.359}O_3$. The phase transition occurred at 310 K.

Using the same growth procedures as before, a KLTN ($H03101, KLTN:Fe,Ti) crystal with the powder composition as in Table 4-3 was grown. Crystal growth began at 1178^{o}C.

4.4.2 Composition of Grown Crystals

Both electron microprobe analysis and atomic absorption were used to determine the composition of the growths. The electron microprobe used was a JEOL Superprobe 733, operating with a 15KeV beam of 50nA, 20 microns in diameter. It was able to detect all elements but lithium, with an atomic concentration accuracy of ~0.003. The samples to be measured were polished and then mounted on aluminum holders. Then a conductive carbon coating was deposited.

The atomic absorption was performed with a Varian furnace AA machine. The samples were dissolved in boiling hydrofluoric acid, then diluted with water to an approximate lithium concentration of 1-20 ng/liter. The

Material	Formula Weight	Mole %	Final Weight (gm)
K_2CO_3	138.21	57.0	45.00
Li_2CO_3	73.82	1.0	0.4217
Ta_2O_5	441.90	14.0	35.3385
Nb_2O_5	265.82	26.0	39.4767
Fe_2O_3	159.69	1.0	0.9122
$2TiO_2$	159.76	1.0	0.9126

Table 4-3. The flux composition of a KLTN:Fe,Ti ($H03101). The seeding temperature was 1178°C.

Table 4-4. (next page) A partial list of the $K_{1-y}Li_yTa_{1-x}Nb_xO_3$:Cu crystals grown to date. The first column is the crystal number. The next two columns show the combined potassium plus lithium (K+Li) and tantalum plus niobium (Ta+Nb) concentrations in the flux. The next two columns show the relative concentrations of niobium and lithium where X=[Nb]/([Nb]+[Ta]) and Y=[Li]/([Li]+[K]). The columns listed under "Crystal Composition" list the mole concentrations of the four constituents in the grown crystal, and the final column is the growth temperature.

Xtl #	Flux Composition				Crystal Composition				T_{seed}
	K+Li %	Ta+Nb %	X	Y	[K]	[Li]	[Ta]	[Nb]	
91	58	37	0.5	0.01724	0.992	.0025	0.830	0.17	1216
85	58	37	0.65	0	0.992	0	0.768	0.29	1177
86	58	37	0.65	0.0086	0.994	.0006	0.700	0.299	1179
99	58	37	0.65	0.01		.00005			1174
84	58	37	0.65	0.0172	0.990	.0019	0.730	0.27	1188
98	58	37	0.65	0.03	1.016	.0023	0.721	0.273	1175
88	58	37	0.7	0	1.00	0	0.667	0.333	1160
97	58	37	0.3	0.0517	1.004	.0091	0.908	0.089	1250
96	58	37	0.35	0.0517	0.998	.0092	0.893	0.105	1241
74	58	37	0.45	0.0517	0.990	.005	0.857	0.144	1240
75	58	37	0.5	0.0517	0.980	.006	0.827	0.176	1219
76	58	37	0.5	0.05417					1225
81	58	37	0.55	0.0517	0.990	.007	0.794	0.206	1197
82	58	37	0.6	0.0517	0.989	.007	0.777	0.223	1185
83	58	37	0.65	0.0517	0.993	.006	0.687	0.314	1171
95	61.05	38.95	0.65	0.0517	1.020	.0044	0.072	0.275	1161
93	58	37	0.7	0.0517	1.031	.0052	0.644	0.347	1153
33	61	34	0.4	0.082	0.999		0.896	0.102	1193
87	57.6	37.4	0.65	0.0877	1.006	.012	0.677	0.32	1169
94	58	37	0.7	0.0862	1.013	.0044	0.635	0.359	1142
44	57	38	0.35	0.1228	0.95	.0511	0.857	0.129	1238
71	57	38	0.35	0.1228					1250
73	57	38	0.35	0.1228	0.991	.0212	0.888	0.112	1243
90	58.5	36.5	0.65	0.1227	0.985	.015	0.708	0.293	1153
58	60	35.5	0.2986	0.2633	0.933	.035	0.894	0.095	1196
60	60	35	0.3	0.3	0.931	.032	0.881	0.108	1123
61	60	35	0.3	0.333	0.604	.320	0.969	0.082	1188
69	63	32.4	0.3	0.333	0.951	.0645	0.975	0.032	1185
64	63	32.4	0.1429	0.333	0.950	.0601	0.979	0.029	1157
67	64.5	34.6	0.1428	0.36511	0.941	.0757	0.979	0.031	1217

standard was prepared from a 100ng/ liter aqueous solution of Li_2CO_3, and was diluted 1:29, 2:28, ..., 5:25 with water to make a standard curve. The lamp was operated with 5.0mA, and a slit width of 1.0nm was used. The results of these measurements are illustrated in Table 4-4. The first two columns under "Flux composition" show the combined potassium plus lithium (K+Li) and tantalum plus niobium (Ta+Nb) concentrations in the flux. In all but one flux (crystal number 95) the sum of the potassium plus lithium and tantalum plus niobium concentrations was 0.95. The fraction remaining from 1.0 (that is, 0.05) was split equally between the copper and vanadium dopants in the same manner as set forth in Tables 4-1 and 4-2. The next two columns in Table 4-4 show the relative concentrations of niobium and lithium where X=[Nb]/([Nb]+[Ta]) and Y=[Li]/([Li]+[K]). The columns listed under "Crystal Composition" list the mole concentrations of the four constituents in the grown crystal. The temperature at which growth started for each crystal is listed in the final column. Of particular interest is the contrast between the flux and crystal compositions (Figure 4-4a,b).

4.5 Discussion of Growth Characteristics

4.5.1 Composition Considerations

The growth characteristics color, structure, and composition are found to depend only on the flux composition, whereas the shape, size, and quality of the as-grown crystal are functions of both flux composition and growth parameters. The effects of composition are discussed first.

The phase diagram for KLTN shown in Figure 4-5 plots the liquidus and solidus curves of temperature versus niobium concentration. Of course,

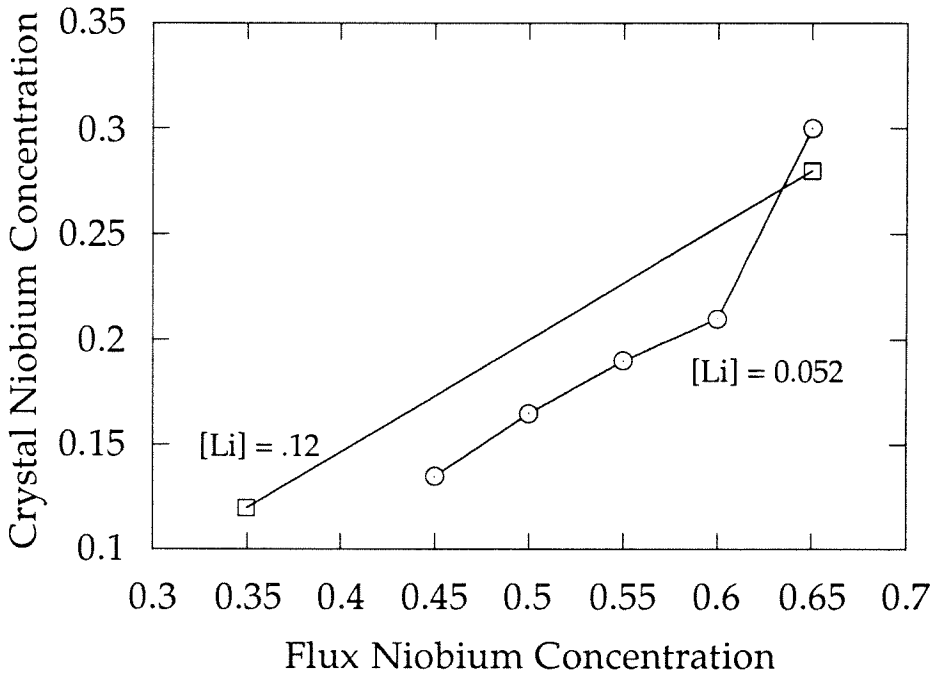

Figure 4-4a. The niobium concentration in the crystal is plotted versus the niobium concentration in the flux for two lithium flux concentrations: [Li] = 0.051 and [Li] = 0.123. The concentration of niobium in the crystal is approximately 1/3 the concentration in the flux.

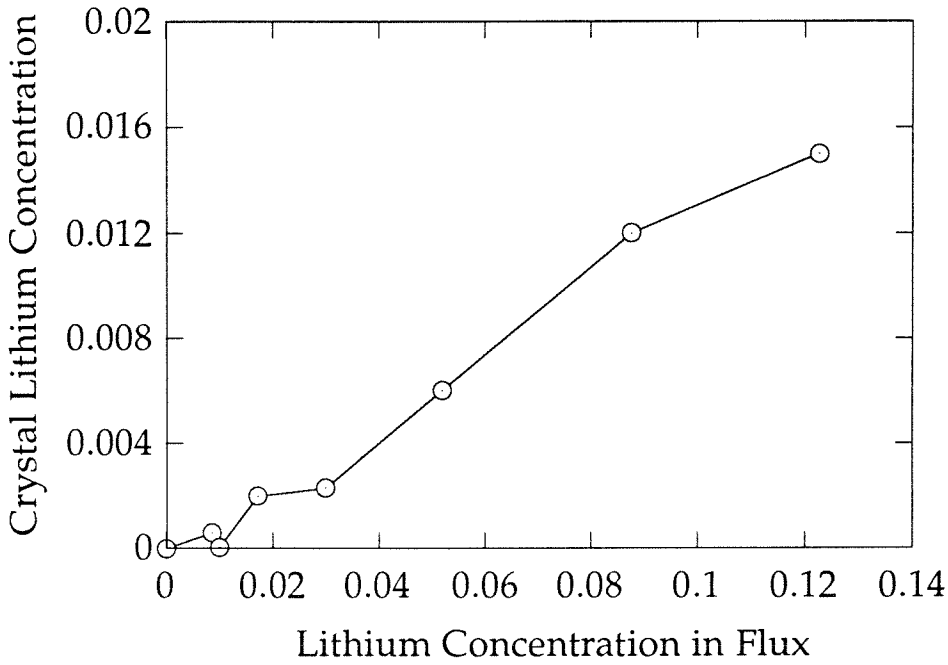

Figure 4-4b. The lithium concentration in the crystal is plotted versus the lithium concentration in the flux for a niobium flux concentration of [Nb] = 0.65. The lithium concentration in the crystal is approximately 1/7 of that in the flux.

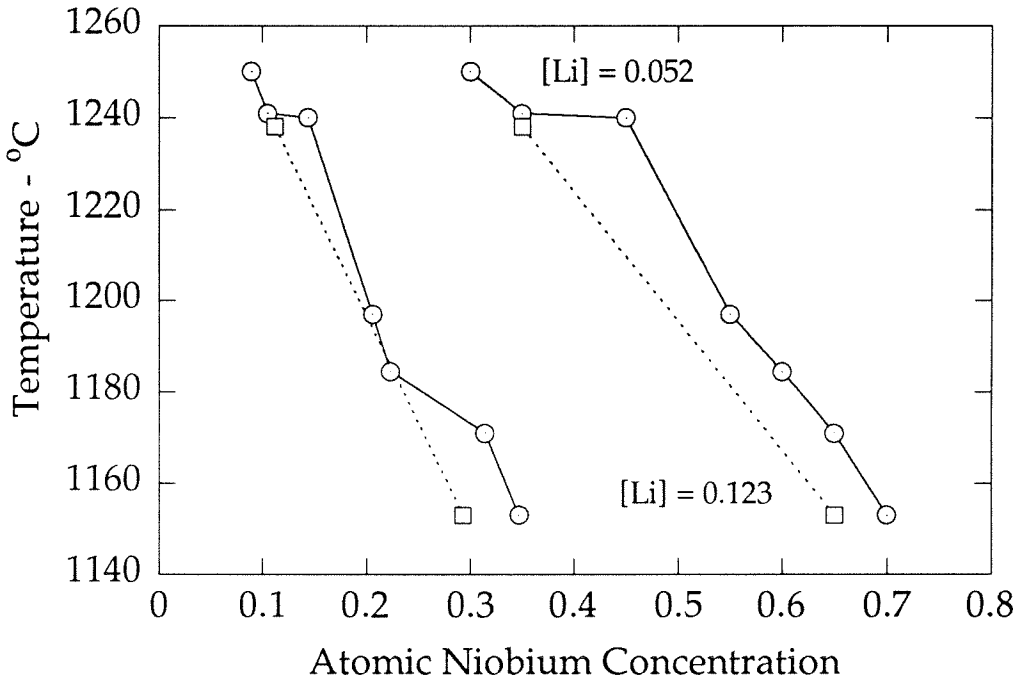

Figure 4-5. The phase diagram of $K_{1-y}Li_yTa_{1-x}Nb_xO_3$ showing liquidus and solidus curves of temperature versus niobium concentration. The change in these curves with increasing lithium concentration is illustrated by the difference in the curves for two lithium flux concentrations: [Li] = 0.052 and [Li] = 0.12.

the liquidus and solidus curves are also functions of the lithium concentration. The phase diagram has been plotted for two lithium flux concentrations: [Li]=0.052 and [Li]=0.12. The niobium/tantalum ratios were found to roughly obey the phase diagram for KTN[16] Here, as shown in Fig. 4-6, if a flux with a given niobium concentration X (X is defined in Table 4-4) is cooled to the liquidus temperature, the crystal begins growing along the solidus with a niobium concentration x (<X). As cooling drives the growth, the flux is concentrated to composition, say, X'> X with a resultant shift in crystal composition to x'(>x). Across a 15gram cube shaped crystal grown in a 100ml crucible with initial flux composition X= 0.65, a series of 200 microprobe measurements determined a variation in x of 0.03; this agrees with calculations.

The phase diagram of KLTN for [Nb] = 0.65 in the flux, as a function of lithium concentration is shown in figure 4-7. The deviations from a smooth curve are caused by variations in the resultant crystal's niobium content. There is, in other words, a coupling between the lithium and niobium flux/crystal concentrations so that a constant niobium flux concentration does not yield a perfectly constant crystal niobium content if the lithium concentration is varied. It is seen that the lithium/potassium ratios exhibit a solid solution behavior for Y < 0.33 (Y is defined in Table 4-4), with y<Y. These growths are all cubic perovskites at room temperature. For Y ≥ .33, however, the composition and structure abruptly changes. These growths, e.g., #61 (Table 4-4), are dense and brittle materials, with the characteristic midnight blue color of oxygen vacancies. The growth habit displayed [100] as well as [110] and [210] faces. These materials were strongly pleochroic, and X-ray diffraction confirmed

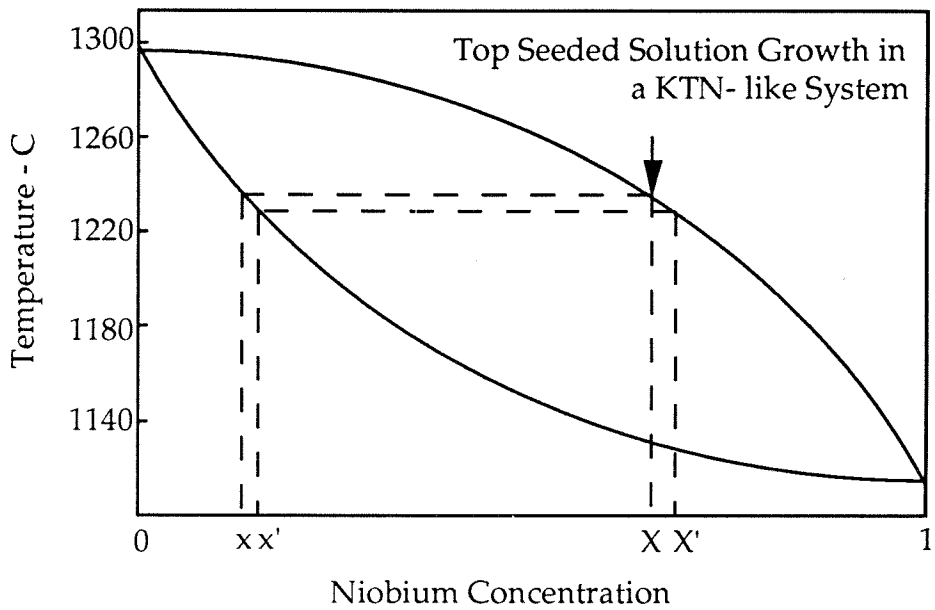

Figure 4-6. The phase diagram for $KTa_{1-x}Nb_xO_3$ illustrating the top seeded solution growth (TSSG) process. The flux with [Nb] = X is cooled to the liquidus, and the crystal begins growing with composition [Nb] = x. As cooling drives the growth, the flux and crystal compositions shift to X' and x' respectively.

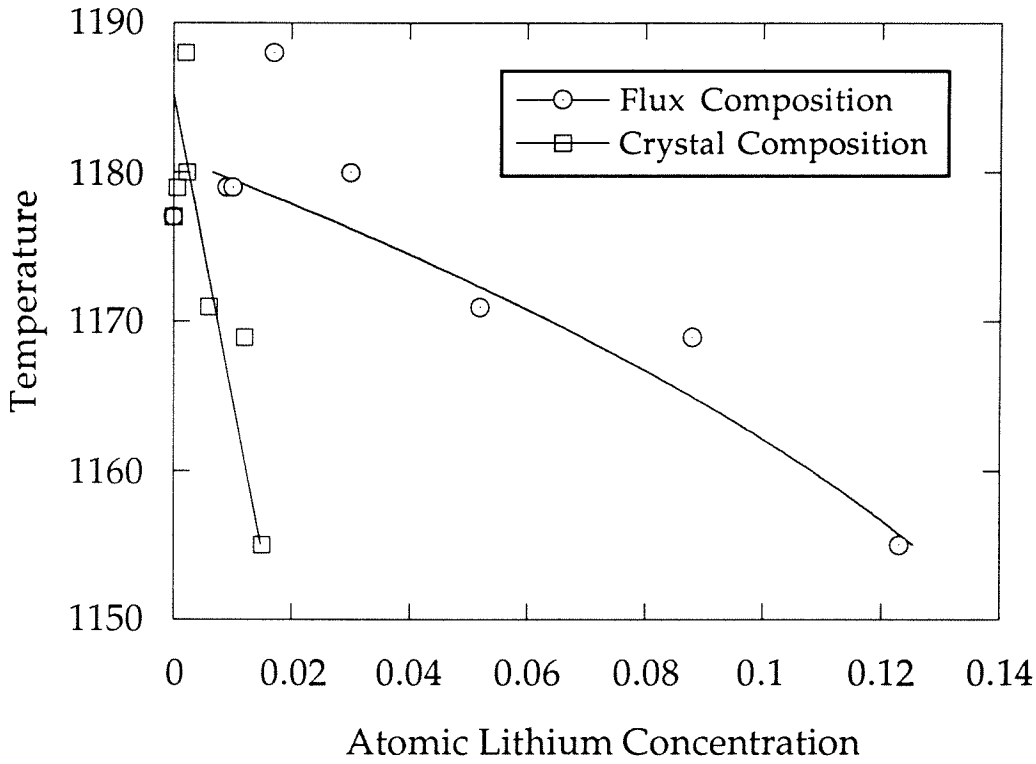

Figure 4-7. The phase diagram of $K_{1-y}Li_yTa_{1-x}Nb_xO_3$ versus lithium concentration for fixed niobium concentration, [Nb] = 0.65, in the flux. Deviations from the smooth curve are determined to be due to variations in [Nb] in the crystal despite a constant flux concentration.

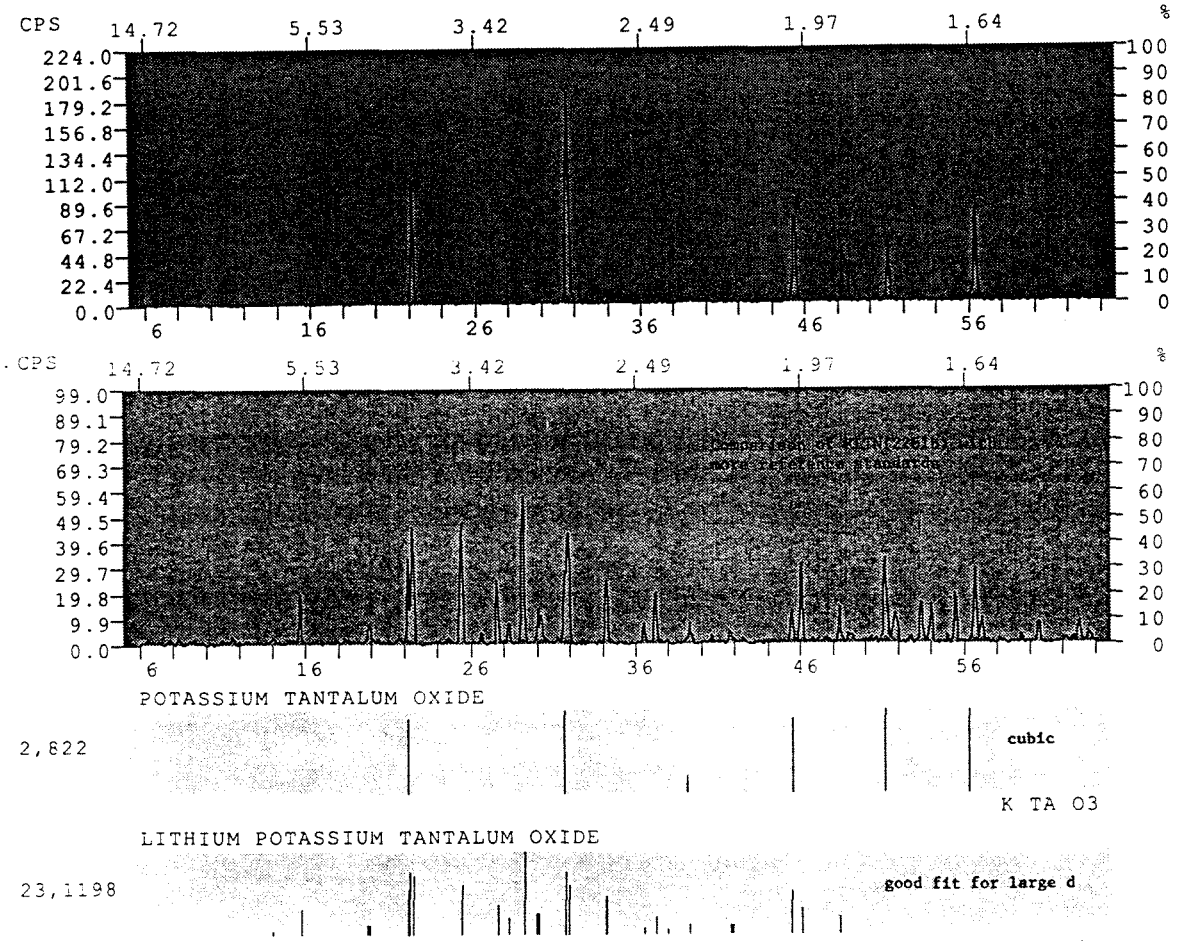

Figure 4-8a. Powder X-ray diffraction of a cubic $K_{1-y}Li_yTa_{1-x}Nb_xO_3$ with small lithium concentration. The potassium tantalate standard is shown for comparison. **4-8b.** Powder X-ray diffraction of a noncubic $K_3Li_2(TaNb)O_3$. A lithium potassium tantalate ($K_3Li_2Ta_5O_{15}$) standard is shown for comparison.

they were not cubic. The X-ray peaks are very similar to those in $K_3Li_2(Ta_{1-x}Nb_x)$compounds[17] (Figure 4-8) which have the ilmenite tungsten bronze structure. The measured composition, $K_{.6}Li_{.32}(TaNb)O_3$, is consistent with this statement. This abrupt compositional and structural change is attributed to an instability due to the size differential between the lithium and potassium ions. It should be noted that the transition from cubic to tungsten bronze growth could be forestalled somewhat by boosting the (potassium + lithium) / (tantalum + niobium) ratios, as in crystal #67, although these materials invariably grew with flux inclusions and were pyramid rather than cube shaped.

The color of the KLTNs grown is due to the transition metal dopant, lithium concentration, and niobium/tantalum ratio. Crystals grown without dopants were colorless. In the copper/vanadium doped crystals, the copper ion is present as either Cu^{1+} or Cu^{2+}, with absorption peaks at 410 and 580nm respectively. The relative strengths of these peaks is a direct indicator of the relative concentrations of these oxidation states, according to Beer's law[18]. In crystals with small niobium concentration, i.e., when $X \leq 0.4$, the color is olive green. As X is increased, however, color banding is observed, from greenish yellow near the seed to bright slightly yellowish green at the later growing parts of the crystal. Optical absorption data confirmed these colors to be the result of a progressively increasing $[Cu^{2+}]/[Cu]$ ratio (Fig. 4-9a), from 0 at the outset of growth to approximately $[Cu^{2+}]/[Cu] = 0.15$ near the end. Additionally, when lithium is omitted from the flux composition, the crystals grow a blue core surrounded by the yellow and green bands. The blue indic-

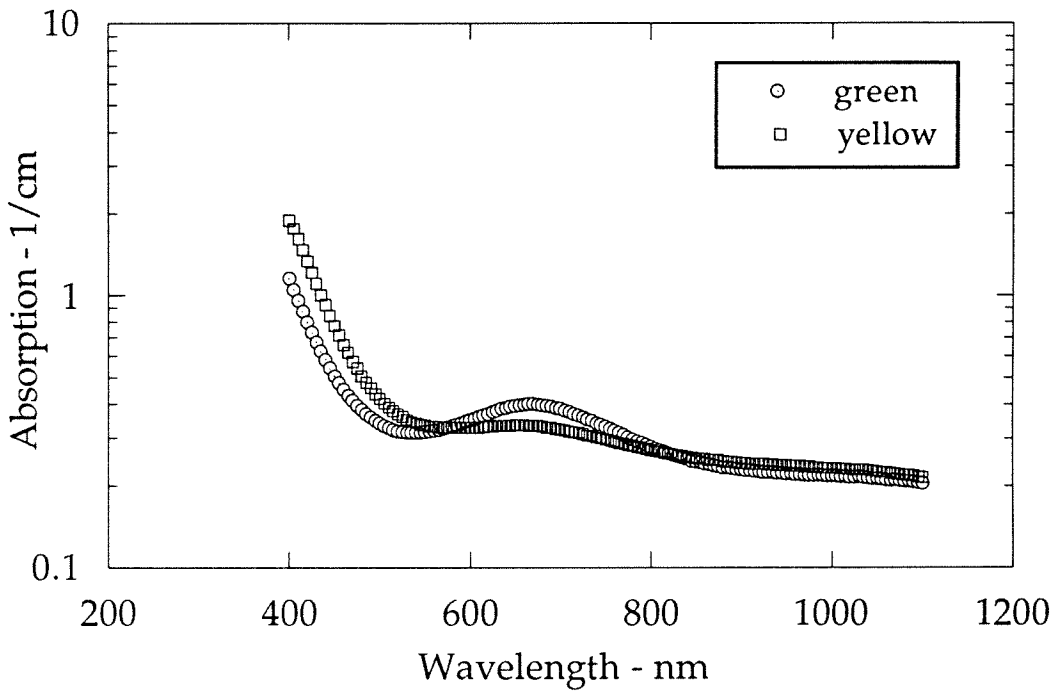

Figure 4-9a. Absorption spectrum of an as grown $K_{1-y}Li_yTa_{1-x}Nb_xO_3$ at two positions along the growth. The color shifts from yellow to green as the concentration of Cu^{2+} increases.

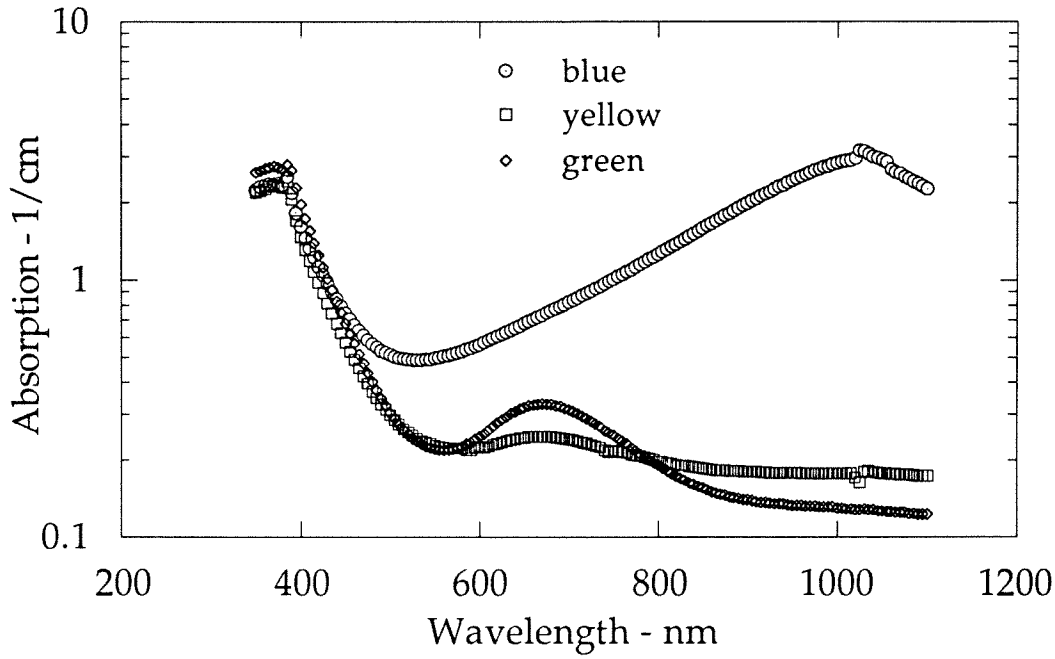

Figure 4-9b. Absorption spectrum of an as-grown $KTa_{1-x}Nb_xO_3$ at three positions along the growth. The strongly absorbing band at 1000nm is due to oxygen vacancies. As the growth continues, the environment becomes progressively more oxidizing. First the oxygen vacancies disappear, then the concentration of Cu^{2+} increases.

cates oxygen vacancies, as evidenced by absorption data (Fig. 4-9b). These blue crystals have been noted by other researchers[19-22] growing KTN. As little as 0.5% of lithium in the flux prevents the blue color, and markedly improves the growth quality of KLTN over that of KTN.

It should be mentioned that the vanadium present in the flux as a dopant plays no role in the coloring, and is only present in minute quantities in the growth. Since multiple growth attempts to grow KTN:Cu without the presence of vanadium in the flux failed to produce high quality doped samples, we conclude that the vanadium assists in the introduction of copper into the perovskite lattice.

KLTN crystals were also grown with iron/titanium doping. In these crystals the iron is present as either Fe^{2+} or Fe^{3+}. The optical absorption spectrum of KLTN:Fe,Ti (#03101) is shown in Fig. 4-10 The curves show the as-grown spectrum as well as the spectrum after one and two thermal reducing treatments. The thermal treatments were performed at ~800°C in an argon atmosphere and they serve to change the relative ratio of Fe^{2+}/Fe^{3+} from the as-grown values. A detailed enumeration of the absorption characteristics of iron doped KTN and the thermal reduction process can be found in Ref. 18.

4.5.2 Growth Parameters

Several parameters of the growth have considerable influence on the quality of the grown crystal. The most critical condition for good growth is the temperature. If seeding takes place more than a degree or so below the proper growth temperature, rapid growth with associated flux inclusions results

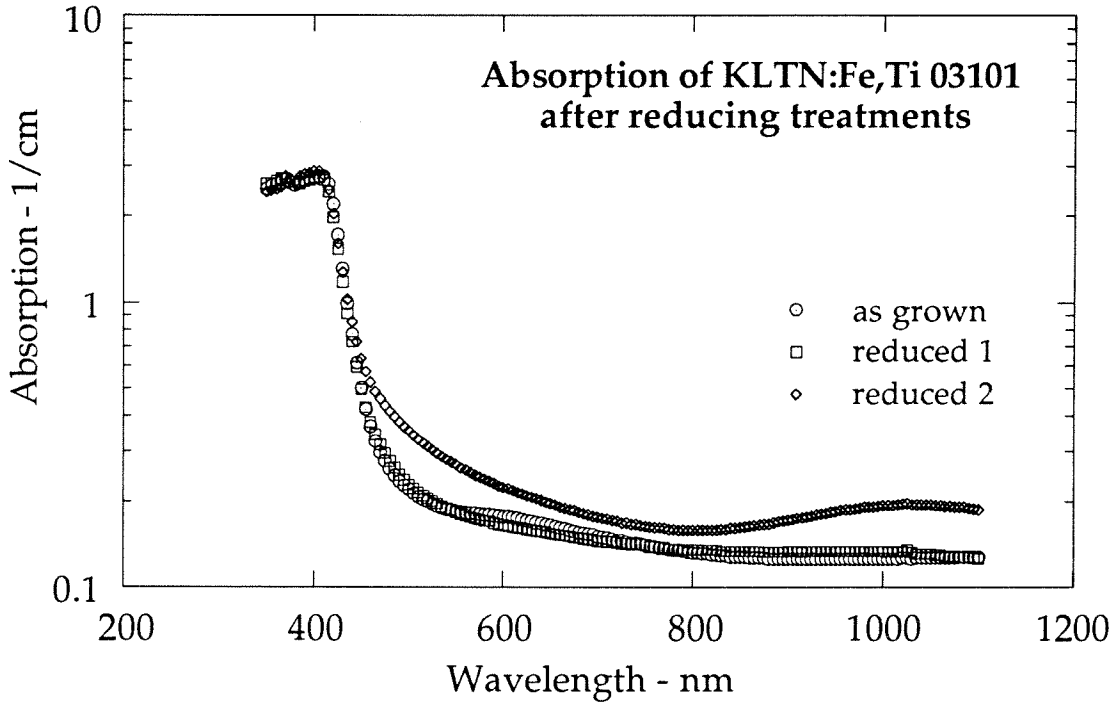

Figure 4-10. Absorption spectrum of an as-grown KLTN:Fe,Ti in the as-grown state and after one and two thermal reduction treatments at 800^{o}C in an argon atmosphere. The thermal treatments serve to change the relative ratio of Fe^{2+}/Fe^{3+} from the as-grown values.

until the system reaches equilibrium. The maintenance of a temperature gradient between the seed and the rest of the furnace is also crucial. If the air flow is inadequate or the seed becomes loose during the growth, the growth will be polycrystalline. Proper cooling always leads to a single nucleation site and single crystal growth.

It is preferred that the flux ingredients remain as uniform as possible at the seed junction because the proper growth temperature is a function of the flux composition. The flux is stirred by rotating the seed. In order to maintain a homogeneous flux composition and temperature profile, the seed rotation direction is periodically reversed. But every time the rotation direction is reversed, growth accelerates briefly, causing striations. A possible explanation for this phenomenon is that the tantalum tends to settle out, and that the rotation reversal generates turbulence bringing the tantalum-rich mixture to the surface. The increase in tantalum concentration (decrease in X) leads to an increased growth temperature, which causes the growth rate acceleration. In support of this theory, the longer the period of time between rotation reversals, the more tantalum settles out, and the more violent the growth rate acceleration on rotation reversal. Accordingly, it is preferred that more frequent rotation reversals be used to reduce the growth rate acceleration. (The newly constructed furnace mentioned at the beginning of this chapter has a facility for rotating the crucible support that is designed to eliminate this problem entirely.)

As an example, when the rotation direction was switched every 13minutes during the growth of crystal #87, flux inclusions resulted along the

growth line boundaries; when the rotation was reversed every 6 minutes (in the same crystal) however, no inclusions were formed. For the same reason, the rotation rate should be kept constant. In one instance, the rotation rate was increased from 25 to 30 rpm causing flux inclusions to be deposited on the face of the developing crystal for approximately one hour.

Figure 4-11a shows results of a series of microprobe measurements taken perpendicular to the growth lines in a KLTN. The tantalum and niobium concentrations are plotted as a function of position; the measurements of tantalum and niobium are completely independent. Figure 4-11b represents the sum of the tantalum and niobium concentrations along the crystal. It is seen that the strongly anticorrelated fluctuations of the tantalum and niobium concentrations individually does not carry over into their sum, which is fairly constant at [Ta]+[Nb] = 1.002. The small variations in figure 4-11b lead to an estimate of the accuracy of the data in figure 4-11a. The region displayed in figures 4-11a,b corresponds to 10-12 growth lines in the crystal. Thus the semiperiodic fluctuations in the niobium concentrations occur in conjunction with the growth lines, lending further support to the hypothesis of composition variation in the flux due to incomplete stirring.

It was mentioned previously that the depletion of the nutrients in the crucible leads to an increase in niobium concentration, and hence, lattice parameter, during the course of the growth. Thus, as the crystal grows onion-style with one cubical shell wrapping around the previous one, the strain gradually increases. This strain is visible under crossed polarizers as a birefringence increasing from the center. Under transmitted light, a faint tetrahe-

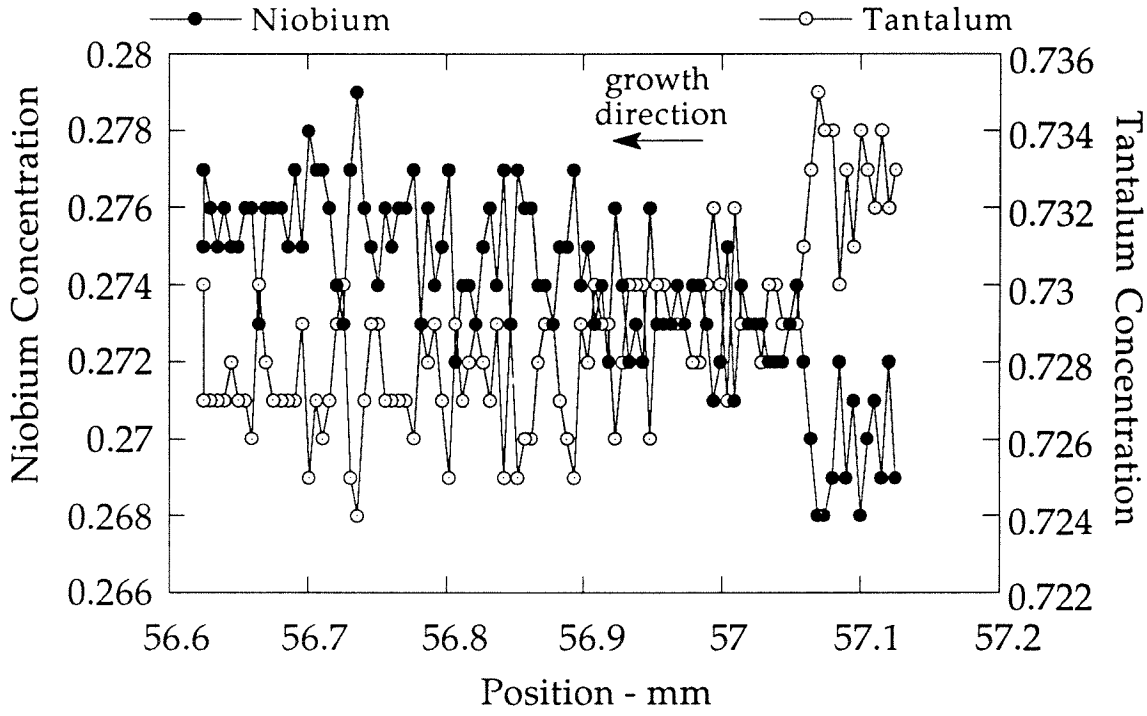

Figure 4-11a. Atomic concentration of niobium and tantalum as a function of position perpendicular to growth lines in crystal 84. The measurements are strongly anticorrelated indicating fluctuations in the the flux composition. The plot corresponds to 10-12 growth lines.

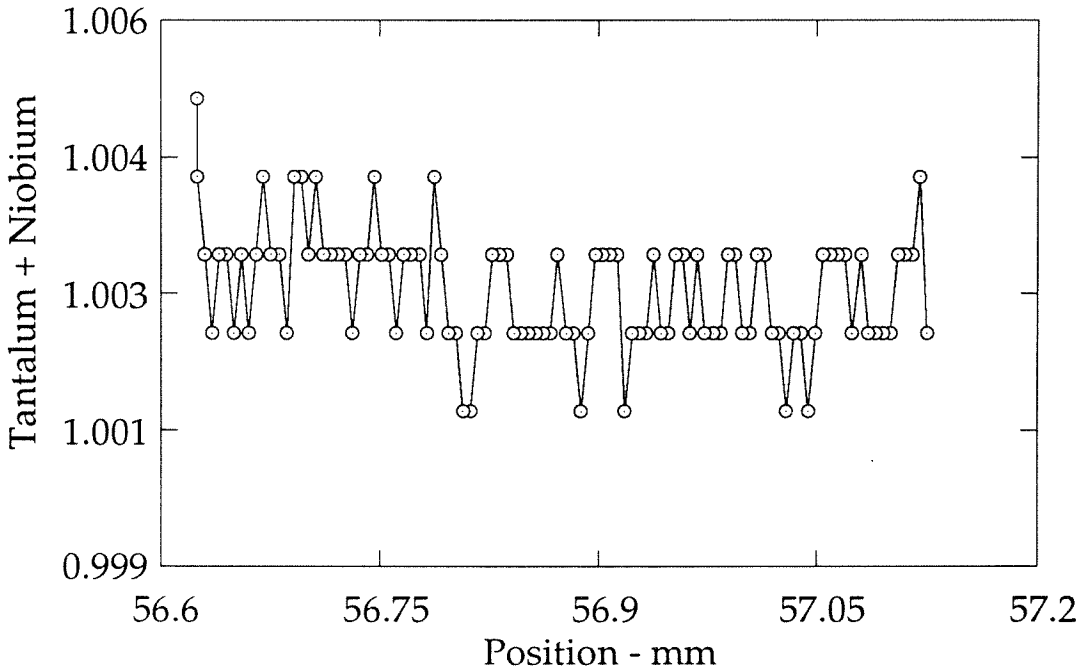

Figure 4-11b. The sum of the tantalum and niobium concentrations is fairly constant at the stoichiometrically expected amount. This verifies the accuracy of the previous figure.

dral pyramid is visible, with its apex at the tip of the seed. If the twins are cut apart most of the strain is relieved.

4 . 6 Influence of Lithium/ Niobium on Transition Properties

KTNs are ferroelectric materials which have a high temperature paraelectric phase and become tetragonal at a Curie temperature $T_c \approx 850[x]$ K, (for small [x]) where [x] is the niobium concentration. At least two more structural transitions occur as the temperature is lowered. The relative dielectric constants versus temperature of a number of KTN and KLTN crystals are illustrated in figures 4-12 through 4-16. The composition of these crystals and the temperature of their highest symmetry phase transition is summarized in table 4-5. Figures 4-13 through 4-16 show the relative dielectric constant measured for both cooling and warming of the crystal. The cooling curve invariably exhibits higher peak dielectric constants and phase transitions at slightly lower temperatures. Since the data were taken at cooling/warming rates of approximately 0.2°C /min the temperature discrepancies of up to 12°C between the cooling and warming curves are not experimental artifacts. In figures 4-12a,b the low frequency dielectric constant of a $K_{.95}Li_{.04}Ta_{.857}Nb_{.13}O_3$ (crystal 44) and a $KTa_{.85}Nb_{.13}$ (crystal 18) are compared. In the KTN the transitions from cubic to tetragonal to orthorhombic to rhombohedral are clearly seen, in the KLTN only the first transition is distinct. Additionally, the transition temperature has been increased almost 50K in the KLTN, although the niobium concentrations of the two crystals are equal. Fig. 4-13 shows the dielectric response of a $K_{0.980}Li_{.006}Nb_{0.827}Ta_{0.176}O_3$ (crystal 75), and Fig. 4-14 shows that of a $K_{0.989}Li_{.007}Nb_{0.777}Ta_{0.223}O_3$ (crystal 82). In both of these plots

Xtl #	Flux Composition		Crystal Composition				T_C °C
	X	Y	[K]	[Li]	[Ta]	[Nb]	
18	-	-	1.00	0	0.86	0.13	-143
44	0.35	0.1228	0.95	.0511	0.857	0.129	-95
75	0.5	0.0517	0.980	.006	0.827	0.176	-112
82	0.6	0.0517	0.989	.007	0.777	0.223	-90
85	0.65	0	0.992	0	0.768	0.29	-41
86	0.65	0.0086	0.994	.0006	0.700	0.299	-28
84	0.65	0.0172	0.990	.0019	0.730	0.27	-24
83	0.65	0.0517	0.993	.006	0.687	0.314	-22
87	0.65	0.0877	1.006	.012	0.677	0.32	-2
90	0.65	0.1227	0.985	.015	0.708	0.293	-21
93	0.7	0.0517	1.031	.0052	0.644	0.347	5
94	0.7	0.0862	1.013	.0044	0.635	0.359	20

Table 4-5. The flux and crystal compositions, as well as the phase transition temperatures of several KLTNs are listed. The crystals are listed in groups of increasing niobium concentration. Within each group the listing is in order of increasing lithium concentration. The phase transition temperature increases with either lithium or niobium concentration increase.

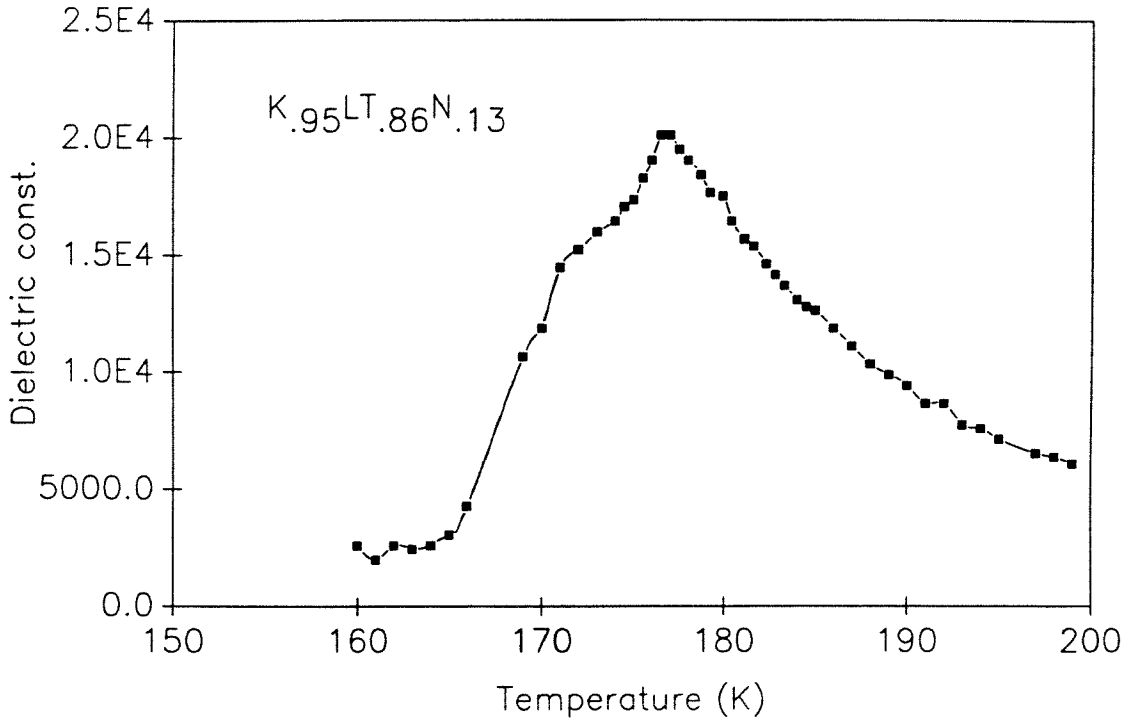
2.5E4
2.0E4
1.5E4
1.0E4
5000.0
0.0
Dielectric const.
$K_{.95}LT_{.86}N_{.13}$
150
160
170
180
190
200
Temperature (K)

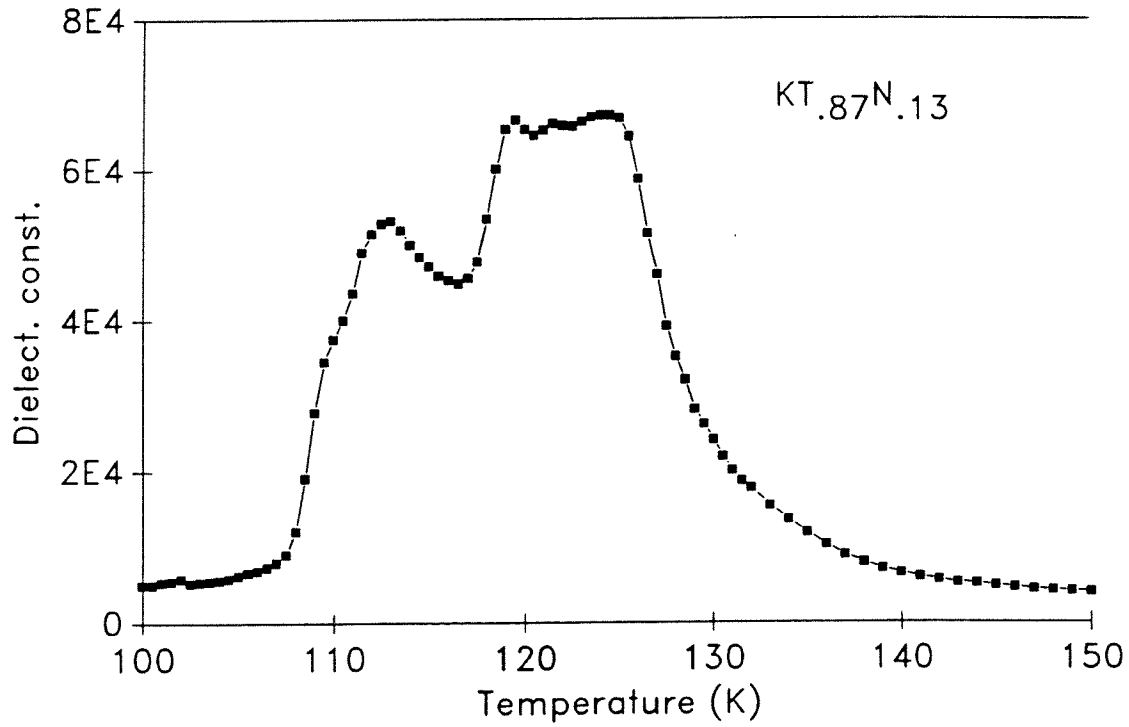
8E4
6E4
4E4
2E4
0
Dielect. const.
$KT_{.87}N_{.13}$
100
110
120
130
140
150
Temperature (K)

Figure 4-12a. (previous page) Dielectric constant of the $K_{.95}Li_{.05}\ Ta_{.857}\ Nb_{.129}\ O_3$ (crystal 44). The phase transition is approximately 50°C higher than a comparable $KTa_{1-x}Nb_xO_3$ (see figure 4-12b). **Figure 4-12b.** Dielectric constant of a $KTa_{.86}\ Nb_{.13}\ O_3$ (crystal 18).

Figure 4-13. (following page) The dielectric response of a $K_{0.980}Li_{.006}\ Nb_{0.827}\ Ta_{0.176}\ O_3$ (crystal 75).

Figure 4-14. (following pages) The dielectric response of a $K_{0.989}\ Li_{.007}Nb_{0.777}\ Ta_{0.223}O_3$ (crystal 82).

Figure 4-15a-f. (following page) The dielectric curves of $K_{1-y}L_yT_{0.7}N_{0.3}$ crystals is illustrated with $0<y<.015$. The number of distinct phase transitions decreases with increasing lithium concentration and, again, the temperature of the highest transition increases with the lithium concentration.

Figure 4-16a, b. The dielectric response of two $K_{1-y}L_yT_{0.65}N_{0.35}$ crystals. Here, the phase transition temperature has been raised to approximately room temperature.

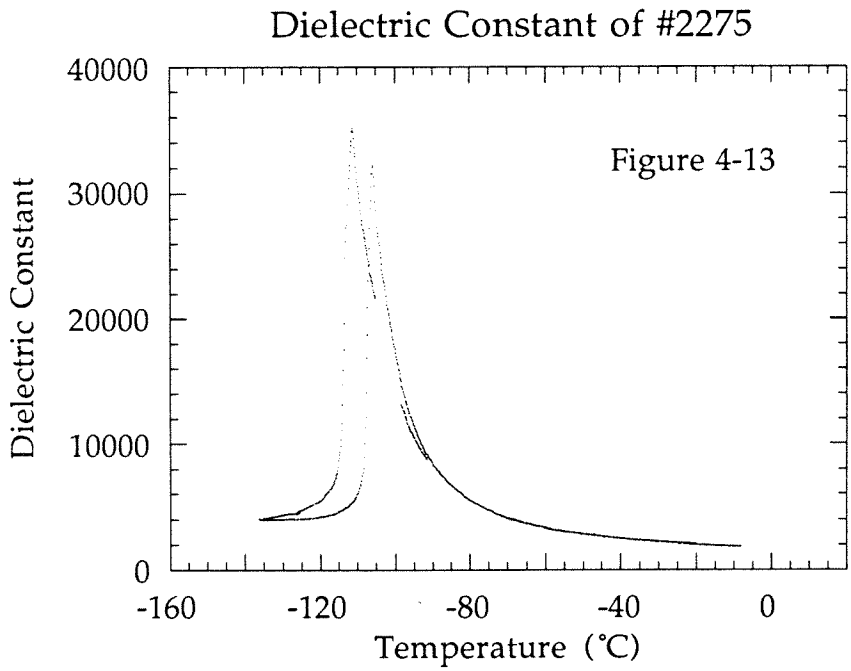
Dielectric Constant of #2275
Figure 4-13
Dielectric Constant
40000
30000
20000
10000
0
-160
-120
-80
-40
0
Temperature (°C)

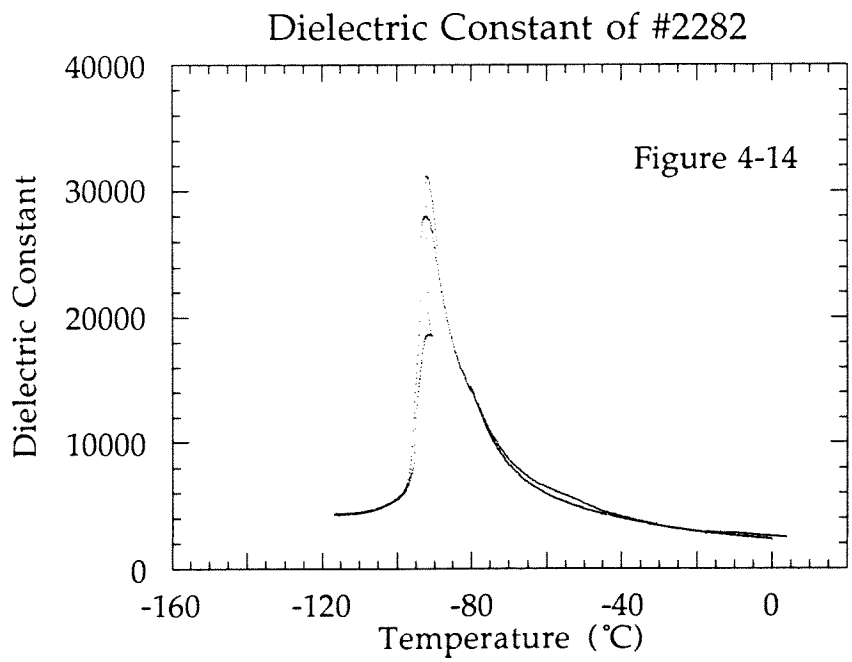
Dielectric Constant of #2282
Figure 4-14
Dielectric Constant
40000
30000
20000
10000
0
-160
-120
-80
-40
0
Temperature (°C)

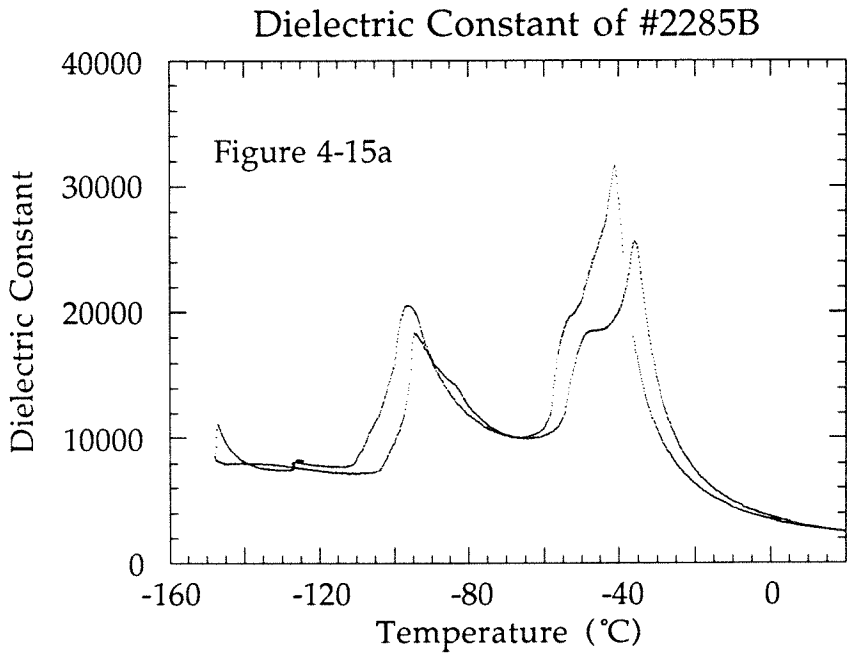
Dielectric Constant of #2285B
Figure 4-15a
Dielectric Constant
40000
30000
20000
10000
0
-160
-120
-80
-40
0
Temperature (℃)

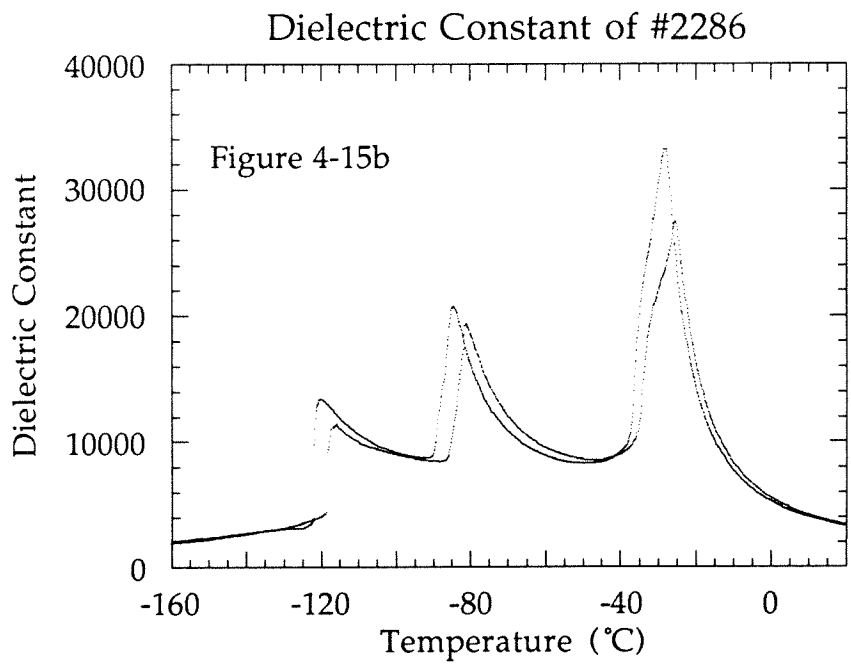
Dielectric Constant of #2286
Figure 4-15b
Dielectric Constant
40000
30000
20000
10000
0
-160
-120
-80
-40
0
Temperature (℃)

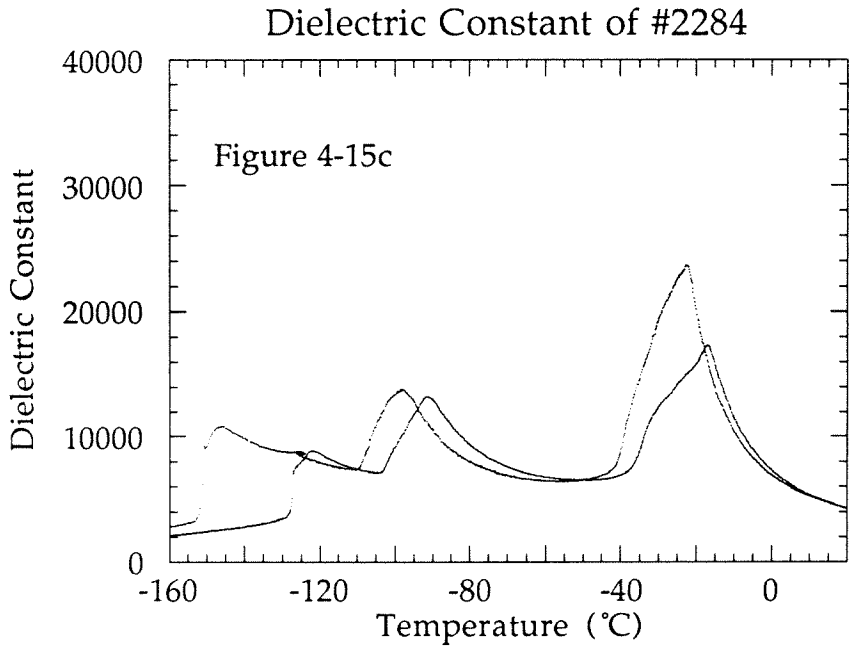
Dielectric Constant of #2284
Figure 4-15c
Dielectric Constant
40000
30000
20000
10000
0
-160
-120
-80
-40
0
Temperature (℃)

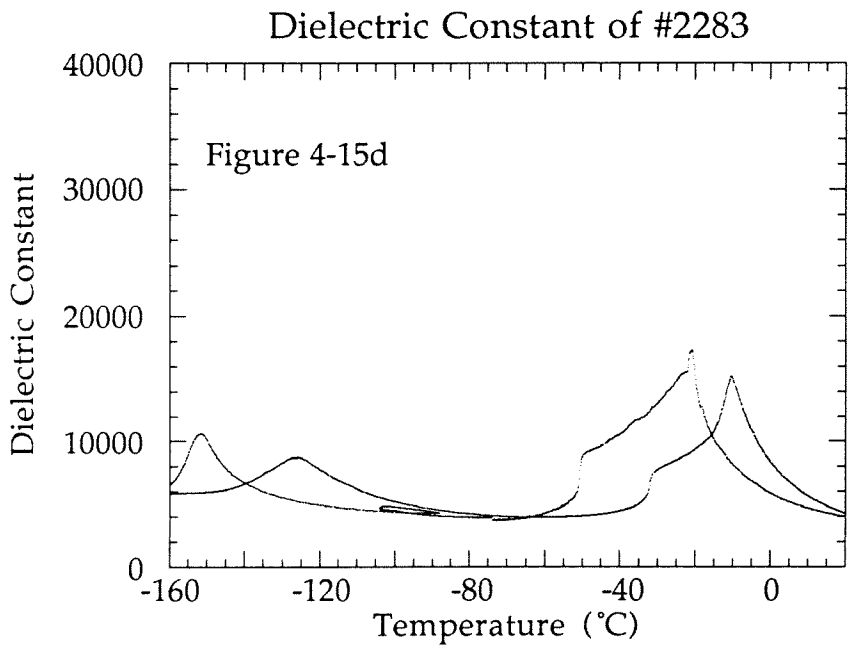
Dielectric Constant of #2283
Figure 4-15d
Dielectric Constant
40000
30000
20000
10000
0
-160
-120
-80
-40
0
Temperature (℃)

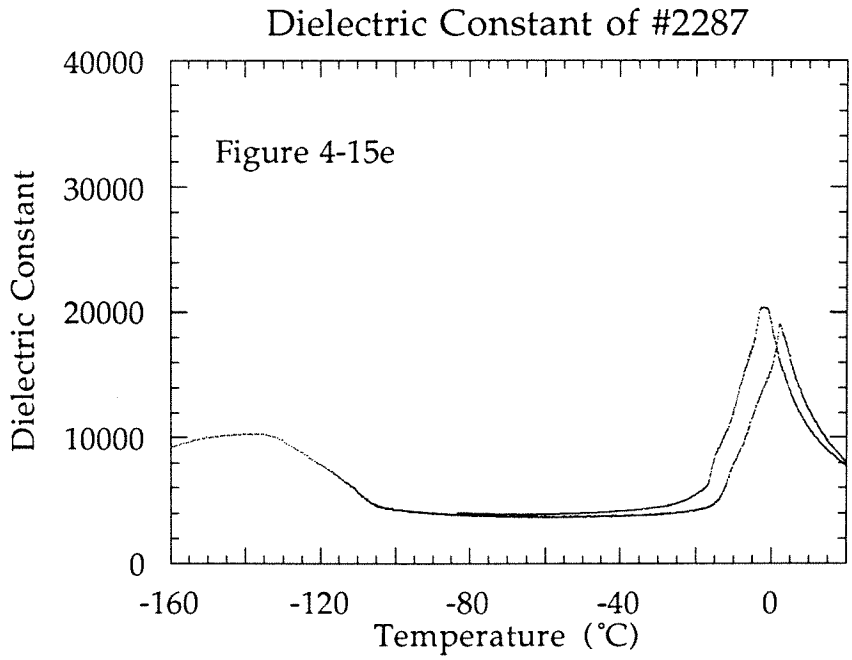
Dielectric Constant of #2287
Figure 4-15e
Dielectric Constant
40000
30000
20000
10000
0
-160
-120
-80
-40
0
Temperature (°C)

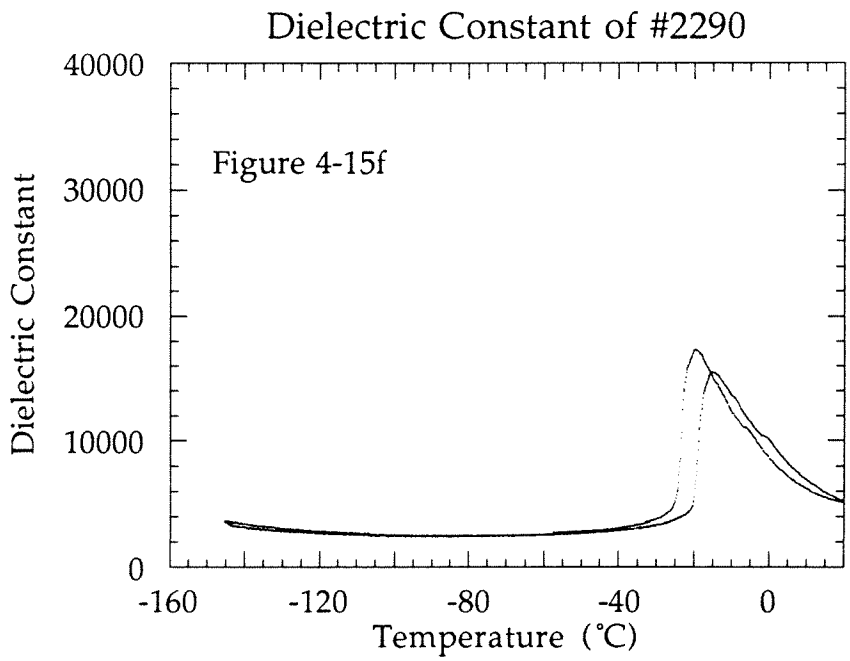
Dielectric Constant of #2290
Figure 4-15f
Dielectric Constant
40000
30000
20000
10000
0
-160
-120
-80
-40
0
Temperature (°C)

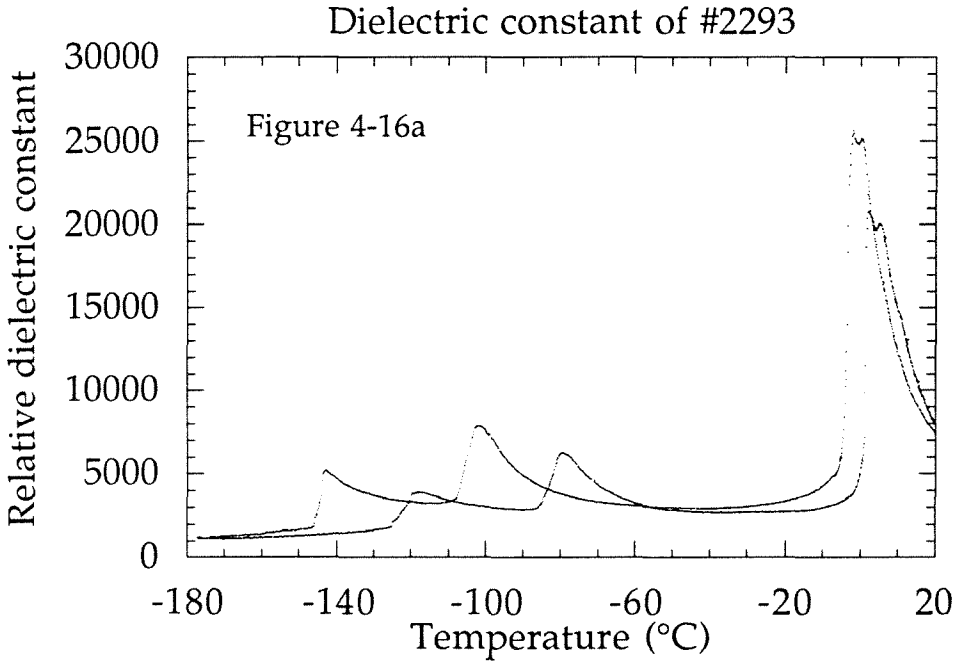
Dielectric constant of #2293
Figure 4-16a
Relative dielectric constant
30000
25000
20000
15000
10000
5000
0
-180
-140
-100
-60
-20
20
Temperature (°C)

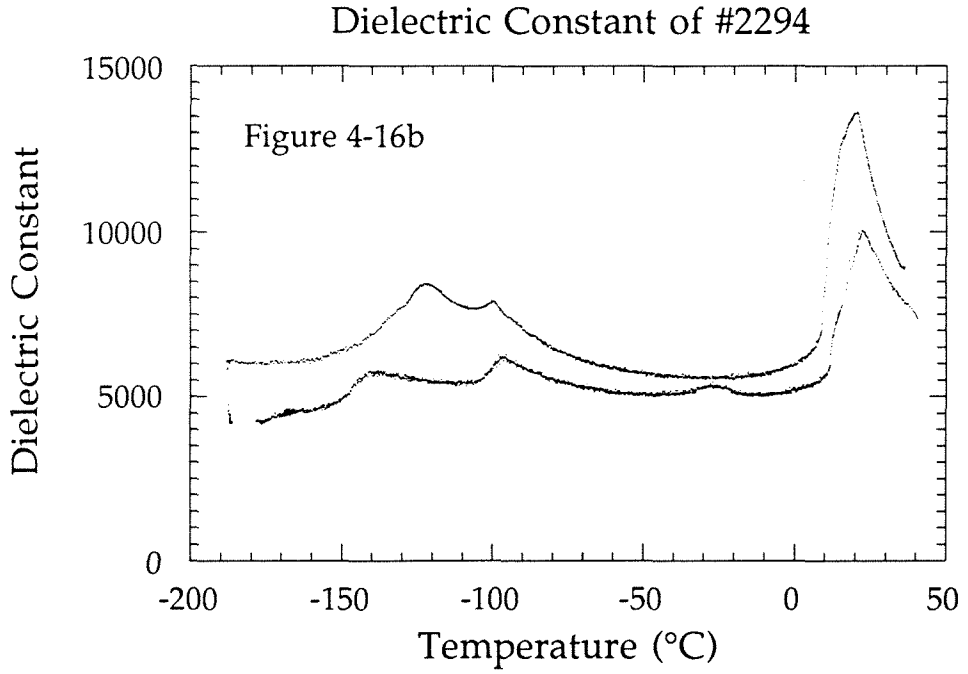
Dielectric Constant of #2294
Figure 4-16b
Dielectric Constant
15000
10000
5000
0
-200
-150
-100
-50
0
50
Temperature (°C)

only one distinct transition is seen and the temperature of the highest transition is higher than would be expected for an equivalent KTN.

In figures 4-15a-f, the dielectric responses of $K_{1-y}L_yT_{0.7}N_{0.3}$ crystals are illustrated with $0<y<.015$. The strength and number of the lower temperature phase transitions decreases with increasing lithium concentration and, again, the temperature of the highest transition increases with the lithium concentration. The lithium concentrations are read from table 4-5. Figures 4-16a,b display the dielectric response of two $K_{1-y}L_yT_{0.65}N_{0.35}$ crystals. Here, the phase transition temperature has been raised to approximately room temperature.

From figures 4-12 through 4-16 it can be concluded that in KLTNs with low niobium concentration, the addition of lithium eliminates two of the dielectric peaks corresponding to phase transitions. Only one very sharp peak remains, at a temperature higher than expected for the cubic to tetragonal transition in KTN. In KLTNs with higher niobium concentrations, the influence of the added lithium has a diminished effect. But in all cases the transition temperature increases with either lithium or niobium concentration increase.

The phase transition temperatures for the KLTNs tabulated in table 4-5 is plotted. The phase transition temperatures of KLTN with a fixed lithium concentration of [Li]=0.052 in the flux versus niobium concentration is shown in figure 4-17. In figure 4-18. the phase transition temperature is plotted versus lithium concentration for a niobium concentration fixed at [Nb] = 0.65 in the flux. The effect of lithium to raise the transition temperature saturates

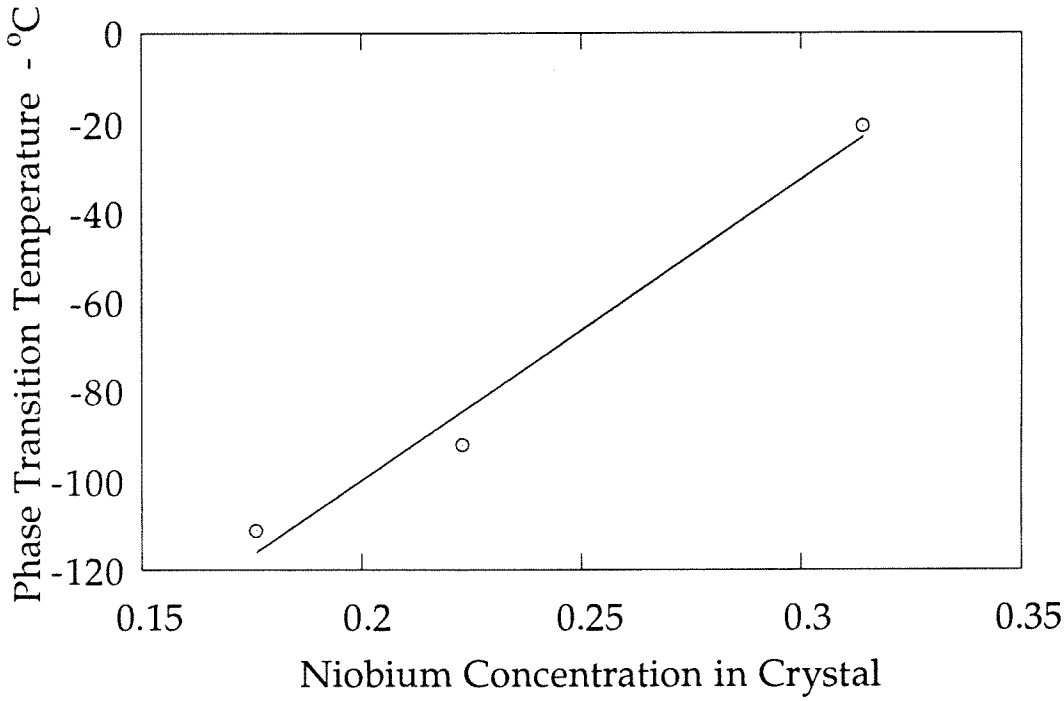

Figure 4-17. The phase transition temperature of $K_{1-y}Li_yTa_{1-x}Nb_xO_3$ with a fixed lithium flux concentration of [Li] = 0.052.

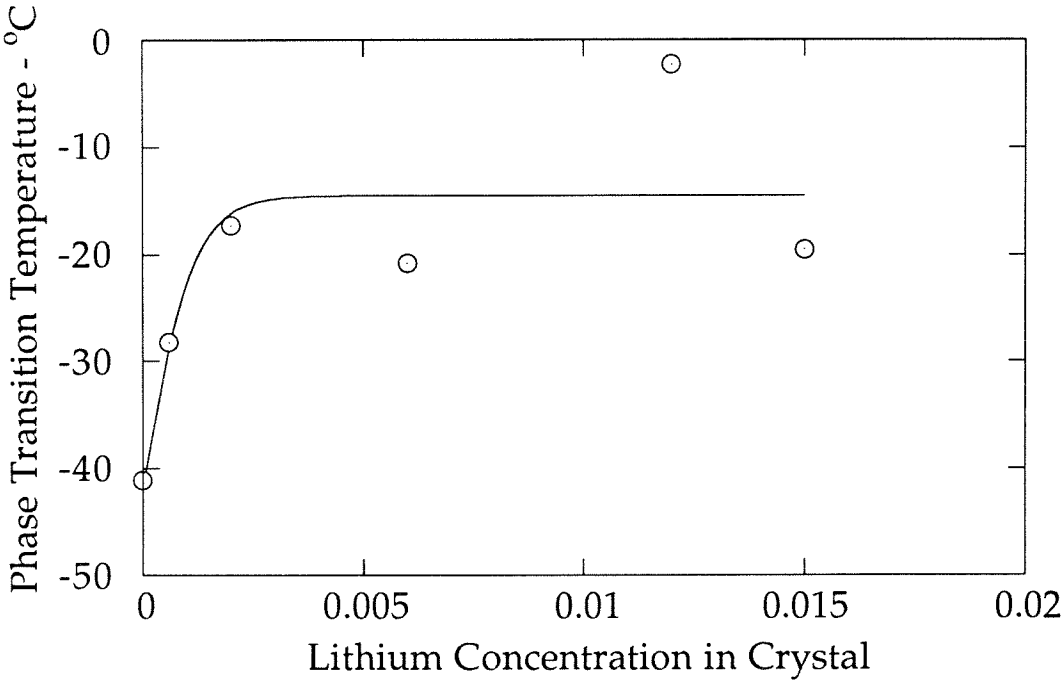

Figure 4-18. The phase transition temperatures of $K_{1-y}Li_yTa_{1-x}Nb_xO_3$ with [Nb] = x = 0.65 in the flux versus lithium concentration. The deviations from a smooth curve are determined to be due to variations in the niobium concentration of the grown crystal.

at y ~ 0.01 where T_c is raised approximately 30°C. For KLTNs with lower niobium concentrations the transition temperature was raised by 50°C in the example given above.

4.7 Summary

A technique has been developed for the preparation of high quality crystals of KLTN. The Top Seeded Solution Growth method is used, pulling the crystal from a flux with an excess of potassium oxide. A range of composition of $K_{1-y}Li_yTa_{1-x}Nb_xO_3$ from $0<y<0.15$ and $0.05<x<0.35$ can be grown using this method. The resultant growths are 10-20g crystals with no inclusions visible under magnification. The partial phase diagrams for $(KLi)Ta_{1-x}Nb_xO_3$ for lithium concentrations of 0, 0.05, and 0.12 are presented as well as the phase diagram for $K_{1-y}Li_yTa_{0.70}Nb_{0.3}O_3$. Growth quality was shown to be a sensitive function of the flux composition and the growth parameters.

References for chapter four

[1] A. Agranat, R. Hofmeister, and A. Yariv, "Characterization of a new photorefractive material: $K_{1-y}L_yT_{1-x}N_x$," Opt. Lett. , **17**, 713-715 (1992).

[2] A. Agranat, V. Leyva, K. Sayano, and A. Yariv, "Photorefractive properties of $KTa_{1-x}Nb_xO_3$ in the paraelectric phase," Proc of SPIE Vol. **1148**, Conference on Nonlinear Optical Properties of Materials, (1989).

[3] A. Agranat, V. Leyva, and A. Yariv, "Voltage-controlled photorefractive effect in paraelectric $KTa_{1-x}Nb_xO_3$:Cu,V," Opt. Lett. **14**, 1017-1019 (1989).

[4] J. P. Wilde and L. Hesselink, "Electric-field controlled diffraction in photorefractive strontium barium niobate," Opt. Lett. **17**, 853 -855 (1992).

[5] V. Leyva, A. Agranat, and A. Yariv, "Fixing of a photorefractive grating in $KTa_{1-x}Nb_xO_3$ by cooling through the ferroelectric phase transition," Opt. Lett. **16**, 554-556 (1991).

[6] A. Agranat, V. Leyva, K. Sayano, and A. Yariv, "Photorefractive properties of $KTa_{1-x}Nb_xO_3$ in the paraelectric phase," Proc of SPIE Vol. **1148**, Conference on Nonlinear Optical Properties of Materials, (1989).

[7] C. M. Perry, R. R. Hayes, and N. E. Tornburg, *Proceedings of the International Conference on Light Scattering in Solids* , M. Balkanski Ed. , Wiley, New York, New York (1975).

[8] S. Triebwasser, "Method of preparation of single crystal ferroelectrics," United States Patent Office, patent number 2,954,300, (1960).

[9] R. Hofmeister, Amnon Yariv, and Aharon Agranat, "Growth and charac-

terization of the perovskite $K_{1-y}Li_yTa_{1-x}Nb_xO_3$:Cu," accepted for publication in J. Crystal Growth.

[10] V. Belruss, J. Kalnajs, and A. Linz, "Top-seeded solution growth of oxide crystals from non-stoichiometric melts," Matl. Res. Bull. **6**, 899-906 (1971).

[11] P. A. C. Whiffen and J. C. Brice, "The kinetics of the growth of $KTa_{1-x}Nb_xO_3$ crystals from solution in excess potassium oxide," J. Crystal Growth **23**, 25-28 (1974).

[12] H. J. Scheel and P. Guenther, "Crystal growth and electro-optic properties of oxide solid solutions," *Crystal Growth of Electronic Materials* , Elsevier Science Publishers, (1984).

[13] W. A. Bonner, E. F. Dearborn, and L. G. Van Uitert, "Growth of potassium tantalate-niobate single crystals for optical applications," Am. Ceram. Soc. Bull. **44**, 9-11 (1965).

[14] J. Y. Wang, Q. C. Guan, J. Q. Wei, M. Wang, and Y. G. Liu, "Growth and characterization of cubic $KTa_{1-x}Nb_xO_3$ crystals," J. Crystal Growth, **116**, 27-36 (1992).

[15] D. Elwell, in *Crystal Growth* , p. 185ff, Ed. B. R. Pamplin, Pergamon press, Oxford (1975).

[16] A. Reisman, S. Triebwasser, and F. Holtzberg, "Phase diagram of the system $KNbO_3$ $KTaO_3$ by the methods of differential thermal and resistance analysis," J. Am. Chem. Soc. **77**, 4228-4230 (1955).

[17] T. Fukuda, Jap. J. Appl. Phys. **9**, 599 (1970).

[18] V. Leyva, Ph.D. thesis, California Institute of Technology, Pasadena CA, unpublished, (1991).

[19] S. H. Wemple, "Polarization effects of magnetic resonances in ferroelectric potassium tantalate," Mass. Inst. Technol. , Res. Lab. Electron. , Tech.. Rept. **#425**, (1964).

[20] W. A. Bonner, E. F. Dearborn, and L. G. Van Uitert, "Growth of potassium tantalate-niobate single crystals for optical applications," Am. Ceram. Soc. Bull. **44**, 9-11 (1965).

[21] W. R. Wilcox and L. D. Fullmer, "Growth of $KTaO_3$ - $KNbO_3$ mixed crystals," J. Am. Ceram. Soc. , **49**, 415-418 (1966).

[22] P. W. Whipps, "Growth of high-quality crystals of KTN," J. Crystal Growth, **12**, 120-124 (1972).

Chapter Five

Electric Field Control of The Photorefractive Effect in Paraelectric KLTN

5.1 Introduction

The use of photorefractive materials to store volume holograms for optical computing and optical memories has long been an active area of research[1-3]. Recently, the use of photorefractive materials in the paraelectric phase has also received attention[4-7]. As discussed earlier, the photorefractive response in the paraelectric phase is controllable with an externally applied electric field. The dielectric constant for these materials obeys the Curie-Weiss law above the phase transition. This leads to very large values for the dielectric constant just above the transition ($\varepsilon = 10^4 - 10^5$). Since the magnitude of the voltage controlled index grating is proportional to the square of the dielectric constant, the optimum operating temperature is just above the phase transition. Crystals operated at this temperature exhibit a strong photorefractive response and achieve extremely high diffraction efficiencies.

In the experiments described in this chapter the crystals were maintained just above the para/ferroelectric transition. Here the material's photorefractive properties are described by the quadratic electro-optic effect. The experimental geometry used is the symmetric one (Fig. 5-1 and 5-4), with both

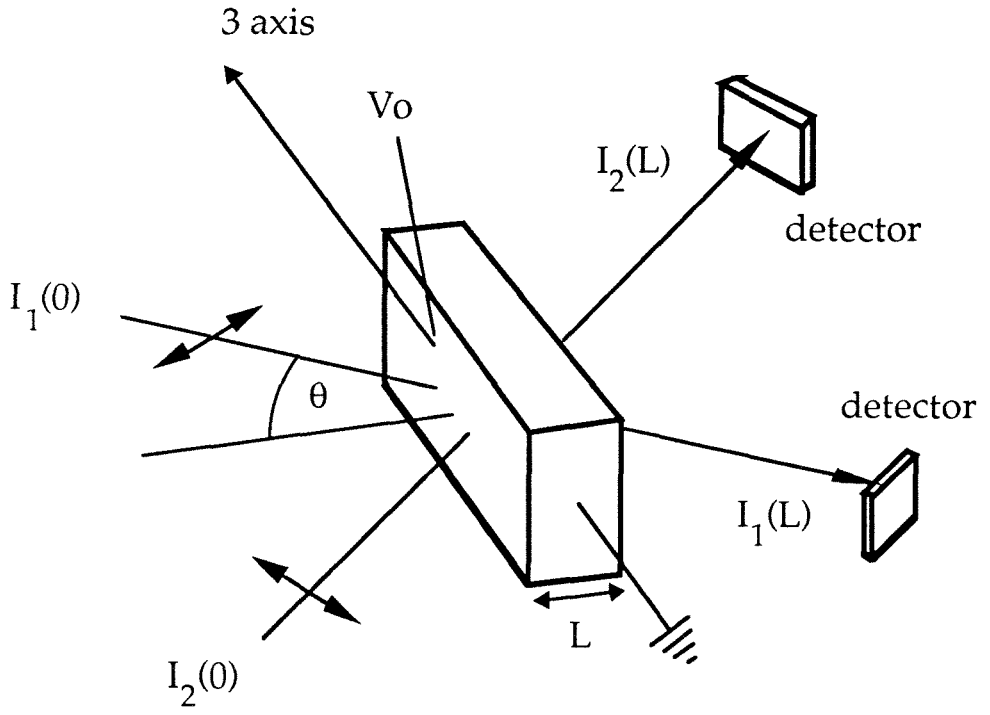

Figure 5-1. The symmetric geometry used for the two beam coupling experiments. The space charge field and the applied field are along the 3-axis. The beams are extraordinarily polarized.

the space charge field and the external applied field directed along the x (3) axis. The change in the refractive index due to $E_{sc}(x)$ was derived in chapter three and is given by

$$\Delta n_{ij}(E_0+E_{sc}) - \Delta n_{ij}(E_0) = \frac{n_0^3}{2} g_{ij33} (\varepsilon_3\varepsilon_0)^2 \{ (E_{sc} + E_0)^2 - E_0^2 \}. \qquad (5.1)$$

Here E_0 is the applied electric field and g_{ijkl} are components of the quadratic electro-optic tensor. n_0 is the nominal index of refraction and ε_3 is the relative dielectric constant along the x axis. The useful, Bragg matched part of the index grating is

$$\Delta n_{ij} = n_0^3 g_{ij33} (\varepsilon_3\varepsilon_0)^2 E_{sc} E_0. \qquad (5.2)$$

Thus the Bragg matched contribution to the index grating is present only with, and is proportional to, an applied electric field.

In the following sections voltage control of the photorefractive effect in paraelectric materials is demonstrated. Voltage dependent two beam coupling and voltage controlled diffraction results are presented. A theory is developed to describe the diffraction versus applied electric field off a grating written with or without an applied field. The theory is applied to the diffraction results with good qualitative agreement.

5.2 Beam Coupling

When two beams $I_1(0)$ and $I_2(0)$ are symmetrically incident on a photorefractive material and write an index grating, intensity coupling occurs between the beams. The output intensities are given by (chapter two)

$$I_1(z) = e^{-\alpha L} \frac{I_1 (I_1 + I_2)}{I_1 + I_2 e^{+\Gamma z}} \tag{5.3a}$$

$$I_2(z) = e^{-\alpha L} \frac{I_2 (I_1 + I_2)}{I_1 e^{-\Gamma z} + I_2} \tag{5.3b}$$

where $\Gamma = 2g \sin\phi$ is the power coupling coefficient and we define $I_1 = I_1(0)$ and $I_2 = I_2(0)$. When $I_1 >> I_2$ we can approximate equations (5.3) as

$$I_1(z) = e^{-\alpha L} I_1 \tag{5.4a}$$

$$I_2(z) = e^{(\Gamma-\alpha) L} I_2. \tag{5.4b}$$

In paraelectric materials the coupling constant g is (conventionally) zero in the absence of an applied field, so that no intensity coupling occurs. In the presence of an electric field the coupling constant is given by

$$g = \frac{\pi n_1}{\lambda} = \frac{\pi}{\lambda} \left(2 n_0^3 g_{11} (\varepsilon_0 \varepsilon)^2 E_0 E_{sc,0}\right) \tag{5.5}$$

where n_1 is the peak to peak index change when $I_1 = I_2$, and $E_{sc,0}$ is the space charge field obtained with unity modulation depth, i.e., when $I_1 = I_2$. This convention is required to ensure that g is purely a material parameter, independent of the beam intensity ratio. From the results of chapter two, the space charge field has a dependence on the applied field given by

$$|E_{sc}| = m E_N \sqrt{\frac{E_d^2 + E_0^2}{E_0^2 + (E_d + E_N)^2}} \cos[2\alpha] \tag{5.6}$$

where the diffusion and trap limited fields are $E_d = kTK/e$ and $E_N = N_A e/(\varepsilon K)$. The modulation depth of the intensity pattern is $m = 2 (I_1 I_2)^{1/2}/I$ (not to be confused with the variable m in (2.5)) and the half angle of beam

intersection within the crystal is α. The beams are polarized in the plane of their intersection within the material. From the same equations one can derive an expression for the phase of the grating

$$\sin \phi = \frac{-[E_0^2 + E_d(E_d+E_N)]}{\sqrt{(E_d^2+E_0^2)\,(E_0^2 + (E_d+E_N)^2)}}. \tag{5.7}$$

Thus the phase $\phi = \pi/2$ (by convention) when no field is applied. (In the next section a new photorefractive mechanism is discussed which yields an index grating with zero applied field. In this case the phase is equal to zero when no field is applied. When a field is applied, the electro-optic grating and the new grating are added in quadrature to obtain the net phase of the sum of the gratings. In this section the new photorefractive mechanism is ignored.) From (5.6) and (5.7) we obtain

$$\Gamma = \frac{-2\pi}{\lambda} n_0^3 g_{11} (\varepsilon_0\varepsilon)^2 E_0 E_N \frac{E_0^2 + E_d(E_d+E_N)}{E_0^2 + (E_d+E_N)^2} \cos[2\alpha] \tag{5.8}$$

with parameters defined as in chapter two. (5.8) gives the intensity coupling coefficient when an index grating is written in a material with an applied electric field. When $E_0 << E_d, E_N$ the intensity coupling coefficient is approximately linear in E_0. The intensity coupling vanishes when $E_0 = 0$.

Equations (5.6-8) are modified if the photorefractive grating is written with zero applied field and the two beam coupling is subsequently measured with applied field. In this case (5.6) and (5.7) reduce to their zero applied field values so that

$$|E_{sc}| = m \frac{E_N E_d}{E_d + E_N} \cos[\, 2\alpha \,] \tag{5.9}$$

and $\sin\phi = 1$. Thus (5.8) becomes

$$\Gamma = \frac{-2\pi}{\lambda} n_0^3 g_{11} (\varepsilon_0 \varepsilon)^2 E_0 \frac{E_N E_d}{E_d + E_N} \cos[2\alpha]. \tag{5.10}$$

Figure 5-1 shows the experimental geometry used to characterize the two beam coupling properties of the KLTN sample with an applied electric field. An index grating was written in the material with zero applied field. A field was applied and the beam coupling was measured. The beam amplification was defined as $e^{\Gamma L} = I_2(L,E_0)/I_2(L)$ where $I_2(L)$ is the output intensity of I_2 when no index grating exists in the crystal and $I_2(L,E_0)$ is the output intensity when a grating has been written and a field is applied. Initially, the value of Γ is given by (5.10). But after several seconds, the beam coupling caused by E_0 modifies the magnitude and phase of the index grating as described by equations (5.6,7) so that Γ evolves to the value dictated by (5.8). As Γ approaches its steady-state value, $I_2(L,E_0)$ changes accordingly.

The crystal used for the following experiment was a copper doped KLTN (#94) with composition $K_{1.013}Li_{.0044}Nb_{.635}Ta_{.359}O_3$. Its phase transition temperature was $T_c = 20^oC$ where its dielectric constant reached $\varepsilon = 13600$. The experiment was performed at 24°C in open air. During writing I_1 was approximately 28 times greater than I_2, and the total intensity incident on the crystal was I ~200mW at 488nm. The two beams I_1 and I_2 were incident on the crystal and wrote an index grating with no field applied. Then a field was

applied and the beam coupling was immediately measured. After approximately 20 seconds the beam coupling was measured again. During this time the grating evolved to its steady-state value with the applied field.

In figure 5-2 the values of the measured intensity coupling are plotted versus applied field. The lower set of data points refers to measurements made immediately after the field was applied. In this case (5.10) applies. The upper data points give the intensity coupling after the grating has evolved to its steady-state value (5.8). The curves are the relevant fits to the theoretical coupling constant. The results for the long write time case do not agree well with the theory, especially for small values of the field. This is possibly explained as follows: It is well known that ferroelectric oxides exhibit substantial frequency dispersion of the dielectric constant down to millihertz frequencies[8] so that the effect of an applied electric field increases over a period of time on the order of several minutes. This effect was observed in a separate series of experiments in KLTN whereby the quadratic electro-optic coefficients (described in chapter six) were determined. Here the birefringence was determined as a function of applied field; with application of a field, the birefringence instantaneously rose to a certain value and then slowly increased over a period of ten seconds or so to a value 10-50% higher. In the experiment of Fig. 5-2 this would indicate that the short write time data was obtained with a smaller effective dielectric constant than the long write time data.

The results in Fig. 5-2 demonstrate linear voltage control of the beam intensity coupling coefficient. Although the magnitude of the beam cou-

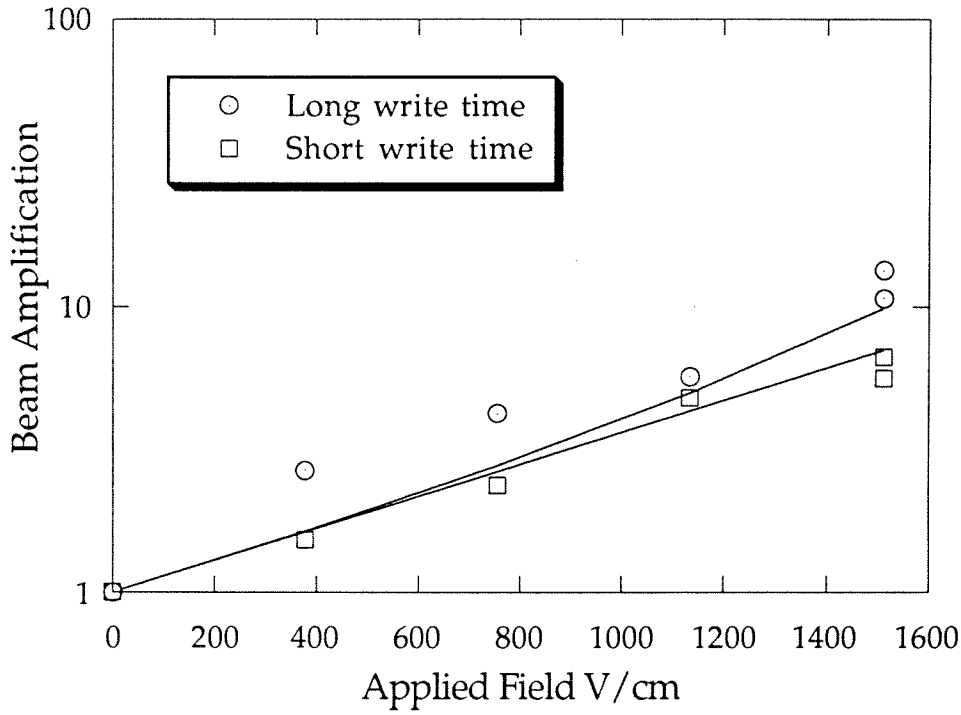

Figure 5-2. The beam amplification caused by the intensity coupling coefficient Γ for a paraelectric KLTN is plotted versus applied electric field. Since the material is centrosymmetric the coupling coefficient is exactly zero with no applied field.

pling is smaller than published results for other materials,[9] the coupling is controllable. In addition, the KLTN crystal displays little beam fanout even with large applied fields. Beam fanout is often a severe problem for most other materials, including $BaTiO_3$ and $LiNbO_3$.

5.3 Electric Field Control of Diffraction

5.3.1 Solution of Coupled Equations

In this section we calculate the diffraction of an incident beam off a dynamically written index grating in a paraelectric material as a function of the applied electric field. The grating is written with an arbitrary applied field. The reading and writing fields are generally not equal. We include the effects of the zero phase ZEFPR grating (see chapter six for details of the ZEFPR effect).

The photorefractive response of paraelectric KLTN is described by the quadratic electro-optic effect in conjunction with the ZEPFR effect[10,11]. The ZEFPR gratings are unique in that they are always $\pi/2$ out of phase with the electro-optically induced index grating. In addition, the ZEFPR index grating is proportional to the space charge field. Thus we can write the nominal index grating as $\Delta n(z) = \Delta n_{EO}(z) + \Delta n_{Zf}(z)$ which has the contribution from both the conventional electro-optic grating as well as the ZEFPR grating.

$$\begin{aligned}\Delta n(z) &= E_{sc}\left(\gamma E_0 \cos(Kz + \phi_E) + \gamma_{Zf} \sin(Kz + \phi_E)\right) \\ &= E_{sc}\sqrt{(\gamma E_0)^2 + \gamma_{Zf}^2}\sin(Kz + \phi_E + \alpha) \\ &= n_1 \ \mathrm{Im}\{\exp[i(Kz + \phi)]\ \}\end{aligned} \tag{5.11}$$

where $\alpha = \tan^{-1}(\gamma E_o/\gamma_{Zf})$. Note that (5.11) is simply the nominal index grating; the dynamically written grating is modified by the beam coupling (see 5.14). Again E_o is the applied uniform electric field and E_{sc} is the photorefractive space charge field. γ is the effective linear electro-optic coefficient induced by the presence of the applied field. It is given by (chapter three) $\gamma = -n_o^3 g(\varepsilon\varepsilon_o)^2 E_o$. γ_{Zf} is a coefficient which relates the index grating due to the ZEFPR effect with the magnitude of the space charge field which inevitably forms in conjunction with the ZEFPR grating. It is experimentally determined by the diffraction observed with zero applied field. Finally ϕ_E is the phase between the intensity and electro-optic gratings (see (5.7)) as dictated by the Kukhtarev solutions of the band transport model in chapter two. We have

$$\phi_E = \tan^{-1}\left(\frac{E_0^2 + E_d^2 + E_d E_N}{E_0\, E_N}\right) \tag{5.12}$$

where E_d and E_N are as defined above. Reference to (5.11) shows that the addition of the ZEFPR grating modifies the net phase of the grating by $\alpha = \tan^{-1}(\gamma E_o/\gamma_{Zf})$, so that the net photorefractive phase $\phi = \phi_E + \alpha$ is not equal to the phase between the intensity and the electro-optic grating. Finally, equation (5.11) gives the coupling constant (contrast with (5.5))

$$\begin{aligned} g_E &= \frac{\pi}{\lambda}\, E_{sc,0} \sqrt{(\gamma E_0)^2 + \gamma_{Zf}^2} \\ &= g \sqrt{\left(\frac{\gamma E_0}{\gamma_{Zf}}\right)^2 + 1}\ . \end{aligned} \tag{5.13}$$

Here $E_{sc,o}$ is the space charge field for unity modulation depth. The applied

field dependence of the space charge field is given in equation (5.6). Therefore, dynamically written gratings in a paraelectric photorefractive material such as KLTN are characterized by a net photorefractive phase $\phi = \phi_E + \alpha$ and a coupling constant given by (5.13).

The two beam coupling of two incident copropagating beams was solved in chapter two. The solution of the beam equations yields the index grating in the material. The result is

$$\Delta n(z) = n_1 \sqrt{I_1 I_2} \left(I_1 e^{-\Gamma z/2} + I_2 e^{+\Gamma z/2}\right)^{i \cot\phi - 1} \tag{5.14}$$

where I_1 and I_2 are the incident beam intensities. If the grating is written with a field E_w applied ("w" = writing), the photorefractive phase $\phi = \phi_w$ follows from (5.12), and the intensity coupling coefficient $\Gamma = 2 g_w \sin\phi_w$ follows from (5.12) and (5.13). n_1 is obtained from (5.11) or (5.13).

The diffraction of an incident beam off the grating of (5.14) is given by the coupled equations

$$A'(z)\cos\beta = i g_r \sqrt{I_1 I_2}\, e^{+i\phi_w} \times \left(I_1 e^{-\Gamma z/2} + I_2 e^{+\Gamma z/2}\right)^{+ i \cot\phi_w - 1} B(z) - \frac{\alpha}{2} A(z) \tag{5.15a}$$

$$B'(z)\cos\beta = i g_r \sqrt{I_1 I_2}\, e^{-i\phi_w} \times \left(I_1 e^{-\Gamma z/2} + I_2 e^{+\Gamma z/2}\right)^{- i \cot\phi_w - 1} A(z) - \frac{\alpha}{2} B(z) \tag{5.15b}$$

where α is the optical absorption coefficient, and β the half-angle of beam intersection inside the material. g_r the coupling constant during reading, fol-

lows from n_1 of (5.14) using the reading electric field as the applied field, whereas ϕ_w and Γ are calculated using the writing electric field. In other words, the photorefractive phase and the intensity coupling coefficient in (5.14) are determined by the writing field, but the material constant n_1 is a function of the reading field. This fact becomes clear on inspection, and it is the replacement of g_w with g_r in (5.15) which is responsible for the complexity of the solutions of (5.15).

Equations (5.15) are solved along similar lines as equations in chapter nine. The motivation for the approach used here is given in chapter nine and a reading of chapter nine is probably required to fully understand the mathematical hoops of the following paragraphs. Since we will only calculate the diffraction off the grating, i.e., only one beam will be incident on the grating, we will hereinbelow ignore the $e^{i\phi}$ terms in the coupled equations. This term can easily be carried through the equations to show that it has no effect. The optical absorption terms are eliminated in the standard fashion (chapter two). On the resultant equation we perform the independent variable transformation

$$\xi = 2 \int \frac{\sqrt{I_1 I_2}\, g_w \sin\phi_w}{I_1 e^{-\Gamma z/2} + I_2 e^{+\Gamma z/2}}\, dz$$

$$= 2 \tan^{-1}[\sqrt{I_2/I_1}\, e^{+\Gamma z/2}]. \qquad (5.16)$$

Equations (5.15) become

$$a'(\xi) = \frac{i}{2\sin\phi_w}\frac{g_r}{g_w}\sqrt{I_1 I_2}^{\,2i\eta}\left(\frac{2}{\sin[\xi]}\right)^{2i\eta} b(\xi)$$

$$= i\,c\,\sin[\xi]^{-2i\eta}\,b(\xi) \qquad (5.17a)$$

$$b'(\xi) = \frac{i}{2\sin\phi_w}\frac{g_r}{g_w}\sqrt{I_1 I_2}^{\,-2i\eta}\left(\frac{2}{\sin[\xi]}\right)^{-2i\eta} a(\xi)$$

$$= i\,c^*\,\sin[\xi]^{+2i\eta}\,a(\xi). \qquad (5.17b)$$

Here $\eta = \cot\phi_w/2$ and $c = g_r/g_w\,(2\,I_1\,I_2)^{1/2}\,/\,(2\sin\phi_w)$. The change to lower case symbols "a" and "b" is used to highlight the change of independent variable from z to ξ. New functions $T(\xi)$ and $V(\xi)$ are defined with $a(\xi) = T(\xi)\sin\xi^{-i\eta}$ and $b(\xi) = V(\xi)\sin\xi^{+i\eta}$. Second-order equations are obtained with

$$T''(\xi) + \left[|q|^2 - \eta^2 - \frac{i\eta\,(i\eta-1)}{\sin^2\xi}\right] T(\xi) = 0 \qquad (5.18a)$$

$$V''(\xi) + \left[|q|^2 - \eta^2 - \frac{i\eta\,(i\eta+1)}{\sin^2\xi}\right] V(\xi) = 0. \qquad (5.18b)$$

It is noted that the quantity $|c|^2 - \eta^2$ is given by

$$|q|^2 - \eta^2 = \frac{1}{4} + \frac{g_r^2 - g_w^2}{4\sin^2\phi\, g_w^2} \equiv 4\,\beta^2 \qquad (5.19)$$

so that when $g_r = g_w$, β as well as $|c|^2 - \eta^2$ reduce to 1/4. The solutions for the diffraction in this special case are obtained in chapter eight; they are comparatively simple. When $g_r \neq g_w$ the solutions are substantially more complicated.

Following a procedure similar to that outlined in chapters eight and nine we obtain solutions for T(ξ) and V(ξ), i.e., a(ξ) and b(ξ), of the form

$$a(\xi)\, e^{\alpha z(\xi)} = a_1 \sin^{1-2i\eta}\xi \cos\xi\, {}_2F_1\left[-i\frac{\eta}{2}+1-\beta, -i\frac{\eta}{2}+1+\beta; \frac{3}{2}-i\eta; \sin^2\xi \right] +$$

$$a_2 \cos\xi\, {}_2F_1\left[i\frac{\eta}{2}+\frac{1}{2}-\beta, i\frac{\eta}{2}+\frac{1}{2}+\beta; \frac{1}{2}+i\eta; \sin^2\xi \right] \qquad (5.20a)$$

$$b(\xi)\, e^{\alpha z(\xi)} = b_1 \cos\xi\, {}_2F_1\left[-i\frac{\eta}{2}+\frac{1}{2}-\beta, -i\frac{\eta}{2}+\frac{1}{2}+\beta ; \frac{1}{2}-i\eta; \sin^2\xi \right] +$$

$$b_2 \sin^{1+2i\eta}\xi \cos\xi\, {}_2F_1\left[i\frac{\eta}{2}+1-\beta, i\frac{\eta}{2}+1+\beta; \frac{3}{2}+i\eta; \sin^2\xi \right] \qquad (5.20b)$$

where ${}_2F_1[\, a, b; c; z]$ is the hypergeometric function and a_1, a_2, b_1, and b_2 are constants determined by the original coupled equations and the boundary conditions. Since we are considering diffraction we take $b(\xi_0) = b_0$ and $a(\xi_0) = 0$, where ξ_0 is the value of ξ when $z = 0$.

$$\xi_0 = 2 \tan^{-1}[\sqrt{I_2/I_1}]. \qquad (5.21)$$

Using the Gauss transformations and the relations for hypergeometric functions in equations (9.11) and (9.12) we obtain, after some manipulation

$$a_1 = \frac{-i\,c\,(1+4\eta^2)}{1-2i\eta}\,\frac{b_0}{\cos\xi_0}\;x \qquad (5.22a)$$

$${}_2F_1\left[i\frac{\eta}{2}-\beta+\frac{1}{2}, i\frac{\eta}{2}+\beta+\frac{1}{2}; \frac{1}{2}+i\eta; \sin^2\xi_0\right]/D$$

$$a_2 = +i\,c \sin^{1-2i\eta}\xi_0\,(1+2i\eta)\,\frac{b_0}{\cos\xi_0}\;x \qquad (5.22b)$$

$${}_2F_1\left[-i\frac{\eta}{2}-\beta+1, -i\frac{\eta}{2}+\beta+1; \frac{3}{2}-i\eta; \sin^2\xi_0 \right]/D$$

$$b_1 = (1 + 4\eta^2)\frac{b_0}{\cos\xi_0} \quad x \tag{5.22c}$$

$$ {}_2F_1[\, i\frac{\eta}{2} - \beta + \frac{1}{2},\, i\frac{\eta}{2} + \beta + \frac{1}{2};\, \frac{1}{2} + i\eta;\, \sin^2\xi_0]/D$$

$$b_2 = \sin^{1-2i\eta}\xi_0\,(\eta^2 + 4\beta^2)\frac{b_0}{\cos\xi_0} \quad x \tag{5.22d}$$

$$ {}_2F_1[\, -i\frac{\eta}{2} + 1 - \beta,\, -i\frac{\eta}{2} + 1 + \beta;\, \frac{3}{2} - i\eta;\, \sin^2\xi_0]/D$$

where the common denominator D is given by

$$D = (1 + 4\eta^2)\, {}_2F_1[\, i\frac{\eta}{2} - \beta + \frac{1}{2},\, i\frac{\eta}{2} + \beta + \frac{1}{2};\, \frac{1}{2} + i\eta;\, \sin^2\xi_0] \quad x$$

$$ {}_2F_1[\, -i\frac{\eta}{2} - \beta + \frac{1}{2},\, -i\frac{\eta}{2} + \beta + \frac{1}{2};\, \frac{1}{2} - i\eta;\, \sin^2\xi_0] \quad +$$

$$\sin^2\xi_0\,(\eta^2 + 4\beta^2)\, {}_2F_1[\, -i\frac{\eta}{2} - \beta + 1,\, -i\frac{\eta}{2} + \beta + 1;\, \frac{3}{2} - i\eta;\, \sin^2\xi_0] \quad x$$

$$ {}_2F_1[\, i\frac{\eta}{2} - \beta + 1,\, i\frac{\eta}{2} + \beta + 1;\, \frac{3}{2} + i\eta;\, \sin^2\xi_0]. \tag{5.23}$$

The equations (5.20a,b) with constant coefficients defined in (5.22a,b,c,d) and (5.23) determine exactly the amplitude and phase of the transmitted beam b(ξ) and the diffracted beam a(ξ). The solutions can be converted back to the independent variable z using (5.16) where

$$\sin\xi = \frac{2\sqrt{I_1\, I_2}}{(I_1\, e^{-\Gamma z/2} + I_2\, e^{\Gamma z/2})} \tag{5.24a}$$

$$\cos\xi = \frac{(I_1\, e^{-\Gamma z/2} - I_2\, e^{\Gamma z/2})}{(I_1\, e^{-\Gamma z/2} + I_2\, e^{\Gamma z/2})} \tag{5.24b}$$

$$\sin\xi_0 = \frac{2\sqrt{I_1 I_2}}{I_1 + I_2} \tag{5.24c}$$

$$\cos\xi_0 = \frac{I_1 - I_2}{I_1 + I_2}. \tag{5.24d}$$

Note that when $I_1 = I_2$ the coefficients (5.22) blow up and the eigenfunctions (5.20) go to zero at z=0. This case must be treated separately because from the outset the equations assume a different form (equations (5.15)). In practice it is easier to take the limit as $I_1 \to I_2$. Another caveat: if $I_2 > I_1$ the coefficients (5.20) are only valid for $z \geq 0$, and vice versa when $I_2 < I_1$. At the point $z = 0$ the coefficients a_1 and a_2 change sign. The reason that z cannot be chosen arbitrarily is that the original index grating (5.14), from which (5.15) was derived, was written with beams incident at z=0.

Finally, the reflectivity of the grating, i.e., diffraction off the grating, is given by $R = |A(L)|^2/|B(L)|^2$. Thus we have solved for the diffracted power of a beam off a grating as a function of the applied (reading) electric field. The grating is written dynamically with an applied (writing) electric field. When the reading field is equal to the writing field the solution simplifies considerably and is given in chapter eight. This previously obtained solution can be used as a check in numeric calculations. In the next section we repeat the above calculations for the special case of zero applied writing field during grating formation.

5.3.2 Solution of Coupled Equations with $E_W = 0$

When the writing electric field is zero, the photorefractive phase ϕ is also zero. In this case the index grating of (5.14) simplifies to

$$\Delta n(z) = n_1 \frac{\sqrt{I_1 I_2}}{I} \exp[\, i\, g\, z\, (I_2 - I_1) / I]. \qquad (5.25)$$

Here n_1 and g are the zero field values of those parameters (use (5.13) and the definition $g = \pi\, n_1/\lambda$) and I is the total incident intensity. The coupled mode equations (5.15) become

$$A'(z)\cos\beta = i\, g_r \frac{\sqrt{I_1 I_2}}{I_1 + I_2} e^{i\,\Delta z} B(z) - \frac{\alpha}{2} A(z) \qquad (5.26a)$$

$$B'(z)\cos\beta = i\, g_r \frac{\sqrt{I_1 I_2}}{I_1 + I_2} e^{-i\,\Delta z} A(z) - \frac{\alpha}{2} B(z) \qquad (5.26b)$$

where $\Delta = g\,(I_2 - I_1)/(I_2 + I_1)$ is a Bragg mismatch term caused by the phase coupling each beam exerts on the other. The solution of (5.26) is relatively straightforward. The optical absorption terms are eliminated by allowing $A(z) = A(z)e^{\alpha z/2}$ and $B(z) = B(z)e^{\alpha z/2}$. The equations are simplified by the corotating transformation $a(z) = A(z)\, e^{-i\Delta z/2}$ and $b(z) = B(z)\, e^{+i\Delta z/2}$. If the boundary conditions are taken as $B(0) = b_0$ and $A(0) = 0$, i.e., diffraction of b_0 off the grating, the solution is easily shown to be

$$A(z)\, e^{\alpha z/2} = b_0\, e^{i\,\Delta z/2} \frac{i\,\kappa}{s} \sin[sz] \qquad (5.27a)$$

$$B(z)\, e^{\alpha z/2} = b_0\, e^{-i\,\Delta z/2} \left[\cos[sz] + \frac{i\,\Delta}{2\,s} \sin[sz]\right] \qquad (5.27b)$$

where s is defined by $s^2 = \kappa^2 + \Delta^2/4$ and $\kappa = g_r\,(I_1\, I_2)^{1/2}/I$. The diffracted intensity off the grating is

$$\frac{I_1(z)}{b_0} e^{\alpha z} = \left(\frac{\kappa}{s}\right)^2 \sin^2[sz]$$

$$= \frac{(\gamma E_0/\gamma_{Zf})^2 + 1}{1 + (\gamma E_0/\gamma_{Zf})^2 \frac{4 I_1 I_2}{(I_1 + I_2)^2}} \frac{4 I_1 I_2}{(I_1 + I_2)^2} \quad x$$

$$\sin^2\left[\frac{g}{2}\left[1 + (\gamma E_0/\gamma_{Zf})^2 \frac{4 I_1 I_2}{(I_1 + I_2)^2}\right]^{1/2} z\right]. \qquad (5.28)$$

Equation (5.89) is considerably simpler than the solution given by equations (5.20) and (5.22). This is a direct consequence of the fact that the index grating is constant amplitude. In the succeeding paragraphs we compare the theoretically expected reflectivity with experimentally obtained data.

5.3.3 Diffraction Experiment Results

The sample used in the following discussion was a 6.8x 4.9x 2.9mm^3 piece cut from a crystal grown by us using the "top seeded solution growth method." The crystal was pale olive green and had only weak striations. Its as-grown weight was 11.6gm. Using electron μprobe and atomic absorption analysis, the composition was determined to be $K_{.950}Li_{.04}Ta_{.857}Nb_{.129}O_3$: $Cu_{.004}$.

Figure 5-3. shows the absorption spectrum of the as-grown sample with peaks at 370nm and 585nm caused by Cu^{1+} donors and Cu^{2+} traps respectively. The concentration of the impurities Cu^{1+} and Cu^{2+} can be determined from the absorption peaks using Beer's law[12]. We calculate $[Cu^{1+}] = 6.0x10^{19}/cm^3$ and $[Cu^{2+}] = 2.1x10^{18}/cm^3$. The optical absorption in the material gave exp[-

$\alpha L] = 0.79$.

White light birefringence measurements between crossed polarizers were used to measure the effective quadratic electro-optic coefficients. The coefficients were determined g_{11}-$g_{12} = 0.186\ m^4\ C^{-2}$ to an accuracy of 5%.

The diffraction experiments with applied field were performed as in figure 5-4a with the sample maintained at a temperature of 15°C above the transition ($T_c = 178\,K$). The writing argon laser beams were at either 488nm or 514nm. They were ordinary-polarized to minimize beam interaction. The diffraction efficiency of the grating thus written was monitored with a weak extraordinary-polarized HeNe beam at 633nm. The 633nm beam was incident at a higher angle of incidence to be Bragg matched to the index grating. The 633nm beam was verified not to erase the grating at the temperature of the experiment. The writing continued until the maximum diffraction was achieved.

Figure 5-4b illustrates a "momentum matching" diagram used to calculate the Bragg matching angles. Two beams with wavevector $\mathbf{k}_1$ interfere to create an index grating with wavevector $\mathbf{K}_g$. By the Bragg condition of scattering from a volume hologram, the angles of the incident and reflected beams must be equal, hence $\mathbf{K}_g = 2\,\mathbf{k}_1 \sin\theta_1$. the same condition applys for the reading beam at 633nm: $\mathbf{K}_g = 2\,\mathbf{k}_2 \sin\theta_2$. The angles are graphically determined by the intersection of two circles of radius k_1 and k_2 as shown in the figure.

After the gratings were written, the crystal was cooled to a few degrees

above the transition, and the diffraction efficiency determined as a function of applied field. The results are illustrated in figures 5-5, 5-6, and 5-7. Figure 5-5 shows the diffraction as a function of applied field for a grating written with zero applied field. The solid curve is a fit of the theory developed above to the data. The best fit occurred for g = 1.3/cm. Figures 5-6 and 5-7 show diffraction versus applied field for gratings which were written at +1450V/cm and -1450V/cm. The solid curves are fits to the data using the same parameters as in figure 5-5 except with g = 3.0/cm, and g = 4.0/cm respectively. When a field is applied during writing an internal compensating field of ±300V/cm seems to be set up. This offset is manually inserted into the theoretical curves for reasons explained below. In all cases, when the grating was optically erased with the argon beams, some residual diffraction (~1%) remained which was not optically erasable and could only be removed by heating the crystal to near room temperature.

The highest diffraction efficiency observed for 488nm writing beams was 75% for a sample of thickness 2.9mm, where corrections were made for fresnel losses. For 514nm writing beams the maximum value was reduced to 30%, and at 633nm, the diffraction was almost undetectable. The writing times for maximum diffraction roughly followed $\tau_{write} \sim 6 sec^2\text{-}cm^2/J$, incident intensity on the crystal.

From the calculated index modulation of $n_1 = 1.7 \times 10^{-4}$, we determine the space charge field to be $E_{sc} = 150V/cm$. Using the writing time of 180sec at beam intensities adding up to 27.2mW, we estimate the sensitivity for this

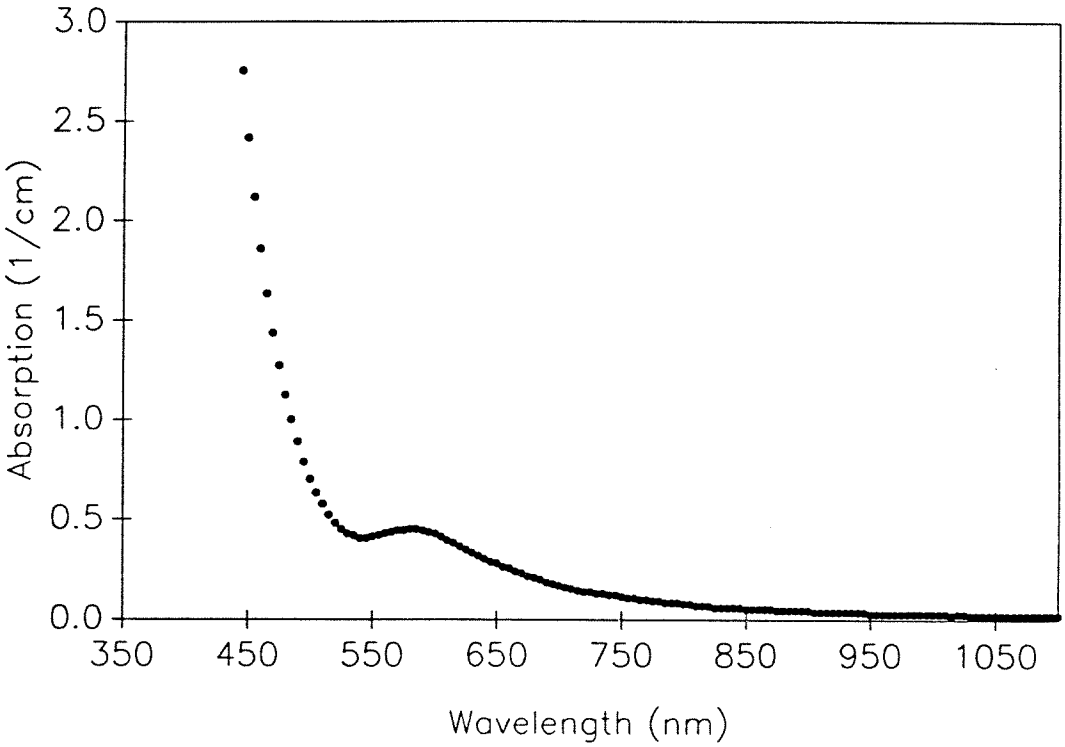

Figure 5-3. Absorption spectrum of the as-grown KLTN:Cu.

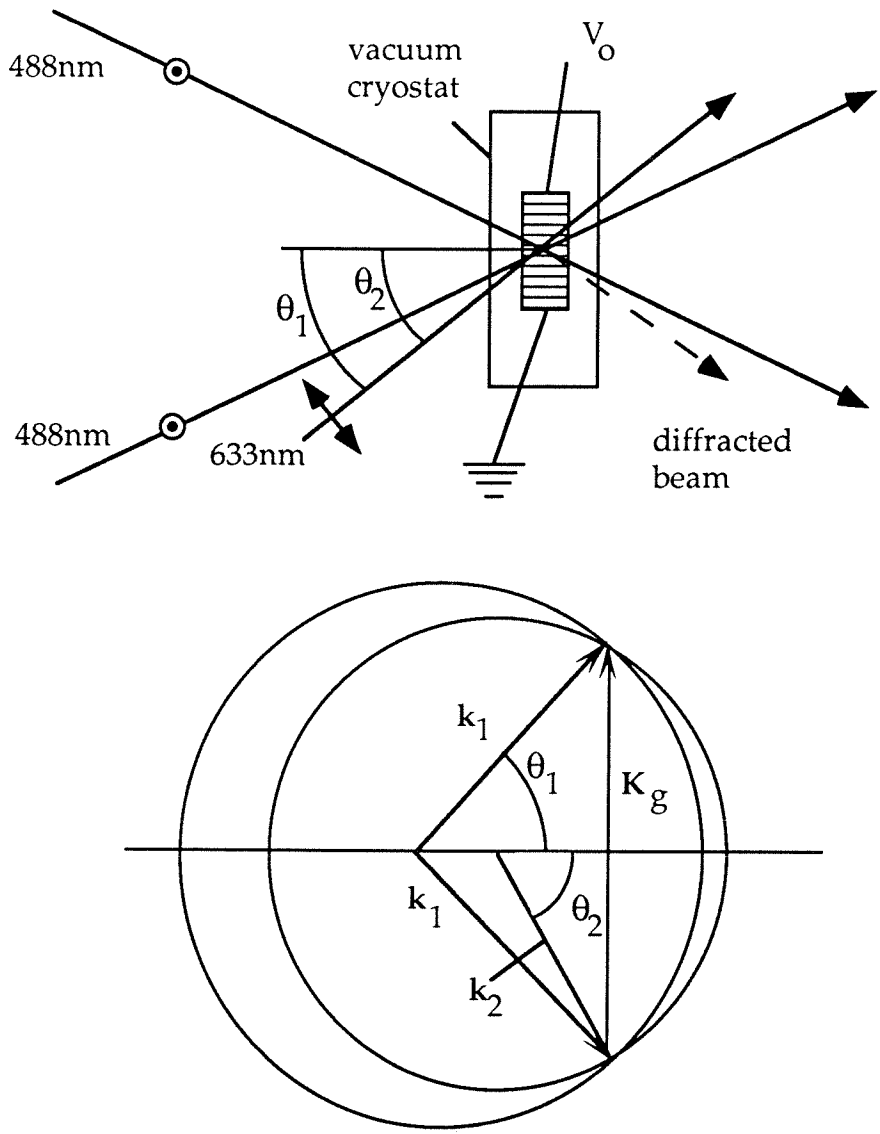

Figure 5-4a. Experimental setup for measurement of diffraction efficiency. A photorefractive crystal is mounted in vacuum cryostat. 488nm light beams write an index grating which is read with the Bragg matched 633nm beam. Diffraction is measured versus applied voltage V_o. **Figure 5-4b.** A momentum matching diagram illustrates the angles required to achieve Bragg matching of a grating to more than one wavelength of incident light.

KLTN of $7.30 \times 10^{-6} cm^3/J$ for an applied field of 1.6kV/cm. Following the procedure outlined above, the erase time near T_c was up to two orders of magnitude longer than the write time at $T_c + 15^o$.

5.4 Discussion of Experimental Results

Several points about figures 5-5,6,7 need to be addressed. The first is the change in the best fit value of g in the three figures. Since g is a material parameter it should be independent of the field applied, however, the best fits were g= 1.3/cm , 3.0/cm, and 4.0/cm. The particulars of the experimental conditions may be able to explain the variations. The diffraction experiments were done using a vacuum chamber which was not well isolated against acoustic vibrations; it was determined that good data could only be taken late at night while standing motionless next to the optical bench. Therefore the gratings were written with an intensity pattern which rapidly flitted back and forth a fraction of a wavelength. This artificial modulation of the effective photorefractive grating phase caused beam coupling which was visible as a 10-30Hz flickering of the output intensities. The varying beam coupling affected the form of the dynamic grating, i.e., smeared it out. This might have caused the variation in the measured value of g for figures 5-6 and 5-7.

As shown in chapters seven and eight, the susceptibility of a grating to vibration is strongest for zero phase $\phi = 0$ gratings (more beam coupling occurs) and decreases as $\phi \rightarrow \pi/2$. Thus when a field is applied during writing the grating, as in figures 5-6 and 5-7, the nonzero phase should decrease the effect of vibration on the beams. In this way a stronger grating can be written

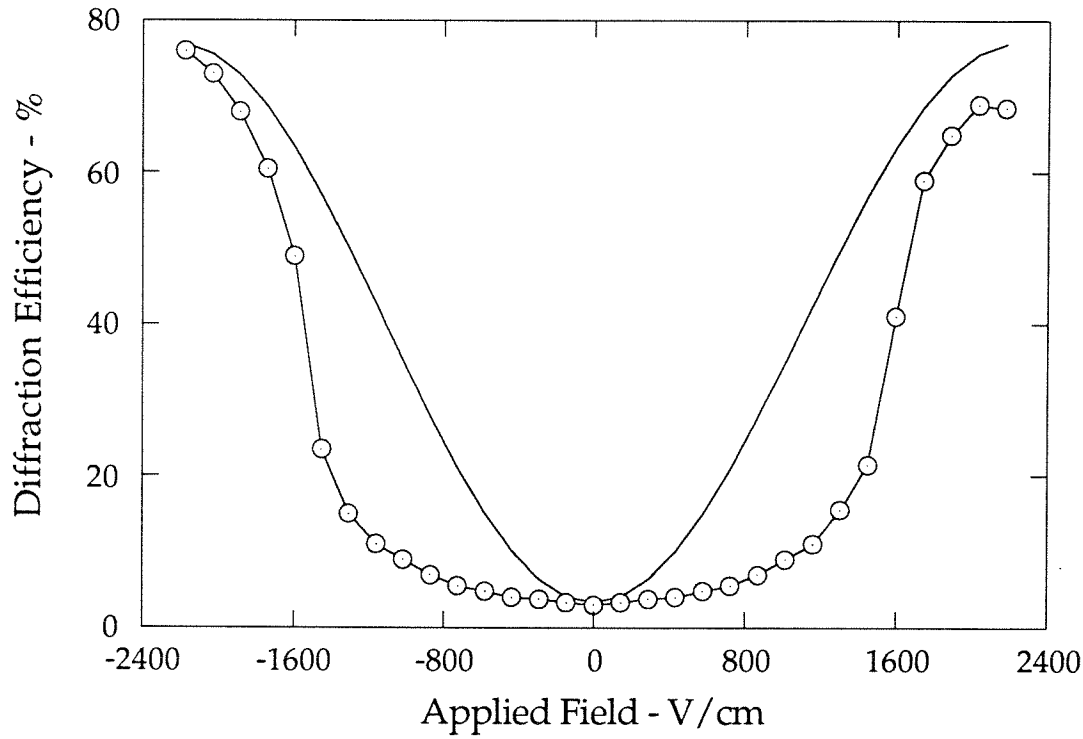

Figure 5-5. The measured diffraction efficiency for an index grating written at T_c + 15° with zero applied field. The crystal was cooled to near T_c and the diffraction monitored versus applied field. The solid curve is the best fit to the theory with g = 1.3/ cm.

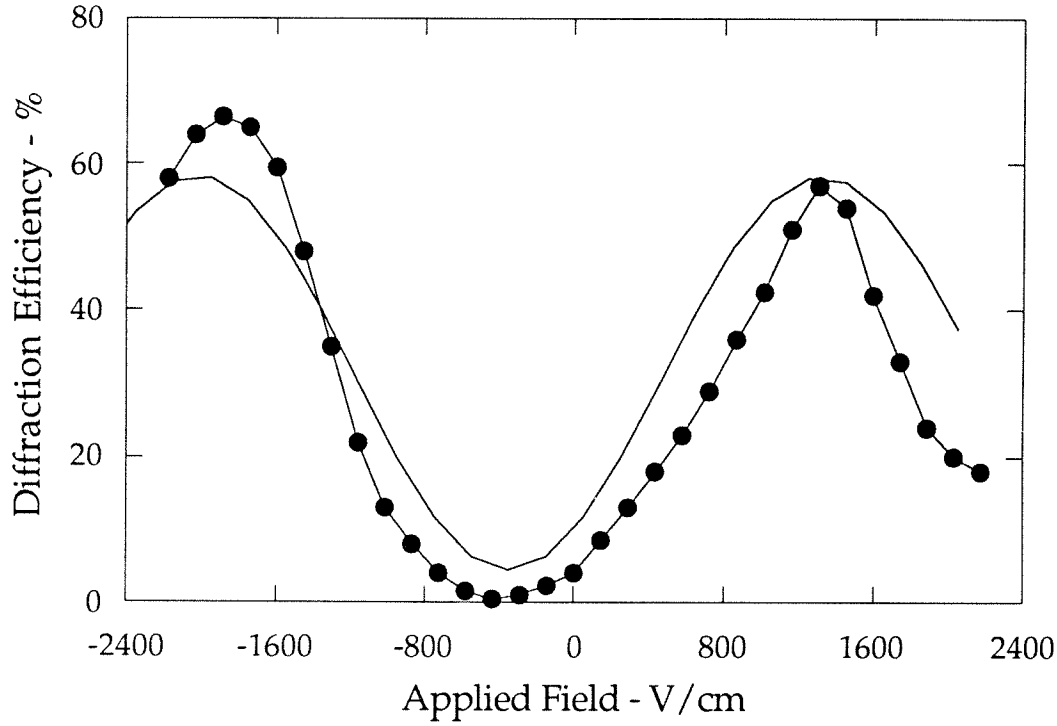

Figure 5-6. The measured diffraction efficiency for an index grating written at T_c + 15° with an applied field of +1450V/cm. The crystal was cooled to near T_c and the diffraction monitored versus applied field. The solid curve is a fit to the theory with g = 3.0/ cm.

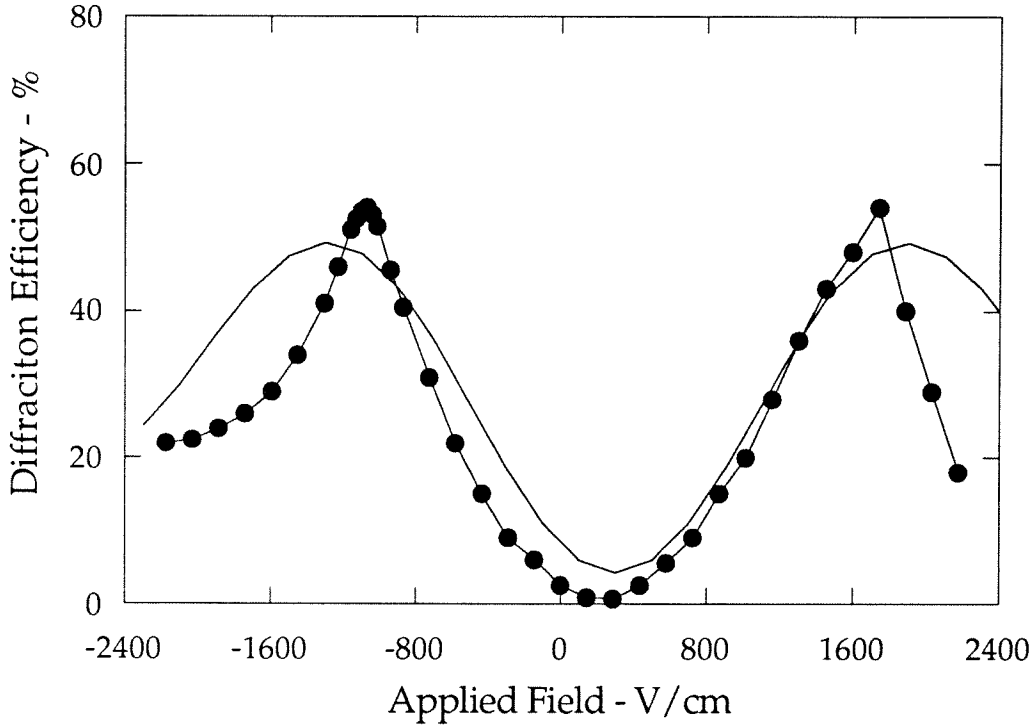

Figure 5-7. The measured diffraction efficiency for an index grating written at $T_c + 15^o$ with an applied field of -1450V/cm. The crystal was cooled to near T_c and the diffraction monitored versus applied field. The solid curve is a fit to the theory with g = 4.0/ cm.

than in the case of zero applied field, so the value of g measured will be higher.

The second point to be discussed is the positions and magnitudes of the maximum diffraction efficiency which seem to have behaved strangely at first blush: The highest diffraction achieved occurred in figure 5-5 with zero applied field during writing (g = 1.3/cm), but at a higher value of the applied reading electric field than in figures 5-6 and 5-7. Also, the maximum diffraction in both figures 5-6 and 5-7 occurred for a net applied field of approximately 1600V/ cm even though the coupling constant g was different in the two cases. Finally, the value of the maximum diffraction efficiency decreased as g increased, and the diffraction in the case of non-zero writing field was no longer periodic with the readout field, that is, with increasing readout field the diffraction would not return to zero. All these characteristics are expected from the theory presented above and are illustrated in the theoretical curves. These results of the theory can be explained fairly intuitively.

When $\phi = 0$ (writing electric field = 0), the diffraction is given by (5.29), and its maximum value is independent of g, and depends only on the beam intensity ratios. (To recapitulate, g and $g_{read}(E)$ are defined in (5.13).) Thus when g is increased, the position of maximum diffraction will shift to a lower value of the reading electric field, but the magnitude of the maximum diffraction will be unchanged. When $\phi > 0$ (non-zero applied writing field) the diffraction maximum decreases with increasing g because the beam coupling causes grating apodization. The higher the value of g, the more apodization, so that the "integral" of the index grating throughout the volume of the crys-

tal decreases. Nevertheless, the position of the diffraction maximum is roughly independent of g over certain ranges (see Figure 5-8) because the decrease of the index grating "area" inversely proportional to g must be compensated by a linear increase in g_{read} to obtain maximum diffraction. The appropriate increase in g_{read} occurs at approximately the same value of E for all g. Meanwhile, the maximum value of the diffraction decreases with increasing g because the grating is apodized in phase as well as in amplitude; thus a highly apodized grating does not Bragg match well to an incident beam. This lowers the maximum value of the diffraction.

In figure 5-8 the theoretical diffraction versus applied reading field is shown for gratings written with an applied field of 1150V/cm, including optical absorption as in the experiment above, and for g = 2.0/cm, 3.0/cm, and 4.0/cm. The last two curves are the same as in Figs. 5-6 and 5-7. It can be seen that the maximum diffraction occurs at roughly the same value of the reading field (~1600V/cm) in all three cases, but the diffraction maximum decreases with increasing g. As a final note, the diffraction never returns to zero with increasing applied electric field during reading. This is again due to the phase apodization of the grating which prevents the coherent buildup of the diffracted wave. The grating written with zero applied field has no apodization and does not suffer from either of these two effects.

When a field was applied during grating formation as in graphs 5-6 and 5-7, a compensating internal field of ±300V/cm was formed. The compensating field is most likely caused by nonuniform illumination of the crystal. When an external field is applied, photoexcited charges drift in a direction de-

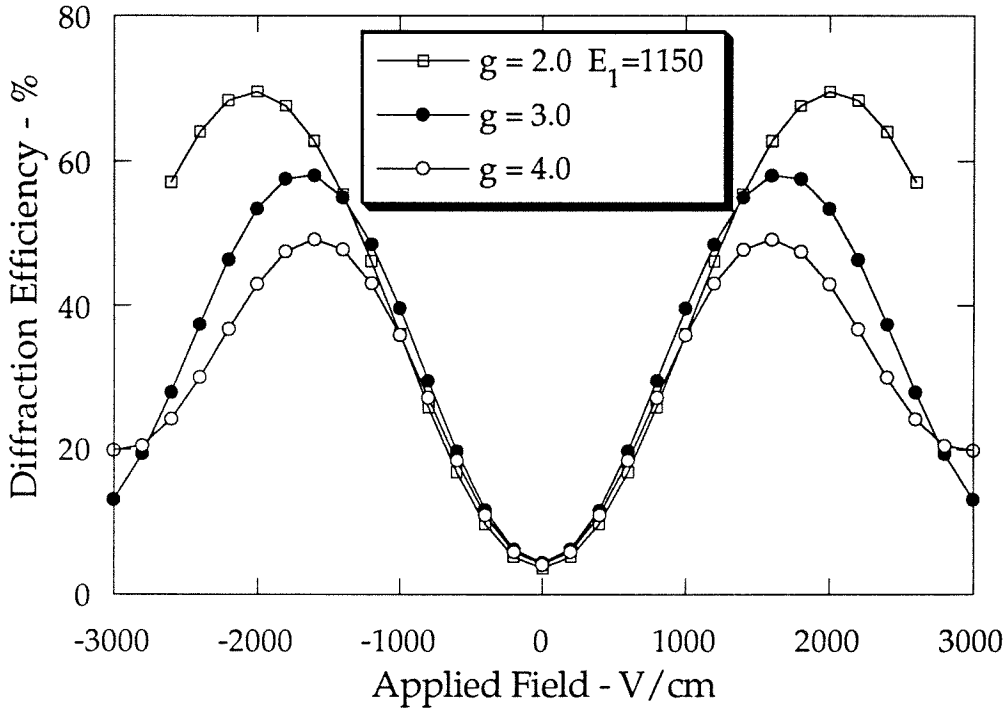

Figure 5-8. The theoretical diffraction efficiency for an index grating written with an applied field of 1150V/cm for g = 2/cm, 3/cm, and 4/cm. The maximum diffraction decreases with increasing g. However, the maximum diffraction occurs at a reading field of approximately 1600V/cm for $g \geq 3$/cm. The diffraction is nonperiodic in the applied field, it does not return to zero when the applied field is increased.

termined by the field before being retrapped. This preferential drift is manifested as a photocurrent proportional to applied field. After repeated excitation and trapping, charges may end up many wavelengths removed from their origin. If certain areas of the crystal are dark, charges will become trapped there, yielding a more or less uniform field opposing the applied field. This explanation of the field offset seems consistent with the theoretical results because the theoretical diffraction matches the experiment much better with a net applied field of 1150V/cm rather than 1450V/cm. If 1450V/cm is used in the theory then the position of maximum diffraction occurs at higher electric fields than were observed (that is, at 2400V/cm rather than 1600V/cm), so the theoretical results indicate that the field is more like 1150V/cm as expected.

From the arguments presented we see that the qualitative features of the experimental data are explained by the theory. However, several discrepancies remain. The shape of the experimental and theoretical curves in figure 5-5 do not agree well. Also the diffraction in the case of an applied field during writing does not exhibit the ZEFPR effect. This can be inferred since the diffraction efficiency is zero for some value of the applied field (±300 V/cm) whereas it has been shown above that the ZEFPR grating is $\pi/2$ out of phase with the electro-optic grating and the two gratings should add in quadrature so that the diffraction efficiency never drops to zero. Apparently the strong internal field during writing seems to inhibit the ZEFPR effect. These two anomalies indicate a possible coupling between the ZEFPR grating and an applied field which is not described by the theory presented above. Nevertheless, despite this possible coupling and the fact that the experiment

was performed near the phase transition temperature (where bizarre effects are typical), the theory still provides good qualitative agreement with the results.

5.5 Summary

The photorefractive effect of paraelectric KLTN material with an applied field was discussed. The photorefractive response has contributions from both the conventional electro-optic index change as well as from the ZEFPR response. In the absence of an applied field no two beam coupling occurs although diffraction is observed. The diffraction of a single beam as a function of applied field off a photorefractive grating was solved analytically using the techniques described in chapter nine. Good qualitative agreement was observed between this theory and experimental results.

References for chapter five

[1] P. J. Van Heerden, Appl. Opt. **2**, 393 (1963).

[2] D. Gabor, IBM J. Res. Dev. **13**, 156 (1969).

[3] D. Von der Linde and A. M. Glass, Appl. Phys. **8**, 85 (1975).

[4] A. Agranat, R. Hofmeister, and A. Yariv, "Characterization of a new photorefractive material: $K_{1-y}L_yT_{1-x}N_x$," Opt. Lett. , **17**, 713-715 (1992).

[5] A. Agranat, V. Leyva, K. Sayano, and A. Yariv, "Photorefractive properties of $KTa_{1-x}Nb_xO_3$ in the paraelectric phase," Proc of SPIE Vol. **1148**, Conference on Nonlinear Optical Properties of Materials, (1989).

[6] A. Agranat, V. Leyva, and A. Yariv, "Voltage-controlled photorefractive effect in paraelectric $KTa_{1-x}Nb_xO_3$:Cu,V," Opt. Lett. **14**, 1017-1019 (1989).

[7] J. P. Wilde and L. Hesselink, "Electric-field controlled diffraction in photorefractive strontium barium niobate," Opt. Lett. **17**, 853 -855 (1992).

[8] M. E. Lines and A. M. Glass, *Principles and Applications of Ferroelectrics and Related Materials* , Clarendon Press, Oxford (1979).

[9] F. Laeri, T. Tschudi, J. Albers, "Coherent cw image amplifier and oscillator using two wave interaction in a $BaTiO_3$ crystal," Opt. Comm. **47**, 387 (1983).

[10] R. Hofmeister, A. Yariv, S. Yagi, and A. Agranat, "A new photorefractive mechanism in paraelectric crystals : A strain coordinated Jahn-Teller relaxation," Phys. Rev. Lett. , **69**, 1459-1462 (1992).

[11] R. Hofmeister, A. Yariv, A. Kewitsch, and S. Yagi, "Simple methods of

measuring the net photorefractive phase shift and coupling constant," to appear Opt. Lett. April 1, 1993.

[12] V. Leyva, Ph.D. thesis, California Institute of Technology, Pasadena, California, unpublished (1991).

Chapter Six

Zero External Field Photorefractive (ZEFPR) Effect in Paraelectric Materials

6.1 Introduction

As indicated in chapter one, the field of photorefractive studies has been thwarted by severe material limitations since its inception some twenty years ago. The photorefractive properties of potassium tantalate niobate (KTN), for example, were reported more than fifteen years ago[1] but the difficulty of growing high quality crystals hindered their study until recently. The photorefractive materials development program at Caltech was conceived largely in response to this demand for better and more cheaply available materials. The program focussed on the growth of a new type of material - the paraelectric photorefractives. These materials had been proposed[2,3] because they possessed the advantages of very high diffraction efficiency and control of the photorefractive diffraction by an external electric field. Both of these predictions were borne out in experiments documented in earlier chapters[4,5]. But in these studies another effect surfaced which could not be explained by conventional theories of photorefractives. Investigations of these paraelectric crystals have revealed a photorefractive response which cannot be explained

by the conventional electro-optic theory. The effect was discovered serendipitously in experiments where the conventional effect was forbidden, that is, when no electric field was applied. This new effect is expected to occur in most transition metal doped perovskites, and possibly other materials as well. But in these materials, the conventional photorefractive effect will mask the new one. Possibly this explains why the effect has been unreported until recently.

Perovskite oxide photorefractives operated above the phase transition temperature (paraelectric and centrosymmetric phase) lack a linear electro-optic coefficient. Instead, the photorefractive mechanism in these symmetric materials arises through the quadratic electro-optic effect. Here the index grating due to a spatially periodic field $E_{sc}(x)$ in the presence of an applied electric field E_o can be written

$$\Delta n_{ij}(E_0+E_{sc}) - \Delta n_{ij}(E_0) = \frac{n_0^3}{2} g_{ij33} (\varepsilon_3\varepsilon_0)^2 \left((E_{sc} + E_0)^2 - E_0^2 \right) \qquad (6.1a)$$

$$\Delta n_{ij} = n_0^3 g_{ij33} (\varepsilon_3\varepsilon_0)^2 E_{sc} E_0 \qquad (6.1b)$$

where $g_{ij33} = g_{m3}$ is the relevant quadratic electro-optic coefficient when all fields are nominally along the z, i.e., the "3," axis, n_o is the index of refraction, and Δn_{ij} is defined as the term on the right-hand side of equation (6.1a) which leads to a Bragg matched grating. We assume that the polarization is linear ($P = \varepsilon E$) and that the dielectric constant $\varepsilon >> 1$. The externally applied field E_o thus induces an effective electro-optic coefficient $r_{eff,m} = 2 g_{m3} (\varepsilon\varepsilon_o)^2 E_o$. Therefore the conventional photorefractive effect is zero in the absence of

a spatially uniform electric field (see chapter three for details).

Nevertheless, photorefractive experiments reveal the existence of a zero electric field photorefractive (ZEFPR) effect in paraelectric KTN and KLTN at temperatures at least 120°C above the phase transition where the crystal is nominally symmetric. No effect is seen with undoped crystals or with thermally reduced samples. The diffraction expected from absorption gratings[6-8] is three orders of magnitude too weak to explain the effect. The studies of the phenomenon which are described here, reveal a new photorefractive mechanism. In this chapter we describe the effect and present what we believe is the most plausible explanation. The experimental results supporting the explanation follow and, finally, a theory of the Jahn-Teller relaxation is given.

6.2 The ZEFPR Effect

The zero external field photorefractive (ZEFPR) effect was first noticed by us[5] in KTN and KLTN crystals. This photorefractive effect was attributed to the presence of a growth induced strain. In addition, Yang et al.[9] have cited an "extremely small" effect in the absence of an applied field, but without explanation. In KTNs and KLTNs grown at Caltech with high niobium concentrations and of high optical quality, the effect is greatly enhanced. Under certain conditions of crystal preparation zero field index gratings with $\Delta n \sim 1.7 \times 10^{-5}$, and diffraction efficiencies of over 20% have been produced in a 4.15mm thick sample using 488nm argon laser beams.

6.2.1 The Jahn-Teller Distortion

In the KTN and KLTN crystals which displayed a strong ZEFPR effect, the photorefractive dopant was copper, which is stable as either Cu^{1+} or Cu^{2+}. The Cu^{2+} ion is known to cause large Jahn-Teller[10,11] (J-T) distortions, especially in octahedral symmetry. The electric field of the six oxygen ligands splits the 3d orbitals into an orbital doublet and a triplet, with E_g - T_{2g} symmetry. Since the copper ion has $3d^9$ configuration the distortion allows, by removing the triplet degeneracy, the vacancy of the tenth electron to go to the highest energy level of the former triplet state, thus lowering the energy of the system. The Cu^{1+} ion by contrast, has a $3d^{10}$ configuration, and consequently has no tendency to distort. The illumination of the crystal by the periodic intensity pattern of the optical field leads to a mimicking spatially periodic Cu^{2+}/Cu^{1+} ratio due to excitation of electrons (from Cu^{1+}) and trapping by Cu^{2+}. This, as explained above, gives rise to a spatially periodic distortion. Since the copper concentration is relatively small in the KLTNs we do not expect strong cooperative ordering of the distortions; rather, their orientation should be random, or display partially ordered regions which are small compared to a wavelength of light. But when a macroscopic (growth induced) strain is present, as is the case in the crystals studied, the distortions will orient preferentially in order to minimize that strain. The result is a spatial modulation of the strain field in phase with the intensity which leads to a corresponding modulation of the index of refraction (index grating) via the photoelastic effect. In the absence of a strain field, J-T distortions will still cause an index grating because the distortion changes the volume of the unit

cell.

Although the J-T effect has previously been reported in photorefractives[12-16] and it has been shown to generate birefringence[17], the ZEFPR effect has not been reported. As explained above, this is probably because the conventional effect obscured any ZEFPR effect which may have existed in those materials. In Refs. 13-16 the possibility of ionization state dependent distortions are considered, and in Refs.13-15 it is shown how the ionization of photorefractive centers may lead to a modulation of the spontaneous polarization and thus a contribution to the photorefractive effect in the polar (noncentrosymmetric) phase. However, the possibility of a ZEFPR-type photorefractive effect in centrosymmetric materials is explicitly disallowed (no macroscopic spontaneous polarization exists in centrosymmetric materials). These erroneous conclusions were reached by ignoring the possibility of unit cell volume change under J-T distortion and ordering of J-T distortions by a macroscopic strain field which can occur in any material, including a centrosymmetric one.

6.2.2 Strain Dependence of ZEFPR Effect

The strain in the crystals is due to the particulars of the growth process; it is only briefly described here since it was already discussed in chapter four. The crystal grows as a series of cubical shells, expanding from the seed. During the growth the composition of the crystal changes which is attendant by an increase in the lattice constant. Thus each face of the cubical shell of the growing crystal must be compressed slightly to mesh with the previous cubical shell. In this way there arises a compressive strain in the plane of each

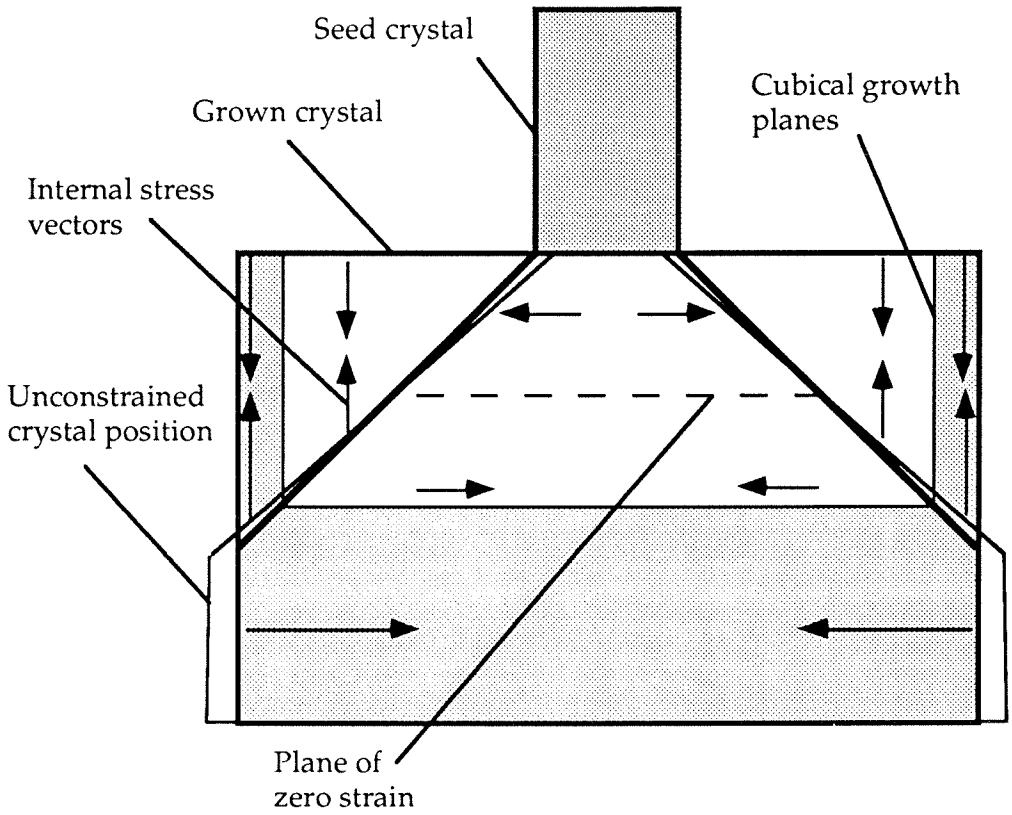

Figure 6-1. Origin of the Growth-induced Strain

A cross section of the grown crystal shows how it grows as a series of cubical shells, expanding from the seed, with a progressively increasing lattice constant. Each face of the cubical shell of the growing crystal must be compressed slightly to mesh with the previous cubical shell (the innermost shells are stretched). The dotted line shows the plane of zero stress. In this way there arises a birefringence in the plane of each face of the cube which increases with distance from the seed crystal.

face of the cube which increases with distance from the seed crystal. Similarly, there is also a tensile strain perpendicular to each face of the cube which also increases with distance from the seed (Figure 6-1). These strains induce a linear birefringence which is readily apparent when the crystal is viewed through crossed polarizers. When a small sample is cut from the grown crystal near the center of one of the cube faces, the strain in the sample will be homogeneous: uniformly compressive in two directions and uniformly tensile in the third.

To test the validity of the theory of J-T relaxation we investigated the dependence of the index grating on the strain present in the crystal. The experimental setup for performing diffraction experiments is illustrated in figure 6-2. Two extraordinary beams at 488nm symmetrically incident, created an optical intensity standing wave inside the sample. After several minutes, one of the beams was blocked with an electronic shutter for 50msec. While the shutter was closed we measured the optical power which was diffracted by the grating into the direction of the blocked beam. The diffraction efficiency, η, is defined as the ratio of the diffracted power to the power incident on the crystal. We corrected for losses from facet reflections.

Unless otherwise indicated, all measurements were performed at room temperature on several KTNs and KLTNs with phase transition temperatures from 180 K - 280 K. It was determined that in homogeneously strained samples the diffraction efficiency increased as the square of the interaction length and was independent of intensity. A two-dimensional vise was constructed (figure 6-3) to allow compensation of the growth induced strain with external

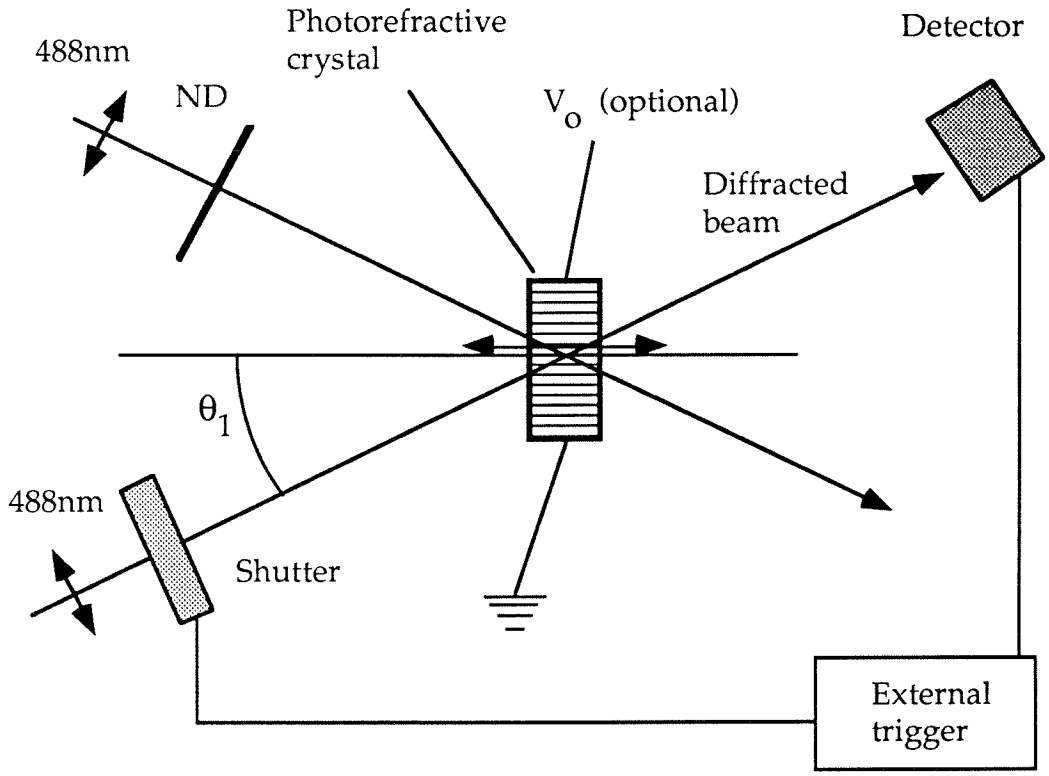

Figure 6-2. The setup used to measure diffraction of an index grating written in paraelectric KTN/KLTN crystals. The beams are extraordinarily polarized and converge at an angle θ_1 on the crystal. θ_1 can be adjusted by moving the crystal assembly along the bisector of the two beams. A shutter is coordinated with a detector to measure the diffraction off the grating. A variable attenuating filter **ND** allows the setting of the beam intensity ratios. The applied voltage is only used when measuring the quadratic electro-optic contribution to the index grating.

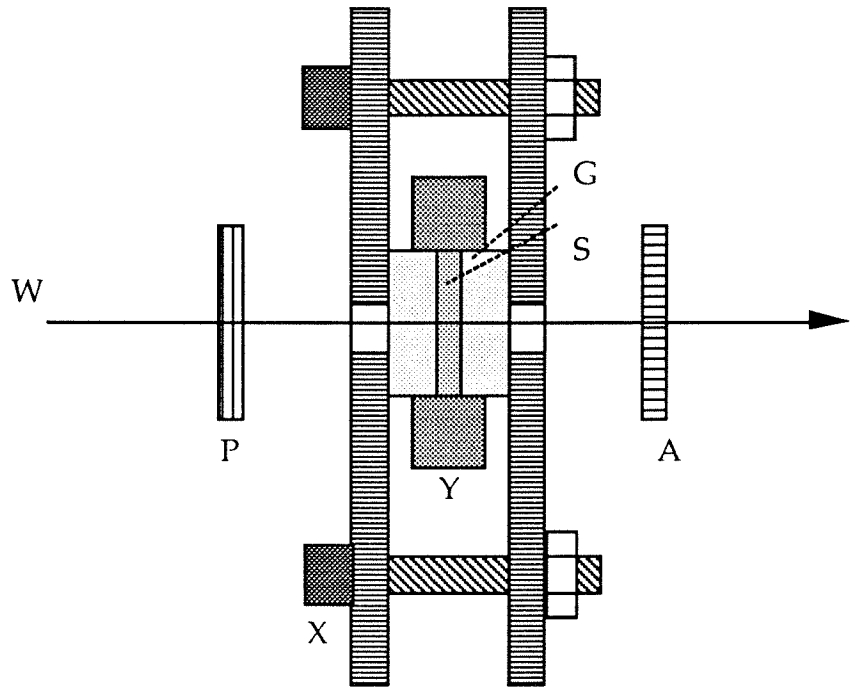

P = polarizer
A = analyser
X = screw, x-axis clamp
Y = y-axis clamp
(electrode)
S = sample
G = glass blocks
W = white light source

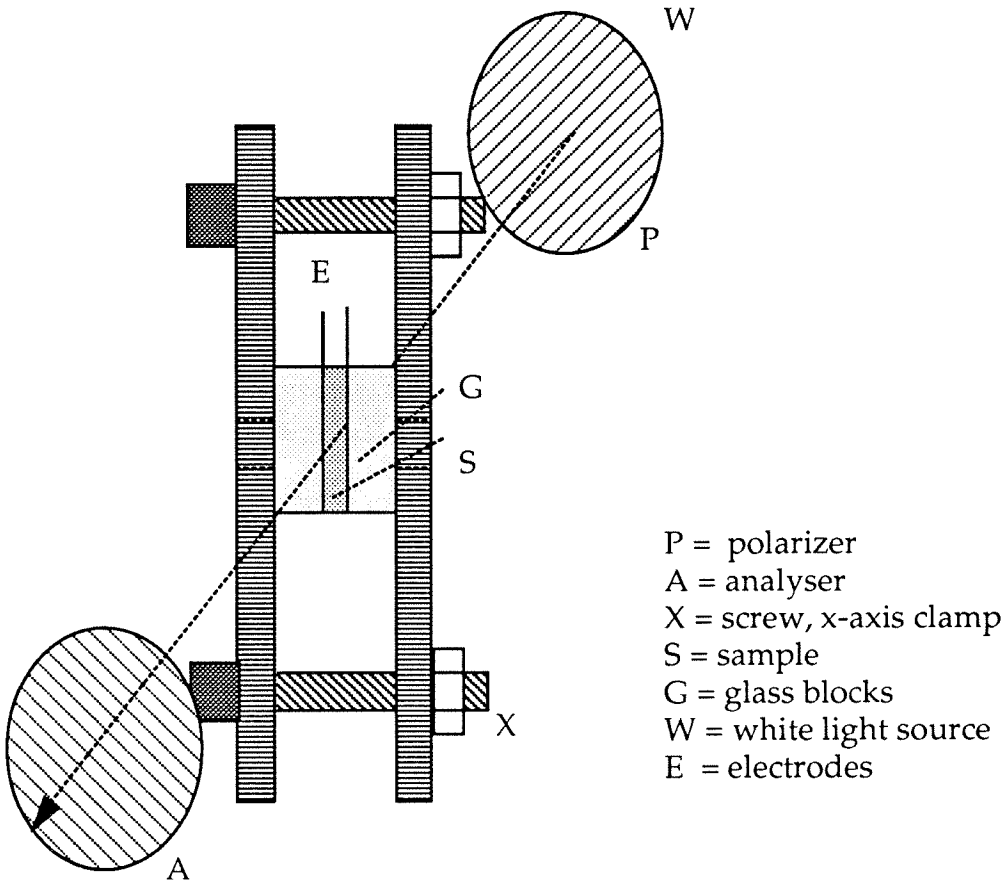

Figure 6-3a,b. Two Axis Strain Compensation Device

A KLTN sample **S** is mounted between glass blocks **G** and brass electrodes **Y** which allow the crystal to be squeezed in dimensions X and Y independently. A white light source and crossed polarizers oriented at ±45° to the crystal axis are used to monitor the birefringence. By adjusting the pressure applied to the X and Y axes, most of the internal strain in the material can be compensated. In figure 6-3b, stress is only applied along one axis.

pressure applied in two dimensions. With the strain nominally compensated, diffraction experiments were performed with the setup in figure 6-2. The diffraction efficiency in a 2.85mm thick sample was reduced by 40% when the internal strain was minimized. Additionally, the effect is reduced when the sample is exposed to heat treatments which reduce the internal strain but which leave the conventional photorefractive properties unchanged[18]. Although this evidence shows that the ZEFPR effect relies partly on the macroscopic strain, it remains to be shown that the strain does not induce a morphic lowering of the crystal symmetry[19,20] (see also chapter three), allowing a linear electro-optic coefficient. We tested for the existence of a linear electro-optic coefficient in a 2.85x5.00x9.50 mm^3 sample of $K_{.993}Li_{.006}Ta_{.687}Nb_{.314}O_3$ by measuring the birefringence induced under application of electric fields in various directions. A Soleil-Babinet compensator between crossed polarizers oriented at 45° to the crystal axes was used to measure the birefringence at 633nm. The results were fitted to a third order polynomial but the best fit was purely quadratic to the resolution of the experiment. The best fit (see figure 6-4) was determined to be

$$\Delta n = 9.47\text{x}10^{-5} + 2.56\text{x}10^{-7}E - 1.07\text{x}10^{-5}E^2 - 8.07\text{x}10^{-8}E^3 \qquad (6.2)$$

where E is in units of 10^3V/cm and individual measurements were repeatable to within $\delta(\Delta n) < 5\text{x}10^{-7}$. This indicates an almost perfect quadratic electro-optic effect with $g_{11} - g_{12} = 0.123 m^4 C^{-2}$, which agrees with previously published values for KTN[21]. The constant term of the birefringence is from the

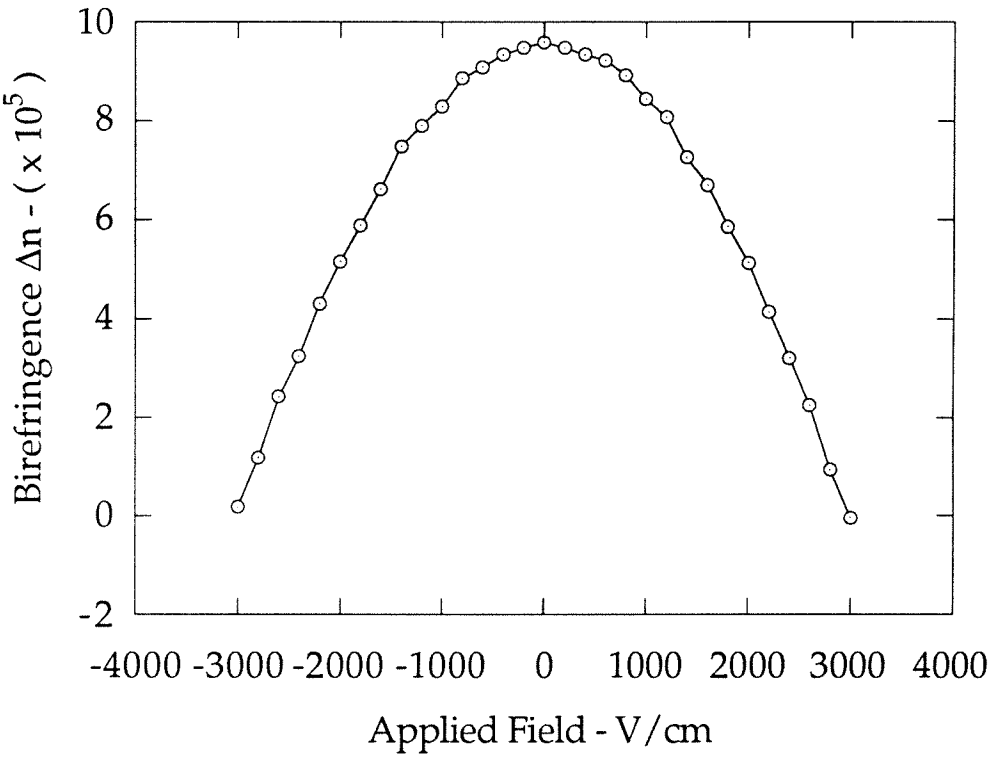

Figure 6-4. The birefringence of a $K_{0.993}Li_{.006}Nb_{0.687}Ta_{0.314}O_3$ at room temperature versus applied field. The birefringence is quadratic with no linear component, thus there is no linear electro-optic coefficient and the crystal is centrosymmetric. The birefringence with zero applied field is due to the uniform growth induced strain.

growth induced strain. The small linear term is effectively zero to the resolution of the experiment. It should be noted that the absence of a significant third order term indicates little or no polarization nonlinearity. We conclude that the strain does not induce a linear electro-optic coefficient and leaves the crystal centrosymmetric. This data also disproves the possibility of an internal polarization which would render the crystal noncentrosymmetric.

6.2.3 E_{sc} Dependence of the ZEFPR Effect

Next, a series of experiments were performed to verify anticipated characteristics of the ZEFPR effect. For these experiments a 8.69 x 4.45 x 4.15 m m^3 sample was used with composition $K_{.990}Li_{.0019}Ta_{.730}Nb_{.270}O_3$: $Cu_{.0015}$. Using optical absorption data[22] we determined $[Cu^{2+}] = 3.1x10^{18}$ cm^{-3}. The crystal was centrosymmetric above its phase transition at $T_c \approx -23°C$.

First, since the ZEFPR effect is due to a strain "grating" which modulates the refractive index via the photoelastic effect, we expect at most weak dependence on the DC/low frequency dielectric constant ε. We confirmed this by measuring the dependence of the ZEFPR effect on temperature near the phase transition (here ε obeys the Curie-Weiss law). Using the setup as in figure 6-2, two interfering 488nm beams with equal intensities of ~500mW cm^{-2} uniformly illuminated the crystal. No field was applied during writing of the diffraction grating. After a writing time of 60 seconds, one beam was blocked and the other beam attenuated to minimize erasure, and the resultant diffraction was measured. After the diffraction due to the ZEFPR effect

was determined, a field was applied to determine the index change due to the quadratic electro-optic effect (equation (6.1b)). Finally, after each measurement, the gratings were completely erased by flooding the crystal with uniform illumination and raising the temperature, if necessary. The results for various temperatures are illustrated in figure 6-5. The quadratic effect increases dramatically as the phase transition temperature ($\approx$ -23° C) is approached because of the concomitant increase in dielectric constant. The phase transition temperature was measured with a different temperature probe from that used to control the diffraction experiment, thus the two temperature scales may have a relative shift between them of a few degrees. The extremely high diffraction efficiencies with a $\sin^2$ rollover at high fields are characteristic of the quadratic effect in paraelectric KLTN[3-5] (and see chapter three). The ~1% diffraction efficiency observed at zero electric field is caused by the ZEFPR effect. It is independent of the dielectric constant since it is nearly a constant for the nine temperatures investigated which range through the ferroelectric transition at -23°C. Although the ZEFPR effect diffraction is weak in the configuration used for this experiment, the same sample yielded 20% diffraction efficiency at a higher angle of beam incidence. The fact that the ZEFPR index grating has no noticeable dependence on the dielectric constant proves that the effect is distinct from the quadratic electro-optic effect or the dielectric photorefractive effect[23-25]. The ZEFPR effect is a new phenomenon which has nothing to do with the polarization caused by a space charge field ($P = \varepsilon E$).

The model stipulates that the magnitude of the ZEFPR index grating

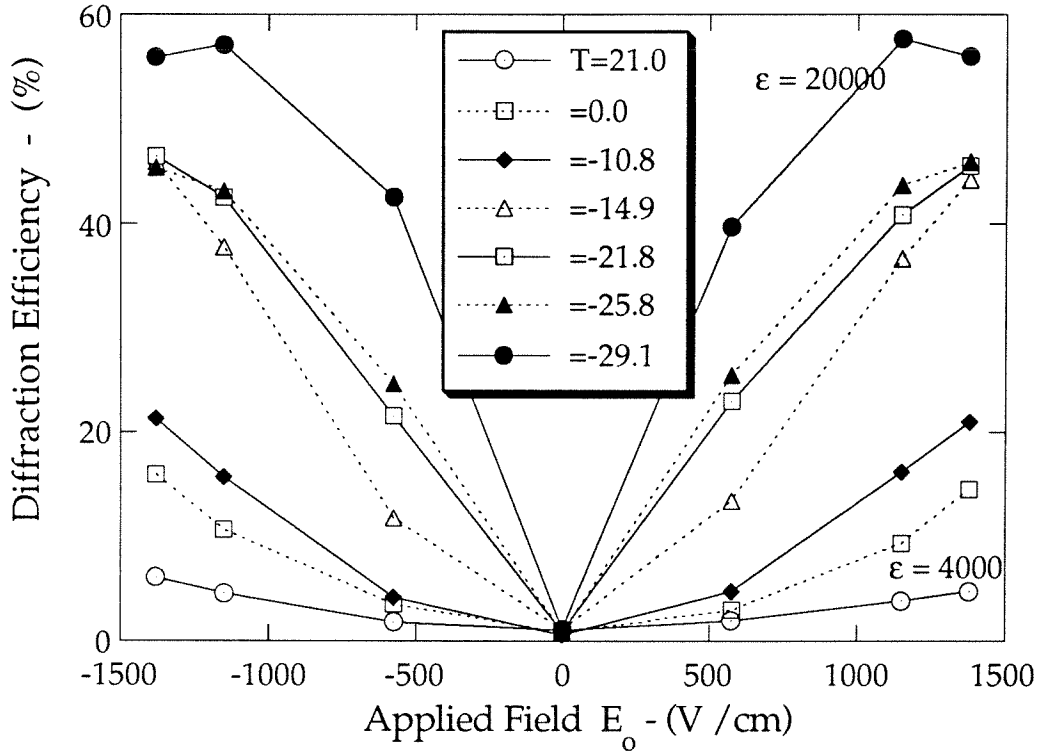

Figure 6-5. The diffraction efficiency versus applied field for an index grating written with zero applied field. Measurements are taken at several temperatures from room temperature to T = -29.1°C. The small zero field value is reasonably independent of temperature although the quadratic electro-optic contribution increases by more than an order of magnitude as the sample is cooled to the phase transition. The lines connecting the data points are only guides to the eye.

depends linearly on the spatial modulation of the Cu^{2+} ions. Since the Cu^{2+} modulation is equal to the modulation of the photoexcitable charge carriers, we expect the ZEFPR index grating to have the same functional dependence as the light induced space charge electric field caused by the charge modulation. From the basic Kukhtarev model for the space charge field induced by the extraordinary polarized interfering beams we have[26]

$$E_{SC} = i \frac{\sqrt{I_1 I_2}}{I_1 + I_2} \frac{E_D E_N}{E_D + E_N} \cos 2\theta$$

$$= i \frac{\sqrt{I_1 I_2}}{I_1 + I_2} \frac{KTk/e}{1 + K^2 kTe/(e^2 N_A)} \cos 2\theta \qquad (6.3)$$

where θ is the angle of beam incidence in the crystal, I_1 and I_2 are the beam intensities, and $K = 2k \sin\theta$ is the index grating wavevector. The dependence on E_{sc} was tested, again using the setup of figure 6-2, by monitoring the diffraction efficiency as a function of the grating wavevector and the beam intensity ratios. We determined a relation between the index change and the space charge field for the ZEFPR effect from the $E_0 = 0$ data of figure 6-5 to be $\Delta n_{ZEFPR} = 5 \times 10^{-9} E_{sc}$ in cgs units. Figure 6-6a shows the diffraction efficiency versus K. Peak diffraction efficiency of 6.1% was observed, corresponding to $\Delta n = 9.1 \times 10^{-6}$. Figure 6-6b shows a plot of $K_g/(\Delta n \cos(2\theta))$ versus K^2 with a fit to equation (6.2). The best fit occurs for $N_a = 3.0 \times 10^{18} cm^{-3}$, which is near the value (3.1×10^{18} cm^{-3}) obtained from absorption data. Figure 6-7 plots the diffraction versus beam intensity ratios, along with the theoretical curve from equation (6.2). The good correspondence of the data in figures 6-6 and 6-7

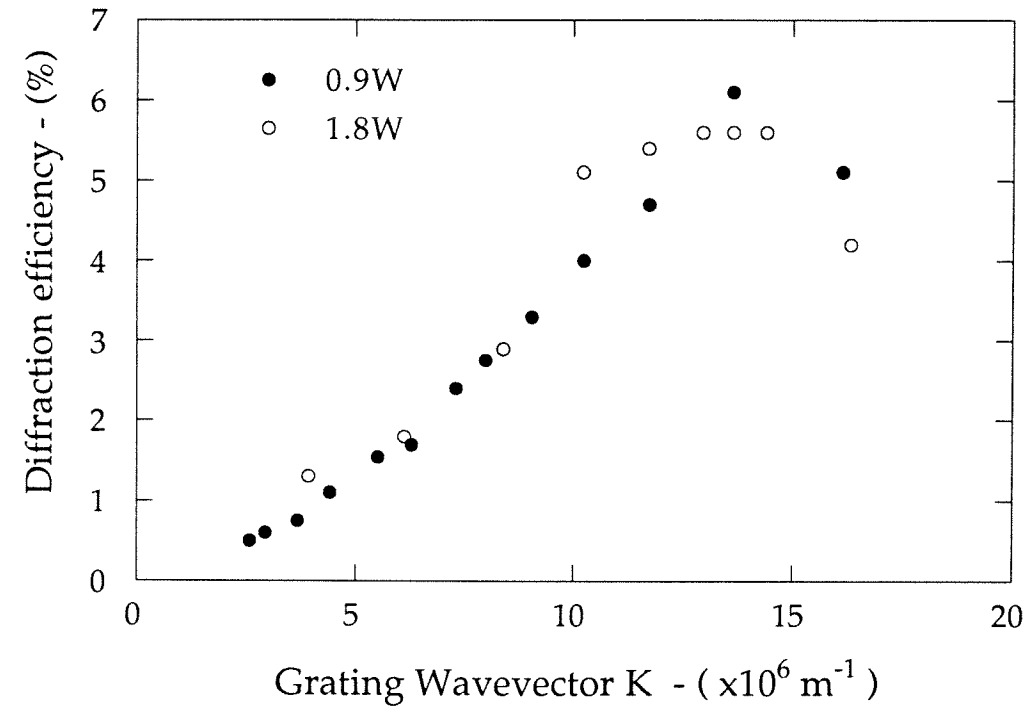

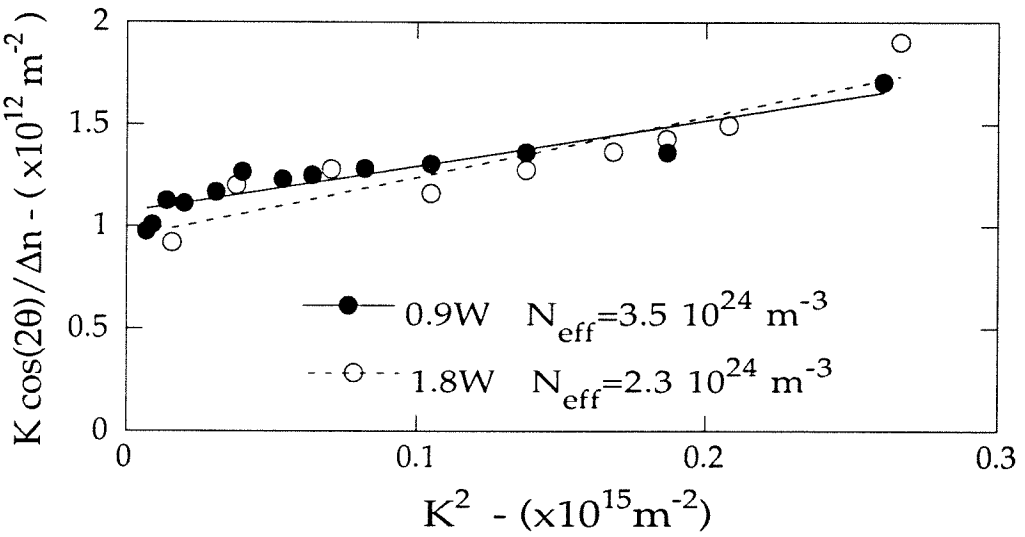

Figure 6-6a. The diffraction efficiency versus grating wavevector (a function of beam incidence angle). **Figure 6-6b.** The same data replotted to allow a fit to the effective donor concentration $N_{D,eff}$= 3.0x10^{18} cm^{-3}, in agreement with results from optical absorption data.

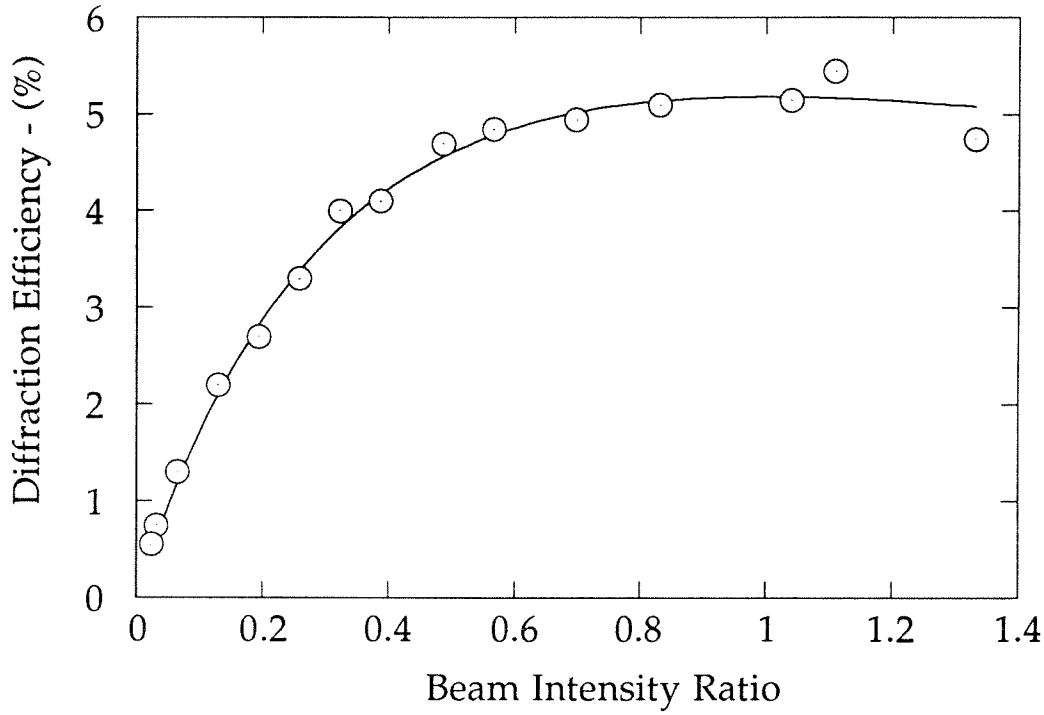

Figure 6-7. The diffraction efficiency of a KLTN crystal versus the beam intensity ratios. The curve is the theoretical dependence of the space charge field on the modulation depth.

with equation (6.2) allows us to conclude that the index change of the ZEFPR effect varies as the space charge field.

The final test of the ZEFPR effect model was a measurement of the phase of the ZEFPR index grating relative to the intensity grating of the writing beams. Since the index grating is modulated by the local Cu^{2+} concentration, we expect it to be in phase with the intensity, so that no two-beam coupling (power exchange between the two writing beams) will occur. This condition was verified by testing for two-beam coupling with the setup of figures 5-1/ 6-2. No power transfer was observed even though strong diffraction occurred when either beam was blocked. Two-beam coupling was observed, however, when an electric field was applied, the sign of the coupling coefficient changing with the direction of the applied field. (Beam coupling with applied field[27] in ZEFPR materials is discussed in chapter five and detailed phase measurements[28] are performed in chapter eight. These two experiments establish, without a doubt, the in-phase condition of the ZEFPR index gratings). The zero phase of the ZEFPR gratings further confirms the distinction of the ZEFPR effect from electro-optic mediated photorefractive effects where the phase must be nonzero because it is due to the intrinsically nonlocal space charge field.

The tests described above form the basis for our conclusion that the ZEFPR effect is caused by a Jahn-Teller relaxation in conjunction with the photoelastic effect. In what follows we present a simple theory of the interaction between the local J-T distortions and a macroscopic strain field.

6.3 Theory of Distortion Coordination

To model the effect of a macroscopic strain on the coordination of J-T distortions consider a crystal with a growth induced tensile strain along the **x**-axis ($u_{11} > 0$) and with compressive strains along **y** and **z** axes ($u_{22} = u_{33} < 0$). All other strain components are zero and by the cubic symmetry where only elastic constants $c_{1111}, c_{1122}, c_{1212}$ are nonzero, it is readily determined that

$$u_{33} = -\frac{c_{1122}}{c_{1122} + c_{1111}} u_{11} = -\sigma u_{11} \tag{6.4}$$

where σ is Poisson's ratio. The elastic coefficients were determined[29] for a KLTN with similar composition to that considered above to be $c_{12} = 7.28\text{x}10^{10}\text{N/m}^2$, $c_{11} = 30.93\text{x}10^{10}\text{N/m}^2$, and $c_{44} = 10.37\text{x}10^{10}\text{N/m}^2$ so that $\sigma = 0.19$. The energy of the strained crystal per unit volume is given by

$$E = \frac{1}{2} c_{ijkl} u_{ij} u_{kl} = \frac{1}{2} c_{1111} \left(u_{11}^2 + 2u_{33}^2\right) + c_{1122} \left(2u_{11}u_{33} + u_{33}^2\right)$$

$$= \frac{u_1^2}{2} \left[c_{11} - 2c_{12}\sigma\right] \tag{6.5}$$

where the convention is that $u_{11} = u_1$, $u_{23} = u_4$, $c_{1111} = c_{11}$, $c_{1122} = c_{12}$, etc.

The J-T distorting centers distributed randomly throughout the volume of the crystal will alter the strain so that $u_i' = u_i + \Delta u_i$ where Δu_i is the change in macroscopic strain due to the summation of the individual J-T distortions. The individual distortions are elongations of the oxygen octahedra in one of three orthogonal directions. We denote y as the fraction of distorting centers oriented along the **x** axis, and (1 - y) as the remaining fraction distributed along either the **y** or the **z** axes. We readily determine

$$\Delta u_1[y] = \Delta u_1[1]\left[(1+\sigma)\,y - \sigma\right] \tag{6.6a}$$

$$\Delta u_2[y] = \Delta u_3[y] = \frac{\Delta u_1[1]}{2}\left[1 - \sigma - (1+\sigma)\,y\right] \tag{6.6b}$$

where $\Delta u_1[1]$ is the strain change when y=1 (complete ordering). We neglect Δu_i for i=4,5,6 and dipole effects, that is, interactions between local distortions are ignored. Since local correlations of distortions have been observed in KTN[30], this approximation will not be strictly accurate in the presence of an applied strain field. However, it is not expected that correlation of distortions will affect the value of y in the absence of such a field. The effect of distortion correlation will average out to zero on a macroscopic scale (the wavelength of light) unless a macroscopic ordering field is present. This follows from the definition of a centrosymmetric material.

The decrease in elastic energy per unit volume resulting from the reduction in strain $\Delta u_1[y]$ and $\Delta u_3[y]$ is obtained as

$$\Delta E[y] = -u_1\,\Delta u_1[1]\left[(1+\sigma)\,y - \sigma\right]\left[c_{11} - 2c_{12}\sigma\right]. \tag{6.7}$$

The entropy change of the ordering follows readily by counting the number of configurations of the distortions. There are (ny) distorting centers oriented along the x axis per unit volume, and n(1-y) oriented along either the y or z axes. The number of configurations W is given by the combinatorial equation

$$W = \binom{n}{ny} \sum_{s=0}^{n(1-y)} \binom{n(1-y)}{s} = \binom{n}{ny} 2^{n(1-y)}. \tag{6.8}$$

Using Stirling's approximation, the entropy change ($\Delta S = k \ln W$) is found to be

$$\Delta S[y] = -n k \left(y \ln[y] + (1-y) \ln\left[\frac{1-y}{2}\right] \right). \tag{6.9}$$

Now the free energy $G = \Delta E - T \Delta S$ can be minimized to determine the temperature dependence of the ordering parameter. We calculate that

$$y(\beta) = \frac{e^{\beta U}}{e^{\beta U} + 2} \tag{6.10}$$

where the "strain alignment energy" per distorting center $U = \Delta E[1] (1 + \sigma)/n$ and $\beta = 1/(kT)$. Thus

$$\Delta u_1[y(\beta)] = \Delta u_1[1] \left(\frac{(1+\sigma) e^{\beta U}}{e^{\beta U} + 2} - \sigma \right). \tag{6.11}$$

The final equation is plotted in figure 6-8 as the amount of strain compensation $\Delta u_1[y]$ along the x axis versus βU, for $\sigma = 0.2$. From it we conclude that large macroscopic strains lead to ordering of distortions.

A plausible value for the photoelastic coefficient[31] p_{11} is $p_{11} = 0.1$. If we take values for the strains consistent with the observed index changes we obtain $u_1 \approx 3 \times 10^{-4}$, $\Delta u_1[1] \approx 10^{-4}$, and $\beta U \approx 0.2$. Since we have not included the effect of spontaneous cooperative ordering due to elastic or electric interactions between the distorting centers, the estimate above is a lower bound for the amount of ordering expected for the strain values considered. The experiment showed that the diffraction was reduced by ~40% when the strain was

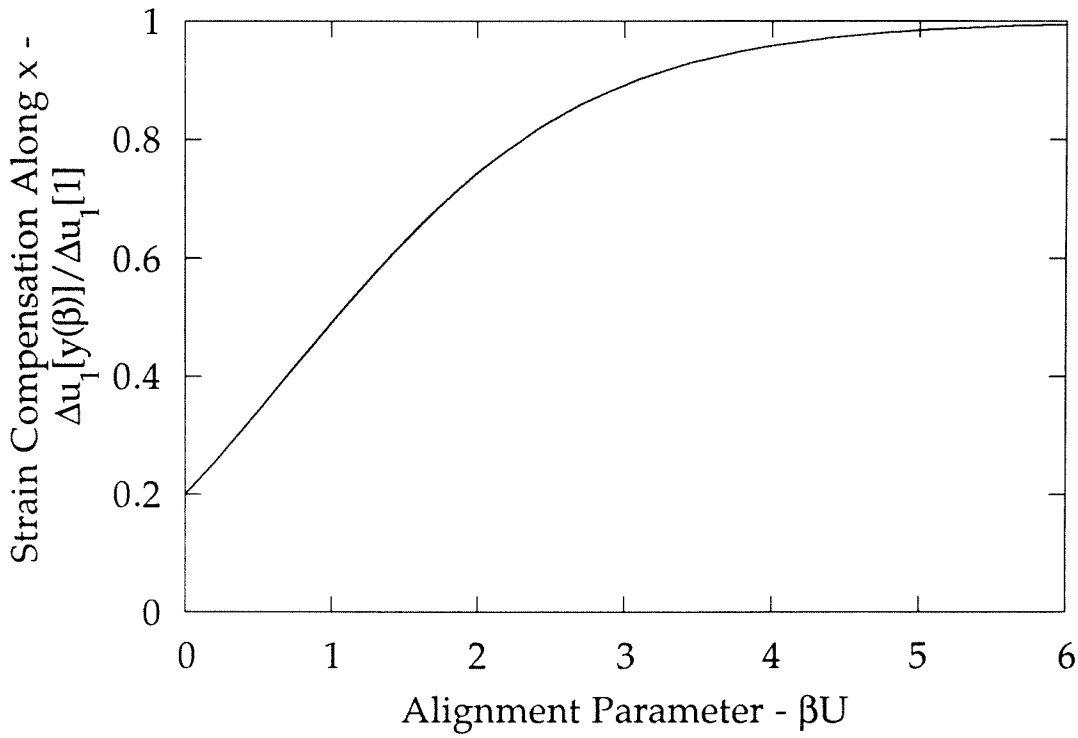

Figure 6-8. The relative strain compensation along the x axis. When the strain alignment energy U is greater than several kT, almost complete alignment occurs. Since $\sigma \approx 0.2$ in KLTN, the distortion causes a substantial volume change of the unit cell, so that strain compensation, and therefore index change, is seen in the absence of any alignment, i.e., $\Delta u_1[y(\beta)]/\Delta u_1[1] = 0.2$ when $\beta U = 0$.

compensated in the material. This indicates that roughly 20% or more of the index grating is coordinated by the strain field, the remainder being due to the volume change of the unit cell under distortion. The 20% experimental figure is a lower bound because the strain compensation vise used in the experiment may not have compensated the strain completely. Nevertheless this measured value is reasonably close to that predicted by equation (6.10), so the noninteracting theory described above is probably adequate if the experimentally measured lower bound is accurate.

6.4 The Photoelastic Photorefractive Effect

When the distortions are ordered as described above, there is a photoelastic change in the index of refraction proportional to Δu_i. If interfering light beams are subsequently incident on the medium, the optical standing wave will create a spatially periodic concentration of distortable ions, in our case, Cu^{2+} ions. Since the relaxation strain Δu_i was assumed proportional to the number of distortable ions, there will be a periodic modulation of the total strain of

$$\delta(\Delta u_i[y]) = \delta[Cu^{2+}] / [Cu^{2+}] \; \Delta u_i[y] \qquad (6.12)$$

where $\delta[Cu^{2+}]$ is the modulation of the atomic Cu^{2+} concentration. Thus the modulated strain field is proportional to the number of displaced electrons (= $\delta[Cu^{2+}]$), and therefore is proportional to the electronic space charge field.

The change in index of refraction due to the strain modulation can be written

$$\Delta n_1[y] = -\frac{n_0^3}{2}\,\delta(u_1[1])\left(p_{12}\,(1-\sigma) - \sigma\,p_{11} + y\,(1+\sigma)\,(p_{11} - p_{12})\right) \qquad (6.13a)$$

$$\Delta n_3[y] = -\frac{n_0^3}{4}\,\delta(u_1[1])\left(p_{11}(1-\sigma) - (1-3\sigma)p_{12} - y(1+\sigma)(p_{11} - p_{12})\right) \qquad (6.13b)$$

where p_{ij} are the photoelastic constants. Here we have ignored local changes in y due to $\delta(\Delta u_i[y])$, i.e., the modulation of the Cu^{2+} concentration modulates the number of distorting centers per unit volume thus modifying y.

6.5 Summary

A new photorefractive mechanism has been demonstrated in KTN/KLTN:Cu with $\Delta n \sim 2\times10^{-5}$ which arises from a periodic strain grating. A Jahn-Teller spatially periodic distortion was shown to be responsible. The J-T distortions are at least partially ordered by a relaxation of a macroscopic strain field. The periodicity of the distortion is due to a spatially periodic Cu^{2+}/Cu^{1+} ratio created by charge redistribution in a spatially periodic optical intensity pattern. This mechanism forms an index grating through the photoelastic effect and causes diffraction in paraelectric photorefractive materials without an applied electric field. This phenomenon is expected to be quite general, although only noticeable when the conventional photorefractive effect is forbidden. The most striking characteristic of this effect is that it is in-phase with the intensity grating. This is in contrast to any phenomenon which is mediated by the nonlocal space charge field. This characteristic is useful for implementing linear optical phase detection devices (chapter seven).

The coordination of the Jahn-Teller distortions in the macroscopic strain field was modeled as a function of temperature. As expected, for strain alignment energies greater than several kT, almost complete ordering occurs. Experimental evidence indicates that the ordering is only partial. Also, the amount of ordering estimated from the parameters of the noninteracting distortion center theory is reasonably close to that observed experimentally. This indicates that the interactions between the J-T centers can probably be safely neglected in this first-order treatment. The index grating caused by the spatial modulation of $[Cu^{2+}]$ ions was calculated.

References for chapter six

[1] F. S. Chen, "A laser-induced inhomogeneity of refractive indices in KTN," J. Appl. Phys. **38**, 3418 (1967).

[2] A. Agranat, V. Leyva, K. Sayano, and A. Yariv, "Photorefractive properties of $KTa_{1-x}Nb_xO_3$ in the paraelectric phase," Proc. of SPIE Vol. **1148**, Conference on Nonlinear Optical Properties of Materials, (1989).

[3] A. Agranat, V. Leyva, and A. Yariv, "Voltage-controlled photorefractive effect in paraelectric $KTa_{1-x}Nb_xO_3$:Cu,V," Opt. Lett. **14**, 1017-1019 (1989).

[4] A. Agranat, R. Hofmeister, and A. Yariv *Technical Digest on Photorefractive Materials, Effects, and Devices* , 1991 (Optical Society of America, Washington DC, Vol **14**, 6-9 (1991).

[5] A. Agranat, R. Hofmeister, and A. Yariv, "Characterization of a new photorefractive material: $K_{1-y}L_yT_{1-x}N_x$," Opt. Lett. , **17**, 713-715 (1992).

[6] A. A. Kamshilin, "Simultaneous recording of absorption and photorefractive gratings in photorefractive crystals," Opt. Comm. **93**, 350 -358 (1992).

[7] R. S. Cudney, R. M. Pierce, G. D. Bacher, and J. Feinberg, "Absorption gratings in photorefractive crystals with multiple levels," J. Opt. Soc. B **8**, 1326 - 1332 (1991).

[8] T. Jaaskelainen and S. Toyooka, "Analysis of absorption reflection gratings," Opt. Comm. **71**, 133 - 137 (1989).

[9] Changxi Yang, Dadi Wang, Peixian Ye, Qincai Guan, and Jiyang Wang,

"Photorefractive diffraction dynamic during writing in paraelectric KTN crystals," Opt. Letters **17**, 106-108 (1992).

[10] H. A. Jahn and E. Teller, "Stability of polyatomic molecules in degenerate electron states. I - Orbital degeneracy," Proc. of the Royal Soc. , **A161**, 220-235 (1937).

[11] A. F. Wells, Structural Inorganic Chemistry 4th Ed. , Clarendon Press, Oxford (1975).

[12] G. Chanussot and C. Thiebaud, "Investigation of the [1,0,0] polarization of iron-doped barium titanate under irradiation, part I. Experimental," Ferroelectrics **8**, 665-670 (1974).

[13] G. Chanussot, "Static pseudo Jahn-Teller effect at point defects in irradiated ferroelectric crystals (perovskite structures), part II. Theorectical," Ferroelectrics **8**, 671-683 (1974).

[14] A. Ouedraogo, B. Dehaut, et G. Chanussot, "Les propriétés photoferroélectriques de $BaTiO_3$ dopé avec cuivre," J. de Physique Lettres **39**, 179-182 (1978).

[15] G. Chanussot, "Physical models for the photoferroelectric phenomena," Ferroelectrics **20**, 37-50 (1978).

[16] S. M. Kostritskii, "Photoinduced structure distortions of the oxygen-octahedral ferroelectrics," Ferroelectrics Letters **13**, 95-100 (1991).

[17] S. L. Gnatchenko, N. F. Kharchenko, V. A. Bedarev, V. V. Eremenko, "Photoinduced linear birefringence and cooperative Jahn-Teller effect in

manganese-germanium garnets," Fiz. Niz. Tem. **15**, 627-632 (1989); also see Sov. J. Low Temp. Phys. **15**, 353 (1989).

[18] V. Leyva, Accuwave corporation, Santa Monica CA, personal communication (1992).

[19] T. S. Narasimhamurty, *Photoelastic and Electro-optic Properties of Crystals* , chapter 8, Plenum Press, New York (1981).

[20] H. Mueller, "Properties of rochelle salt, IV ," Phys. Rev. **58**, 805-811 (1940).

[21] F. S. Chen *et al.* J. Appl. Phys. **37**, 388 (1966).

[22] V. Leyva Ph.D. Thesis, California Institute of Technology, Pasadena, California, unpublished (1991).

[23] A. Agranat and Y. Yacoby, "Dielectric photorefractive crystals as the storage medium in holographic memory systems," J. Opt. Soc. Am. B **5**, 1792 - 1799 (1988).

[24] A. Agranat, Y. Yacobi, "The dielectric photorefractive effect - a new photorefractive mechanism," IEEE Ultras. **33**, 797 -799 (1986).

[25] A. Agranat and Y. Yacobi, "Temperature dependence of the dielectric induced photorefractive effect," Ferroelec. Lett. **4**, 19 -25 (1985).

[26] N. V. Kukhtarev, V. B. Markov, S. G. Odulov, M. S. Soskin, and V. L. Vinetskii, "Holographic storage in electrooptic crystals. I. steady state," Ferroelectrics **22**, 949-960 (1979).

[27] R. Hofmeister and A. Yariv, "Vibration detection using dynamic photorefractive gratings in KTN/KLTN crystals," Appl. Phys. Lett. , **61**, 2395-2397 (1992).

[28] R. Hofmeister, A. Yariv, A. Kewitsch, and S. Yagi, "Simple methods of measuring the net photorefractive phase shift and coupling constant," to appear Opt. Lett. April 1, 1993.

[29] J. Werner and R. Hofmeister, undergraduate senior thesis project (1992).

[30] J. Toulouse, X. M. Wang, L. A. Knauss, and L. A. Boatner , "Dielectric nonlinearity and spontaneous polarization of $KTa_{1-x}Nb_xO_3$ in the diffuse transition range," Phys. Rev. B **43**, 8297-8302 (1991).

[31] A. Yariv and P. Yeh, *Optical Waves in Crystals* , chapter 9, John Wiley & Sons, New York (1984).

Chapter Seven

Applications of the ZEFPR Effect

7.1 Introduction

As discussed in the previous chapter, gratings written with the Zero External Field PhotoRefractive effect (ZEFPR) exhibit a unique phase relationship (ϕ=0) between the phase and intensity gratings. This feature will be shown to enable implementation of numerous interesting devices, and, in particular, an all-optical self-aligning holographic vibration sensor. Under the zero-phase condition, no intensity coupling of two beams occurs. However, the transmitted intensity of two interfering beams varies linearly with displacement of the medium along the grating vector or with phase shift of one of the interfering beams. The phase shift must be $\theta << \pi/2$, with a frequency much higher than the inverse grating rewrite time, and the average position of the phase must be zero or very slowly varying. Figures 7-1 and 7-2 illustrate a vibration sensor utilizing this principle. Optical fiber is used to deliver the interfering light beams to the sensor, and to collect the transmitted light. One beam is phase modulated by reflection off a vibrating membrane. In this way, vibrations can be sensed remotely without any electrical signals in the vicinity of the sensor. In addition, since the detecting element is a holographic grating which is continually rewritten, the device is self-aligning and resis-

tant to mechanical shocks. The device is useful in applications where electric fields cannot be permitted into the sensing environment, or where electronic wiretapping is a problem.

Other devices are also discussed but are not demonstrated here. Specifically the application of the ZEFPR zero-phase response to performing image subtraction and to implementing a high-speed interferometric data link is described.

7.2 Self-Aligning Vibration Sensor/ Microphone

7.2.1 Introduction

All-optical sensors have received considerable attention recently[1-4] for use in applications where electrical signals cannot be used or are impractical. These include aqueous, explosive, corrosive, and electromagnetically sensitive environments. Traditionally, intensity modulating sensors have been preferred over interferometric methods[5,6] because of their relative ease of alignment. Unfortunately, even these techniques require precise fiber positioning in order to gain sensitivity[5,6]. Thus they are not robust. There is a need for an all-optical sensor which combines sensitivity with robustness. Here an interferometric vibration detector and microphone is described which overcomes the alignment and stability problems of conventional optical devices.

As discussed before, in the KTN and KLTN crystals which displayed a strong ZEFPR effect, the photorefractive dopant was copper, which is stable as

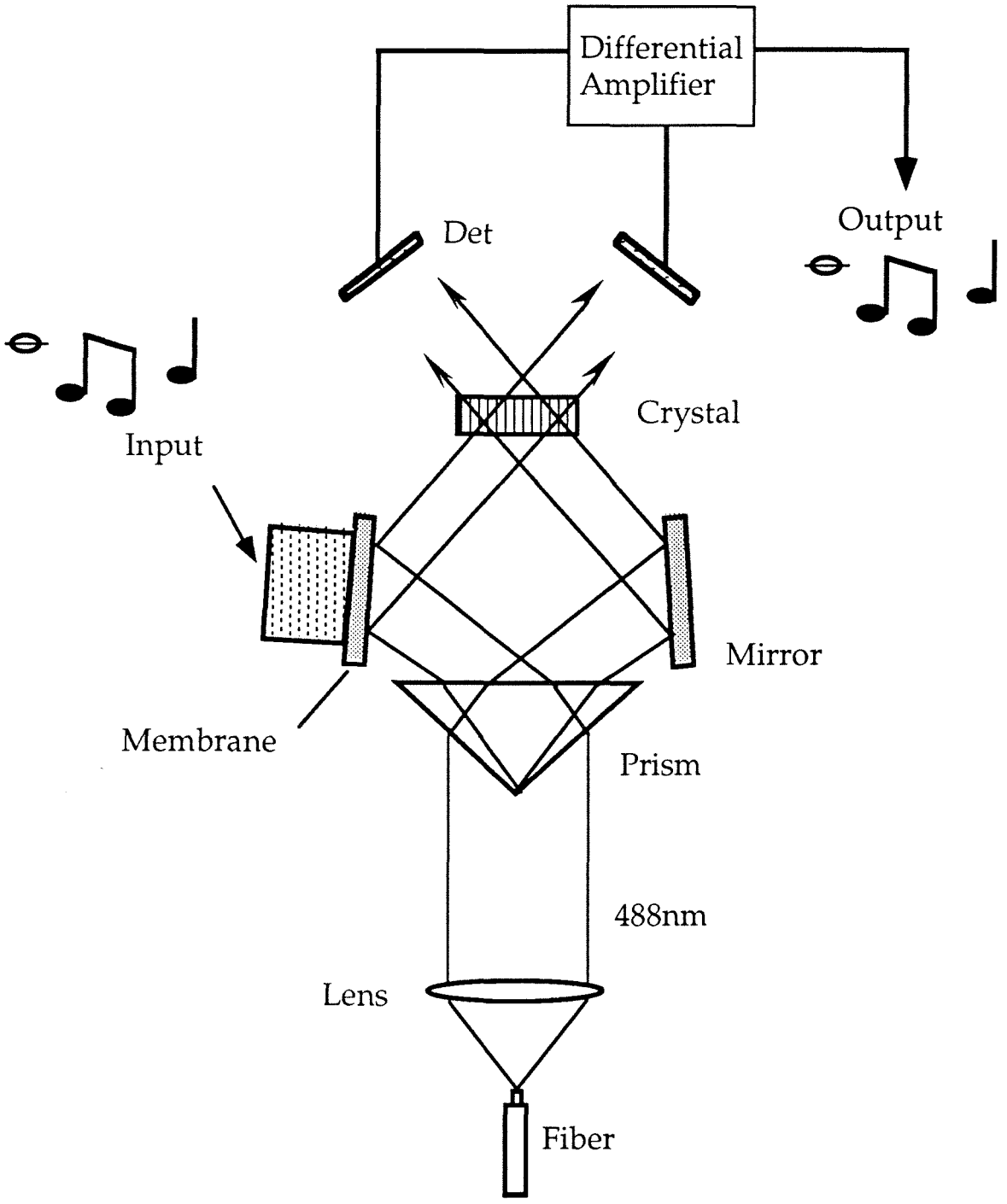

Figure 7-1. The setup of the ZEFPR microphone. The light is delivered with a single-mode fiber and is split with a prism. Vibrations of the membrane cause two-beam coupling differentially detected **Det** at the exit facet.

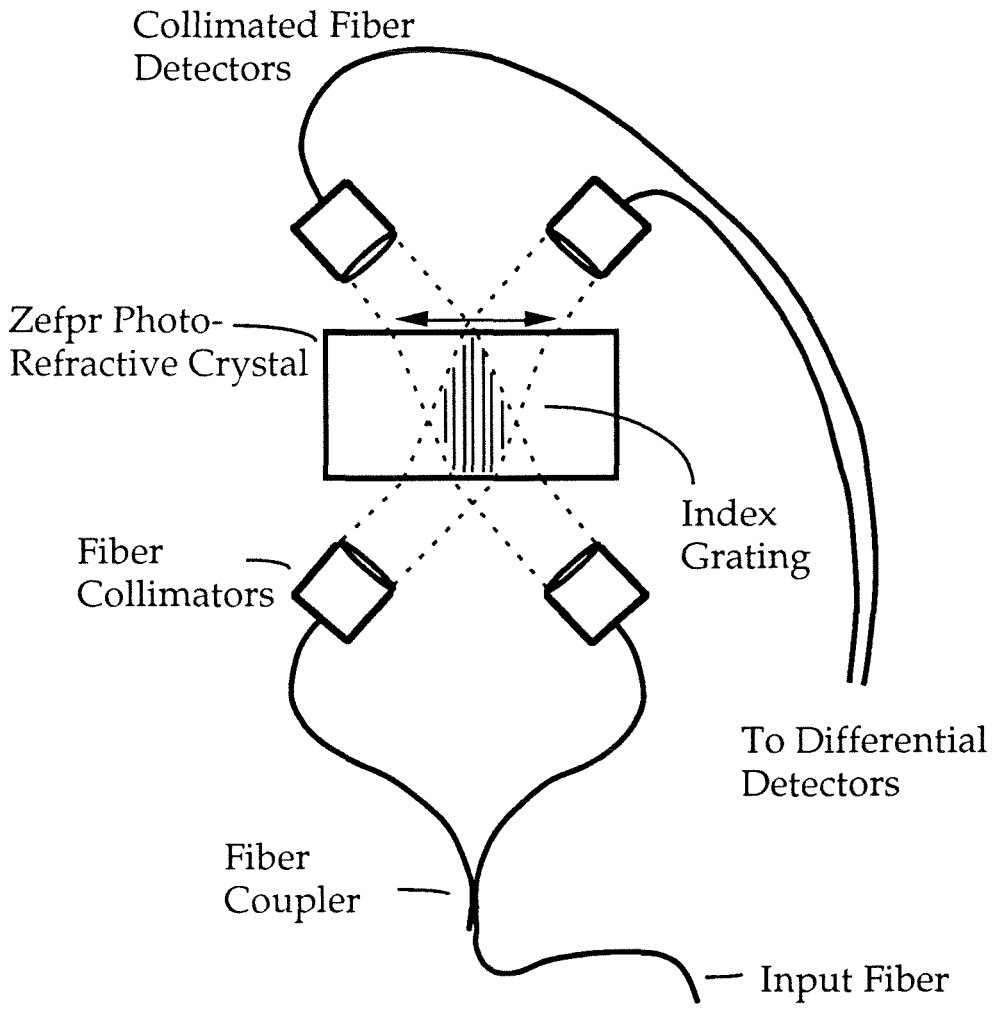

Figure 7-2. A ZEFPR material all-optical microphone. The light is delivered with a single-mode fiber and is collected with multimode fibers at the exit facet of the crystal. In this way, all electrical devices and signals can be removed to a remote location; the sensing device is then all-optical.

either Cu^{1+} or Cu^{2+}. The Cu^{2+} ion is known to cause large Jahn-Teller (J-T) distortions. The Cu^{1+} ion, by contrast, has no tendency to distort. Illumination of the crystal by the periodic intensity pattern of the optical field leads to a mimicking spatially periodic Cu^{2+}/Cu^{1+} ratio due to excitation of electrons from Cu^{1+} and trapping by Cu^{2+}. This, as explained above, gives rise to a spatially periodic distortion. The result of this is a spatial modulation of the strain field in phase with the intensity which leads to a corresponding modulation of the index of refraction (index grating) via the photoelastic effect.

Since the index grating is modulated by the local Cu^{2+} concentration, we expect it to be in phase with the intensity ($\phi = 0$) so that no two-beam coupling (power exchange between the two writing beams) will occur. When either the phase of the index grating or of the interfering beams is modulated with $\theta \ll \pi/2$, however, a power exchange, proportional to θ, takes place between the two beams. If the vibration frequency is much higher than the inverse of the grating rewrite time, and if the time averaged value of α is zero, the vibration will not erase the grating.

7.2.2 Experiment

The setup of the fiber microphone reported on here is illustrated in figure 7-1. A single mode fiber was used to deliver the 488nm light to the device. The emerging beam was collimated and split by a 90^{o} prism. This method of beamsplitter was chosen over a fiber coupler, because couplers at

this wavelength are expensive and problematic. One beam was reflected off a mirror, and the other off a reflective membrane. The equal intensity beams interfered in the volume of the crystal, and the outputs of the two beams were detected differentially. Differential detection improved the signal to noise ratio substantially. Differential detection normalized to the sum of the intensity (see (7.4)) would, in addition, eliminate noise due to intensity fluctuations of the source; this was not done in the following experiment. Most of the light was blocked in order to prevent saturation of the detectors. The beams were detected locally for convenience; in an operational device the outputs would be coupled into fibers for remote sensing. Since the beams are not deflected, but only intensity modulated, we conclude that it will be relatively easy to couple the output light into multimode fibers so that the experimental shortcut described above will not alter the performance.

The membrane was a uniformly stretched circular film of reflective mylar. Since both sides were open to the air, it operated as a pressure gradient sensor, with resultant poor low-frequency response. The first resonance of the membrane was at 900Hz. The usable range of operation was from 1.2 - 25kHz (the limit of the spectrum analyzer).

The detector outputs were processed with an audio spectrum analyzer. The performance of the microphone was evaluated for both single ended and differential detection. Figure 7-3a shows the output of a single detector with a 58dB sound pressure level (SPL relative to 0.0002μbar) signal at 4.9kHz incident on the microphone. The background noise floor is also plotted. From the figure, we measure a noise equivalent power (NEP) in a 10Hz bandwidth, of

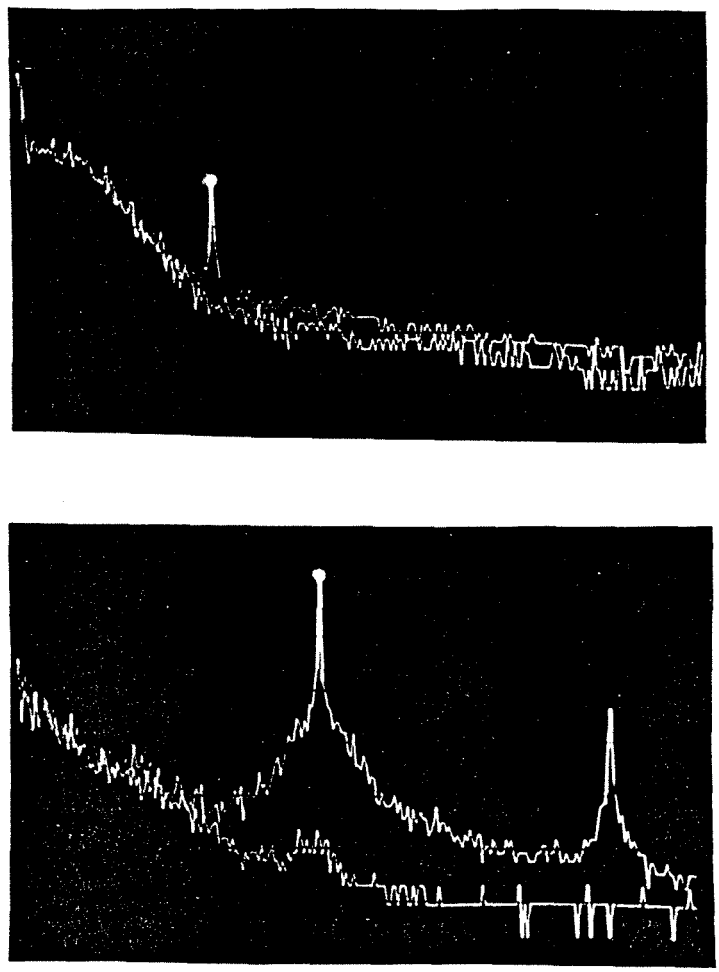

Figure 7-3a. The output of one detector with a 58dB signal at 4.9kHz incident on the microphone. The lower trace is the noise floor without the signal. The NEP is 38dB. **Figure 7-3b.** The differential output of both detectors under the same experimental conditions. Compensation of intensity fluctuations lowers the noise floor 26 dB yielding NEP = 12dB.

38dB. Figure 7-3b shows the same incident signal detected differentially. The compensation of intensity fluctuations (equation (7.3)) with differential detection lowers the noise floor by more than 30dB, leading to an NEP of 12dB SPL. Between the range of 1.6 - 15.5kHz we determined the NEP ≤ 15dB (Fig. 7-4). The useful upper limit of the microphone (determined by listening to the output) was approximately 95dB SPL, giving a dynamic range of about 80dB. Above 95dB, the third harmonics of the input signals became noticeable to the ear.

7.2.3 Coupled Wave Analysis

When two beams $I_1(0)$ and $I_2(0)$ are symmetrically incident (Fig. 5-1) on a ZEFPR ($\phi = 0$) material it can be shown (chapter 8) that the resultant index grating is given by

$$n(r,t) = n_0 + \frac{n_1}{2I_0} |A_1(0)| |A_2(0)| e^{i\Delta z} e^{-i(k_1 - k_2)z} + c.c. \qquad (7.1)$$

where $\Delta = (g/I_0)(I_2(0) - I_1(0))$, $g = \pi n_1/\lambda$, and n_1 is the peak-to-peak index modulation for $I_2(0) = I_1(0)$. I_0 is the total intensity and $A_i(0)$ are the complex amplitudes of the input beams. If this index grating is considered fixed in the crystal and one beam is phase shifted by $\theta = \theta_1 \sin \omega t$, where $\theta_1 \ll \pi/2$ and $1/\omega \ll \tau_{write}$ then the coupled mode equations can be solved to yield

$$I_1(z) = I_1 \left(1 - \frac{\kappa^2}{s^2} \sin^2[sz]\right) + I_2 \frac{\kappa^2}{s^2} \sin^2[sz] - \frac{\kappa}{s} \sqrt{I_1 I_2} \sin[2sz] \sin\theta$$

$$- \frac{\kappa\Delta}{s^2} \sqrt{I_1 I_2} \sin^2[sz] \cos\theta \qquad (7.2a)$$

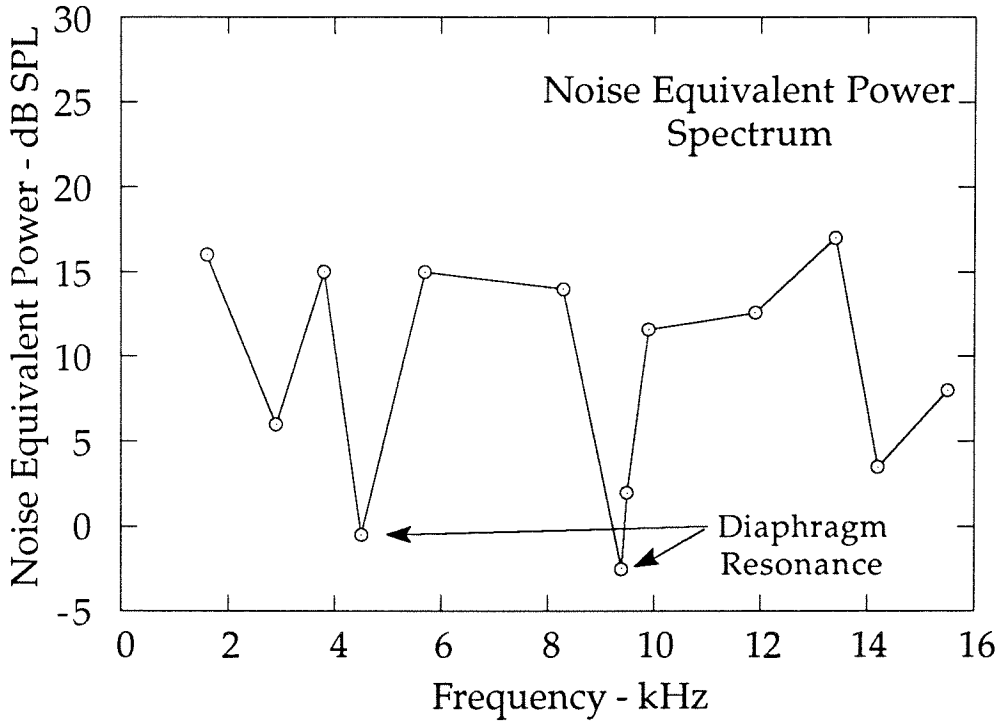

Figure 7-4. The measured noise equivalent power (NEP) of the microphone across the audio spectrum. In the range of frequencies 1.6kHz ≤ ν ≤ 16kHz, the sensitivity of the device was NEP≤ 15dB SPL. Two mechanical resonances of the membrane are marked.

$$I_2(z) = I_2\left(1 - \frac{\kappa^2}{s^2}\sin^2[sz]\right) + I_1\frac{\kappa^2}{s^2}\sin^2[sz] + \frac{\kappa}{s}\sqrt{I_1 I_2}\,\sin[2sz]\,\sin\theta$$

$$+ \frac{\kappa\Delta}{s^2}\sqrt{I_1 I_2}\,\sin^2[sz]\,\cos\theta \qquad (7.2b)$$

where $s^2 = \kappa^2 + \Delta^2/4$, and $\kappa = g\,A_1A_2^*/I_o$. We defined $I_2(0) = I_2$ and $I_1(0) = I_1$. When the beam intensities are equal $I_2 = I_1 = I$ the solution for arbitrary phase ϕ is given by (chapter eight)

$$I_1(z)/I = 1 - \tanh[\Gamma z/2]\cos\theta - \frac{\sin(g\,\cos\phi\,z)}{\cosh[\Gamma z/2]}\sin\theta \qquad (7.3a)$$

$$I_2(z)/I = 1 + \tanh[\Gamma z/2]\cos\theta + \frac{\sin(g\,\cos\phi\,z)}{\cosh[\Gamma z/2]}\sin\theta \qquad (7.3b)$$

where $\Gamma = 2g\sin\phi$. When $\phi = 0$ as in (7.2) and the equal intensities are detected differentially, the signal is

$$I_2(z) - I_1(z) = S = 2\,I\sin[g\,z]\,\sin\theta \qquad (7.4)$$

which is linear in θ (for small θ).

The same calculation can be performed for a conventional photorefractive material ($\phi = \pi/2$). The result for arbitrary incident intensities is

$$I_1(z) = I_1\left[\cos^2[\gamma-\delta] + \zeta^2\sin^2[\gamma-\delta] - \zeta\,\sin[2(\gamma-\delta)]\,\cos\theta\right] \qquad (7.5a)$$

$$I_2(z) = I_1\left[\zeta^2\cos^2[\gamma-\delta] + \sin^2[\gamma-\delta] + \zeta\,\sin[2(\gamma-\delta)]\cos\theta\right] \qquad (7.5b)$$

where $\zeta^2 = I_2(0)/I_1(0)$, $\gamma = \mathrm{Tan}^{-1}[\zeta\,e^{\kappa z}]$, and $\delta = \mathrm{Tan}^{-1}[\zeta]$. When the intensities are equal, $I_2 = I_1 = I$, the differentially detected signal may be obtained from ei-

ther (7.3) or (7.5) as

$$I_2(z) - I_1(z) = 2\, I \tanh[g\, z] \cos\theta. \qquad (7.6)$$

The details of these calculations are performed in chapter 9 for arbitrary phase ϕ. Only the two extremes $\phi = 0$ and $\phi = \pi/2$ are considered here because they are sufficient to illustrate the point made. In figure 7-5a the output intensities for the $\phi = 0$ case (equation 7.2) are plotted for $\theta_1 = 0.1$rad, for $\kappa z = 0.5$, and $A_2(0)/A_1(0) = 1.0$ and 2.0. Figure 7-5b plots the output signal of equation (7.5) for the same experimental conditions as in figure 7-5a. The signal amplitude is much weaker than in the $\phi = 0$ case and is at twice the modulating frequency. From these figures it is clear that only a material with zero-phase gratings is sensitive to small phase fluctuations. The sensitivity of a conventional photorefractive material is quite low and peaks near $gL \approx 1.0$/cm; beyond that value it decreases with increasing coupling constant. In addition, the zero-phase grating yields a linear response whereas the conventional photorefractive gives the second harmonic. Calculations performed in chapter eight show that for a material with $0 \le \phi \le \pi/2$ the output is a combination of the linear terms and the second harmonic. However the phase must approach zero very closely before the second harmonic term becomes negligible. Thus only an identically zero-phase material is suitable as an all-optical vibration sensor (though a conventional material can be made to approximate the zero-phase condition by applying a field, introducing birefringent plates[7], or frequency shifting one of the beams).

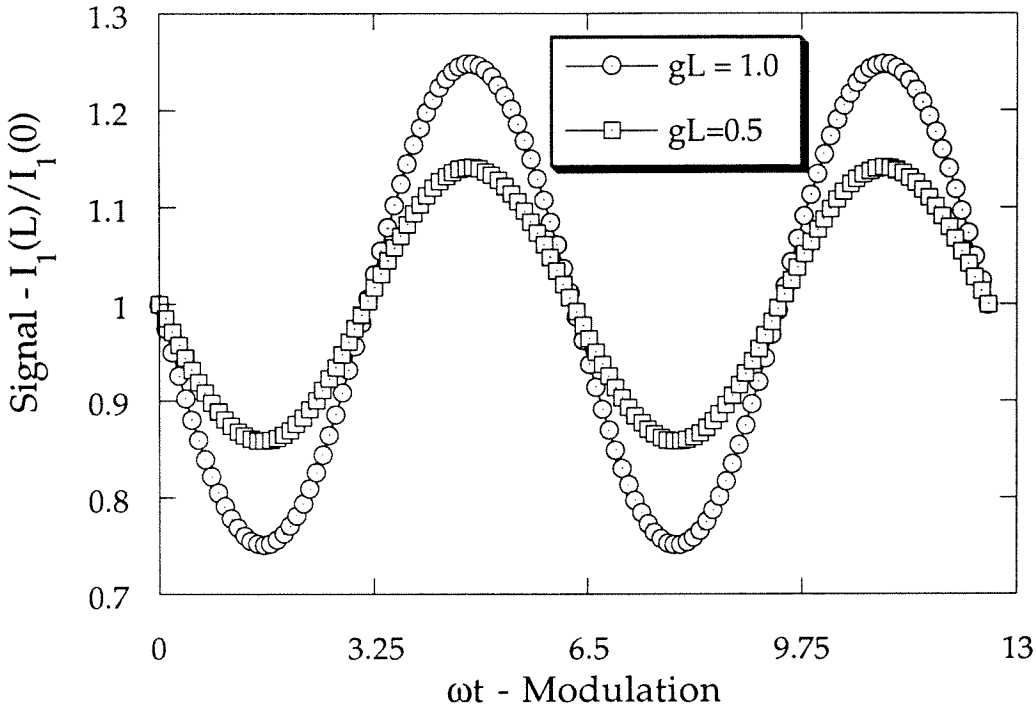

Figure 7-5a. Intensity modulation of beams interfering in a ZEFPR material in the geometry of figure 5-1 for a sinusoidal input phase modulation of 0.1rad. The output approximates a sine wave at the same frequency even for large amplitudes of the signal modulation.

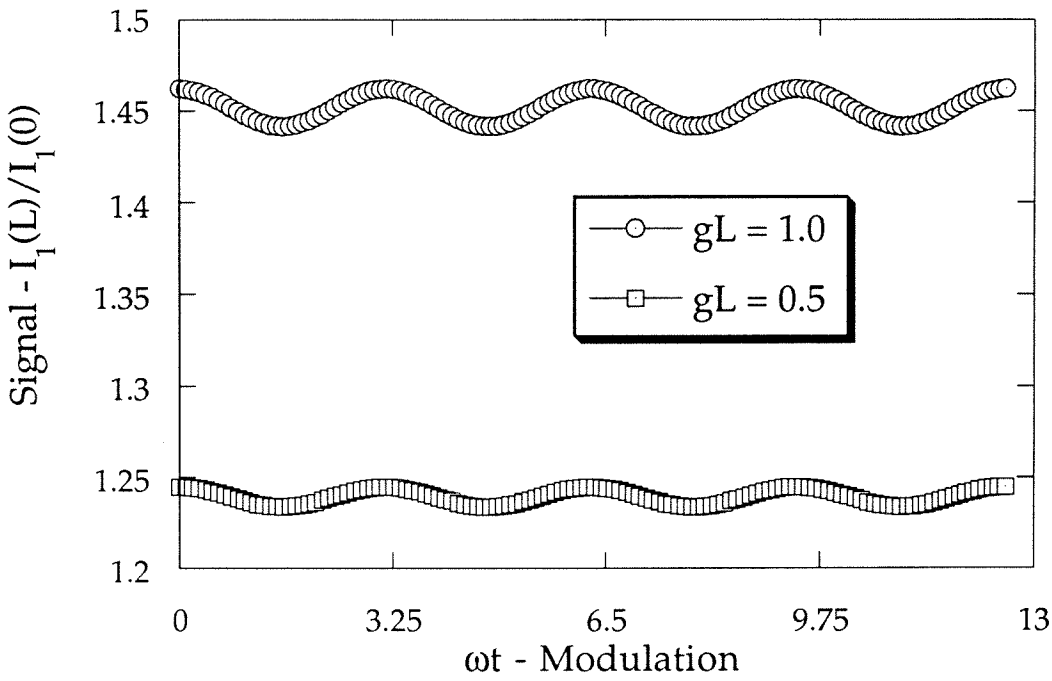

Figure 7-5b. Intensity modulation of beams interfering in a diffusion limited conventional photorefractive ($\phi = \pi/2$) under the same conditions as in Fig. 7-5a. The output is a weak modulation (different y-axis scale) at twice the input frequency. Thus a material with $\phi \approx \pi/2$ is insensitive to vibrations and gives a second harmonic response of intensity fluctuations to input phase fluctuations.

7.2.4 Discussion of Results

A sensitive all-optical microphone/vibration detector has been demonstrated utilizing the ZEFPR effect. The response was measured from 1.2kHz - 25kHz, limited by the membrane at the low end and by the spectrum analyser at the high end. Since the microphone relies on physical motion of the membrane, the ZEFPR microphone is expected to have the same fundamental limitations to flatness of response as a conventional microphone. Nevertheless it may not be advisable to simply place the membrane of a good capacitive microphone into the ZEFPR setup of figure 7-1, for several reasons. First, the membrane would be metallic which may be undesirable in a corrosive environment. Also a nonmetallic membrane would be lighter - a substantial advantage. Second, conventional membranes derive flatness of response by following the air motion of the acoustic wave. This requires large excursions at low frequencies[8-10]. The ZEFPR device must stay within the linear regime where the motion d of the membrane obeys $d<<\lambda/4$. Finally, a conventional membrane is tuned with regard to the average response of the membrane: the response at any one point is generally unknown[11]. The ZEFPR microphone does not require a large membrane; it senses phase modulation only where the membrane is illuminated. It is unclear whether the solution of this engineering problem would be more or less difficult than that of a conventional microphone.

The dynamic range of the device tested was only 80dB. This is substantially less than that of conventional microphones. However, no attempt was made to stabilize the laser intensity or the coupling into the fiber; thus the in-

tensity fluctuations were quite large, also, the signal was not normalized to eliminate the common mode noise from fluctuations in intensity (7.4). It is expected that the fundamental sensitivity of the optical microphone will be much higher.

Conventional microphones are limited by shot noise in the sensing unit and by corruption of the microvolt signals before preamplification. Thus they are quite sensitive to external electrical signals which cause noise and feedback. A ZEFPR microphone, by contrast, is immune to electrical noise because the detected signal (proportional to intensity) will always be on the order of volts. Also the electrical part of the device is remote and can be placed in an electrically isolated environment. The fundamental limit of the ZEFPR device is given by Brownian motion of the membrane. The noise equivalent power (NEP) of Brownian motion will scale inversely with membrane area, but as stated above we are free to use a large membrane and only sample a small part of it. In any case, the ZEFPR microphone with a $1cm^2$ membrane should have an NEP of about -15dB SPL which is much better than any electronic microphone. This would yield a dynamic range of about 110dB, which would be acceptable for most (music) recording purposes[11]. Finally, it is noted that the upper limit of detection can be raised from 95dB SPL to any value simply by partially isolating the microphone from the acoustic source. The dynamic range would be unaffected.

7.3 Other Applications of the ZEFPR Effect

7.3.1 Interferometric Data Link

Materials displaying the ZEFPR effect perform a linear phase to intensity transduction when one beam scattering off a dynamically written index grating is suddenly phase shifted. In the previous section this phase shift was achieved by reflecting one beam off a vibrating membrane, but any method of phase shift will yield the same result. In this section the phase shift is accomplished with an electro-optic modulator.

A conventional high-speed fiber optic data link is illustrated in figure 7-6a. A laser is coupled into a fiber optic Mach-Zender interferometer. Data is impressed onto the signal beam with an electro-optic phase modulator. A second fiber coupler is used to complete the interferometer. The outputs are detected differentially and normalized. Inevitably, the fiber lengths will fluctuate due to thermal changes or stretch, so the outputs of the interferometer drift over time if the lengths are not actively stabilized. The length changes can be tracked and corrected with a feedback device. Usually a low-frequency (10^5 - 10^6 Hz) reference oscillator is employed to dither the reference beam (the fiber is stretched with a piezoelectric device). The transmitted optical signal is multiplexed with the reference oscillator, and the time integrated product is used to generate a feedback signal which is amplified and directed to a fiber stretcher in the signal arm. This procedure is complicated and undesirable: Loss of phase lock is a common problem. Often acquisition of lock requires different feedback parameters than maintaining lock. The output intensities must be rectified in the time averaging process, and the frequency of the dither places constraints on the lower frequency limit of the signal. Usually the signal must be placed on a high-frequency carrier, otherwise a long string of "0" or "1" bits will lead to loss of phase lock.

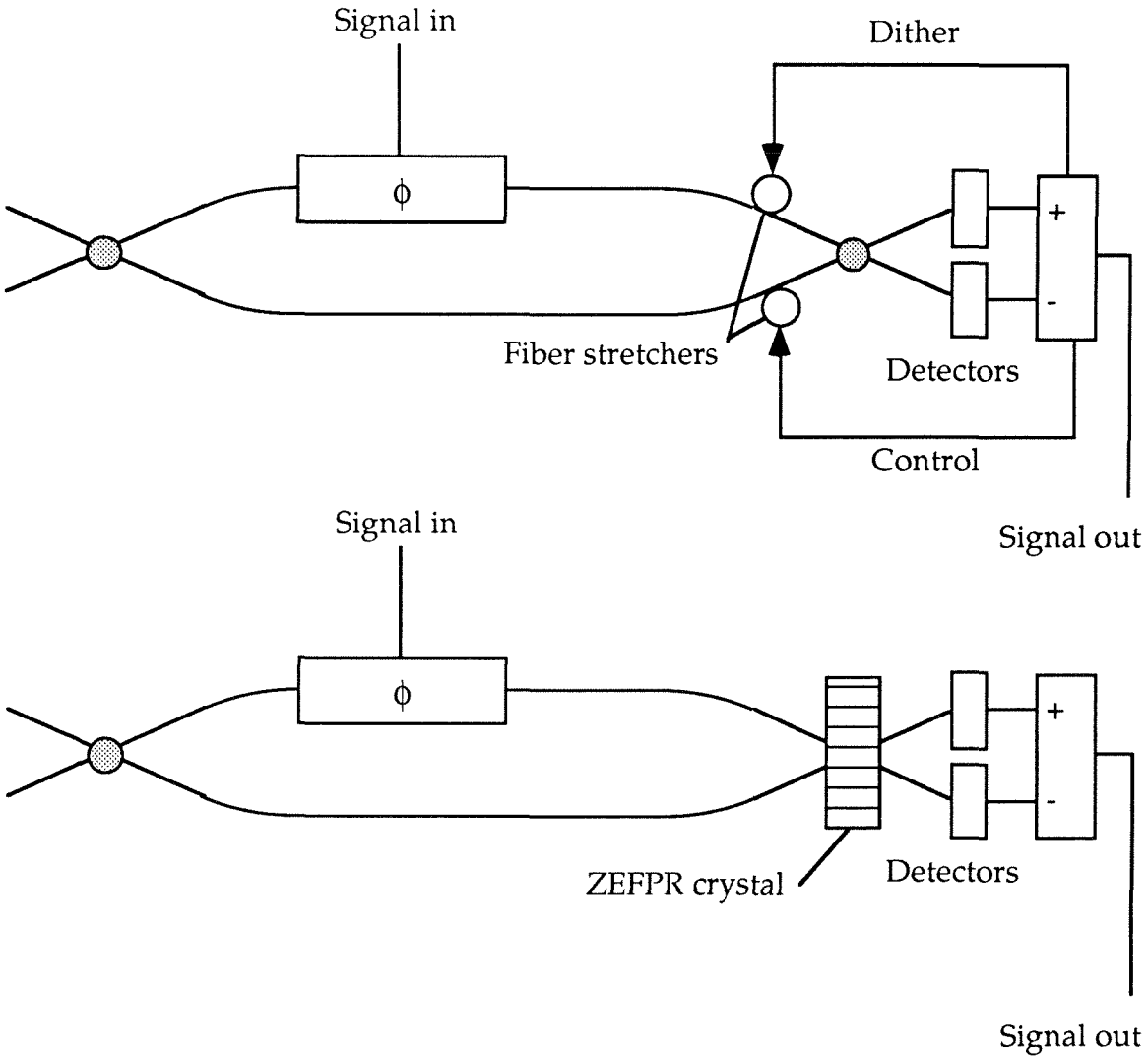

Figure 7-6a. A conventional high-speed fiber optic data link is illustrated in figure 7-6a. A laser is coupled into a fiber optic Mach-Zender interferometer. Data is impressed onto the signal beam with an electro-optic phase modulator. A second fiber coupler is used to complete the interferometer. Path length changes are corrected with a feedback device and fiber stretchers. **Figure 7-6b.** The second fiber coupler is replaced with a ZEFPR crystal. The dynamic zero-phase response of the crystal automatically tracks the path length changes eliminating the need for a feedback control system.

In figure 7-6b a schematic of a self-aligning fiber-optic interferometric data link is shown. The second fiber coupler of figure 7-6a is replaced by a ZEFPR crystal. The intensities transmitted through the crystal obey equations (7.2) or (7.3). These intensities are detected differentially and normalized to the intensity as before. Any variations in the lengths of the fibers will be dynamically compensated by the ZEFPR crystal as long as the rate of change of fiber length in units of wavelength is small compared to the grating rewrite time. For a 1km data link with the fibers cabled together, the averaged temperature difference between the two fibers is normally controllable to better than $0.1^{o}C$/hr. This rate will give a fringe velocity of approximately one wavelength in 10 seconds. For moderate intensities (10-100mW), a ZEFPR crystal can track this motion. In addition, the ZEFPR material has no upper limit to the path length mismatch it can accommodate; it is only limited by the laser coherence length. A fiber stretcher, by comparison is usually limited to 0.5% stretch. For certain applications, the ZEFPR interferometer would seem to be a drastically simpler solution than the conventional interferometer

7.3.2 Phase Image Subtraction and Phase to Intensity Conversion

This section describes how the characteristics of the ZEFPR gratings can be used to perform image subtraction and transform phase transparency images into intensity modulated images. As discussed above, two beams interfering in a ZEFPR material show linear intensity coupling with relative phase change between the beams. This concept can be extended to include many beams within the same crystal (one for each pixel of an image). If the individ-

ual pairs of beams are not overlapping within the volume of the crystal, they will not affect each other and the phase to intensity relationship will hold for each pair of beams individually. Figure 7-7 illustrates the setup.

The device in figure 7-7 has two input phase images, $T_1(x,y)$ **(28)** and $T_2(x,y)$ **(30)**. These images can be provided, for example, by a liquid crystal television with the polarizing sheets removed. Two beam splitters **(38)** and **(40)** provide outputs. The operation is as follows: Two input phase transparencies are imaged onto a ZEFPR crystal **(12)** in exactly counterpropagating geometry with lenses **(32)** and **(34)**. The focal depth of the lens configuration must be longer than the interaction region within the crystal. Because of the counterpropagating geometry of the setup, each imaged pixel from one transparency interacts only with one imaged pixel of the other transparency. Thus each pair of pixels can be considered independently. When one pixel's phase is changed, the output intensity of one pixel increases at the expense of the other. Thus the instantaneous output intensities are given qualitatively by $a(T_1(x,y)-T_2(x,y)) +C_1$ and $b(T_2(x,y)-T_1(x,y)) +C_2$ **(18)**, where a, b, C_1, and C_2 are determined by the specifics of the crystal and relative beam intensities. The device acts as a "novelty filter" because if the images remain fixed the outputs evolve back to zero as the hologram is rewritten.

The device can be used to calculate the derivative of an image. For example if $T_2(x,y)$ is the same image as $T_1(x,y)$ but spatially shifted, the subtraction performs a gradient operation. If $T_2(x,y)$ is the same image as $T_1(x,y)$ but delayed in time, the time derivative is calculated. One application for novelty filters which is often bandied about but never implemented is quality control

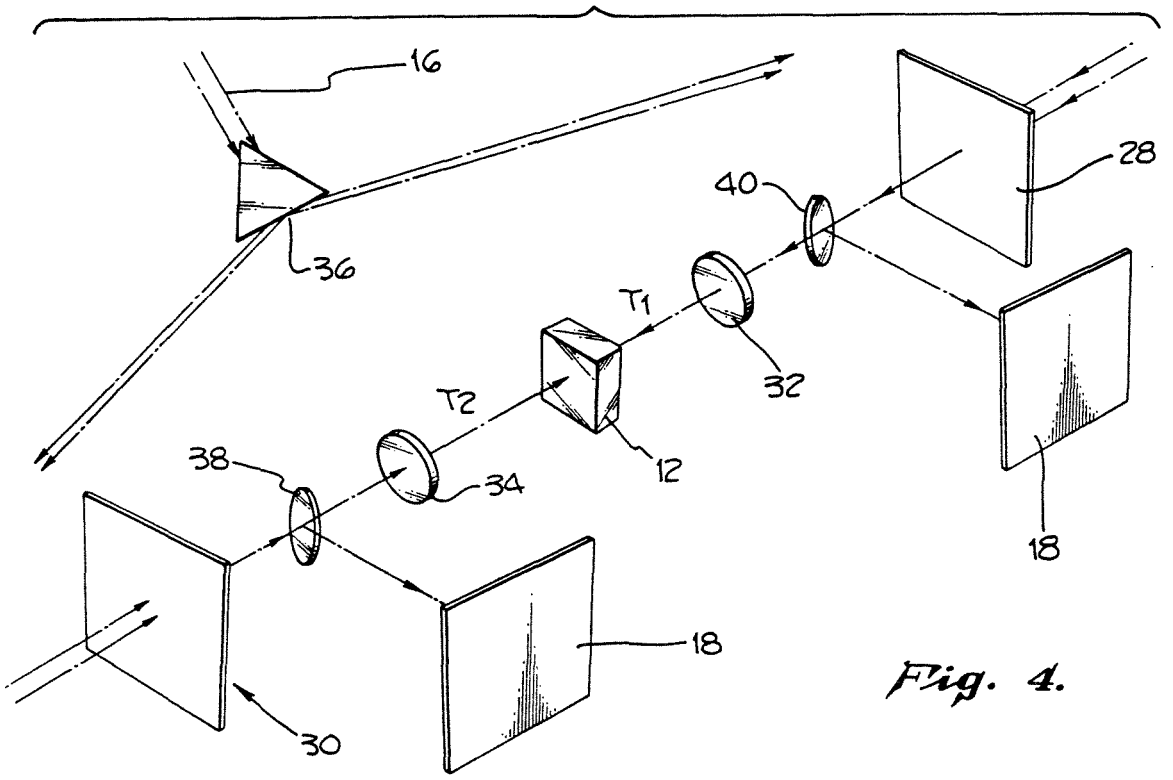

Fig. 4.

Figure 7-7. A schematic of a ZEFPR crystal based phase image subtracter and novelty filter. Images $T_1(x,y)$ **(28)** and $T_2(x,y)$ **(30)** are imaged on the ZEFPR crystal with lenses **(32)** and **(34)**. in exactly counterpropagating geometry, so that each pixel from T_1 interferes with only one pixel of T_2. The beam coupling between each pair of pixels is governed by the relative phase between them. Outputs **(18)** are picked off with beamsplitters **(38)** and **(40)**. The device act as a novelty filter because the gratings in the material evolve back to the zero-phase condition if the images are stationary.

for complicated manufactured parts. For example, a photographic image of a semiconductor die ($T_1(x,y)$) can be compared to a reference image for the same part ($T_2(x,y)$). Any discrepancies between the two images will stand out as a bright spot in the output. The subtraction operation can also be used to calculate the difference of the images in the Fourier plane.

7.4 Summary

The ZEFPR effect is unique in that the phase between the index grating and the intensity grating is identically zero. This quality cannot easily be achieved with an electro-optic grating. The applications of this effect arise naturally from the linear phase to intensity transduction of beams interfering in the ZEFPR material.

The use of a crystal of paraelectric KLTN as a microphone and vibration sensor was established. The device is expected to have practical applications. The use of a ZEFPR crystal in a self-aligning data link and in an image subtracting "novelty filter" was discussed. The latter two applications have not been demonstrated experimentally.

References for chapter seven

[1] W. J. Bock R. Wisniewski, T. R. Wolinski, "Fiberoptic strain-gauge manometer up to 100MPa," IEEE-Instru **41**, 72-76 (1992).

[2] R. I. Macdonald and R Nychka "Differential measurement technique for optical fiber sensors," Electr. Lett. **27**, 2194-2196 (1991).

[3] P. Y. Chien and C. L. Pan, "An active fiberoptic interferometric sensor based on a low finesse fiberoptic Fabry-Perot," J. Mod. Opt. **38**, 1891-1900 (1991).

[4] W. A. Gambling, "Optical fibers for sensors," Sens. Actu. A. **25**, 191 -196 (1991).

[5] D. Garthe, "A fiberoptic microphone," Sens. Actu. A, **26**, 341-345 (1991).

[6] D. Garthe, "A purely optical microphone," Acustica **73**, 72 -89 (1991).

[7] I. Rossomakhin and S. Stepanov, "Linear adaptive interferometers via diffusion recording in cubic photorefractive crystals," Opt. Comm. **86**, 199-204 (1991).

[8] J. W. S. Rayleigh, *The Theory of Sound* , Vol I chapter 9, Dover, New York (1945).

[9] B. A. Auld, *Acoustic Fields and Waves in Solids* , Vol I chapter 6, Wiley Interscience, New York, New York (1973).

[10] I. Malecki, *Physical foundations of technical acoustics* , Pergamon Press, Oxford (1969).

[11] J. Boyk, California Institute of Technology, Pasadena, California, private communication (1992).

Chapter Eight

Determination of Photorefractive Phase and Coupling Constant

8.1 Introduction

It is clear from the analysis of the photorefractive effect in chapter two that the most important parameters in describing the photorefractive coupling are the photorefractive phase ϕ and and the coupling constant g. In fact, if one ignores the ill-quantifiable effect of fanout, these two material parameters, in addition to the optical absorption coefficient, are the only ones needed to calculate the interaction of two or more coherent beams in a photorefractive material in the steady state. This conclusion follows directly from the coupled mode equations. In light of this it is surprising that the exact determination of these parameters has received little attention to date. One exact treatment, the 1975 paper by Vahey[1] follows a similar analysis to the one described in this chapter. Unfortunately, Vahey's paper is of limited usefulness since he assumed an intensity dependent term describing the index change in the coupled equations. Vahey's paper predated the intensity independent Kukhtarev model[2] of the photorefractive effect which is now the accepted formulation. In another paper, Kondilenko et al.[3] present a theory to evaluate the phases of fixed holographic gratings. Since that time, all pub-

lished reports have been content to describe approximate methods of phase and coupling constant determination[4-8]. The general trend has been to assume beam coupling in which one beam (the "signal beam") is much weaker than the other. In some cases even this approximation is treated incorrectly[7,8] (see section 8.8). Here an exact solution of the coupled equations is reported describing the evolution of two arbitrary beams incident at the Bragg angle on a dynamically written photorefractive grating. The incident beams need not possess the same phase nor the same intensity as the beams which wrote the grating. In this analysis, all the beams are of the same frequency, but the treatment could easily be extended to beams not of the same frequency (see chapter nine) if a reason for such an extension arose.

Two coherent beams are symmetrically incident on a photorefractive crystal. They induce a spatially periodic space charge field E_{sc} which is phase shifted with respect to the intensity interference pattern by the photorefractive phase ϕ. A dynamically written refractive index grating is the result. The writing beams are then replaced with two beams of arbitrary intensity and phase and of the same frequency, incident along the same directions as the initial beams, i.e., at the Bragg angles. We calculate the instantaneous beam coupling experienced by these new beams off the dynamically written grating which for the short initial period, is considered fixed. The time dependent formation of dynamic gratings written by the new beams is ignored. This condition is only valid for a time period on the order of a second, depending on the intensity, but this is much longer than is required to obtain the necessary data. If the new beams continued to illuminate the crystal for a longer

time period, they would first generate secondary gratings caused by diffraction off the original grating[9,10], and eventually they would completely erase the original grating, replacing it with a new grating.

8 . 2 Formulation of the Problem

The starting point is calculation of the two beam coupling of two incident copropagating beams with amplitudes A(z) and B(z) in a photorefractive material (Figure 8-1) as in chapter two. The well known coupled beam equations follow from (2.35a,b)

$$A'(z)\cos\beta = i\,g\,e^{i\phi}\frac{|B(z)|^2}{I(z)}A(z) - \frac{\alpha}{2}A(z) \tag{8.1a}$$

$$B'(z)\cos\beta = i\,g\,e^{-i\phi}\frac{|A(z)|^2}{I(z)}B(z) - \frac{\alpha}{2}B(z) \tag{8.1b}$$

where λ is the wavelength of the interfering beams, α the optical absorption coefficient, and β the half-angle of beam intersection inside the material. The definitions $g = \pi n_1/\lambda$ and $I(z)$ as sum of the intensities $I(z) = |A(z)|^2 + |B(z)|^2$ are employed as usual. Here ϕ is the photorefractive phase between the optical intensity grating and the induced index grating; $K = 2k\sin\beta$ is the nominal grating wavevector with $k = 2\pi n_o/\lambda$. In obtaining (8.1) the coupled equations of chapter two are used with

$$n(z) = n_0 + \frac{1}{2}\left(\Delta n(z)e^{i\phi}e^{i\,K\,z} + c.c.\right) \tag{8.2}$$

where Δn is formed dynamically by the writing beams:

$$\Delta n(z) = n_1 A(z)\ B^*(z)/I(z) \tag{8.3}$$

where I(z) is the total intensity, and n_1 is the peak-to-peak amplitude of the index grating when A(z) = B(z).

$$I_1(z) = e^{-\alpha L}\ \frac{I_2\,(I_1 + I_2)}{I_1 + I_2\, e^{+\Gamma z}} \tag{8.4a}$$

$$I_2(z) = e^{-\alpha L}\ \frac{I_1\,(I_1 + I_2)}{I_1\, e^{-\Gamma z} + I_2} \tag{8.4b}$$

where $A(z) = [I_1(z)]^{1/2}\exp[i\zeta_1]$ and $B(z) = [I_2(z)]^{1/2}\exp[i\zeta_2]$, and $\Gamma = 2g\sin\phi$ is the power coupling coefficient. The variable z is, for convenience, taken to be the unit of length in the propagation direction. L is the effective thickness of the crystal: $L = d/\cos\beta$. We have defined $I_1 = I_1(0)$ and $I_2 = I_2(0)$. The phases of the two beams are given by (see chapter two)

$$\zeta_1(z) = \frac{1}{2}\cot\phi\ \ln[I_1 + I_2\, e^{+\Gamma z}] \tag{8.5a}$$

$$\zeta_2(z) = -g\cos\phi\ z - \frac{1}{2}\cot\phi\ \ln[I_1 + I_2\, e^{+\Gamma z}]. \tag{8.5b}$$

The index grating in the material follows from equations (8.3), (8.4), (8.5), and the definition of A(z) and B(z) in terms of phase and intensity. It is given by the surprisingly simple form

$$\Delta n(z) = n_1 \sqrt{I_1\, I_2}\ \left(I_1\, e^{-\Gamma z/2} + I_2\, e^{+\Gamma z/2}\right)^{i\,\cot\phi\ -\ 1}. \tag{8.6}$$

Thus we have used the coupled mode equations to solve self consistently for the amplitudes and phases of two dynamically coupled beams in a photorefractive material. Dynamically coupled beams are those which yield

an index grating given by (8.3). The solution for Δn (or A(z) and B(z)) given above can be reinserted into equations (2.35) (or equation (8.1)) to verify that the solution is self-consistent, as advertised.

The next step on the way to calculating the coupling constant and phase is to solve for the beam coupling of two arbitrary intensity and phase beams incident at the Bragg angle off the grating given by (8.6). When the new beams are the same intensities as the old ones but with different phases it is equivalent to simply phase shifting one of the original beams. When, instead, the phases of the new beams are unchanged with respect to the original beams but the intensity of one new beam is reduced to zero, we are calculating the diffraction off the grating. The general case when both the phases and/ or the intensities are different in the new beams yields the response of the holographically coupled beams to fluctuations in the interferometer system. This last point would be of importance in calculating how phase and intensity fluctuations at the input of a photorefractive interferometer are magnified in the outputs. The solutions for all these problems are developed in this chapter, however we are only concerned with the application of the solutions to the determination of the photorefractive phase and coupling constant.

8.3 Solution of Beam Coupling

We calculate the beam coupling of a new set of Bragg matched beams $T(0) = [P_1]^{1/2}\exp[i\psi_1]$ and $V(0) = [P_2]^{1/2}\exp[i\psi_2]$ off the index grating of equation (8.6). In analogy to equations (8.1a,b) and (2.35a,b), the coupled mode equations are written

$$T'(z)\cos\beta = i g \sqrt{I_1 I_2}\, e^{+i(\phi+\theta)} \times \left(I_1 e^{-\Gamma z/2} + I_2 e^{+\Gamma z/2}\right)^{+i\cot\phi - 1} V(z) - \frac{\alpha}{2} T(z) \tag{8.7a}$$

$$V'(z)\cos\beta = i g \sqrt{I_1 I_2}\, e^{-i(\phi+\theta)} \times \left(I_1 e^{-\Gamma z/2} + I_2 e^{+\Gamma z/2}\right)^{-i\cot\phi - 1} T(z) - \frac{\alpha}{2} V(z) \tag{8.7b}$$

where I_1 and I_2 are the intensities of the writing beams, not to be confused with the new intensities P_1 and P_2. The phase $\theta = \zeta_1(0) - \zeta_2(0) - \psi_1(0) + \psi_2(0)$ is the phase difference between the intensity pattern of the beams which wrote the grating and the intensity pattern formed by T(z) and V(z). If $\theta = 0$ and $P_i = I_i$ for $i = 1,2$, it is easy to see how (8.7) reduces to (8.1). Since the photorefractive effect is intensity independent, it is also true that if $\theta = 0$ and $P_i = c\, I_i$ for $i = 1,2$ where c is an arbitrary constant, the solutions are essentially unchanged except that all intensities are scaled by the constant factor c. Equations (8.7a,b) ignore the new dynamic grating which is written by beams T(z) and V(z) in the case $\theta \neq 0$. In addition, as intimated in the introduction to this chapter, if the new beams are allowed to continue illuminating the crystal, they will eventually overwrite the existing grating with a new one given by

$$\Delta n(z) = n_1 T(z)\, V^*(z)/P(z) \tag{8.8}$$

where T(z) and V(z) are different beams than the original A(z) and B(z) although both sets of beams propagate along the same directions. It is clear now that this new grating will have the identical form of equation (8.6) with the change $I_i \rightarrow P_i$. The new grating would also be shifted in phase by an

amount θ. In the experiments which follow, however, the data will be collected immediately after introducing the new beams T and V. Therefore the beams will have no chance to alter the existing grating and we are justified in applying equations (8.7).

The solution of (8.7) is outlined in detail in chapter 9. After a whole bunch of work the solutions are reduced to the following form

$$T(z)\, e^{\alpha L/2} = C_1 \left(I_2 + I_1\, e^{-\Gamma z}\right)^{+i\eta\, -\, 1/2} + C_2 \left(I_2\, e^{+\Gamma z} + I_1\right)^{+i\eta\, -\, 1/2} \qquad (8.9a)$$

$$V(z)\, e^{\alpha L/2} = C_3 \left(I_2 + I_1\, e^{-\Gamma z}\right)^{-i\eta\, -\, 1/2} + C_4 \left(I_2\, e^{+\Gamma z} + I_1\right)^{-i\eta\, -\, 1/2} \qquad (8.9b)$$

where $\eta = \cot\phi/2$, and C_j are constants which are determined by the coupled equations and the boundary conditions.

Equations (8.9) are the solutions for beam coupling off a dynamically written grating; it only remains to determine the coefficients C_j for particular special cases. In this way, methods for determining the coupling constant and phase will be established.

8.3.1 Harmonics Method

We solve the coefficients C_j for the special case where one or two of the reading beams are phase shifted relative to the recording beams but their intensities are unchanged. This can be accomplished in practice by merely inserting a phase shift in the path of one of the recording beams. From equations (8.5a,b) and the definition of θ in equations (8.7a,b) we use the boundary conditions $T(0) = I_1^{1/2}\,[I_1 + I_2]^{i\eta}$ and $V(0) = I_2^{1/2}\,[I_1 + I_2]^{-i\eta}$. It should be

stressed again that the term $[I_1 + I_2]$ raised to $\pm i\eta$ is purely a phasor which is required to ensure that the index grating have the proper form. With simple differentiation and insertion into the coupled equations (8.1) we determine the coefficients as

$$C_1 = \sqrt{I_1/(I_1+I_2)}\; I_2 \left(1 - e^{i\theta}\right) \tag{8.10a}$$

$$C_2 = \sqrt{I_1/(I_1+I_2)}\; \left(I_1 + I_2\, e^{i\theta}\right) \tag{8.10b}$$

$$C_3 = \sqrt{I_2/(I_1+I_2)}\; \left(I_2 + e^{-i\theta}\, I_1\right) \tag{8.10c}$$

$$C_4 = \sqrt{I_2/(I_1+I_2)}\; I_1 \left(1 - e^{-i\theta}\right). \tag{8.10d}$$

The combination of equations (8.9) and (8.10) completely determines the output amplitudes A(L) and B(L). The intensities are given by

$$P_1(z) = e^{-\alpha z} \frac{I_1}{I_1+I_2} \frac{1}{I_2\, e^{+\Gamma z} + I_1} \quad x$$

$$\left[2I_2^2\, e^{+\Gamma z} (1 - \cos\theta) + \left(I_1^2 + I_2^2 + 2I_1I_2\cos\theta\right) + 2\, I_2\, e^{+\Gamma z/2} \quad x \right.$$

$$\left. \left\{ (I_1 - I_2)\left((1-\cos\theta)\cos[gz\cos\phi]\right) - (I_1 + I_2)\sin\theta\, \sin[g\cos\phi\, z] \right\} \right] \tag{8.11a}$$

$$P_2(z) = e^{-\alpha z} \frac{I_2}{I_1+I_2} \frac{1}{I_1\, e^{-\Gamma z} + I_2} \quad x$$

$$\left[2I_1^2\, e^{-\Gamma z} (1 - \cos\theta) + \left(I_1^2 + I_2^2 + 2I_1I_2\cos\theta\right) + 2\, I_1\, e^{-\Gamma z/2} \quad x \right.$$

$$\left. \left\{ (I_2 - I_1)\left((1-\cos\theta)\cos[gz\cos\phi]\right) + (I_1 + I_2)\sin\theta\, \sin[g\cos\phi\, z] \right\} \right]. \tag{8.11b}$$

When $I_1 = I_2 = I$ the transmitted intensities reduce to a simple form given by

$$P_1(z)/I = e^{-\alpha z}\left(1 - \tanh[\Gamma z/2]\cos\theta - \frac{\sin(g\cos\phi\, z)}{\cosh[\Gamma z/2]}\sin\theta\right) \tag{8.12a}$$

$$P_2(z)/I = e^{-\alpha z}\left(1 + \tanh[\Gamma z/2]\cos\theta + \frac{\sin(g\cos\phi\, z)}{\cosh[\Gamma z/2]}\sin\theta\right). \tag{8.12b}$$

The approximate solutions for the case $I_2 << I_1$ also follow readily from equations (8.11) with

$$P_1(z) = e^{-\alpha z} I_1 \tag{8.13a}$$

$$P_2(z) = e^{-\alpha z}\left[\begin{array}{l} I_2 e^{\Gamma z} + 2 I_2 e^{\Gamma z/2}\sin\theta \sin[g\cos\phi\, z] \\ + 2 I_2 (1 - \cos\theta)(1 - e^{\Gamma z/2}\cos[gz\cos\phi])\end{array}\right]. \tag{8.13b}$$

We consider the effects of phase shifting one of the interfering beams by an amount θ using a piezoelectrically driven mirror. The experimental configuration is as in figure 8-1. When the mirror is driven sinusoidally we have $\theta(t) = \theta_0 \sin(\omega t)$. If $\omega >> 1/\tau$, where τ is the writing time of the grating, and $\theta_0 << \pi/2$, and $I_1 = I_2$ then inspection of (8.12) shows that the optical powers of the transmitted beams at DC, ω, and 2ω frequencies are related by

$$\left|\frac{P_{DC}}{P_{2\omega}}\right| = \frac{4}{\theta_0^2}(\coth[g\sin\phi\, z] \pm 1) \tag{8.14a}$$

$$\left|\frac{P_{\omega}}{P_{2\omega}}\right| = \frac{4}{\theta_0}\frac{\sin[g\cos\phi\, z]}{\sinh[g\sin\phi\, z]} \tag{8.14b}$$

where we have used the Taylor expansions for the sin and cos functions. The powers in (8.14) are taken to be peak-to-peak values, so that P_{DC} is actually twice the power of the beam coupling. This convention is used to comply with that of many spectrum analyzers. The "+" in equation (8.14a) refers to

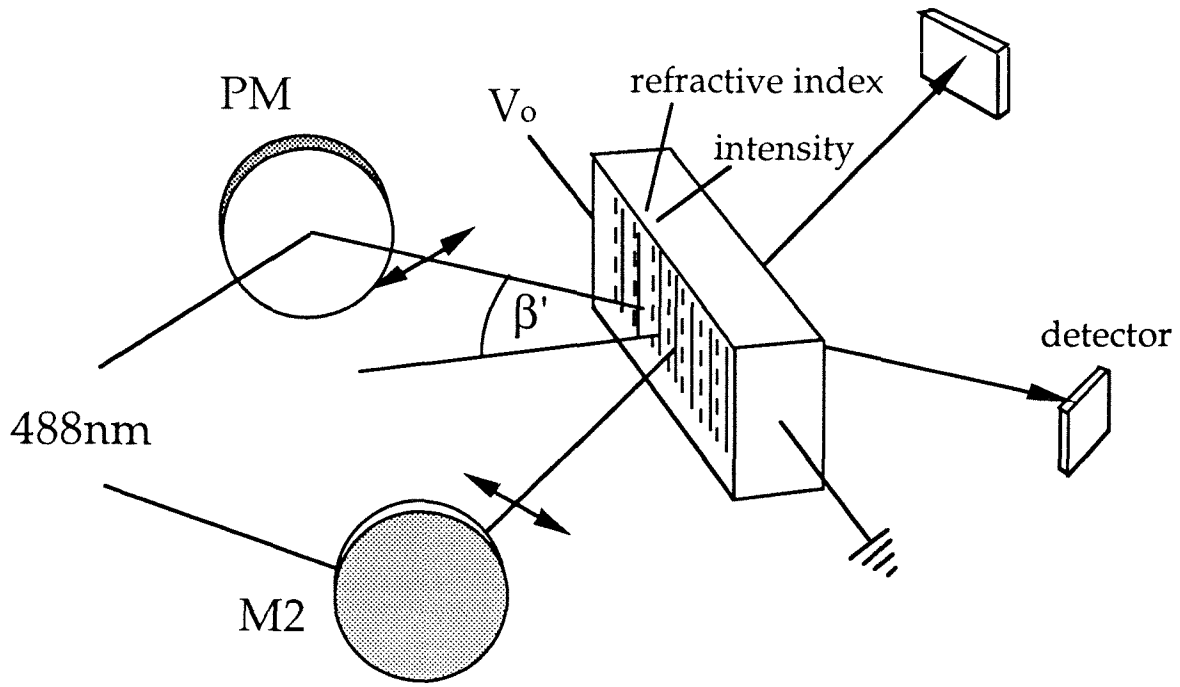

Figure 8-1. The setup for determining the photorefractive phase ϕ via beam coupling and diffraction measurements. Two beams incident on a photorefractive material write an index grating spatially shifted by a phase ϕ from the intensity pattern. A voltage applied to the piezoelectric mirror **(PM)** phase modulates one of the incident beams, shifting the position of the intensity pattern. The response of the beam coupling to this phase shift can be used to determine the photorefractive phase.

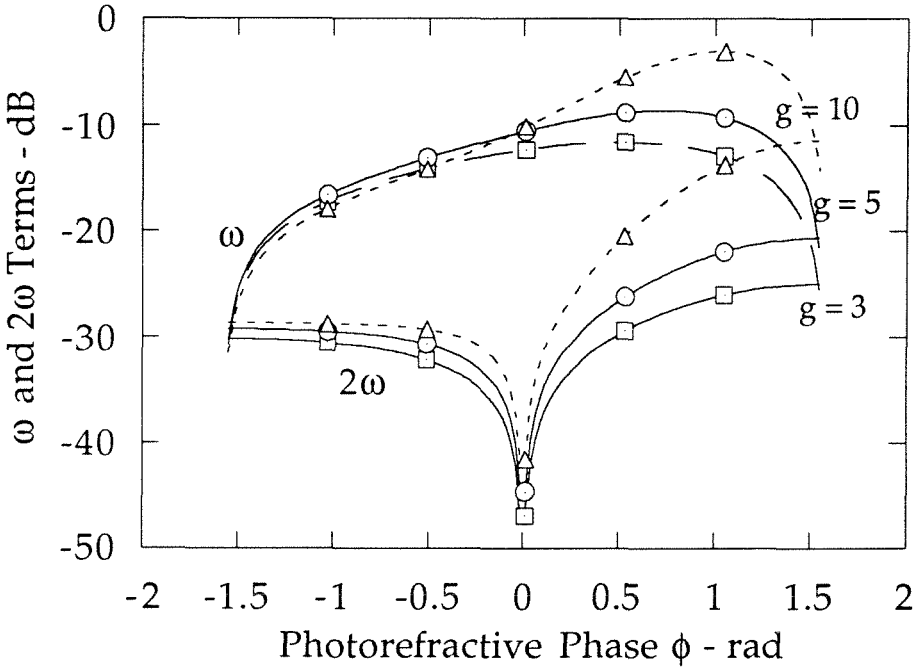

Figure 8-2. The intensity $I_1(L)$ of figure 8-1 at frequencies ω and 2ω relative to the DC power (= 0 dB) when one of two interfering beams is phase modulated at ω, as a function of the photorefractive phase ϕ. The results are plotted for various coupling constants: gL = 3, 5, 10. For positive values of ϕ, $I_1(L)$ is deamplified so the ω and 2ω terms are relatively large compared to the DC term; for $\phi < 0$ the reverse is true.

the beam which is amplified, and the "-" to the beam which is attenuated. Figure 8-2 illustrates the relative powers of the DC, ω, and 2ω. Inspection of (8.14) reveals that they are equations with independent variables $g\cos\phi$ and $g\sin\phi$. As mentioned earlier, g and ϕ never appear individually as parameters in experimental measurables. Two equations in two variables have been obtained. Thus g and ϕ can be determined from (8.14).

To recap, we write a grating in a photorefractive material. One of the writing beams is phase modulated with a small amplitude, high frequency, sinusoidal modulation. The intensity of either of the transmitted beams is detected and spectrally separated into a DC component and components oscillating at ω and 2ω. The relative powers at these frequencies are used in (8.14) to obtain the coupling constant and photorefractive phase. This procedure has been attempted before for the case $I_2 << I_1$[5] but has not been treated for the general case. The results presented above reduce to simpler expressions (after some work) when the phase $\phi = 0, \pi/2$, and are given in chapter seven equations (7.2) and (7.5) or in Ref. 11.

8.3.2 Beam Coupling/ Diffraction Method

Another method of determining g and ϕ follows from an examination of the photorefractive beam coupling and the diffraction off a dynamic grating. The formula for beam coupling is well known (8.4). But this only yields the value of $g\sin\phi$. In order to determine $g\cos\phi$ we need to consider diffraction of a single incident beam off the grating. Here, we take B(0) = 0 and A(0)

as before. In this case we follow the same steps as leading to (8.10) to obtain,

$$C_1 = \sqrt{I_1/(I_1+I_2)}\ I_2 \tag{8.15a}$$

$$C_2 = \sqrt{I_1/(I_1+I_2)}\ I_1 \tag{8.15b}$$

$$C_3 = \sqrt{I_2/(I_1+I_2)}\ I_1 \ = -C_4. \tag{8.15c,d}$$

Equations (8.9) and (8.15) are combined to yield the transmitted and diffracted intensities

$$I_1(z) = e^{-\alpha z}\ \frac{I_1}{I_1 + I_2}\ \frac{\left[I_2^2\, e^{\Gamma z} + I_1^2 + 2\, I_1\, I_2\, e^{\Gamma z/2} \cos[\, g \cos\phi\, z]\right]}{I_1 + I_2\, e^{\Gamma z}} \tag{8.16a}$$

$$I_2(z) = e^{-\alpha z}\ \frac{I_1^2\, I_2}{I_1 + I_2}\ \frac{\left[e^{\Gamma z} + 1 - 2\, e^{\Gamma z/2} \cos[\, g \cos\phi\, z]\right]}{I_1 + I_2\, e^{\Gamma z}}. \tag{8.16b}$$

Again, for the condition $I_1=I_2$ the transmitted and diffracted intensities reduce to a simple form

$$P_1(z)\, e^{\alpha z} = \frac{I_1}{2}\left(1+ \cos(g \cos\phi\, z)/\cosh(g \sin\phi\, z)\right) \tag{8.17a}$$

$$P_2(z)\, e^{\alpha z} = \frac{I_1}{2}\left(1- \cos(g \cos\phi\, z)/\cosh(g \sin\phi\, z)\right). \tag{8.17b}$$

Equations (8.17) give an expression functionally dependent on both $g \sin\phi$ and $g \cos\phi$. But $g \sin\phi$ can be determined directly from the expression for beam coupling (8.4). In this way, (8.4) and (8.17) can be used to determine g and ϕ in the material.

8.3.3 Phase Ramping Method

Returning to the harmonics method of section 8.3.1, if one beam is

shifted linearly in phase instead of sinusoidally, information about g and ϕ can be obtained from the beam coupling. When one beam is shifted through π radians, the phase positions during the ramp corresponding to the minimum and maximum of the transmitted intensities can be used to determine g and ϕ. In particular, the maximum of $P_2(z)$ from equation (8.12b) occurs at

$$\theta_{max} = \tan^{-1}\left(\frac{\sin[g\cos\phi\, z]}{\sinh[g\sin\phi\, z]}\right). \tag{8.18}$$

The harmonics method and the beam coupling/diffraction method constitute two independent methods of measuring g and ϕ in a photorefractive material. Equation (8.18) is a third method which cannot independently determine both g and ϕ, but can be used to verify the results obtained with the previous two methods. The experimental use of these methods is described in section 8.5.

8.4 Photorefractive Coupling and Phase in Paraelectric Materials

In this section a theory is developed to describe the photorefractive parameters of paraelectric KLTN under an applied electric field. The photorefractive response of paraelectric KLTN is described by the quadratic electro-optic effect in conjunction with the Zero Electric Field Photorefractive (ZEFPR) effect[12]. The ZEFPR gratings are unique[13] in that they are always $\pi/2$ out of phase with the electro-optic induced index grating (see chapter six). In addition, the ZEFPR index grating is proportional to the space charge field. Thus we can write $\Delta n(z) = \Delta n_{EO} + \Delta n_{Zf}(z)$ which has the contribution from

both the conventional electro-optic grating as well as the ZEFPR grating.

$$\Delta n(z) = E_{sc}(\gamma E_0 \cos(Kz + \phi_E) + \gamma_{Zf} \sin(Kz + \phi_E))$$
$$= E_{sc}\sqrt{(\gamma E_0)^2 + \gamma_{Zf}^2}\sin(Kz + \phi_E + \alpha). \qquad (8.19)$$

Here E_o is the applied uniform electric field and E_{sc} is the photorefractive space charge field. γ is the effective linear electro-optic coefficient induced by the presence of the applied field. It is given by (chapter three) $\gamma = -n_o^3 g(\varepsilon\varepsilon_o)^2$, where n_o is the refractive index, g is the relevant quadratic electro-optic coefficient and $\varepsilon\varepsilon_o$ is the dielectric constant. γ_{Zf} is a coefficient which relates the index grating due to the ZEFPR effect with the magnitude of the space charge field which inevitably forms in conjunction with the ZEFPR grating. It is experimentally determined by the diffraction observed with zero applied field. Finally ϕ_E is the phase between the intensity and electro-optic gratings as dictated by the Kukhtarev solutions of the band transport model in chapter two. We have

$$\phi_E = \tan^{-1}\left(\frac{E_0^2 + E_d^2 + E_d E_N}{E_0\, E_N}\right) \qquad (8.20)$$

where E_d and E_N are the photorefractive diffusion and maximum charge fields. The addition of the ZEFPR grating modifies the net phase of the grating by $\alpha = \tan^{-1}(\gamma E_o/\gamma_{Zf})$, so that the net photorefractive phase $\phi = \phi_E + \alpha$ is not equal to the phase between the intensity and the electro-optic grating. Finally, the coupling constant is given by $g = \pi\,[(\gamma E_o)^2 + \gamma_{Zf}^2]^{1/2} E_{sc,o}/\lambda$. Here $E_{sc,o}$ is the space charge field for unity modulation depth. The applied field

dependence of the space charge field is given by[14]

$$E_{sc} = 2\frac{\sqrt{I_1 I_2}}{I}\frac{E_N(E_0 + iE_d)}{E_N + E_d - iE_0}. \tag{8.21}$$

Therefore, with an applied field, a paraelectric photorefractive material such as KLTN should exhibit beam coupling characterized by a net photorefractive phase $\phi = \phi_E + \alpha$ and a coupling constant described by (8.21) and the value for g given above. The following section provides experimental results which corroborate this theory.

8.5 Experimental Results

The methods described above were used to experimentally determine g and ϕ for an iron doped lithium niobate crystal, an iron doped barium titanate, and a paraelectric potassium lithium tantalate (KLTN) crystal doped with copper. We note that the use of independent methods (the harmonics method and beam coupling/diffraction method) was instrumental in obtaining accurate data. Before the experimental setup was sufficiently isolated from air currents and vibration, each method yielded different results which, however, were remarkably consistent among themselves. This would indicate that any experiment which used only one method to determine the photorefractive parameters and which relied on consistency of data to ascertain the reliability of the measurement, would consistently and radically underestimate the error. The experimental setup is illustrated in figure 8-1. All the experiments were performed at room temperature. The crystal dimensions were 3.82 x 5.49 x 2.34 mm^3 for the KLTN, 5.0 x 5.0 x 2.20 mm^3 for the $LiNbO_3$,

and 5.0 x 5.0 x 5.23 mm^3 for the $BaTiO_3$, where the last dimension is the thickness of the sample. The KLTN was grown and prepared as described in chapter four. The laser beams were at 488nm with polarization in the plane of their intersection (extraordinarily polarized). The c-axis of the samples was perpendicular to the bisector of the light beams and in the plane of polarization. For the experimental geometry used, the grating wavevector was K = $1.7x10^7$/m. The sinusoidal phase modulation was performed with θ_o = 0.0613rad at 10.6kHz. The phase was not modulated during writing of the grating, although the effect of concurrent modulation and writing was almost negligible. When the phase was ramped through π radians to determine the phase positions of the intensity extrema, a similar procedure was used. Data was taken using a Stanford Research SR760 spectrum analyzer and an HP7090A x-y plotter. The results for the samples tested are shown in table 8-1. The lithium niobate had ϕ = 0.41 so that, despite a coupling constant of g = 13.3/cm, it showed fairly weak beam coupling. For the barium titanate the phase was much closer to $\pi/2$ as is expected for a material with a weak photovoltaic effect. Paraelectric KLTN is forbidden from having a conventional photorefractive response without an applied field, hence it only displays the ZEFPR effect in this case[13]. As predicted in chapter six, the ZEFPR gratings show ϕ = 0 to within the accuracy of the experiment.

The photorefractive parameters of the paraelectric KLTN were determined as a function of applied electric field. The data were taken in the manner described above and the results compared to the theory of the previous

Material	g/cm			ϕ - rad		
	1	2	Best Fit	1	2	Best Fit
$LiNbO_3$	12.75	13.67	13.3	0.40	0.42	0.41
$BaTiO_3$	2.25	2.33	2.30	1.5	1.46	1.47
KLTN	2.41	2.45	2.43	0.0	0.00	0.00
KLTN(2.2kV/cm)	7.18	7.0	7.1	1.28	1.00	1.1

Table 8-1. Values of the coupling constant g and the photorefractive phase ϕ for the crystal samples tested. Column **1** is data from the beam coupling/diffraction method, column **2** is from the harmonics method, and column 3 is the best fit to data. The KLTN is paraelectric so its photorefractive response in the absence of an applied field is due to formation of zero phase ($\phi = 0$) ZEFPR gratings. When a 2200V/cm field is applied (last row), the electro-optic gratings dominate, and the phase is far from zero.

section.

The sample used had composition $K_{0.99}Li_{0.01}Ta_{0.71}Nb_{0.29}O_3:Cu_{0.004}$. The acceptor concentration was determined with absorption data and grating spacing dependence of the space charge field to be $N_A = 1.5x10^{24}m^{-3}$. Capacitive dielectric measurements yielded $\varepsilon = 12000$ at 24°C (the temperature of the experiment). The crystal was paraelectric above its phase transition at 15°C.

Experimental results and theoretical curves are shown in figures 8-3a and 8-3b. There is good agreement between the experimentally determined values for g and ϕ versus applied field with the theory described above.

8.6 Discussion of Results

As noted earlier in this chapter, the solutions of beam coupling and diffraction off dynamically written holograms are generally considered in the nondepleted pump approximation where one beam is much weaker than the other. This requirement may be undesirable because the photorefractive effect may be weak and difficult to observe in this limit. The reason this restriction is often acceptable is that in materials such as $LiNbO_3$ and $BaTiO_3$ fanout is such a problem that it dictates the use of the crystal in the weak signal limit. Since the KLTN family of materials does not exhibit fanout without an applied electric field (and only weak fanout with an applied field) there is no reason to use the weak signal limit.

Second, having solved the equations in the general case, it is easily de-

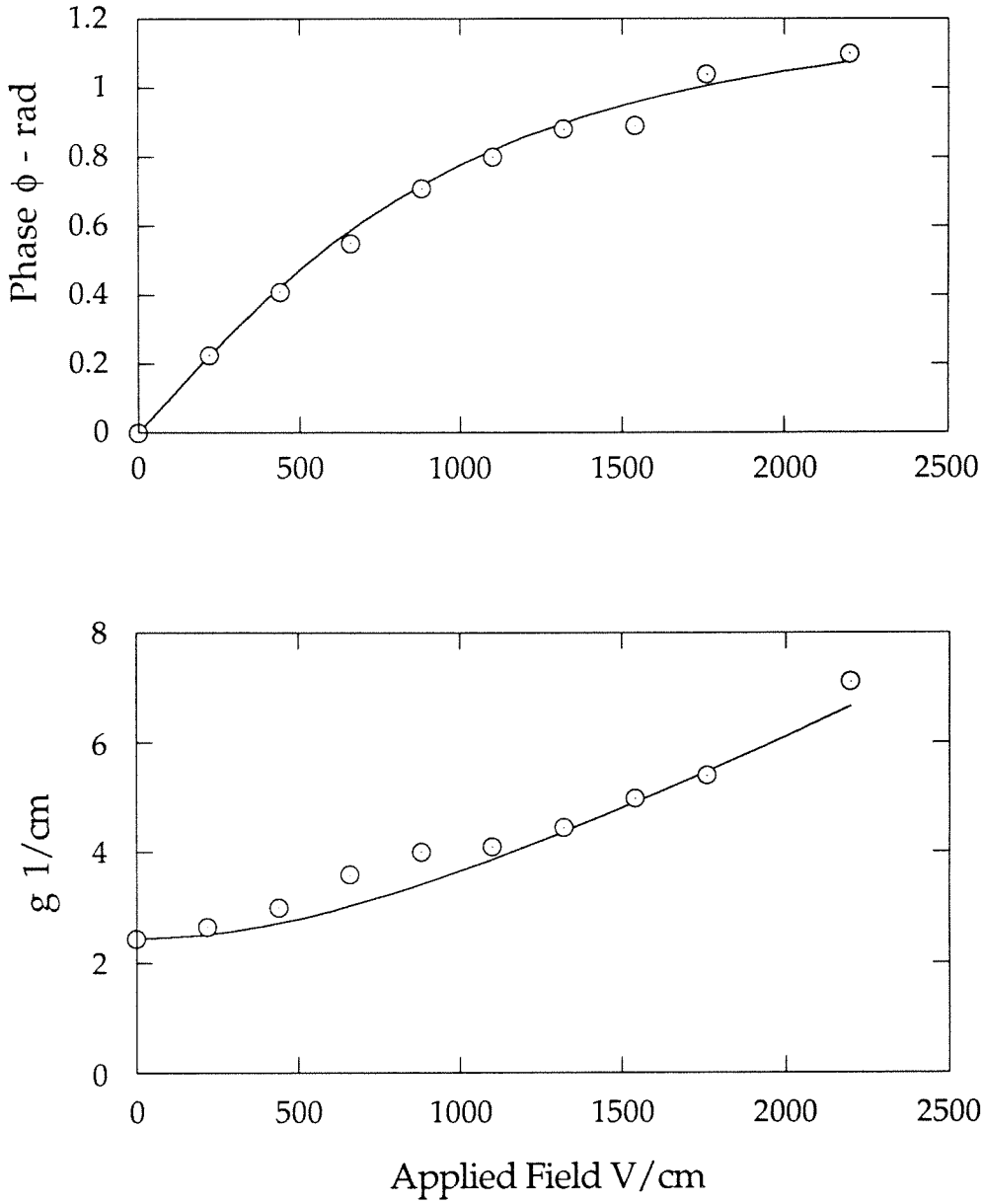

Figure 8-3a. The photorefractive phase of gratings written in KLTN versus applied electric field. Solid line is the theoretical curve describing the interaction between a ZEFPR- and an electro-optic grating. **8-3b.** The coupling constant g of KLTN versus applied field. Again, the data are in accord with the theory (solid line).

termined which experimental configuration will yield the best quality data. Comparison of equations (8.12) and (8.13) show that the beam coupling response for $I_1 = I_2$ yields a much more sensitive measurement of the photorefractive phase than the case $I_1 << I_2$ when the phase is near zero. This results from the coefficient of the $\cos\theta$ term approaching zero as $\sin\phi \rightarrow 0$ in (8.12), i.e., the second harmonic of the output vanishes when $\phi = 0$. In the weak signal limit (8.13), however, no such sensitivity is exhibited. In fact, depending on the value of $g \cos\phi\, z$ either the first or the second harmonic of the phase modulation can dominate the detected signal, i.e., the thickness of the crystal is a major factor in determining the response. We conclude that the equal intensity solution to the diffraction and beam coupling is more experimentally useful to the determination of photorefractive coupling constant and phase, especially when the phase is near zero. In any case, the existence of the general solution allows the calculation of the photorefractive parameters for arbitrary input intensities, and allows the optimization of the experimental setup to suit the particular material being characterized.

The effect of a phase shift of one beam on a dynamic hologram has apparently been misconceived on occasion. It has been proposed[8], for example, to measure the photorefractive phase in the following way: The intensity coupling of two beams in a photorefractive material in the weak signal approximation $I_2 << I_1$ is roughly given by

$$I_2(z) = I_2(0)\, e^{2g \sin\phi\, z}. \tag{8.22}$$

If one of the beams is shifted by a phase δ then the beam coupling equation

will be transformed to

$$"I_2(z) = I_2(0)\, e^{2g \sin(\phi \pm \delta)\, z}" \tag{8.23}$$

where the "+" and "-" depend on which beam is phase shifted, i.e., the sign of the phase shift. The quotation marks are to remind the reader of the dubious nature of the above equation.

This approximation is not very useful. Comparison with the correct calculations show that it is not accurate under most conditions. The reasoning behind (8.23) is specious because it assumes that the weak signal beam amplification coefficient is proportional to the phase difference between the intensity gratings and the phase gratings. Since this relative phase can be manually adjusted by phase shifting one of the beams, the effective photorefractive phase is altered and the beam coupling is expected to follow suit by (8.23). What this argument neglects is that (8.22) only holds for dynamically written gratings! and dynamic gratings have a spatial phase and intensity profile which depends on ϕ. The law of exponential gain of one beam at the expense of another (8.22) derives from two effects. The first is that the intensity coupling of one beam to another is governed by the phase ϕ. The second is that the efficiency of the coupling is modified by the amplitude of the index grating, which is itself a function of the beam coupling. It is the combination of these two effects which leads to (8.22). By varying the phase manually, we are changing one of the parameters while leaving the other (the grating) fixed. This approximation is particularly misleading because in the weak signal limit the grating is most strongly apodized and is a strong function of the photorefractive phase.

8.7 Summary

In summary, the problem of two-beam coupling and diffraction off a dynamic photorefractive grating written in the copropagating geometry has been analyzed. The solutions allow the determination of the coupling constant and phase of the photorefractive grating with several methods. These parameters were measured in several crystal samples with no applied field, and in KLTN as a function of applied field. The latter data are in agreement with a theory describing the coherent addition of a normal electro-optic grating and the ZEFPR grating.

References for chapter eight

[1] D. Vahey, "A nonlinear coupled-wave theory of holographic storage in ferroelectric materials," J. Appl. Phys. **46**, 3510-3515, (1975).

[2] N. V. Kukhtarev, V. B. Markov, S. G. Odulov, M. S. Soskin, and V. L. Vinetskii, "Holographic storage in electro-optic crystals. I. steady state," Ferroelectrics **22**, 949-960 (1979).

[3] V. Kondilenko, V. Markov, S. Odulov, and M. Soskin, "Diffraction of coupled waves and determination of phase mismatch between holographic grating and fringe pattern," Opt. Acta. **26**, 239-251 (1979).

[4] R. M. Pierce, R. S. Cudney, G. D. Bacher, and Jack Feinberg, "Measuring photorefractive trap density without the electro-optic effect," Opt. Lett. , **15**, 414-416, (1990).

[5] R. S. Cudney, G. D. Bacher, R. M. Pierce, and J. Feinberg, "Measurement of the photorefractive phase shift," Opt. Lett. **17**, 67-69, (1992).

[6] W. B. Lawler, C. J. Sherman, and M. G. Moharam, "Direct measurement of the amplitude and the phase of photorefractive fields in $KNbO_3$:Ta and $BaTiO_3$," J. Opt. Soc. Am. B, **8**, 2190-2195, (1991).

[7] P. M. Garcia, L. Cescato, and J. Frejlich, "Phase-shift measurement in photorefractive hologram recording," J. Appl. Phys. **66** (1), 47-49, (1989).

[8] M. Z. Zha, P. Amrhein, and P. Günter, "Measurement of phase shift of photorefractive gratings by a novel method," IEEE J. Quan. Elec. **26**, 788-792, (1990).

[9] C. Gu and P. Yeh, "Diffraction properties of fixed gratings in photorefractive media," J. Opt. Soc. B **7**, 2339-2346, (1990).

[10] M. Segev, A. Kewitsch, A. Yariv, and G. Rakuljic, "Self-enhanced diffraction from fixed photorefractive gratings during coherent reconstruction," Appl. Phys. Lett. , **62**, to appear March 1, 1993.

[11] R. Hofmeister and A. Yariv, "Vibration detection using dynamic photorefractive gratings in KTN/KLTN crystals," Appl. Phys. Lett. , **61**, 2395-2398, (1992).

[12] R. Hofmeister, A. Yariv, A. Kewitsch, and S. Yagi, "Simple methods of measuring the net photorefractive phase shift and coupling constant," to appear Opt. Lett. April 1, 1993.

[13] R. Hofmeister, A. Yariv, S. Yagi, and A. Agranat, "A new photorefractive mechanism in paraelectric crystals : A strain coordinated Jahn-Teller relaxation," Phys. Rev. Lett. , **69**, 1459-1462, (1992).

[14] J. O. White, S. Z. Kwong, M Cronin-Golomb, B. Fischer, and A. Yariv, in *Photorefractive Materials and their Applications II* , Eds. P. Günther and J. P. Huignard, chapter 4, Springer-Verlag, Berlin, (1989).

Chapter Nine

General Solutions of Coupled Mode Equations with Applications to Fixed Holographic Gratings

9.1 Introduction

In the scientific disciplines of electromagnetics and optics it is often necessary to solve sets of coupled differential equations. Only a tiny proportion of the equations typically encountered have been solved. The complexity of the solutions for even relatively simple differential equations can be discouraging; usually solutions are performed numerically. Unfortunately, numerical solutions are more difficult to verify than analytic ones, and the methods in which they are computed can easily lead to errors[1,2]. Also, a numerical solution requires a great deal of computation so it may take an unacceptably long time to map out a family of solutions for a set of equations with several varying parameters. Finally, with numerical computation all sense of intuition about the nature of the solution in terms of its variables is lost. For these reasons, analytic solutions are generally preferable to numerical ones.

In this chapter, attention is devoted to a general solution of a specific type of linear coupled differential equation. The usefulness of the solution of this type of equation will then be demonstrated by its application in several problems of beam coupling and diffraction off fixed and dynamically written

holographic gratings. The results of these applications are used in chapters two, five, seven, and eight of this thesis (and also this chapter).

9.2 Solution of Coupled Differential Equations

In the study of beam coupling and holography in photorefractive materials one often encounters equations of the form

$$A'(z) = i\kappa f_1(z) e^{i\delta z} B(z) \tag{9.1a}$$

$$B'(z) = \pm i\kappa^* f_2(z) e^{-i\delta z} A(z). \tag{9.1b}$$

Here we define both $f_1(z)$ and $f_2(z)$ to possess the same sign, usually $f_i(z) > 0$. The typical method of solving this type of equation set is to differentiate either equation, obtaining a second-order equation, and then substitute the remaining equation in to obtain a second-order equation which contains terms of only one dependent variable, i.e., A(z) and A''(z), or B(z) and B''(z), but no mixed terms. As seen in chapter two, the solution of the archetype of this family of equations (equation 2.29) leads to eigenfunctions of A(z) and B(z) which are sin and cos when the "+" is used in (9.1b), and are sinh and cosh when the "-" is used. These eigenfunctions are plugged into the original set of equations and, in conjunction with boundary conditions, yield the specific solutions.

The presence of the δ term and the $f_1(z)$ and $f_2(z)$ terms in (9.1a,b) complicate the use of this method since they contribute terms to the derivative. In general, after following the procedure outlined above, we are left with second-order equations containing terms of A(z), A'(z), and A''(z). The difficulty in solving the equations is that the coefficients of these terms are functions of

z. In order to overcome this problem we seek a simplifying transformation of the dependent variables of (9.1a,b) which will enable the equations to be solved. The method developed in the succeeding paragraphs is capable of solving a few important cases, but in instances where it might fail it is not to be construed that the equation is intractable: the solution presented below is not a general solution for all such equations with arbitrary $f_1(z)$ and $f_2(z)$, however, it has been able to solve every naturally occurring set of linear coupled equations put to the test so far.

First we seek a transformation which enables the expression of (9.1a,b) to be expressed as two second-order equations without A'(z) or B'(z) terms. We perform the transformation

$$A(z) = a(z)\, e^{i\, F(z)} \tag{9.2a}$$

$$B(z) = b(z)\, e^{-i\, F(z)} \tag{9.2b}$$

where F(z) is a function to be determined. Equations (9.1a,b) become (using the "-" sign)

$$a'(z) = i\, \kappa\, b(z)\, e^{i\,(\delta\, z\, -\, 2F(z)\,)}\, f_1(z) \; - i\, F'(z)\, a(z) \tag{9.3a}$$

$$b'(z) = -\, i\, \kappa^*\, a(z)\, e^{i\,(2F(z)\, -\, \delta\, z)}\, f_2(z) \; + i\, F'(z)\, b(z). \tag{9.3b}$$

When (9.3a) is differentiated and (9.3b) is used to eliminate terms containing b(z) and b'(z) we obtain

$$a''(z) \; = \left[i\, \delta \; - \; 2\, i\, F'(z) \; + \; f_1'(z)/f_1(z)\right]\, a'(z) \; +$$

$$\left[|\kappa|^2\, f_1(z)\, f_2(z) - \delta\, F'(z) + [F'(z)]^2 + i\, F'(z)\, f_1'(z)/f_1(z) - iF''(z)\right] a(z). \tag{9.4}$$

The a'(z) term vanishes when $F'(z) = \delta/2 + f_1'(z)/(2\,i\,F_1(z))$ or

$$F(z) = \frac{\delta\, z}{2} + \frac{\ln[\, f_1(z)\,]}{2\,i}. \tag{9.5}$$

An analysis of b''(z) similar to that leading up to (10.4) gives the condition

$$F(z) = \frac{\delta\, z}{2} - \frac{\ln[\, f_2(z)\,]}{2\,i} \tag{9.6}$$

in order that the b'(z) term be zero. Comparison of (9.5) and (9.6) shows that the two conditions can be met simultaneously if and only if

$$f_2(z) = \frac{1}{f_1(z)}. \tag{9.7}$$

When $f_1(z)$ is purely imaginary, the stipulation of (9.7) reduces to $f_2(z) = f_1^{*}(z)$. When the condition (9.7) is satisfied, equations (9.3a,b) can be written as

$$a''(z) = \left[|\kappa|^2 - [F'(z)]^2 - iF''(z)\right] a(z) \tag{9.8a}$$

$$b''(z) = \left[|\kappa|^2 - [F'(z)]^2 + iF''(z)\right] b(z). \tag{9.8b}$$

If we had taken the "+" in equations (9.3), then (9.8a,b) would be modified by replacing $|\kappa|^2$ with $-|\kappa|^2$. The transformation described above will be referred to as the "corotating transform."

The advantage of expressing the coupled equations in this way is that many second-order equations of the form of (9.8) have been solved and their solutions can be referenced[3]. In the following sections it will be shown that when coupled equations describing photorefractive beam coupling are sub-

jected to the procedure described above, the two second-order equations which result are often of the form

$$\psi''(r) = \alpha^2\left[\frac{\kappa(\kappa-1)}{\sinh^2(\alpha r)} - \frac{\lambda(\lambda+1)}{\cosh^2(\alpha r)} + (2l-1)^2\right]\psi(r). \tag{9.9}$$

This form is the second Pöschl-Teller equation which has been solved[4] using a modification of the factorization method[5]. The equation is used to describe the bound and scattering states of diatomic molecules, hence the quantum mechanical notation.

The method of solution will not be described here (see reference 2) instead we merely list the solutions. Two eigenfunctions are solutions of (9.9); they are

$$\psi_1(r) = \sinh^{1-\kappa}(\alpha r)\cosh^{\lambda+1}(\alpha r) \quad \times$$
$$ {}_2F_1\left[\left(\frac{\lambda-\kappa}{2} - l + 1\right) + \frac{1}{2}, \left(\frac{\lambda-\kappa}{2} + l\right) + \frac{1}{2}; \frac{3}{2} - \kappa; -\sinh^2(\alpha r)\right] \tag{9.10a}$$

$$\psi_2(r) = \sinh^{\kappa}(\alpha r)\cosh^{\lambda+1}(\alpha r) \quad \times$$
$$ {}_2F_1\left[\left(\frac{\lambda+\kappa}{2} - l + 1\right), \left(\frac{\lambda+\kappa}{2} + l\right); \frac{1}{2} + \kappa; -\sinh^2(\alpha r)\right] \tag{9.10b}$$

where ${}_2F_1[\ldots.]$ is the hypergeometric function, defined by

$${}_2F_1[a,b;c;z] = {}_2F_1[b,a;c;z] =$$
$$\frac{\Gamma(c)}{\Gamma(a)\Gamma(b)}\sum_{n=0}^{\infty}\frac{\Gamma(a+n)\,\Gamma(b+n)}{\Gamma(c+n)}\frac{z^n}{n!}. \tag{9.11}$$

The particular solutions of the first-order coupled equations (9.1) which led to the second-order Pöschl-Teller equations will consist of linear combinations

of the eigenfunctions ψ_1 and ψ_2, with coefficients determined by boundary conditions. Calculation of the coefficients is generally tedious. Use is made of the Gauss transformations for hypergeometric functions[6], the differential relation

$$\frac{d}{dz}\,{}_2F_1[a, b; c; z] = \frac{a\,b}{c}\,{}_2F_1[a+1, b+1; c+1; z], \tag{9.12}$$

and the linear transformation

$${}_2F_1[a, b; c; z] = (1 - z)^{c - a - b}\,{}_2F_1[c - a, c - b; c; z]. \tag{9.13}$$

The handbook by Abramowitz and Stegun (Ref. 6) is a useful reference for manipulation of these functions.

The following sections will describe several applications of the mathematical formalism elaborated above. These examples will illustrate exactly how the procedure is used, and will clarify any abstractions in the foregoing discussion.

9.3 Spectral Response of Fixed Holographic Grating Interference Filters

9.3.1 Introduction

Fixed photorefractive gratings have received interest recently for application as narrow-band optical interference filters and wavelength multiplexed optical memories[7,8,9,10]. The advantages of photorefractive filters over conventional methods are ease of fabrication and extremely narrow spectral response. We consider Bragg gratings which are written in a photorefractive material in exactly counterpropagating geometry (reflection geome-

try) as in figure 2-4. This method allows tuning the bandpass of the filter by adjusting the frequency of the laser writing beams. The index gratings written by the beams are then considered to be fixed by either thermal fixing or other methods. We calculate the spectral response of these filters to broadband or tunable incident radiation.

9.3.2 Theoretical Investigation, Lossless Case

We start by calculating the two beam coupling (see also chapter 2) of two incident counterpropagating beams A(z) and B(z) in a photorefractive material. The well known coupled mode equations in the absence of optical absorption are (chapter two)

$$A'(z) = \frac{i\,\pi\,\Delta n}{\lambda}\, e^{i\phi}\, B(z) \tag{9.14a}$$

$$B'(z) = \frac{-i\,\pi\,\Delta n^{*}}{\lambda}\, e^{-i\phi}\, A(z) \tag{9.14b}$$

where λ is the wavelength of the interfering beams, and the index of refraction is

$$n(z) = n_0 + \frac{1}{2}\left(\Delta n(z) e^{i\phi} e^{i K z} + \text{c.c.}\right). \tag{9.15}$$

Here ϕ is the phase between the optical intensity grating and the induced index grating. This grating phase is a property of the material; it can be altered with applied electric fields but is independent of the illuminating beams. We require, without loss of generality, that B(z) be the amplified beam. That is, the propagation direction of B(z) is nearer the z-axis (optic axis) than that of A(z). Generally B(z) propagates parallel to the optic axis and A(z) propagates

antiparallel to the same. This is equivalent to restricting ϕ to the range $[0, \pi]$. Since the index grating is formed dynamically by the writing beams we have

$$\Delta n(z) = n_1 A(z)\ B^*(z)/I(z) \tag{9.16}$$

where I(z) is the total intensity, and n_1 is the peak-to-peak amplitude of the index grating when A(z) = B(z) (see figure 2-5). Thus in the case of dynamic holography, the coupled mode equations can be simplified to

$$A'(z) = i\ g\ |B(z)|^2 /I(z)\ e^{i\phi}\ A(z) \tag{9.17a}$$

$$B'(z) = -i\ g\ |A(z)|^2 /I(z)\ e^{-i\phi}\ B(z) \tag{9.17b}$$

with $g = \pi n_1/\lambda$. We postulate solutions of the form

$$A(z)=a(z)e^{i\psi_1} \qquad B(z)=b(z)e^{i\psi_2} \tag{9.18}$$

where a(z) and b(z) are real. Equations (9.17a,b) can be separated into two equations each describing the evolution of the amplitude and phase of the two beams.

$$a'(z) = -\ g\ \sin\phi\ |b(z)|^2/I(z)\ a(z) \tag{9.19a}$$

$$b'(z) = -\ g\ \sin\phi\ |a(z)|^2/I(z)\ b(z) \tag{9.19b}$$

$$\psi_1'(z) = \ \ g\ \cos\phi\ |b(z)|^2 /I(z) \tag{9.20a}$$

$$\psi_2'(z) = -\ g\ \cos\phi\ |a(z)|^2 /I(z). \tag{9.20b}$$

Equations 9.19a,b are solved by converting them to equations for intensities using $I_1' = (a^2)' = 2\ a\ a'$, and similarly for I_2. Simple Bernoulli equations are obtained with solutions

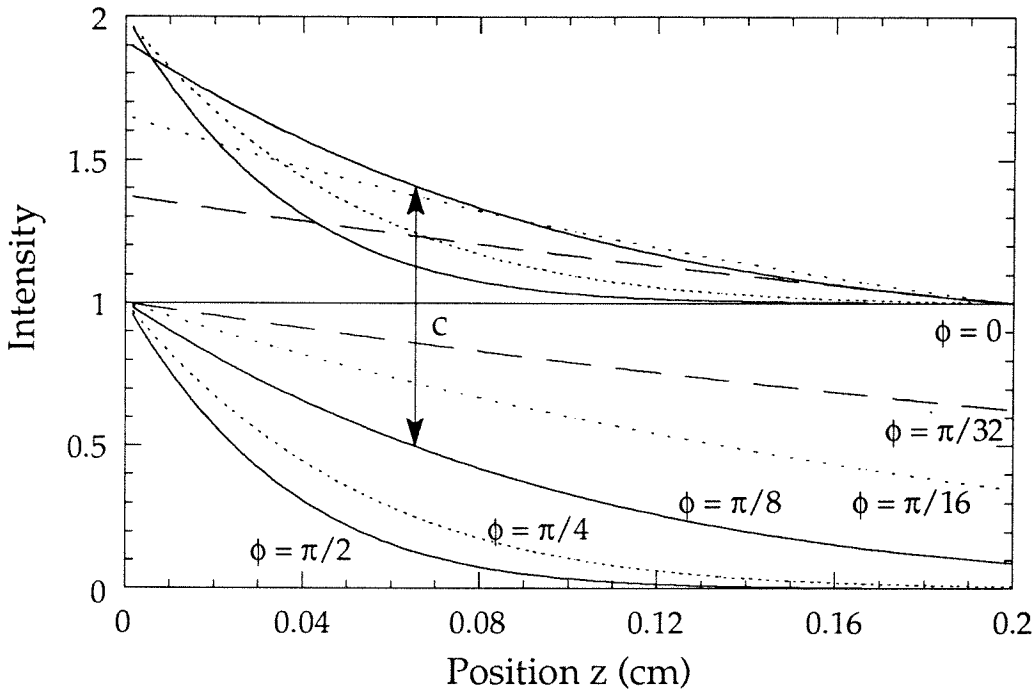

Figure 9-1. The effect of the photorefractive grating phase ϕ on the intensity coupling of two equal intensity input beams. For $\phi = 0$, the intensity coupling is zero, and the beams are purely phase coupled. As ϕ deviates from zero, the beams are coupled more and more strongly near the entrance face of the crystal. The coupling constant is g = 20/cm, and the crystal length is L = 0.2cm.

$$I_1(z) = \frac{1}{2}\left(\sqrt{c^2+v^2e^{-\Gamma z}} + c\right) \tag{9.21a}$$

$$I_2(z) = \frac{1}{2}\left(\sqrt{c^2+v^2e^{-\Gamma z}} - c\right). \tag{9.21b}$$

Here we have used the constants $\Gamma = 2g\sin\phi$, $c = I_1(z) - I_2(z)$ and $v^2 = 4\, I_1(0)\, I_2(0) = 4\, I_1(z)\, I_2(z)\, e^{\Gamma z}$. Also $I_1(z) = |A(z)|^2$ and $I_2(z) = |B(z)|^2$. In the case of equal intensity inputs ($I_1(0) = I_2(L)$) these constants are given by $v^2 = 4\, I_1^2(0)$ Exp[$\Gamma L/2$]/ Cosh[$\Gamma L/2$] and $c = -I_1(0)$ Tanh[$\Gamma L/2$]. We note that c as it is defined is a constant by conservation of energy. This follows immediately from the coupled equations whereby any decrease in intensity of one beam is added to the intensity of the other beam - propagating in the opposite direction[11]. The intensities are plotted in figure 9-1 for the case of equal intensity inputs, for g = 20/cm, L = 0.2cm, and several values of ϕ. The intensity coupling increases as the photorefractive phase ϕ deviates from zero. From the solutions in equations (9.21) we readily solve equations (9.20a,b) to give

$$\psi_1(z) = \frac{1}{2}\left(g\cos\phi\, z - \cot\phi\, \coth^{-1}[\sqrt{1+(v/c)^2e^{-\Gamma z}}]\right) \tag{9.22a}$$

$$\psi_2(z) = -\frac{1}{2}\left(g\cos\phi\, z + \cot\phi\, \coth^{-1}[\sqrt{1+(v/c)^2e^{-\Gamma z}}]\right). \tag{9.22b}$$

Thus equations (9.22), (9.21) and (9.18) completely describe the beam coupling in the counterpropagating geometry for arbitrary input beams and arbitrary material grating phase ϕ. The index grating in the material follows from equations (9.15) and (9.16) and is given by

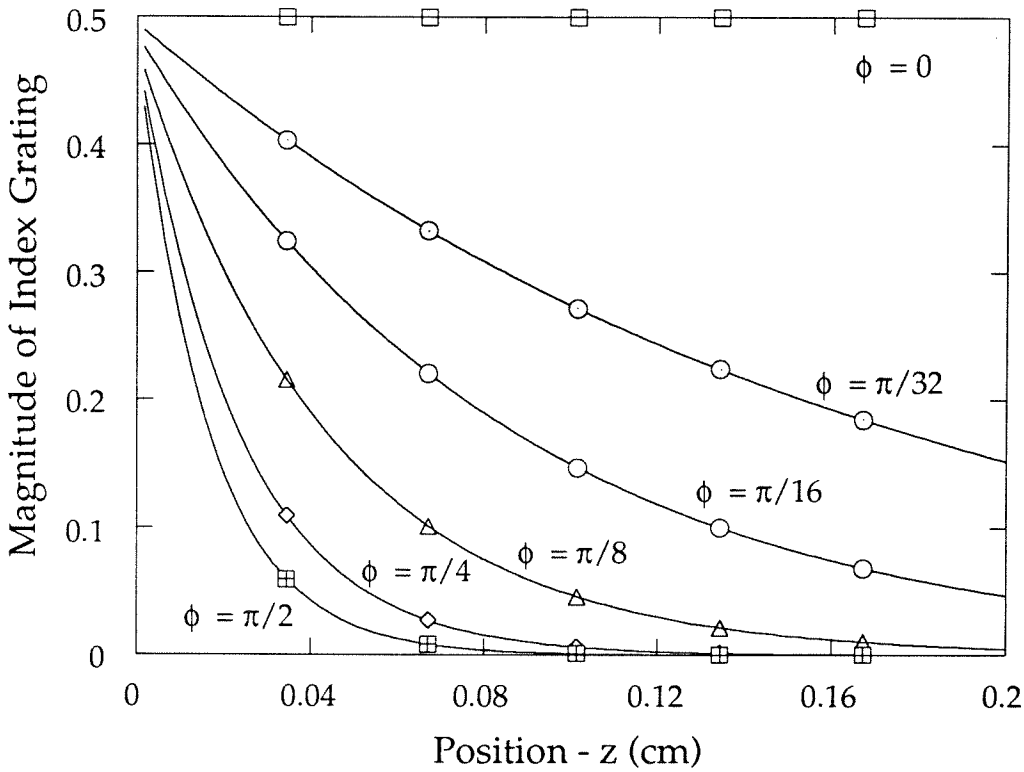

Figure 9-2. The magnitude of the index grating $|\Delta n|/n_1$ formed by the intensity coupled beams from figure 9-1. For $\phi = 0$, the index grating is constant, and as ϕ increases, the index grating is more strongly apodized with its maximum at the entrance facet of the crystal.

$$\Delta n\, e^{i\phi} = n_1 \frac{v}{2} \frac{e^{-\Gamma z/2 + i g \cos\phi\, z + i\phi}}{\sqrt{c^2+v^2e^{-\Gamma z}}}. \tag{9.23}$$

The functional form of the index grating is simplified by the partial cancellation of the beam phases in equation (9.22). The spatial variation of the magnitude of the index grating is plotted in figure 9-2 for the case of equal intensity inputs and for several values of ϕ.

We calculate the frequency reflectivity of a new incident beam A(0) off this index grating. In analogy to equations (9.14a,b) we write the coupled mode equations

$$A'(z) = i g \frac{v}{2} \frac{e^{-\Gamma z/2 + i g \cos\phi\, z + i\phi}}{\sqrt{c^2+v^2e^{-\Gamma z}}} e^{-2i\,\Delta\beta\, z}\, B(z) \tag{9.24a}$$

$$B'(z) = -i g \frac{v}{2} \frac{e^{-\Gamma z/2 - i g \cos\phi\, z - i\phi}}{\sqrt{c^2+v^2e^{-\Gamma z}}} e^{+2i\,\Delta\beta\, z}\, A(z) \tag{9.24b}$$

where $\Delta\beta = (\omega_o - \omega)\, n_o / c$ is the frequency mismatch between the beams which wrote the grating and the one undergoing Bragg reflection. We have ignored the new dynamic grating which is written by the interference of the incident and reflected beams[12,13] since we are calculating the filter response to broadband illumination. Any such secondary grating would be bleached by the majority of light which is not reflected. In equations (9.24), B(z) is the new reflected beam so that we take $B(L) = 0$, where L is the length of the crystal.The analytic solution of equations (9.24) subject to this boundary condition follows.

We first note that equations (9.24a,b) can be written in the form

$$A'(z) = i\, g(z)\, f(z)\, B(z) \tag{9.25a}$$

$$B'(z) = -\, i\, [g(z)/f(z)]\, A(z) \tag{9.25b}$$

where $f(z) = \exp[\, -2i\Delta\beta z + ig\cos\phi\, z + i\phi\,]$ and $g(z) = g\, v \exp[-\Gamma z/2]/\{2\,[c^2 + v^2 \exp[\, -\Gamma\, z\,]\,]^{1/2}\}$. We can eliminate g(z) by performing the independent variable transformation of z to ξ where $\xi/\sin\phi = \int g(z)\, dz$

$$\xi = -\frac{\Gamma v}{2c} \int \frac{e^{-\Gamma z/2}}{\sqrt{1+(v/c)^2 e^{-\Gamma z}}}\, dz = \sinh^{-1}[\, \frac{v}{c} e^{-\Gamma z/2}\,]. \tag{9.26}$$

Inverting, we obtain $e^{-\Gamma z/2} = (c/v)\sinh[\xi]$. Applying this transform to (9.25a,b) yields a set of coupled equations in ξ:

$$a'(\xi) = i\,\kappa\, f(\xi)\, b(\xi) \tag{9.27a}$$

$$b'(\xi) = -\, i\,\kappa^*\, f^*(\xi)\, a(\xi) \tag{9.27b}$$

where

$$f(\xi) = \left(\frac{c}{v}\sinh[\xi]\right)^{4\, i\, \Delta\beta'/\Gamma} \tag{9.28}$$

$$\kappa = -\, e^{i\,\phi}/(2\, \sin\phi) \tag{9.29}$$

and $\Delta\beta' = \Delta\beta - (g/2)\cos\phi$.

Equations (9.27a,b) are clearly of the form (9.1a,b) with $\delta = 0$, and can be transformed with the corotating transform of the last section. We define

$$a(\xi) = T(\xi)\, e^{iF(\xi)} \quad \text{and} \quad b(\xi) = V(\xi)\, e^{-iF(\xi)} \tag{9.30}$$

where

$$F(\xi) = 1/(2i)\ \mathrm{Ln}[f(\xi)] = \Delta\beta'/(g\sin\phi)\ \mathrm{Ln}[\sinh[\xi]]. \tag{9.31}$$

In analogy to (9.9) we obtain the simple second-order equations

$$T''(\xi) = \left[|\kappa|^2 - (F'(\xi))^2 - iF''(\xi)\right] T(\xi) \tag{9.32a}$$

$$V''(\xi) = \left[|\kappa|^2 - (F'(\xi))^2 + iF''(\xi)\right] V(\xi). \tag{9.32b}$$

Here $F(\xi)$ was chosen to eliminate the first derivative terms $T'(\xi)$ and $V'(\xi)$ in the equation (9.32). From (9.31) we can write $F'(\xi) = \Delta\beta'/(g\sin\phi)\ \coth[\xi]$ and $F''(\xi) = -\Delta\beta'/(g\sin\phi\sinh^2[\xi])$ so that

$$T''(\xi) + \left(\frac{-1}{4\sin^2\phi} + \eta^2 - \frac{i\eta(i\eta+1)}{\sinh^2\xi}\right) T(\xi) = 0 \tag{9.33a}$$

$$V''(\xi) + \left(\frac{-1}{4\sin^2\phi} + \eta^2 - \frac{i\eta(i\eta-1)}{\sinh^2\xi}\right) V(\xi) = 0 \tag{9.33b}$$

where we define $\eta = 2\Delta\beta'/\Gamma$. Comparison with equation (9.9) confirms that (9.33a and b) are examples of the second Pöschl-Teller equation where $\lambda = 0$, $\alpha = 1$, and the "quantum" parameters are

$$l = \frac{1}{2}\sqrt{\frac{1}{4\sin^2\phi} - \eta^2} + \frac{1}{2} \tag{9.34}$$

$$\kappa_T = 1 + i\,\eta \tag{9.35}$$

$$\kappa_V = i\,\eta. \tag{9.36}$$

The parameters κ_T and κ_V are those required for (9.33a) and (9.33b) respective-

ly to match the notation of (9.9). The quantity "l" is the angular momentum quantum number in the diatomic system. Here it assumes not only noninteger values, but, for $\Delta\beta' > g\sin\phi/2$, becomes complex. Thus little intuition can be drawn from the quantum system to help us in this application. Fortunately, the solution of the Pöschl-Teller works with complex parameters and can be utilized as is.

Using (9.10a,b) we can directly write solutions for $T(\xi)$ and $V(\xi)$:

$$T(\xi) = t_1 \sinh^{-i\eta}\xi \cosh\xi \; {}_2F_1[\tfrac{1}{2} - i\tfrac{\eta}{2} - \beta, \tfrac{1}{2} - i\tfrac{\eta}{2} + \beta; \tfrac{1}{2} - i\eta; -\sinh^2\xi] +$$

$$t_2 \sinh^{1+i\eta}\xi \cosh\xi \; {}_2F_1[i\tfrac{\eta}{2} - \beta + 1, i\tfrac{\eta}{2} + \beta + 1; \tfrac{3}{2} + i\eta; -\sinh^2\xi] \qquad (9.37a)$$

$$V(\xi) = v_1 \sinh^{1-i\eta}\xi \cosh\xi \; {}_2F_1[1 - i\tfrac{\eta}{2} - \beta, 1 - i\tfrac{\eta}{2} + \beta; \tfrac{3}{2} - i\eta; -\sinh^2\xi] +$$

$$v_2 \sinh^{i\eta}\xi \cosh\xi \; {}_2F_1[i\tfrac{\eta}{2} - \beta + \tfrac{1}{2}, i\tfrac{\eta}{2} + \beta + \tfrac{1}{2}; \tfrac{1}{2} + i\eta; -\sinh^2\xi] \qquad (9.37b)$$

where t_1, t_2, v_1, and v_2 are arbitrary constants and we define

$$\beta = \frac{1}{2}\sqrt{\frac{1}{4\sin^2\phi} - \eta^2} = l - \frac{1}{2}. \qquad (9.38)$$

Using equations(9.26), (9.30), (9.31), and (9.37), the expressions for A(z) and B(z) are obtained

$$A(z) = \sqrt{1+(\frac{v}{c})^2 e^{-\Gamma z}}\ x$$

$$\Big[C_1\ {}_2F_1[\frac{1}{2} - i\frac{\eta}{2} - \beta, \frac{1}{2} - i\frac{\eta}{2} + \beta; \frac{1}{2} - i\eta; -(\frac{v}{c})^2 e^{-\Gamma z}] +$$

$$C_2\, e^{-(1+2i\eta)\Gamma z/2}\ {}_2F_1[i\frac{\eta}{2} - \beta + 1, i\frac{\eta}{2} + \beta + 1; \frac{3}{2} + i\eta; -(\frac{v}{c})^2 e^{-\Gamma z}]\Big] \qquad (9.39a)$$

$$B(z) = \sqrt{1+(\frac{v}{c})^2 e^{-\Gamma z}}\ x$$

$$\Big[C_3\ e^{-(1-2i\eta)\Gamma z/2}\ {}_2F_1[-i\frac{\eta}{2} - \beta + 1, -i\frac{\eta}{2} + \beta + 1; \frac{3}{2} - i\eta; -(\frac{v}{c})^2 e^{-\Gamma z}] +$$

$$C_4\ {}_2F_1[i\frac{\eta}{2} - \beta + \frac{1}{2}, i\frac{\eta}{2} + \beta + \frac{1}{2}; \frac{1}{2} + i\eta; -(\frac{v}{c})^2 e^{-\Gamma z}]\Big] \qquad (9.39b)$$

where C_1, C_2, C_3, C_4 are constants. The constants are determined from the boundary condition B(L)=0 and equations (9.24), using the hypergeometric function identities (9.12) and (9.13). The result is

$$C_1 = \frac{A(0)\ 4\sin^2\phi\ (1+4\eta^2)}{\sqrt{1+(v/c)^2}}\ e^{(1-2i\eta)\,\Gamma L/2}\ x$$

$${}_2F_1[i\frac{\eta}{2} - \beta + \frac{1}{2}, i\frac{\eta}{2} + \beta + \frac{1}{2}; \frac{1}{2} + i\eta; -(\frac{v}{c})^2 e^{-\Gamma L}]/D \qquad (9.40a)$$

$$C_2 = \frac{-A(0)}{\sqrt{1+(v/c)^2}}\ (\frac{v}{c})^2\ x$$

$${}_2F_1[-i\frac{\eta}{2} - \beta + 1, -i\frac{\eta}{2} + \beta + 1; \frac{3}{2} - i\eta; -(\frac{v}{c})^2 e^{-\Gamma L}]/D \qquad (9.40b)$$

$$C_3 = -A(0)\left(\frac{v\ (2+4i\eta)\ \sin\phi}{i\ c\ e^{i\phi}\ \sqrt{1+(v/c)^2}}\right) e^{(1-2i\eta)\Gamma L/2}\ x$$

$${}_2F_1[i\frac{\eta}{2} - \beta + \frac{1}{2}, i\frac{\eta}{2} + \beta + \frac{1}{2}; \frac{1}{2} + i\eta; -(\frac{v}{c})^2 e^{-\Gamma L}]/D \qquad (9.40c)$$

$$C_4 = A(0)\left(\frac{v\,(2+4i\eta)\sin\phi}{i\,c\,e^{i\phi}\sqrt{1+(v/c)^2}}\right) \quad x$$

$$_2F_1[\,-i\frac{\eta}{2} - \beta+1,\ -i\frac{\eta}{2} + \beta+1;\ \frac{3}{2} - i\eta;\ -\left(\frac{v}{c}\right)^2 e^{-\Gamma L}]/D \qquad (9.40d)$$

where the common denominator D is given by

$$D = 4\sin^2\phi\,(1+4\eta^2)\,e^{(1-2i\eta)\,\Gamma L/2} \quad x$$

$$_2F_1[\,i\frac{\eta}{2} - \beta+\frac{1}{2},\ i\frac{\eta}{2} + \beta+\frac{1}{2};\ \frac{1}{2} + i\eta;\ -\left(\frac{v}{c}\right)^2 e^{-\Gamma L}] \quad x$$

$$_2F_1[\,-i\frac{\eta}{2} - \beta+\frac{1}{2},\ -i\frac{\eta}{2} + \beta+\frac{1}{2};\ \frac{1}{2} - i\eta;\ -\left(\frac{v}{c}\right)^2] \quad -$$

$$\left(\frac{v}{c}\right)^2\ _2F_1[\,-i\frac{\eta}{2} - \beta+1,\ -i\frac{\eta}{2} + \beta+1;\ \frac{3}{2} - i\eta;\ -\left(\frac{v}{c}\right)^2 e^{-\Gamma L}] \quad x$$

$$_2F_1[\,i\frac{\eta}{2} - \beta+1,\ i\frac{\eta}{2} + \beta+1;\ \frac{3}{2} + i\eta;\ -\left(\frac{v}{c}\right)^2]. \qquad (9.41)$$

The equations (9.39a,b) with constant coefficients defined in (9.40a,b,c,d) and (9.41) determine exactly the amplitude and phase of the incident beam A(z) and the reflected beam B(z).

To recap, the reflected wave is generated by interaction of A(z) with the previously dynamically written hologram defined by the index grating of (9.23). Since B is a reflected wave, the solutions obey the boundary conditions B(L) = 0. Both A(z) and B(z) are expressed in terms of, and are proportional to, the input beam A(0). The reflectivity of the grating is given by $R = |B(0)|^2/|A(0)|^2$. It is plotted in figure 9-3 for the case of equal intensity input beams (during the writing phase), and for several values of the grating phase ϕ. In general, the reflectivity maximum occurs at a different frequency than that of

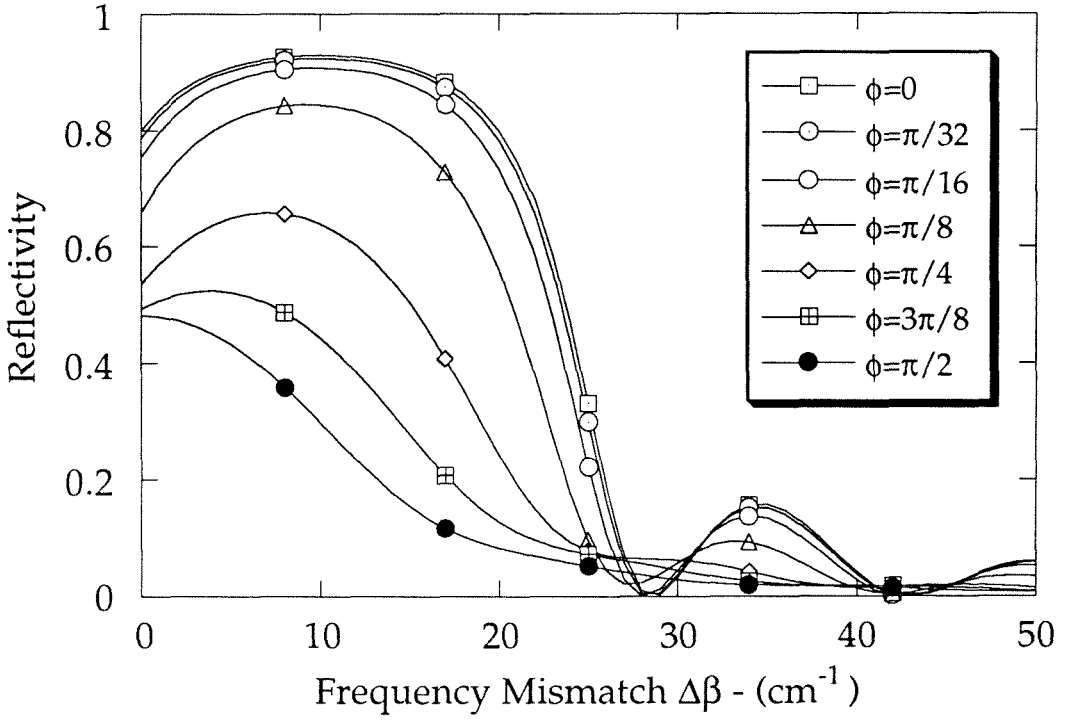

Figure 9-3. The reflectivity from the fixed index gratings of figure 9-2. The reflectivity maximum occurs at a frequency mismatch given by $\Delta\beta = (g/2)\cos\phi$. The overall reflectivity as well as the sidelobes are reduced by the grating apodization for $\phi > 0$.

the writing beams; it occurs at a frequency mismatch of $\Delta\beta = g\cos\phi/2$, i.e., it occurs at $\Delta\beta' = 0$. This mismatch arises simply because the two writing beams influence each other's phase (as well as intensity) by a total amount $\Delta\phi(z) = g\cos\phi\, z$.(see (9.22a,b)) This increases (or decreases) the spatial frequency of the index grating, altering the frequency at which maximum reflectivity is achieved. The reflectivity curves plotted in figure 9-3 are reflected about the line $\Delta\beta = 0$ when ϕ is reflected about $\pi/2$, i.e., when $\cos\phi \rightarrow -\cos\phi$ the reflectivity transforms as $R[\Delta\beta] \rightarrow R[-\Delta\beta]$. For this reason the reflectivity versus frequency mismatch has only been illustrated for $0 \leq \phi \leq \pi/2$. We note that the grating apodization caused by intensity coupling for $\phi \neq 0$ or π leads to reduced sidelobes in the reflectivity at large values of frequency mismatch, as well as lower overall reflectivity. This is illustrated in figure 9-4 where the reflectivity of the $\phi = 0$ and $\phi = \pi/2$ cases are compared at large values of mismatch.

We now consider how the previous equations are simplified under special conditions. For $\phi = \pi/2$ note that the beam coupling consists purely of intensity coupling rather than phase coupling. This leads to a simpler form of the index grating (Equation (9.23)), however, little simplification of the final solutions occurs. Since the phase coupling is absent in this case, the reflectivity maximum of the grating occurs at the same frequency as that of the writing beams.

The case $\phi = 0$, is completely different. Here, there exists no intensity

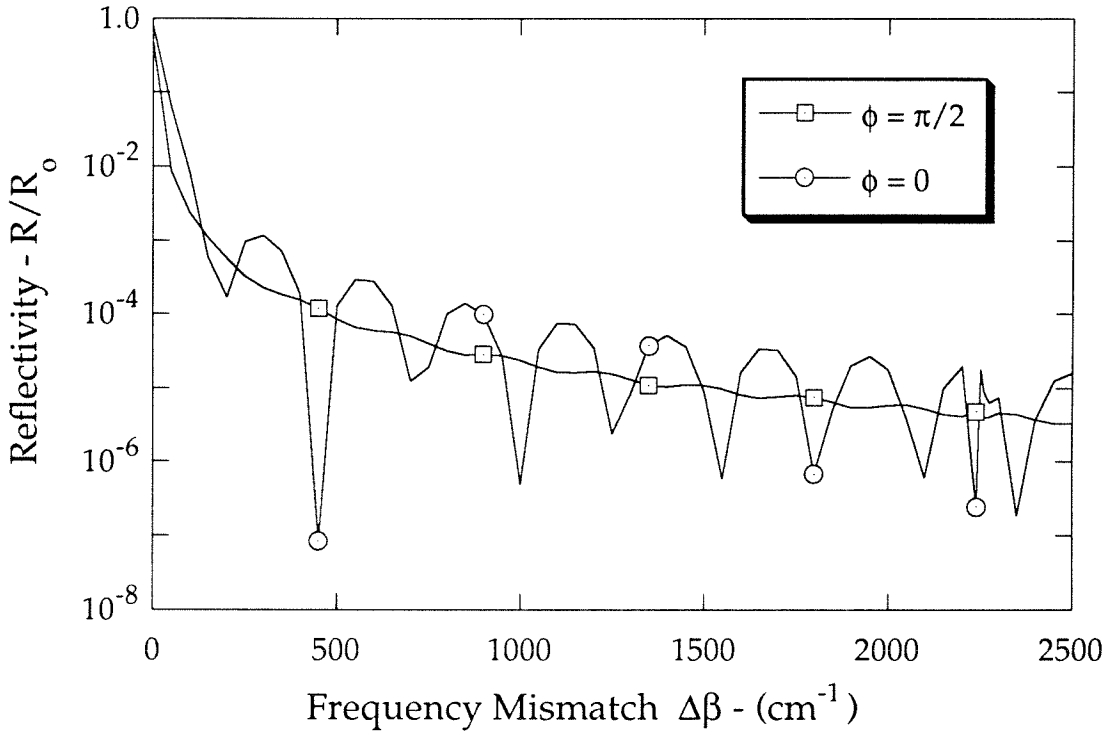

Figure 9-4. The reflectivity from the fixed index gratings for $\phi = 0$ and $\phi = \pi/2$ at large values of frequency mismatch. The $\phi = \pi/2$ grating reflectivity has reduced sidelobes whose peaks are approximately 8dB lower than the $\phi = 0$ case.

coupling while the phase coupling is maximum. Hence the magnitude of the index grating is a constant throughout the volume of the crystal. We obtain, in analogy to equation (9.23),

$$\Delta n = n_1 \frac{\sqrt{I_1(0)I_2(0)}}{I} e^{i g z}. \tag{9.42}$$

This grating is fixed and the equations describing reflection off it are

$$A'(z) = i \kappa e^{i (g - 2 \Delta\beta) z} B(z) \tag{9.43a}$$

$$B'(z) = -i \kappa e^{- i (g - 2 \Delta\beta) z} A(z) \tag{9.43b}$$

where

$$\kappa = g \frac{\sqrt{I_1(0)I_2(0)}}{I}. \tag{9.44}$$

The reflectivity is easily shown to be

$$R = \frac{\kappa^2 \sinh^2[sL]}{\kappa^2 \sinh^2[sL] + s^2} \tag{9.45}$$

where

$$s = \sqrt{\kappa^2 - \delta^2/4} \tag{9.46a}$$

$$\delta = g - 2\Delta\beta. \tag{9.46b}$$

Equation (9.45) has the simple form characteristic of Bragg reflection from a constant amplitude grating[14]. The only difference is that the maximum reflectivity occurs at a frequency shift of $\Delta\beta = g/2$ rather than $\Delta\beta = 0$. Again, this is due to the mutual phase coupling of the two beams which shift δ by an amount g. Also the parameter s is complex for large values of the frequency

mismatch; this is no problem analytically, but may cause problems during numeric calculations. If this occurs, s can simply be redefined as s -> is, so that sinh -> i sin, and so on.

A similar case occurs for arbitrary phase ϕ under the special condition c=0, that is, when the coupled beams are everywhere of equal intensity (see figure 9-1). Starting again from equations (9.17a,b), we derive in analogy to equations (9.21) and (9.22), intensities and phases of the coupled beams

$$I_1(z) = I_2(z) = \frac{1}{2} v\, e^{-\Gamma z/2} = I_1(0)\, e^{-\Gamma z/2} \tag{9.47}$$

$$\psi_1(z) = -\psi_2(z) = \cos\phi\ g/2\ z \tag{9.48}$$

where v is as defined following equation (9.21a,b). From these we derive the index grating to be a constant magnitude

$$\Delta n(z) = \frac{n_1}{2}\, e^{\,i\, g \cos\phi\, z}. \tag{9.49}$$

In comparing (9.49) with (9.42), note the important difference between the two cases $c = 0$ and $\phi = 0$. Here the beams are intensity coupled with a gain coefficient of g $\sin\phi$; this reduces the phase coupling coefficient from g to g $\cos\phi$. Also note that since the beams are everywhere of equal intensity, the term $[I_1(0)\, I_2(0)]^{1/2}/\ I$ from (9.42) reduces to 1/2 in (9.49). Since the formation of the index grating is intensity independent (9.16), the index grating is constant although the intensities of the beams are not. In the case $\phi = 0$ the beams need not be equal intensity because their intensities are constant throughout the

volume of the photorefractive medium.

The grating (9.49) is fixed in the material. The coupled mode equations describing reflection become

$$A'(z) = i\frac{g}{2} e^{i\phi} e^{i(g\cos\phi - 2\Delta\beta)z} B(z) \tag{9.50a}$$

$$B'(z) = -i\frac{g}{2} e^{-i\phi} e^{-i(g\cos\phi - 2\Delta\beta)z} A(z) \tag{9.50b}$$

these equations are readily solved to yield a reflectivity identical in form to that in the case $\phi = 0$ (equation (9.45)) with the modified definitions $\kappa = g/2$ and $\delta = g\cos\phi - 2\Delta\beta$.

9.3.3 Investigation, Lossy Case

The previous section investigated the problem of frequency dependent reflectivity off a dynamically written photorefractive hologram. The effects of optical absorption were ignored. When the loss in the material is considered, the equations become substantially more complicated. Fundamentally, the problem arises because the absorption changes the relative beam intensities as a function of z. (This would not occur if the beams were copropagating.) Analytic expressions are only obtained for $\phi=0$. Reflectivities of the fixed holograms are calculated numerically. We start with the dynamic coupled mode equations as in equations (9.17a,b).

$$A'(z) = i\,g\,|B(z)|^2/I(z)\,e^{i\phi}\,A(z) - \alpha/2\,A(z) \tag{9.51a}$$

$$B'(z) = -i\,g\,|A(z)|^2/I(z)\,e^{-i\phi}\,B(z) + \alpha/2\,B(z). \tag{9.51b}$$

Performing the same transformation as in equation (9.18) we are led to the following equations for the phases and magnitudes of the coupled beams.

$$a'(z) = - \sin\phi\, g\, |b(z)|^2/I(z)\; a(z) \;\; - \alpha/2\; a(z) \tag{9.52a}$$

$$b'(z) = - \sin\phi\, g\, |a(z)|^2/I(z)\; b(z) \;\; + \alpha/2\; b(z) \tag{9.52b}$$

$$\psi_1'(z) = \;\; \cos\phi\, g\, |b(z)|^2\, /I(z) \tag{9.53a}$$

$$\psi_2'(z) = -\cos\phi\, g\, |a(z)|^2\, /I(z). \tag{9.53b}$$

Again, the special case ϕ=0 yields considerably simplified formulas. In this special case, analytic solutions of equations (10.52) and (10.53) are obtained easily. They are

$$A(z) = A(0)\, e^{-\alpha z/2}\left[\frac{B(0)^2 e^{2\alpha z}+A(0)^2}{B(0)^2+A(0)^2}\right]^{\frac{ig}{2\alpha}} \tag{9.54a}$$

$$B(z) = B(0)\, e^{+\alpha z/2}\left[\frac{B(0)^2+A(0)^2 e^{-2\alpha z}}{B(0)^2+A(0)^2}\right]^{\frac{ig}{2\alpha}}. \tag{9.54b}$$

Thus the index grating is given by

$$\Delta n(z) \;\; = \;\; n_1 \frac{A(0)\; B(0)\; e^{igz}}{A(0)^2\; e^{-\alpha z} + B(0)^2\; e^{\alpha z}}. \tag{9.55}$$

When this grating is fixed, we can formulate the coupled equations describing reflectivity in analogy to (9.14a,b and 9.24a,b), using equations (9.51a,b). These equations can be manipulated following identical steps as in the analysis up to equation(9.32a,b). In this case, however, instead of the Pöschl-Teller

(Equation (9.33a,b).), the second-order equation obtained is of the form

$$y'' = \left[\frac{M^2 + K^2 - \frac{1}{4} - 2MK\cos x}{\sin^2 x} + \left(\sigma + K^2 + \frac{1}{4}\right) \right] y \qquad (9.56)$$

which is a symmetric top equation. Although its solution is documented[5], we do not present it here, since it is useful only for ϕ=0.

Alternatively, equations (9.51a and b) have been solved numerically for arbitrary photorefractive phase ϕ in order to obtain the index grating which is fixed in the material. This calculated index grating is then fitted to a high order polynomial (usually 9th order), and that polynomial approximation is then used in the reflectivity equations. In solving the dynamic equations we specify boundary conditions at a given value of z, usually at z = 0 (i.e. , A(0) and B(0)). Since the physical inputs to the crystal are A(0) and B(L), B(0) must be iteratively modified by trial and error to obtain the desired value for B(L). This procedure yields the dynamic index grating for inputs A(0) and B(L) in a material with optical absorption. This grating is considered fixed when the reflectivity is calculated. Here, we use the standard procedure of fixing B(L) = 0 and A(L) = 1[12] and working backwards toward z=0. Finally, the reflectivity is defined as $R = |B(0)|^2/|A(0)|^2$ where $|A(0)| > 1$. The addition of a nonzero optical absorption coefficient has two noticeable effects on the results. First, the reflectivity of the filter is now strongly nonreciprocal; that is, the reflectivity is different if the crystal is flipped by 180°. Second, since energy is no longer conserved, the quantity $|A(z)|^2 - |B(z)|^2$ is no longer constant. In

the previous (lossless) case, the intensity difference was defined as c. This parameter appeared in the final solution. In this case, c is no longer constant, and may change sign (compare figures 9-5a and 9-5b). When c = 0, the intensities are equal; this may happen at any arbitrary point within the volume of the crystal. Thus the index grating may have its maximum at any point in the volume of the crystal, rather than only at the entrance or exit facet (compare figure 9-6 with 9-2).

In the following calculations we have used a coupling constant $g = 20/cm$, a crystal length of $L = 0.2cm$, and we have assumed equal intensity inputs A(0) and B(L). The loss coefficient is taken to be $\alpha = 6/cm$. First the equations for the dynamically coupled beams A(z) and B(z) are computed from equations (9.51a and b). The results for various values of the grating phase ϕ are shown in figures 9-5a and b. The nonzero loss mostly affects the growth of the amplified beam, B(z), incident from z = L. This occurs because the beam coupling and loss mechanisms are opposed. Thus B(z) has a minimum at the position where the material loss is balanced by the beam coupling. Also, as discussed above, the loss allows the two beams to have equal intensities at a point within the volume of the crystal. From equations (9.52) we determine that this condition is allowed roughly when $g \sin\phi < \alpha/2$. The index grating formed by the two beams (Figure 9-6.) illustrates this effect. For $\phi = 0$, it is clear that the index grating is maximum in the center of the crystal when the input intensities are equal since only absorption, and no intensity coupling occurs.

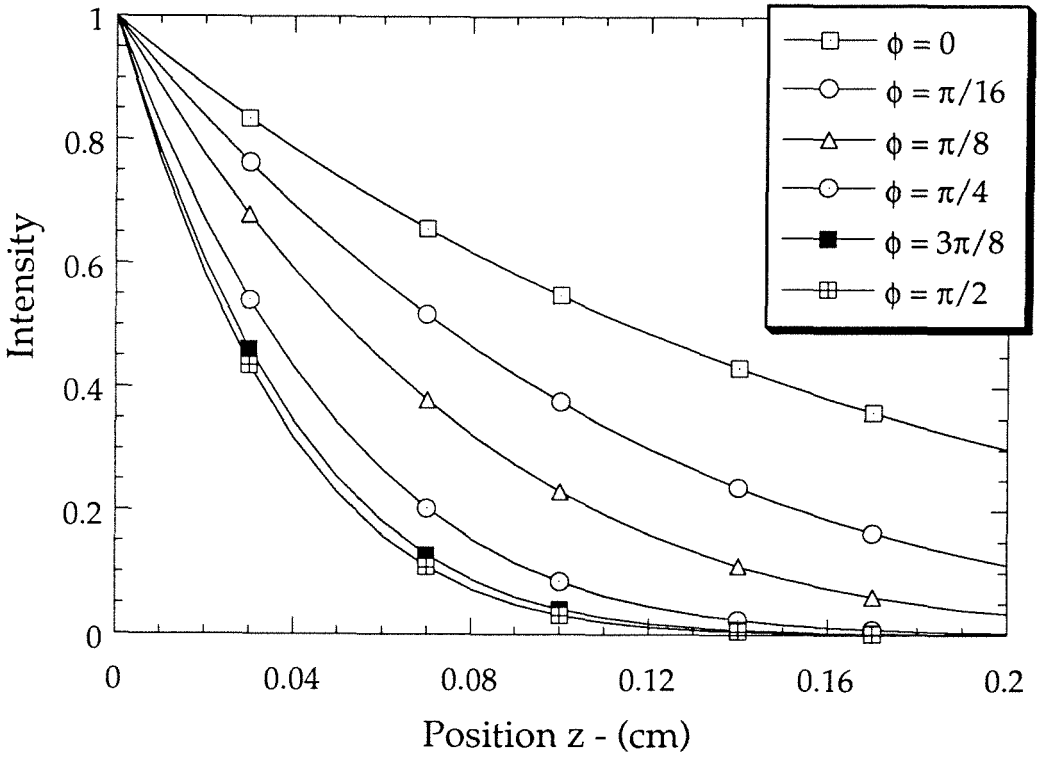

Figure 9-5a. The intensity of beam 1, A(z), incident at z=0 for various values of ϕ, for a loss constant of α = 6/cm, and for equal intensity inputs. The coupling constant is g = 20/cm, and the crystal length is L = 0.2cm. When ϕ = 0, the decrease in amplitude of A(z) is due entirely to the optical absorption. As ϕ increases, progressively more beam coupling occurs (which depletes A(z)) and the beam is attenuated more rapidly.

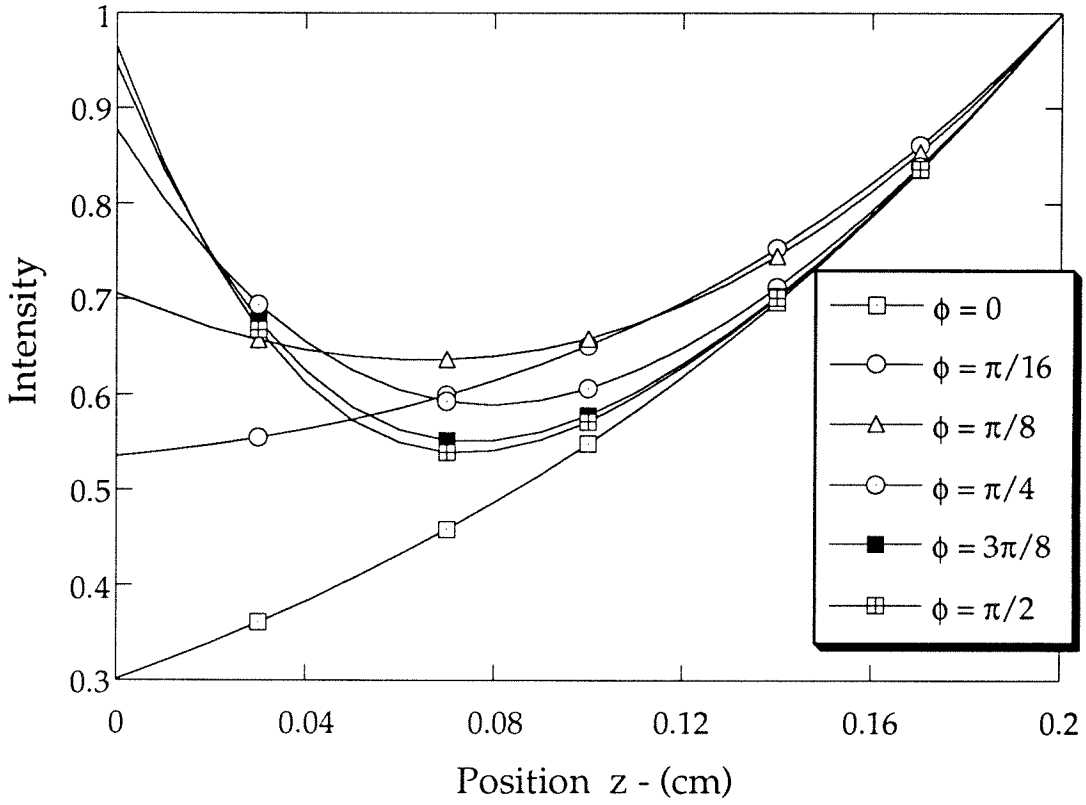

Figure 9-5b. The intensity of beam 2, B(z), incident at z=L under identical conditions as figure 9-5a. When $\phi = 0$, the decrease in amplitude of B(z) propagating toward z=0 is due entirely to the optical absorption. As ϕ increases, progressively more beam coupling occurs (which amplifies B(z)) counteracting the absorption and eventually causing net beam amplification. The competition between the optical absorption and the beam coupling gain makes the amplitude of B(z) a complicated function of ϕ in the range z=0.00 - 0.08.

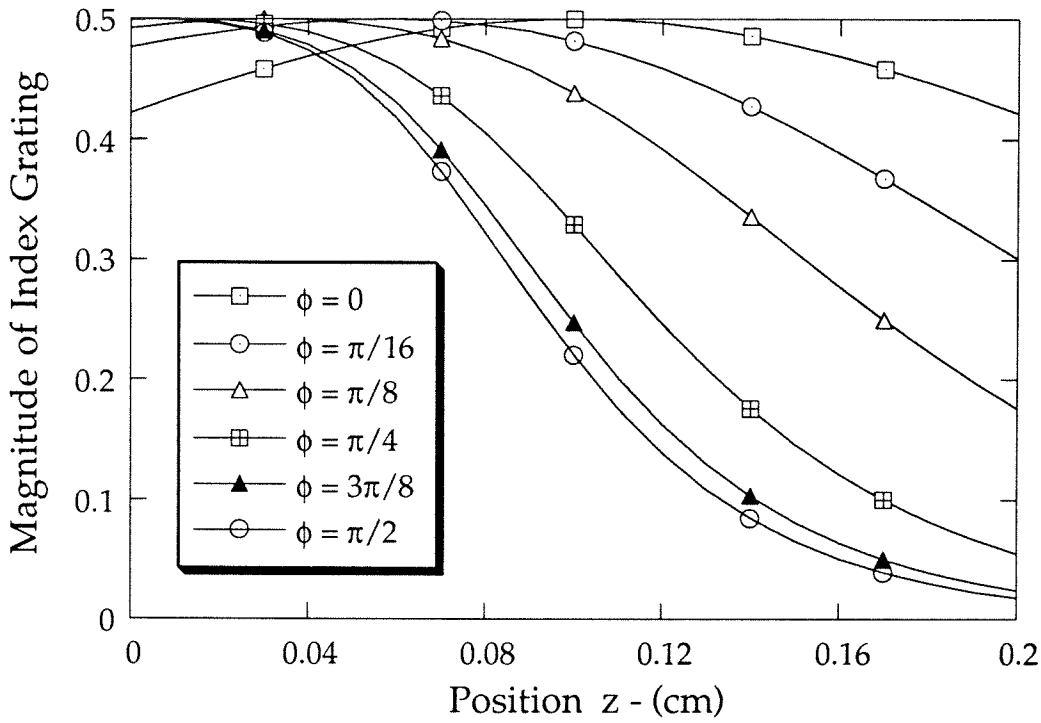

Figure 9-6. The index grating formed in the crystal by the coupled beams in figures 9-5. One effect of the loss is to eliminate the "no crossing" rule for the two beam intensities, i.e., with zero loss, c = constant, so that the two beam intensities cannot cross. In the figures above,when g $\sin\phi \leq \alpha$ (roughly), the intensities can be equal within the volume of the crystal. This leads to a maximum in the magnitude of the index grating located away from the edge of the crystal.

Next we calculate numerically the reflectivity from the index gratings of figure 9-6. Figure 9-7. shows the reflectivity for a beam incident on the z=0 side of the crystal, and figure 9-8. shows the reflectivity under the same conditions for a beam incident from z=L. Since the index grating is, in general, stronger near z = 0, the reflectivity is higher for a beam incident at z = 0. The difference between the two cases is most pronounced when the grating phase ϕ is near $\pi/2$. This follows from the fact that the case $\phi = \pi/2$ results in the strongest spatial variation of the index grating. When the c-axis of the material is defined as the direction of power transfer of symmetrically incident beams in a two-beam coupling experiment, we can say that a beam incident antiparallel to the c-axis is reflected more strongly. Also we point out that the behavior of the reflectivity as ϕ increases is more complex in the case of reflection from the z = 0 side. The reason is that the index grating near z = 0 (the most efficient region of reflection for a beam incident at z = 0) first increases, then decreases with increasing photorefractive phase ϕ. This is fundamentally due to the competitive interplay between the intensity coupling and the absorption. We can see how the effect arises by an inspection of the shape of B(z) in figure 9-5b. The concept of nonreciprocal reflection has recently been employed to determine the photorefractive phase in $LiNbO_3$[13]

9 . 3 . 4 Summary of Spectral Response of Fixed Holographic Grating Interference Filters

In summary, an analytic solution for the frequency response of interference filters written with counterpropagating beams in a photorefractive mate-

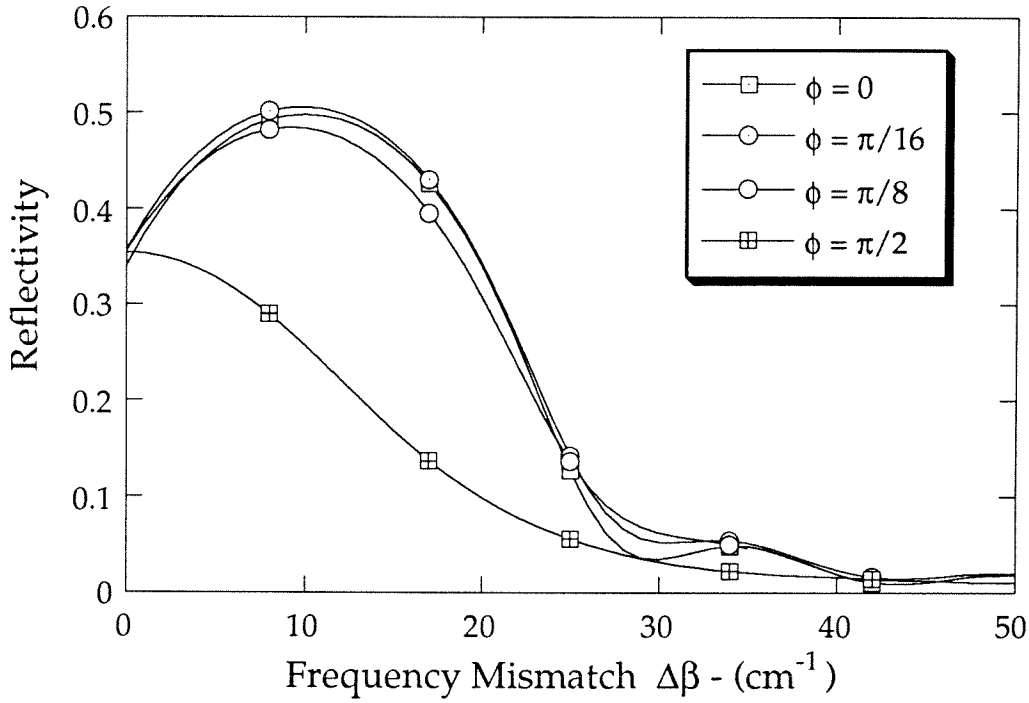

Figure 9-7. Reflectivity for the case $\alpha = 6/\text{cm}$, versus frequency mismatch, for a beam incident at z=0 on the index gratings of figure 9-6. The behavior is complex because the magnitude of the index grating near z=0 (the most efficient region of reflection) first increases then decreases with increasing photorefractive grating phase ϕ.

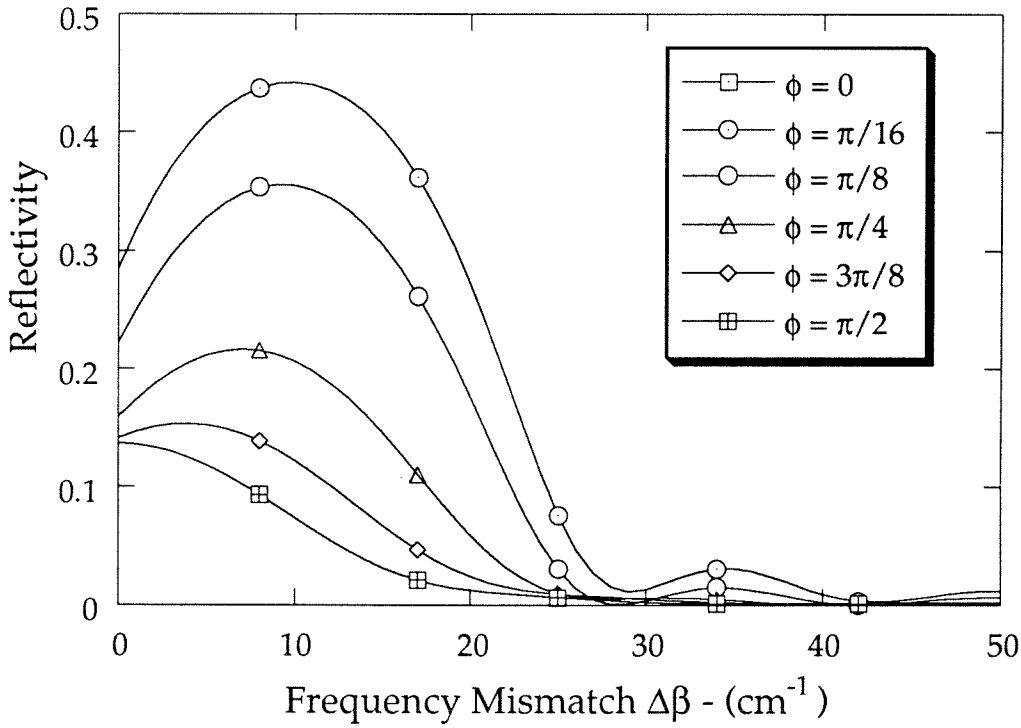

Figure 9-8. Reflectivity for the case α = 6/cm, versus frequency mismatch, for a beam incident at z=L on the index gratings of figure 9-6. Note the strong non-reciprocity compared with figure 9-7. The behavior for this case is simpler than that of figure 9-7. because the magnitude of the index grating near z=L (the most efficient region of reflection) decreases monotonically with increasing photorefractive grating phase ϕ.

rial has been described. Solutions were performed for arbitrary photorefractive grating phase ϕ. These solutions were obtained from the coupled equations by application of the corotating transform and subsequent reduction to second-order Pöschl-Teller equations. A significant result of the analysis was that the maximum of the frequency reflectivity occurs at a frequency different from that of the writing beams. This frequency shift is due to the phase coupling which the two beams enact on each other. In other words, when two beams interfere to write a grating in a photorefractive material, that grating is generally not Bragg matched to the beams.

In addition, numeric solutions of the identical procedure with a nonzero optical absorption in the material were presented. The chief differences between this case and the previous case are that with $\alpha \neq 0$, (1) the index grating can have its maximum at any plane in the volume of the crystal, rather than only at the entrance or exit facets and, (2) the reflectivity of the grating is nonreciprocal. Generally a beam incident antiparallel to the c-axis is reflected more strongly than a beam incident parallel to that axis.

9.4 Response of Fixed Holographic Gratings Written in the Copropagating Geometry

9.4.1 Introduction

In the previous sections the response of gratings written in the antisymmetric (counterpropagating) geometry were investigated. In particular, we examined the spectral response of the reflectivity of fixed gratings. In this section, a similar analysis is performed for fixed gratings written in the sym-

metric copropagating geometry (figure 2-4). Here the emphasis is not on the spectral response, but on the response of the beam coupling to phase modulation of one of the beams. In addition, the diffraction off dynamically written gratings is discussed. Diffraction is simply the reflectivity of the grating when $\Delta\beta = 0$, that is, when the beam being reflected is the same frequency as the beams which wrote the grating. The results of this section are applied in chapters two, five, seven, and eight. In chapter two the results are used to characterize the nature of the photorefractive two-beam coupling, and to describe the diffraction. In chapter five, the following results enable the explanation of diffraction phenomena in paraelectric KLTN crystals. In chapter seven, they are used in the development of methods for determining the photorefractive phase shift ϕ. Finally, in chapter eight, the results are applied to vibration detection in materials displaying the zero external field photorefractive (ZEFPR) effect; further applications to image processing and coherent data links are discussed there.

As illustrated in figure 2-4, two beams are symmetrically incident on a photorefractive crystal. A dynamically written refractive index grating is the result. This dynamically written grating is assumed to be fixed against optical erasure by some means. In practice, the grating will not actually be fixed, but the experimental conditions will allow this approximation. The writing beams are then replaced with two beams of arbitrary intensity and phase and of the same frequency incident along the same directions as the initial beams, i.e., at the Bragg angles. We calculate the beam coupling experienced by these new beams off the dynamically written grating now considered fixed. We ig-

nore the time dependent formation of dynamic gratings written by the new beams. This condition is only valid for a time period on the order of a second, depending on the intensity, but, as will be seen, this is much more than is required to obtain the necessary data.

9.4.2 Formulation of the Problem

The starting point is calculation of the two-beam coupling of two incident copropagating beams with amplitudes A(z) and B(z) in a photorefractive material. The well known coupled beam equations are given again as

$$A'(z)\cos\beta = \frac{i\pi\Delta n}{\lambda} e^{i\phi} B(z) - \frac{\alpha}{2} A(z) \tag{9.57a}$$

$$B'(z)\cos\beta = \frac{i\pi\Delta n^*}{\lambda} e^{-i\phi} A(z) - \frac{\alpha}{2} B(z) \tag{9.57b}$$

where λ is the wavelength of the interfering beams, α the optical absorption coefficient, and β the half-angle of beam intersection inside the material. Since these equations describe copropagating beams, the equation describing B'(z) is multiplied by the factor -1 as compared to (9.14b). The index of refraction is

$$n(z) = n_0 + \frac{1}{2}\left(\Delta n(z) e^{i\phi} e^{i K z} + c.c.\right). \tag{9.58}$$

Here ϕ is the photorefractive phase between the optical intensity grating and the induced index grating; $K = 2k \sin\beta$ is the nominal grating wavevector with $k = 2\pi n_o/\lambda$. Since the index grating is formed dynamically by the writing beams we have as before

$$\Delta n(z) = n_1 A(z) B^*(z)/ I(z) \tag{9.59}$$

where I(z) is the total intensity, and n_1 is the peak-to-peak amplitude of the index grating when A(z) = B(z) (see figure 2-5). Thus in the case of dynamic holography equations (9.57a) and (9.57b) can be rewritten

$$A'(z)\cos\beta = i\,g\,e^{i\phi}\frac{|B(z)|^2}{I(z)}A(z) - \frac{\alpha}{2}A(z) \qquad (9.60a)$$

$$B'(z)\cos\beta = i\,g\,e^{-i\phi}\frac{|A(z)|^2}{I(z)}B(z) - \frac{\alpha}{2}B(z) \qquad (9.60b)$$

where the coupling constant is defined as $g = \pi n_1/\lambda$ and I(z) is the sum of the intensities $I(z) = |A(z)|^2 + |B(z)|^2$. Again, since g is defined in terms of n_1 rather than Δn, it becomes a pure material parameter, the dependence on the relative beam intensities being factored out.

The method of solution of equation (9.60a) and (9.60b) is straightforward. First the optical absorption term is eliminated by the change of independent variable $A(z) = A(z)\exp[\alpha z/2]$ and $B(z) = B(z)\exp[\alpha z/2]$. Then we postulate solutions of the form

$$A(z) = a(z)e^{i\zeta_1} \qquad B(z) = b(z)e^{i\zeta_2} \qquad (9.61)$$

where a(z) and b(z) are real. Equations (9.60a, b) can be separated into two equations each describing the evolution of the amplitude and phase of the two beams:

$$a'(z) = -\sin\phi\; g\; b(z)^2 / I(z)\;\; a(z) \qquad (9.62a)$$

$$b'(z) = +\sin\phi\; g\; a(z)^2 / I(z)\;\; b(z) \qquad (9.62b)$$

$$\zeta_1'(z) = \cos\phi \; g \; b(z)^2 / I(z) \tag{9.63a}$$

$$\zeta_2'(z) = \cos\phi \; g \; a(z)^2 / I(z). \tag{9.63b}$$

Equations (9.62a,b) are solved in the usual way by converting them to equations for intensities using $I_1' = (a^2)' = 2\,a\,a'$, and similarly for I_2. Note that these "intensities" are not the true optical intensities, but are related to them by the multiplication of exp[αz]. We use the identity $b(z)^2 = I(z) - a(z)^2$ in (9.62a) and $b(z)^2 = I(z) - a(z)^2$ in (9.62b) to obtain simple Bernoulli equations[15] which are readily solved to yield

$$I_1(z) = e^{-\alpha z} \frac{I_1 (I_1 + I_2)}{I_1 + I_2 e^{+\Gamma z}} \tag{9.64a}$$

$$I_2(z) = e^{-\alpha z} \frac{I_2 (I_1 + I_2)}{I_1 e^{-\Gamma z} + I_2} \tag{9.64b}$$

where $A(z) = [I_1(z)]^{1/2}\exp[i\zeta_1]$ and $B(z) = [I_2(z)]^{1/2}\exp[i\zeta_2]$, and $\Gamma = 2g \sin\phi$ is the power coupling coefficient. The variable z is, for convenience, taken to be the unit of length in the propagation direction, so that $z = z_{old}/\cos\phi$. L is the effective thickness of the crystal: $L = d/\cos\beta$. We have defined $I_1 = I_1(0)$ and $I_2 = I_2(0)$ for convenience. The phases of the two beams are readily determined from equations (9.64a,b) and (9.63a,b) to be

$$\zeta_1(z) = \frac{1}{2} \cot\phi \; \ln[I_1 + I_2 e^{+\Gamma z}] \tag{9.65a}$$

$$\zeta_2(z) = -g \cos\phi \; z - \frac{1}{2} \cot\phi \; \ln[I_1 + I_2 e^{+\Gamma z}]. \tag{9.65b}$$

Note that the phases do not go to zero at $z = 0$! This condition is necessary for

equations (9.58/9.59) to hold, the phase difference $\zeta_2 - \zeta_1$ corresponding roughly to the phase difference between the intensity grating and the index grating (see equation (9.66) below). It is imperative to remember this condition when performing calculations, especially numeric ones; the results otherwise will be completely erroneous. The index grating in the material follows from equations (9.59), (9.64), (9.65), and the definition of A(z) and B(z) in terms of phase and intensity following (9.64). It is given by the form

$$\Delta n(z) = n_1 \sqrt{I_1 I_2} \left(I_1 e^{-\Gamma z/2} + I_2 e^{+\Gamma z/2} \right)^{i \cot\phi - 1} \qquad (9.66a)$$

when $\phi = 0$, we either take the limit with care in (9.66), or backtrack to equations (9.63). The index grating in this case reduces to

$$\Delta n(z) = n_1 \frac{\sqrt{I_1 I_2}}{I} \exp[\, i\, g\, z\, (I_2 - I_1)/I\,]. \qquad (9.66b)$$

Thus we have used the coupled mode equations to solve self consistently for the amplitudes and phases of two dynamically coupled beams in a photorefractive material. Dynamically coupled beams are those which yield an index grating given by (9.59). The solution for Δn given above can be reinserted into equations (9.57) or (9.60) to verify that the solution is self-consistent, as advertised.

The dynamic grating calculated above is considered fixed and we solve for the beam coupling of two arbitrary intensity and phase beams incident at the Bragg angle. When the new beams are the same intensities as the old ones but with different phases it is equivalent to simply phase shifting one of the original beams. When, instead, the phases of the new beams are un-

changed with respect to the original beams but the intensity of one new beam is reduced to zero, we are calculating the diffraction off the grating. The general case when both the phases and the intensities are different in the new beams is equivalent to calculating the response of the holographically coupled beams to fluctuations in the interferometer system. This application would be of importance in determining how phase and intensity fluctuations at the input of a photorefractive interferometer are magnified in the outputs.

9.4.3 Solution of Beam Coupling

We calculate the beam coupling of a new set of Bragg matched beams $T(0) = [P_1]^{1/2}\exp[i\psi_1]$ and $V(0) = [P_2]^{1/2}\exp[i\psi_2]$ off the index grating of equation (9.66). In analogy to equations (9.57a,b) we write the coupled mode equations

$$T'(z)\cos\beta = i g\sqrt{I_1 I_2}\, e^{+i(\phi+\theta)} \times \left(I_1 e^{-\Gamma z/2} + I_2 e^{+\Gamma z/2}\right)^{+i\cot\phi - 1} V(z) - \frac{\alpha}{2} T(z) \qquad (9.67a)$$

$$V'(z)\cos\beta = i g\sqrt{I_1 I_2}\, e^{-i(\phi+\theta)} \times \left(I_1 e^{-\Gamma z/2} + I_2 e^{+\Gamma z/2}\right)^{-i\cot\phi - 1} T(z) - \frac{\alpha}{2} V(z) \qquad (9.67b)$$

where I_1 and I_2 are the intensities of the writing beams, not to be confused with the new intensities P_1 and P_2. The phase $\theta = \zeta_1(0) - \zeta_2(0) - \psi_1(0) + \psi_2(0)$ is the phase difference between the intensity pattern of the beams which wrote the grating and the intensity pattern formed by T(0) and V(0). If $\theta = 0$ and $P_i = I_i$ for $i = 1,2$, it is easy to see that (9.67) reduces to (9.57) with the

index grating as defined in (9.66). Since the photorefractive effect is intensity independent, it is also true that if $\theta = 0$ and $P_i = c\, I_i$ for $i = 1,2$ where c is an arbitrary constant, the solutions are essentially unchanged except that all intensities are scaled by the constant factor c. Equations (9.67a,b) ignore the new dynamic grating which is written by beams T(z) and V(z) in the case $\theta \neq 0$.[12]

In order to solve (9.67a,b) we first eliminate the optical absorption term by the transformation $T(z) = T(z) \exp[\, \alpha z/2\,]$ and $V(z) = V(z) \exp[\, \alpha z/2\,]$, and then proceed along the same lines as before. (9.67a,b) are clearly of the correct form (9.25) to perform the independent variable transformation (9.26) to $\xi = \int g(z)\, dz$. By inspection of (9.67a,b) we write

$$\xi = 2 \int \frac{\sqrt{I_1 I_2}\; g \sin\phi}{I_1\, e^{-\Gamma z/2} + I_2\, e^{+\Gamma z/2}}\, dz$$

$$= 2 \tan^{-1}[\, \sqrt{I_2/I_1}\; e^{+\Gamma z/2}\,] \qquad (9.68)$$

which yields, after inverting,

$$e^{\Gamma z/2} = \sqrt{I_1/I_2}\, \tan[\xi/2]. \qquad (9.69)$$

This transformation is applied to (9.67a,b) and gives

$$a'(\xi) = \frac{i}{2 \sin\phi}\, e^{i(\phi+\theta)} \sqrt{I_1\, I_2}^{\,2i\eta} \left(\frac{2}{\sin[\xi]}\right)^{2i\eta} b(\xi) \qquad (9.70a)$$

$$b'(\xi) = \frac{i}{2 \sin\phi}\, e^{-i(\phi+\theta)} \sqrt{I_1\, I_2}^{\,-2i\eta} \left(\frac{2}{\sin[\xi]}\right)^{-2i\eta} a(\xi) \qquad (9.70b)$$

where $\eta = \cot\phi/2$. The lower case variables $a(\xi)$ and $b(\xi)$ are used to repre-

sent the functions $T(z)$ and $V(z)$; the change in notation is simply to emphasize the change in independent variable from z to ξ. Equations (9.70) are recognized to be of the form amenable to the corotating transform, where, by comparison with (9.1-8), we identify $f_1(\xi) = \sin(\xi)^{-2i\eta}$ so that

$$F(\xi) = -\eta \ln[\sin\xi]. \tag{9.71}$$

As in equation (9.30) we perform the transformation

$$a(\xi) = S(\xi)\, e^{iF(\xi)} \quad \text{and} \quad b(\xi) = W(\xi)\, e^{-iF(\xi)}. \tag{9.72}$$

Using (9.8a,b) with the previous two equations yields the second-order equations

$$S''(\xi) + \left[\frac{1}{4} + \frac{i\eta\,(i\eta-1)}{\sinh^2[i\xi]}\right] S(\xi) = 0 \tag{9.73a}$$

$$W''(\xi) + \left[\frac{1}{4} + \frac{i\eta\,(i\eta+1)}{\sinh^2[i\xi]}\right] W(\xi) = 0. \tag{9.73b}$$

Numerous manipulations were used to obtain the above results, including the identity $\sin^2 x = -\sinh^2[ix]$. Comparison with (9.9) shows that the above equations are again examples of the second Pöschl-Teller with parameters given by $\lambda = 0$, $\alpha = i$, and

$$l = \frac{3}{4} \qquad \kappa_T = i\eta \qquad \kappa_V = 1 + i\eta. \tag{9.74}$$

The parameters κ_T and κ_V are those required for (9.73a and b) respectively to match the notation of (9.9).

We apply the recipe (9.10a,b) to solve (9.73) and obtain

$$S(\xi) = t_1 \sin^{1-i\eta}\xi \cos\xi \; {}_2F_1[\tfrac{3}{4} - i\tfrac{\eta}{2}, \tfrac{5}{4} - i\tfrac{\eta}{2}; \tfrac{3}{2} - i\eta; \sin^2\xi] +$$

$$t_2 \sin^{i\eta}\xi \cos\xi \; {}_2F_1[i\tfrac{\eta}{2} + \tfrac{1}{4}, i\tfrac{\eta}{2} + \tfrac{3}{4}; \tfrac{1}{2} + i\eta; \sin^2\xi] \qquad (9.75a)$$

$$W(\xi) = v_1 \sin^{-i\eta}\xi \cos\xi \; {}_2F_1[\tfrac{1}{4} - i\tfrac{\eta}{2}, \tfrac{3}{4} - i\tfrac{\eta}{2}; \tfrac{1}{2} - i\eta; \sin^2\xi] +$$

$$v_2 \sin^{1+i\eta}\xi \cos\xi \; {}_2F_1[i\tfrac{\eta}{2} + \tfrac{3}{4}, i\tfrac{\eta}{2} + \tfrac{5}{4}; \tfrac{3}{2} + i\eta; \sin^2\xi] \qquad (9.75b)$$

which, using (9.72) is transformed back to

$$a(\xi) = a_1 \sin^{1-2i\eta}\xi \cos\xi \; {}_2F_1[\tfrac{3}{4} - i\tfrac{\eta}{2}, \tfrac{5}{4} - i\tfrac{\eta}{2}; \tfrac{3}{2} - i\eta; \sin^2\xi] +$$

$$a_2 \cos\xi \; {}_2F_1[i\tfrac{\eta}{2} + \tfrac{1}{4}, i\tfrac{\eta}{2} + \tfrac{3}{4}; \tfrac{1}{2} + i\eta; \sin^2\xi] \qquad (9.76a)$$

$$b(\xi) = b_1 \cos\xi \; {}_2F_1[\tfrac{1}{4} - i\tfrac{\eta}{2}, \tfrac{3}{4} - i\tfrac{\eta}{2}; \tfrac{1}{2} - i\eta; \sin^2\xi] +$$

$$b_2 \sin^{1+2i\eta}\xi \cos\xi \; {}_2F_1[i\tfrac{\eta}{2} + \tfrac{3}{4}, i\tfrac{\eta}{2} + \tfrac{5}{4}; \tfrac{3}{2} + i\eta; \sin^2\xi] \qquad (9.76b)$$

where t_1, t_2, v_1, v_2, are arbitrary constants and a_1, a_2, b_1, b_2 are constants to be determined. To simplify (9.76) we apply the hypergeometric identity[6]

$${}_2F_1[a, a+\tfrac{1}{2}; 2a; z] = 2^{2a-1} \frac{[1+\sqrt{1-z}]^{1-2a}}{\sqrt{1-z}} \qquad (9.77)$$

from which we readily obtain

$$a(\xi) = a'_1 \sin^{1-2i\eta}\xi \; (1+\cos\xi)^{i\eta-1/2} + a'_2 \; (1+\cos\xi)^{1/2-i\eta} \qquad (9.78a)$$

$$b(\xi) = b'_1 \; (1+\cos\xi)^{i\eta+1/2} + a'_2 \sin^{1+2i\eta}\xi \; (1+\cos\xi)^{-1/2-i\eta}. \qquad (9.78b)$$

Finally we convert back to the independent variable z using (9.68) and (9.69), and with some manipulation arrive at

$$T(z)\, e^{\alpha z/2} = C_1 \left(I_2 + I_1\, e^{-\Gamma z}\right)^{+i\eta\, -\, 1/2} + C_2 \left(I_2\, e^{+\Gamma z} + I_1\right)^{+i\eta\, -\, 1/2} \qquad (9.79a)$$

$$V(z)\, e^{\alpha z/2} = C_3 \left(I_2 + I_1\, e^{-\Gamma z}\right)^{-i\eta\, -\, 1/2} + C_4 \left(I_2\, e^{+\Gamma z} + I_1\right)^{-i\eta\, -\, 1/2}. \qquad (9.79b)$$

Here C_j are constants which are determined by the coupled equations and the boundary conditions. After comparing with equations (9.66) and (9.67) we see that the eigenfunctions of (9.79) seem quite plausible, and might perhaps have been arrived at without the cumbersome machinery of the intervening mathematics. But this retrospective argument is based on the knowledge that a solution actually exists, whereas that fact might not have been obvious before the mathematical analysis. The method described above, although tedious, is quite straightforward, and is guaranteed to yield the solution for problems which reduce to one of several forms of second-order differential equation.

In addition, the verification of solutions arrived at by guesswork is not completely trivial either. If one were to test the equations (9.79) in the original set of coupled differential equations, the result would be (using boundary conditions) four linear equations in the variables C_i (i = 1,4). The solution would be verified by confirming that the "constants" C_i were actually constant for several values of z. This procedure and many others were employed using the software package *Mathematica* to verify every equation in this chapter both analytically and numerically. It should be noted that the use of *Mathematica* was indispensable in debugging the solutions given throughout this thesis.

9.4.4 Determination of Coefficients

The equations for beam coupling off a dynamically written grating have been solved and it only remains to determine the coefficients C_j for the special cases of interest.

We solve the coefficients C_j for the special case where one or two of the reading beams are phase shifted relative to recording beams but their intensities are unchanged. This can be accomplished in practice by merely inserting a phase shift in the path of one of the recording beams. From equations (9.67a,b) and the definition of θ we use the boundary conditions $T(0) = I_1^{1/2} [I_1 + I_2]^{i\eta}$ and $V(0) = I_2^{1/2} [I_1 + I_2]^{-i\eta}$. It should be stressed that the term $[I_1 + I_2]$ raised to $\pm i\eta$ is purely a phasor which is required to ensure that the index grating have the proper form. With simple differentiation and insertion into the coupled equations (9.67) we determine the coefficients as

$$C_1 = \sqrt{I_1/(I_1+I_2)}\; I_2 \left(1 - e^{i\theta}\right) \tag{9.80a}$$

$$C_2 = \sqrt{I_1/(I_1+I_2)}\; \left(I_1 + I_2\, e^{i\theta}\right) \tag{9.80b}$$

$$C_3 = \sqrt{I_2/(I_1+I_2)}\; \left(I_2 + e^{-i\theta}\, I_1\right) \tag{9.80c}$$

$$C_4 = \sqrt{I_2/(I_1+I_2)}\; I_1 \left(1 - e^{-i\theta}\right). \tag{9.80d}$$

The combination of equations (9.79) and (9.80) completely determines the output amplitudes T(z) and V(z). Combination of the two equations yields

$$T(z)\, e^{\alpha z/2} = \sqrt{I_1/(I_1+I_2)}\; \Big[\; I_2 \left(1 - e^{i\theta}\right)\left(I_2 + I_1\, e^{-\Gamma z}\right)^{+i\eta\, -\, 1/2} + \left(I_1 + I_2\, e^{i\theta}\right)\left(I_2\, e^{+\Gamma z} + I_1\right)^{+i\eta\, -\, 1/2}\Big] \tag{9.81a}$$

$$V(z)\, e^{\alpha z/2} = \sqrt{I_2/(I_1+I_2)}\ \Big[\ (I_2 + e^{-i\theta} I_1)(I_2 + I_1 e^{-\Gamma z})^{-i\eta\ -\ 1/2} +$$

$$I_1 (1 - e^{-i\theta})\ (I_2 e^{+\Gamma z} + I_1)^{-i\eta\ -\ 1/2}\ \Big]. \qquad (9.81b)$$

From (9.81) the output intensities are calculated as

$$P_1(z) = e^{-\alpha z} \frac{I_1}{I_1+I_2} \frac{1}{I_2 e^{+\Gamma z} + I_1} \quad x$$

$$\Big[\ 2I_2^2 e^{+\Gamma z}(1 - \cos\theta) + (I_1^2 + I_2^2 + 2I_1I_2\cos\theta) + 2 I_2 e^{+\Gamma z/2} \quad x$$

$$\{(I_1 - I_2)(\,(1-\cos\theta)\cos[gz\cos\phi]) - (I_1 + I_2)\sin\theta\,\sin[g\cos\phi\, z]\}\ \Big] \qquad (9.82a)$$

$$P_2(z) = e^{-\alpha z} \frac{I_2}{I_1+I_2} \frac{1}{I_1 e^{-\Gamma z} + I_2} \quad x$$

$$\Big[\ 2I_1^2 e^{-\Gamma z}(1 - \cos\theta) + (I_1^2 + I_2^2 + 2I_1I_2\cos\theta) + 2 I_1 e^{-\Gamma z/2} \quad x$$

$$\{(I_2 - I_1)((1-\cos\theta)\cos[gz\cos\phi]) + (I_1 + I_2)\sin\theta\,\sin[g\cos\phi\, z]\}\ \Big]. \qquad (9.82b)$$

To summarize the work leading up to (9.82), we use two inputs A(0) and B(0) to write a dynamic grating in a photorefractive material. One beam is suddenly shifted in phase by θ, and the beams are now designated T and V. Equations (9.82) represent the output intensities $P_1(z) = |T(z)|^2$ and $P_2(z) = |V(z)|^2$ as a function of θ and ϕ. When $\theta = 0$, (9.82) reduce to the simple beam coupling equations (9.64).

In the special case $I_1 = I_2 = I$ the transmitted intensities reduce to a par-

ticularly simple form:

$$P_1(z)/I = 1 - \tanh[\Gamma z/2]\cos\theta - \frac{\sin(g\cos\phi\, z)}{\cosh[\Gamma z/2]}\sin\theta \qquad (9.83a)$$

$$P_2(z)/I = 1 + \tanh[\Gamma z/2]\cos\theta + \frac{\sin(g\cos\phi\, z)}{\cosh[\Gamma z/2]}\sin\theta. \qquad (9.83b)$$

The results for the cases $\phi = 0$ and $\pi/2$ also assume a particularly simple form for arbitrary I_1 and I_2[16]. For $\phi = 0$ we obtain

$$P_1(z) = I_1\left(1 - \frac{\kappa^2}{s^2}\sin^2[sz]\right) + I_2\frac{\kappa^2}{s^2}\sin^2[sz] - \frac{\kappa}{s}\sqrt{I_1I_2}\sin[2sz]\sin\theta$$
$$- \frac{\kappa\Delta}{s^2}\sqrt{I_1I_2}\sin^2[sz]\cos\theta \qquad (9.84a)$$

$$P_2(z) = I_2\left(1 - \frac{\kappa^2}{s^2}\sin^2[sz]\right) + I_1\frac{\kappa^2}{s^2}\sin^2[sz] + \frac{\kappa}{s}\sqrt{I_1I_2}\sin[2sz]\sin\theta$$
$$+ \frac{\kappa\Delta}{s^2}\sqrt{I_1I_2}\sin^2[sz]\cos\theta \qquad (9.84b)$$

where $s^2 = \kappa^2 + \Delta^2/4$, and $\kappa = g A_1A_2^*/I$, and $\Delta = (g/I_o)(I_2(0) - I_1(0))$. When $\phi = \pi/2$ the result is

$$P_1(z) = I_1\left[\cos^2[\gamma-\delta] + \zeta^2\sin^2[\gamma-\delta] + \zeta\sin[2(\gamma-\delta]\cos\theta\right] \qquad (9.85a)$$

$$P_2(z) = I_1\left[\zeta^2\cos^2[\gamma-\delta] + \sin^2[\gamma-\delta] - \zeta\sin[2(\gamma-\delta)]\cos\theta\right] \qquad (9.85b)$$

where $\zeta^2 = I_2(0)/I_1(0)$, $\gamma = \mathrm{Tan}^{-1}[\zeta e^{\kappa z}]$, and $\delta = \mathrm{Tan}^{-1}[\zeta]$.

The other special case considered is diffraction of a single incident beam off the fixed grating. Here, we take V(0) = 0 and T(0) as before. In this case we obtain, after following the same steps as leading to (9.80)

$$C_1 = \sqrt{I_1/(I_1+I_2)}\ I_2 \qquad (9.86a)$$

$$C_2 = \sqrt{I_1/(I_1+I_2)}\ I_1 \qquad (9.86b)$$

$$C_3 = \sqrt{I_2/(I_1+I_2)}\ I_1 = -C_4. \qquad (9.86c,d)$$

It can be shown easily that a phase shift θ of the incident beam does not change the diffracted intensities, it merely shifts the diffracted beam by θ. This, of course, is in stark contrast to the case of beam coupling where the magnitude and sign of the power transfer depend strongly on a beam phase shift.

Combining (9.79) with the coefficients (9.86) yield the transmitted and diffracted intensities. They are

$$P_1(z) = e^{-\alpha z}\ \frac{I_1}{I_1 + I_2}\ \frac{\left[I_2^2\, e^{\Gamma z} + I_1^2 + 2\, I_1\, I_2\, e^{\Gamma z/2} \cos[\, g \cos\phi\, z]\right]}{I_1 + I_2\, e^{\Gamma z}} \qquad (9.87a)$$

$$P_2(z) = e^{-\alpha z}\ \frac{I_1^2\, I_2}{I_1 + I_2}\ \frac{\left[e^{\Gamma z} + 1 - 2\, e^{\Gamma z/2} \cos[\, g \cos\phi\, z]\right]}{I_1 + I_2\, e^{\Gamma z}}. \qquad (9.87b)$$

Again, for the condition $I_1 = I_2 = I$ the transmitted and diffracted intensities reduce to a simple form

$$P_1(z)/I = \frac{e^{-\alpha z}}{2}\left(1 + \cos[g \cos\phi\, z]/\cosh[g \sin\phi\, z]\right) \qquad (9.88a)$$

$$P_2(z)/I = \frac{e^{-\alpha z}}{2}\left(1 - \cos[g \cos\phi\, z]/\cosh[g \sin\phi\, z]\right). \qquad (9.88b)$$

To recap, the analysis leading to (9.81) entails writing a dynamic grating in a photorefractive material using two inputs A(0) and B(0). B(0) is suddenly blocked so that only A(0) illuminates the crystal. (These beams are renamed

T(0) and V(0).) Equation (9.87) represents the transmitted intensity $P_1(z) = |T(z)|^2$ and the diffracted intensity $P_2(z) = |V(z)|^2$ as a function of ϕ. This quantity is fundamental to many experiments in beam coupling; for example, one figure of merit of a photorefractive material is its diffraction efficiency in a given length.

9.5 Summary

A general mathematical formalism was developed to solve certain linear first-order coupled differential equations which commonly occur in optical beam coupling analyses. The formalism entailed the reduction of first-order coupled equations to two second-order equations - either second Pöschl-Teller equations or symmetric top equations - by application of the "corotating transform." Reductions to other types of solvable equations might also occur, although none were encountered in the preceding studies. The formalism was applied to beam coupling and diffraction off dynamically written fixed holographic gratings in both the copropagating and the counterpropagating geometries. The spectral response of fixed holographic interference filters was examined. A numerical study of the case $\alpha \neq 0$ was also described and compared to the lossless analytic solution. The coupling of beams phase shifted with respect to a dynamically written grating was discussed.

The mathematical tools derived in this chapter should be applicable to a variety of problems in the study of beam coupling. Several examples which were not addressed in this chapter are the response of counterpropagating beams to phase fluctuations and the frequency response of copropagating

beams with a grating written at a reference wavelength. In chapter five the methods described above are applied to solve the diffraction in a photorefractive material material with an electric field controlled coupling constant.

References for chapter nine

[1] S. Wolfram, *Mathematica* , 2nd ed. , pp. 684ff, Addison-Wesley, Redwood City, California, (1991).

[2] R. J. Burden, J. D. Faires, A. C. Reynolds, *Numerical Analysis* , 2nd ed. , chapter 5, Prindle, Weber, & Schmidt, Boston, Massachusetts, (1981).

[3] D. Zwillinger, *Handbook of Differential Equations* , Academic Press, New York, New York, (1989). This is an excellent reference for solving differential equations.

[4] A. O. Barut, A. Inomata, and R. Wilson, "Algebraic treatment of second Pöschl-Teller, Morse-Rosen, and Eckart equations," J. Phys. A: Math. Gen. **20**, 4083-4090 (1987).

[5] L. Infeld and T. E. Hull, "The factorization method," Rev Mod Phys **23**, 21-68 (1951).

[6] A. Abramowitz and I. Stegun, *Handbook of Mathematical Functions* , chapter 15, Dover Publishing, New York, (1972).

[7] G. Rakuljic, A. Yariv, and V. Leyva, "High resolution volume holography using orthogonal data storage," Photorefractive Materials, Effects, and Devices Conference of OSA, July 29-31, 1991, Beverley, MA, paper MD-3.

[8] G. Rakuljic, V. Leyva, and A. Yariv, "Optical data storage using orthogonal wavelength multiplexed volume holograms," Opt. Lett. Oct 15, 1992.

[9] V. Leyva, G. Rakuljic, and A. Yariv, "Volume holography using orthogonal data storage approach," OSA annual meeting Nov. 3-8, 1991, San Jose,

California, paper FU-7.

[10] G. Rakuljic, V. Leyva, K. Sayano, and A. Yariv, "Comparison of angle and wavelength multiplexing in holographic data storage," (invited paper) OSA annual meeting Sept 20-25, 1992, Albuquerque, New Mexico, paper WE-2.

[11] J. O. White, S. Z. Kwong, M Cronin-Golomb, B. Fischer, and A. Yariv, in *Photorefractive Materials and their Applications II* , Eds. P. Günther and J. P. Huignard, chapter 4, Springer-Verlag, Berlin, (1989).

[12] C. Gu and P. Yeh, "Diffraction properties of fixed gratings in photorefractive media," J. Opt. Soc. B **7**, 2339-2346 (1990).

[13] M. Segev, A. Kewitsch, A. Yariv, and G. Rakuljic, "Self-enhanced diffraction from fixed photorefractive gratings during coherent reconstruction," Appl. Phys. Lett. , **62**, to appear March 1, 1993.

[14] A. Yariv, *Optical Electronics* 4th ed. , p. 496, Saunders college publishing, Philadelphia, (1991).

[15] J. Mathews and R. L. Walker, *Mathematical Methods of Physics* , chapter 1, Addison-Wesley, Redwood City, California, (1970).

[16] R. Hofmeister and A. Yariv, "Vibration detection using dynamic photorefractive gratings in KTN/KLTN crystals," Appl. Phys. Lett. , **61**, 2395-2398 (1992).

Chapter Ten

Summary and Future Directions

10 . 1 Summary

Both research and applications in the field of photorefractive materials have been hindered by a severe dearth of high quality, readily obtainable materials. The photorefractive crystal growth effort at the California Institute of Technology was initiated to respond to this need, and it was the aim of this thesis to develop a new photorefractive material and explore applications particular to its characteristics.

Photorefractive potassium lithium tantalate niobate (KLTN) was grown using the top seeded solution growth method. The composition of the material was tailored to yield a phase transition at a predetermined temperature within the range $180^{o}K \leq T_{c} \leq 310^{o}K$. Various transition metal dopants, most notably copper and vanadium, were admixed in the flux to provide the photorefractive donor species. These photorefractive crystals were of exemplary optical quality over the composition range described, and ranged in size from 4-20gm.

The photorefractive properties of the KLTNs were investigated in the paraelectric (centrosymmetric) phase as functions of a uniform applied elec-

tric field. In this high temperature phase, the linear electro-optic effect is forbidden by the symmetry of the material, and the photorefractive response is described by the Kerr effect. It was shown that the applied electric field induces effective linear electro-optic coefficients that are proportional to the applied field. This property was harnessed to demonstrate electric field control of two-beam coupling and diffraction in the material.

When no electric field was applied, however, the photorefractive response did not vanish as expected by the conventional electro-optic theory. This zero electric field photorefractive (ZEFPR) effect was proved to result from local Jahn-Teller distortions of ions whose concentration in the material was spatially modulated by an incident intensity pattern. The distortions created a photoelastic strain index grating that was identically in-phase with the intensity pattern. The ZEFPR effect has not been previously reported, probably because it is weaker than the conventional effect and would be obscured in any material in which the conventional effect is not forbidden.

The identically in-phase condition of the ZEFPR index grating lends unique properties to this effect. No two-beam intensity coupling occurs with such a grating, however, if the phase of the grating is suddenly and artificially shifted, beam coupling occurs in linear proportion to the amount of phase shift. This allows the implementation of numerous self aligning (robust) and yet extremely sensitive linear phase-to-intensity transducers. An all-optical microphone was demonstrated with this principle and several other devices were proposed.

A mathematical theory of the response of beams incident on a photore-

fractive grating was developed to explain the results observed in the ZEFPR materials. The mathematical machinery was used to prove the linear vibration response of the ZEFPR material and the quadratic response of a diffusion limited photorefractive material. Subsequently it was expanded to determine the response of a material with arbitrary phase shift. With these techniques, the photorefractive phase and coupling constant of photorefractive materials could be measured. The diffraction properties of paraelectric KLTN were also described using the new mathematical tools. Finally, the frequency response of reflection of an incident beam off a fixed holographic grating was derived for the case that the grating was written with counterpropagating beams. The mathematical framework established in solving these beam coupling problems was presented in a sufficiently general manner to be easily applicable to other problems.

10 . 2 Future Directions

The most clear-cut projects for future work are in crystal growth. Extensive effort has been expended in the design and construction of a new crystal growth system which incorporates numerous improvements over the old system. The new system will have a more uniform temperature profile and better insulating components. A ceramic spindle has been added to allow crucible rotation and thus a more homogeneous mixing of the flux during growth. The process parameters will all be computer controlled to provide greater flexibility of the growth variables. The improved system will be used to grow KLTNs with previously untried dopants including certain lanthanides, as well as an entirely new class of ferroelectric oxide material which will require the higher operating temperature capacity of this new system.

Substantial research remains to be done to characterize the photorefractive response of paraelectric centrosymmetric materials near their phase transition. Hologram fixing has been observed in KLTN near the phase transition but has not yet been quantified sufficiently to merit disclosure. It also remains to be seen whether such fixed gratings can be obtained at room temperature. This will likely depend on the photorefractive dopant used. Thermal fixing is being investigated as an alternate means of permanent data storage. This may allow the electric field controlled readout of fixed holograms when the crystal is operated near its para/ferroelectric phase transition.

Finally, the applications of the ZEFPR effect have been demonstrated only in an inchoate form, or not at all. The fundamental limits of sensitivity of the all-optical ZEFPR microphone have not yet been explored. Development of the microphone should be pursued to the prototype stage. Other applications of the ZEFPR effect, the self-aligning data link, for example, should be demonstrated in the lab, to prove their feasibility.